



Degradation of Nile Blue by Photocatalytic, Ultrasonic, Fenton, and Fenton-like Oxidation Processes

Nuket Kartal Temel 

Faculty of Science, Sivas Cumhuriyet University, Sivas, Türkiye

Abstract: The aim of this study is to investigate new catalytic systems for the degradation of a dye that has been classified as first-degree toxic pollutant. Advanced oxidation process such as photocatalytic oxidation, ultrasonic oxidation, Fenton, and Fenton-like constitute a promising technology for the treatment of wastewater containing organic compounds. Waste effluents from textile industries are a major source of water pollution. These wastewaters contain dyes, which have high toxicity and low biodegradability. In this study, degradation of Nile Blue (NB), an azo dye, was studied using the photocatalytic oxidation (TiO_2 and silver-loaded TiO_2 (Ag-TiO_2) as catalyst), ultrasonic oxidation, Fenton ($\text{Fe(II)/H}_2\text{O}_2$), and Fenton-like ($\text{Cu(II)/H}_2\text{O}_2$, $\text{V(IV)/H}_2\text{O}_2$) processes. It was found that the photocatalytic degradation of NB increased with decreasing pH, and the degradation rate also increased in the presence of TiO_2/UV compared to UV irradiation alone. In addition, Ag loading on TiO_2 dramatically reduced the degradation time. The ultrasonic degradation of NB was also studied using different initial dye concentrations at different pH values and amplitudes. Concentrations of Fe(II) , Cu(II) , V(IV) and H_2O_2 on degradation ratio were investigated. It is found that Fe(II) ion is more effective than Cu(II) and V(IV) ions in the degradation of NB.

Keywords: Photocatalytic oxidation, Ultrasonic oxidation, Fenton's reagent, Fenton-like reagent, Dye.

Submitted: March 01, 2024. **Accepted:** May 13, 2024.

Cite this: Kartal Temel, N. (2024). Degradation of Nile Blue by Photocatalytic, Ultrasonic, Fenton, and Fenton-like Oxidation Processes. Journal of the Turkish Chemical Society, Section B: Chemical Engineering, 7(1), 77-86.

*Corresponding author. E-mail: nkartal@cumhuriyet.edu.tr.

1. INTRODUCTION

Today, water pollution is one of the main factors that adversely affect human health. At the beginning of the 21st century, mankind has to face the problem of water as a major threat. Especially, industrial activity generates high amounts of wastewater, which resistant the biodegradability. Indeed, azo dyes represent a significant class of synthetic organic compounds widely used in various industries, including textiles, cosmetics, food, and pharmaceuticals. They are characterized by the presence of one or more azo ($-\text{N}=\text{N}-$) groups, which give them their distinctive color properties (Hsueh et al., 2005; Neamtu et al., 2003; Chacón et al., 2006).

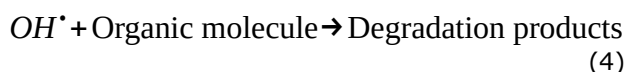
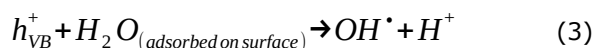
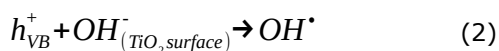
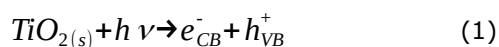
These industries effluents vary widely in composition, containing organic, inorganic compounds and high color and COD levels. Colored textile wastewater contains persistent dyes. Many of these dyes have been reported to be toxic and carcinogenic to humans (Anliker, 1979). Direct discharge of these effluents can result in the

creation of toxic aromatic amines in the receiving environment under anaerobic conditions. This can lead to soil and groundwater contamination, necessitating appropriate treatment before discharge into the environment. Various methods are used to remove color from dye wastewater. However, these methods are not effective when treating wastewater that contains both soluble and insoluble dyes. For instance, the process of ozonation oxidation can efficiently remove color from wastewater that contains soluble dyes, such as reactive dyes (Perkins et al., 1980). However, it is important to note that ozonation oxidation is not effective in the degradation insoluble dyes, such as disperse dyes. Coagulation is an effective method for the degradation insoluble dyes, but it is not effective for soluble dyes (Netpradit et al., 2003). Finally, Fenton's reagent (Fenton, 1894) has been demonstrated to be effective in the degradation both soluble and insoluble dyes (Kuo 1992).

The Advanced Oxidation Techniques (AOPs) are primarily based on the generation of the hydroxyl radical (OH^\bullet), which has significant oxidation power.

The destruction of pollutants is traditionally attributed to the highly reactive hydroxyl radical (OH^\bullet). The application of these methods for various chemicals involving different processes was well reviewed by Titus et al. (Titus et al., 2004).

Photocatalytic oxidation processes are commonly known as AOPs. When a photon with energy matching or exceeding the semiconductor's band gap energy strikes the semiconductor surface, a conductive band electron will move to its valence band, leaving a positively charged hole (Saien et al., 2003). The first step in this photo-oxidation process is thought to be the creation of free hydroxyl radicals (Ollis et al., 1991; Wu et al., 1999). Hydroxyl radicals are produced through the oxidation of water (OH^- ions) by valence band positively charged holes. The mechanism of TiO_2 based photocatalytic degradation of dyes was described in previous work (Sökmen et al., 2001).

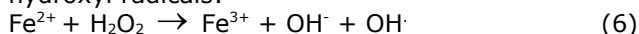


However, the dissolved O_2 molecules are transformed into anionic superoxide ($\text{O}_2^{\bullet -}$) radicals via electrons from conductive band.

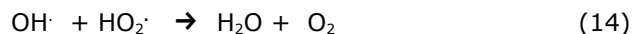
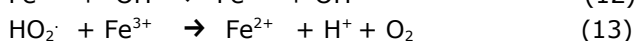
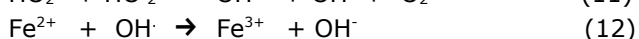
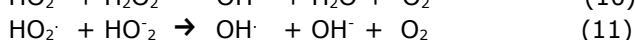
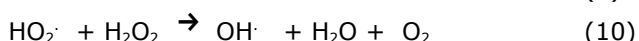
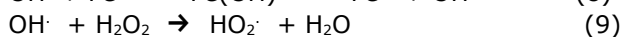
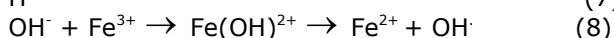
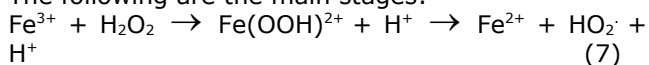


Fenton's reagent is a mixture of ferrous (Fe (II)) ions and hydrogen peroxide that produces OH^\bullet radicals (as shown in equations 6-14). It has been widely used for the oxidation of organic matter in water (Goldstein et al., 1993; Nidheesh et al., 2013). The main advantage of this method is the complete destruction of contaminants, which are converted into harmless compounds such as CO_2 , water, and inorganic salts (Xu et al., 2004). The mechanism of Fenton and Fenton-like oxidation of dyes was described in a previous work (Sökmen et al., 2011).

Ferrous ions react with hydrogen peroxide to form hydroxyl radicals:



The following are the main stages:



Fenton oxidation has been used to degradation effluents from textile dyeing and dye manufacturing processes (Kim et al., 2004). Compared to other oxidation processes, such as $\text{UV}/\text{H}_2\text{O}_2$, Fenton oxidation is relatively inexpensive (Dutta et al., 2001). Recently, Fenton oxidation has been increasingly used in various treatment processes due to its ease of operation, simple system, and ability to work in a wide range of temperatures (Solozhenko et al., 1995).

For the oxidation of organic matter in water, Fenton's reagent has been widely used (Safarzadeh-Amiri et al., 1996). Its main advantage is that it thoroughly removes contaminants, producing innocuous materials such as CO_2 , water, and inorganic salts (Neyens and Baeyens 2003). As discussed by Goldstein et al. (1993), new homogenous catalyst systems producing hydroxyl radicals can be developed for the oxidative degradation of organic compounds. Employing this type of catalyst systems would be an alternative to classical Fenton catalyst since it would help reducing hydroxide mud. On the other hand, it was previously reported that (Allen et al., 2002) multiple hydroxylated oxidation products were produced in Fenton-like systems employing Cu^{2+} , V^{4+} , Ti^{3+} catalyst which were more effective oxidant in some cases (Sökmen et al., 2002). Therefore, application of these type systems should be studied for oxidative degradation of different organic compounds.

Heterogeneous metal-supported catalysts are replacing homogeneous catalysts (Wang et al., 2016; Liu et al., 2021). The catalytic activity can be attributed to the generation of hydroxyl radicals from hydrogen peroxide, which are activated by iron ions and are simultaneously leached from the support material as a homogeneous catalyst (Jiang et al., 2010; Liu et al., 2007; Kumar et al., 2020; Sun et al., 2021; Abo-Farha 2010).

In this study, the degradation of NB dye from wastewater by AOP methods such as photocatalytic oxidation, ultrasonic oxidation, Fenton and Fenton-like were investigated. Catalytic action of copper(II) and vanadium(IV) ions in the presence of hydrogen peroxide were studied and compared with Fenton's reagent.

2. EXPERIMENTAL SECTION

Nile Blue (NB, $\text{FW} = 353.85 \text{ g mol}^{-1}$) was kindly supplied from a textile dye branch of Ciba (Germany) in Turkey. Deionized water (100 mL) was used to make the NB solutions of desired concentration (100 μM).

2.1. Degradation of NB by Photocatalytic Process

Initially, 100 mL of an aqueous dye (NB) sample and 0.1 g of TiO_2 (either neat TiO_2 or Ag-loaded

TiO₂) were placed in a 250 mL Pyrex flask, which was covered with aluminum foil and fitted with a condenser. After adjusting the pH of the dye solution, the stirred suspension was illuminated with one OSRAM-Ultra Vitalux 300W lamp at about 5.8W at 254nm. To separate the TiO₂ for residual dye analysis, 3-mL aliquots of the irradiated sample were taken at regular intervals and centrifuged twice at 3500 rpm for 10 minutes. The concentration of the residual dye in the supernatant was monitored by spectrophotometry at a wavelength of 600 nm for 60 minutes.

2.2. Degradation of NB by Fenton and Fenton-like Processes

Hydrogen peroxide (%33 w/w) was obtained from Merck and used at a various range of concentration. Required amount of catalyst was dissolved in 5 mL of 0.1 M H₂SO₄ solution. H₂O₂ concentration was adjusted to desired ratio of catalyst to H₂O₂. Catalyst and H₂O₂ concentration ratios were used as 1:1, 1:5, 1:10 and 1:20.

Experimental studies were designed in a sealed flask. In the first stage 100 mL stock solution of dye and desired amount of catalyst were placed and pH was adjusted to 2.0. H₂O₂ was then slowly added to the reaction mixture. The reaction time in both Fenton and Fenton-like process was recorded after addition of H₂O₂ solution and 3-mL portions were withdrawn at certain intervals and absorbance of NB were measured at 600 nm.

2.3. Degradation of NB by Ultrasonic Process

Sonolyses were performed with an ultrasonic processor (Cole Parmer Instruments, Vernon Hills, Illinois, USA) operating at 20 kHz and 25 °C. In each experiment, 250 mL of aqueous dye sample with

desired concentration was placed in to a 500 mL pyrex flask and its pH was adjusted. The solution was poured into ultrasonic processor and mechanical stirrer was used. At certain reaction intervals, 3 mL of sample was withdrawn. Concentrations of the residual dye in the supernatant were spectrophotometrically monitored for 60 min at 600 nm.

The following equation was used to calculate the degradation percentage from the relative abundance of the corresponding NB.

$$\text{Degradation} = \frac{[NB]_0 - [NB]_t}{[NB]_0} \times 100 \quad (15)$$

t: time of sample collection

3. RESULTS AND DISCUSSION

The structure of the NB is given in Fig.1. Absorption spectra of the dye solutions were recorded and given in Figure 2 in the absence and presence of catalyst. NB has a maximum at 600 nm in aqueous solution at pH 2.0. From the observation it is visible that no new absorption peaks occurred near the original maximum wavelength.

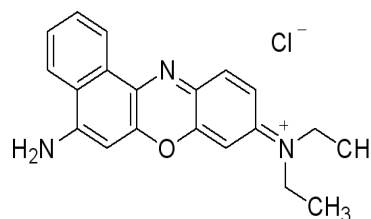


Figure 1: Chemical structure of NB.

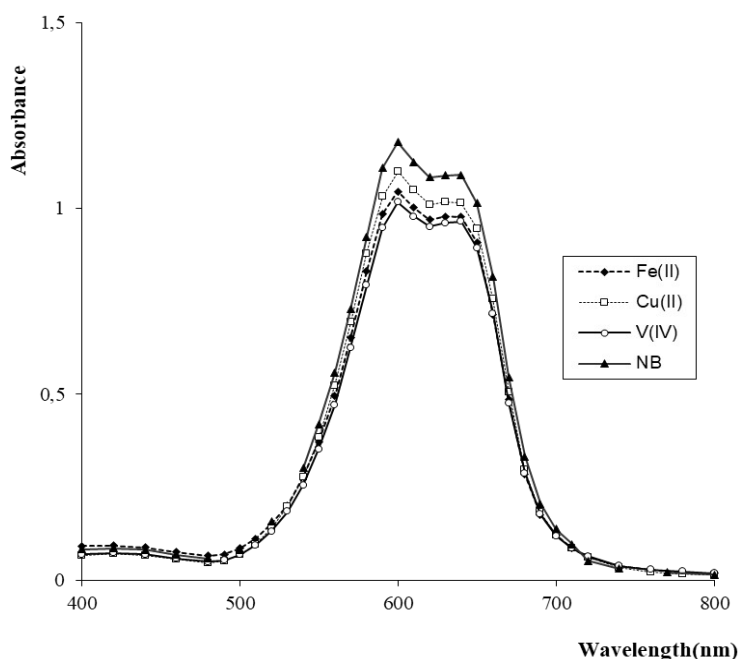


Figure 2: Spectrum of NB and spectra when Fe(II), Cu(II), V(IV) salts are added to the NB solution.

3.1. Photocatalytic Degradation of NB

In the presence of TiO₂ particles, with and without UV illumination, a series of experiments were performed using NB dye. The same procedure was repeated for Ag-loaded TiO₂. The results are shown in Figure 3. Each data point shown in all the figures represents the average of three replicates.

It can be seen that the degradation time for the NB dye is dramatically reduced by the Ag-loading. While the undoped TiO₂ degradation approximately 50% of the initial amount within 15 min, the Ag-loaded TiO₂

degradation 90% of the initial amount in the same time period. As shown in Figure 3, the degradation of the dye in the absence of TiO₂ was very slow with UV irradiation, and the degradation with only TiO₂ without UV irradiation (in the dark) is also very slow. Complete degradation time is approximately 30-60 min with TiO₂ and UV irradiation. Complete degradation of the dye took as little as 20 minutes with the Ag-loaded catalyst.

As noted previously, the Ag-loading dramatically shortened the degradation time for the NB dye. Increasing the amount of Ag-TiO₂ steadily affected the degradation as shown in Figure 4.

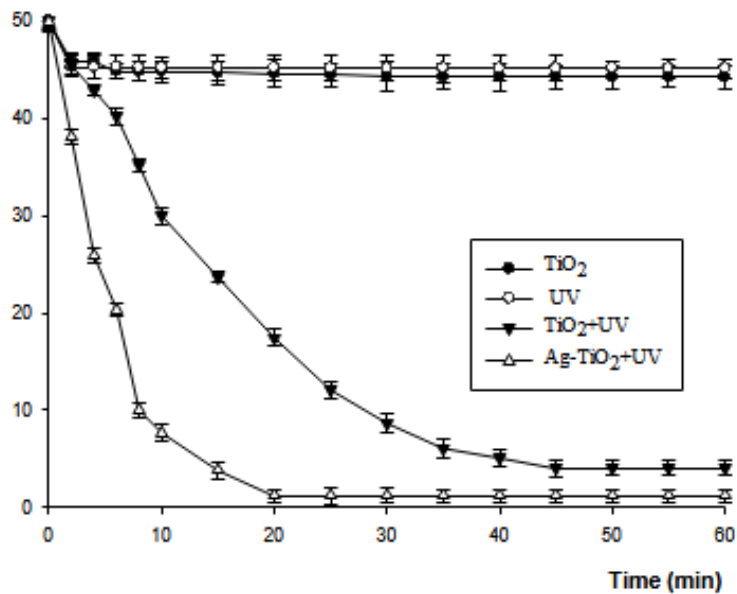


Figure 3: Photocatalytic degradation of NB versus irradiation time for several systems at pH 2.0.

The increase in removal rate is due to: (i) increasing the amount of catalyst, which increases the number of adsorbed dye molecules, and (ii) increasing the density of particles in the area of illumination (Woislawski 1953). The degradation rate is

proportional to the TiO₂ concentration at TiO₂ concentrations below about 1.0 g L⁻¹. It is likely that the degradation rate was limited above 2.0 g L⁻¹ of TiO₂ because the UV light can be blocked by the catalyst itself.

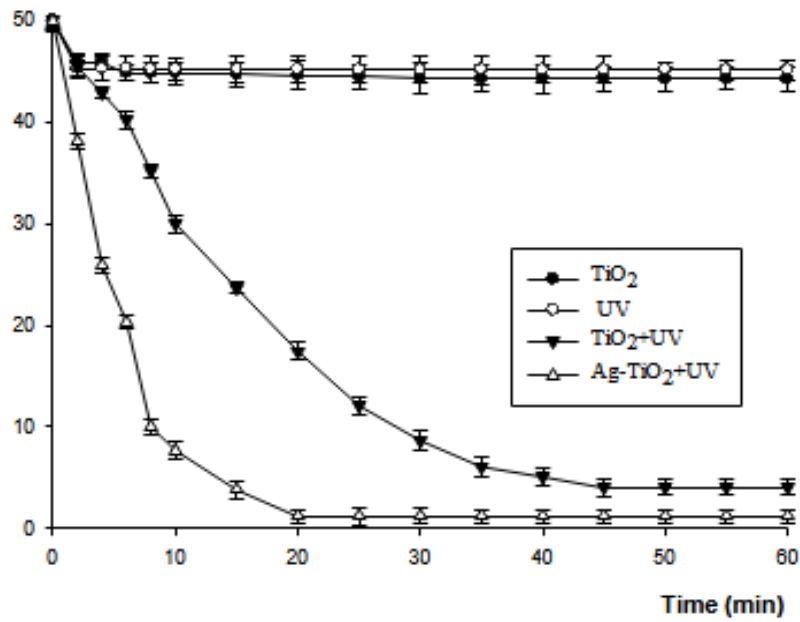


Figure 4: Photocatalytic degradation of NB versus irradiation time in TiO₂/UV and different amount of Ag-TiO₂/ UV systems at pH 2.0.

3.2. Ultrasonic Degradation of NB

The amplitude is another important factor that influences the efficiency of ultrasonic degradation. The study examined the impact of amplitude within the 20-50% range. The results are presented in Figure 5. As shown in the figure, the final

concentration of NB decreases as the amplitude increases. According to reference (Kidak and Ince 2006), the reason for this is that as the volume decreases at the same energy input, there is a higher amount of energy dissipated to the system.

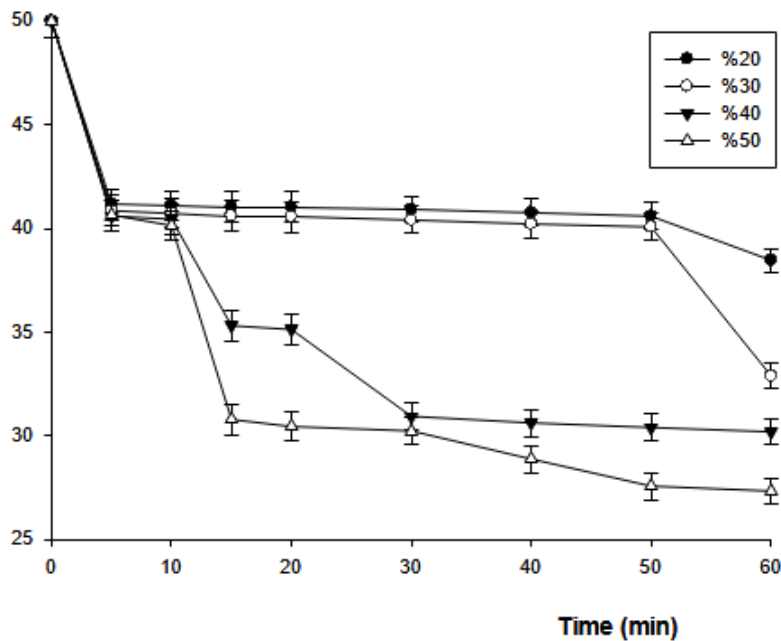


Figure 5: Effect of amplitude on the ultrasonic decolorization of NB at pH 2.0.

3.3. Degradation of NB with Fenton and Fenton-like processes

Time-dependent degradation of NB with Fenton’s reagent is shown in Figure 6 employing different catalysts to hydrogen peroxide ratio at pH 2.0.

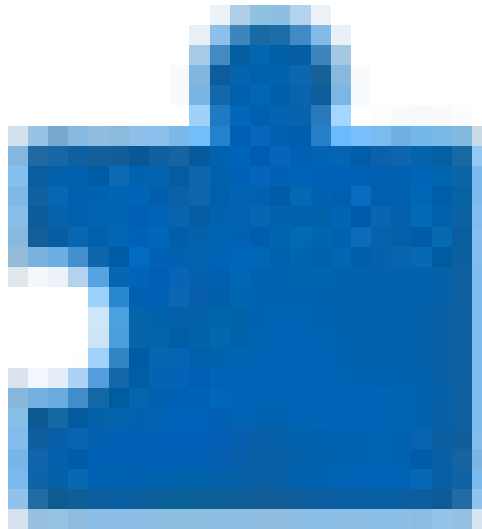


Figure 6: Time-dependent degradation of NB with Fenton’s reagent at pH 2.0.

Time-dependent degradation of NB with Fenton-like’s reagents are shown in Figure 7 and in Figure 8.

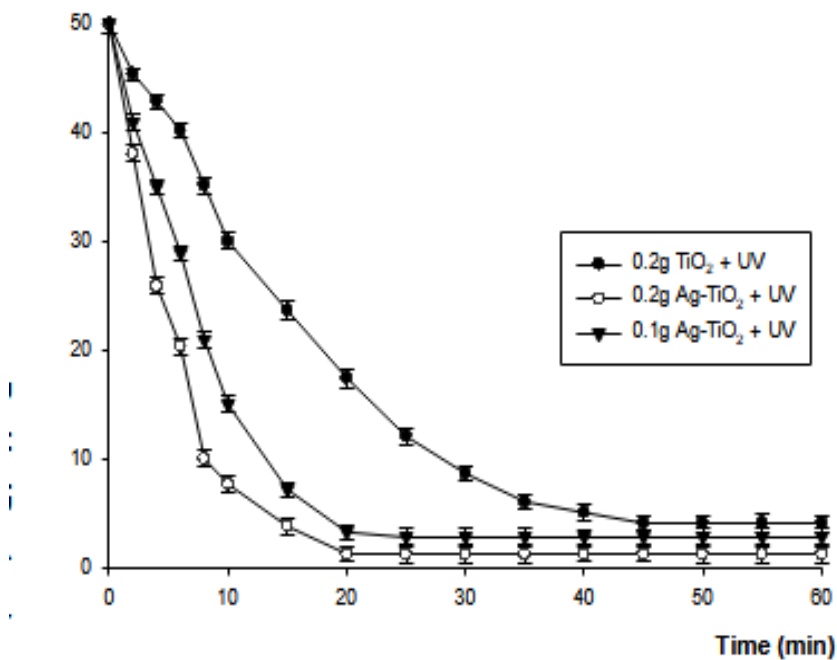


Figure 7: Time-dependent degradation of NB with Fenton-like’s reagent (Cu(II)/H₂O₂) at pH 2.0.

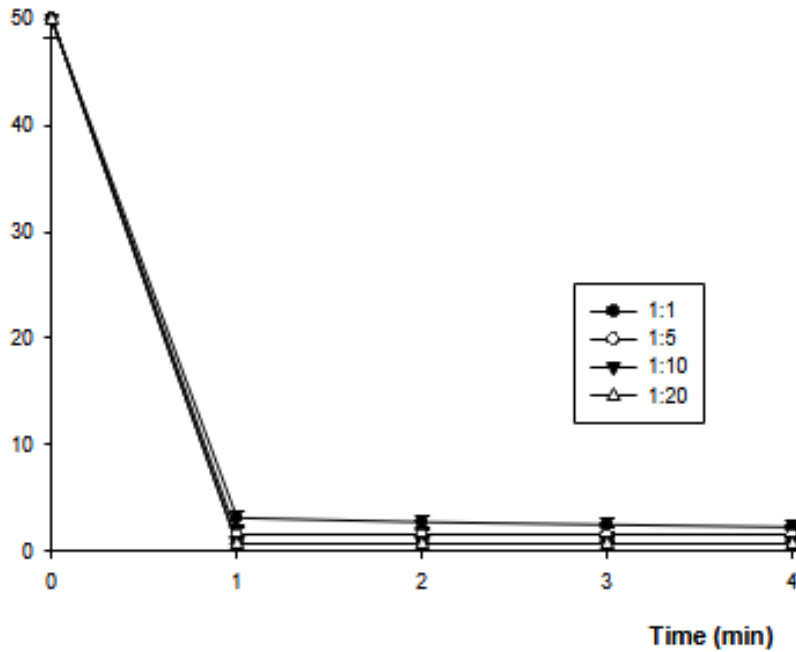


Figure 8: Time-dependent degradation of NB with Fenton-like reagent (V(IV)/H₂O₂) at pH 2.0.

The concentration of the residual dye in solution was calculated. Time versus concentration of the residual dye in solution results are shown Figure 9.

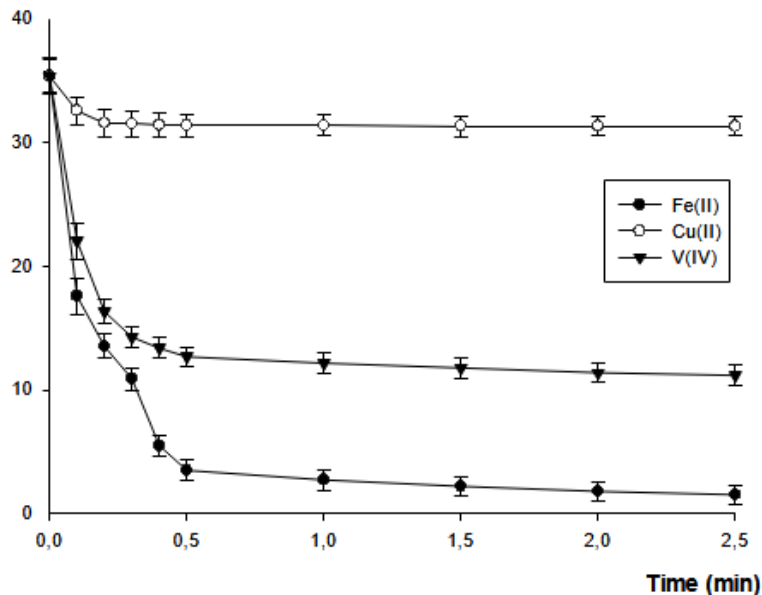


Figure 9: The concentration of the residual dye in solution after every process as a function of reaction time at pH 2.0.

4. CONCLUSION

NB dye is a common chemical used in the dyeing and printing industries, particularly in the production of cellulose acetate rayon, calico cotton, and wool. Consequently, the compound was selected as a model contaminant with which to

evaluate the photocatalytic, ultrasonic, Fenton processes and Fenton-like activity. Singha, j. et al. were concluded that the photocatalytic oxidation shows high photocatalytic activities for the degradation of NB exhibited excellent degradation (93% removal in 120 min). Saleem and co-workers degradation NB by using TiO₂ nanoparticles as

Kartal Temel, N., JOTCSB. (2024), 7(1), 77-86.

photocatalyst in the presence of H₂O₂ (95% removal in 100 min).

In a similar study, Yasmeen, S., et al. observed a 97% reduction in NB in a 220-minute photocatalytic oxidation process. Yasmeen, S., et al. also found 90% removal of NB in 5 hours by photocatalytic oxidation. Kushwaha^a et al. (2019) and Kushwaha^b et al. (2018), obtained 66% removal of NB in 12 min and 92.46% removal in 20 min by Fenton and Fenton-like oxidation, respectively. The results obtained in our study are 95.64% for Fenton, 11.51% for Fenton-like(Cu(II)), 71.73% for Fenton-like (V(IV)) after 2 minutes. A comparison of the results obtained in this study with those reported in the literature reveals that the Fenton process is more efficient than other methods, with higher yields achieved in a shorter time.

In this work, the degradation of NB by photocatalytic processes, ultrasonic processes, Fenton processes and Fenton-like processes is studied. Among these methods, Fenton and Fenton-like processes was found to be the most effective method. In this process, complete degradation was observed after 2 minutes of treatment. Ag-loaded TiO₂/UV photocatalysis was found to be the most efficient method after Fenton oxidation to degrade NB. The Fenton and Fenton-like processes described here are more advantageous than other oxidation processes because they are faster, they require less energy, and the catalyst can be reused many times without the need for further treatment. It has been found that the H₂O₂ and iron concentration in the solution were the main factors that influence the degradation. FeSO₄ and H₂O₂ concentration ratios were studied as Fe(II):H₂O₂ ratio (1:1), (1:5), (1:10) and (1:20). The optimum Fe(II):H₂O₂ ratio for Fenton-like processes were found as 1:5. The results are %95.64 for Fenton, %11.51 for Fenton-like(Cu(II)), %71.73 for Fenton-like (V(IV)) after 2 minutes.

5. CONFLICT OF INTEREST

There is no conflict of interest between the authors.

6. REFERENCES

- Abo-Farha, S. A. (2010). Comparative study of oxidation of some azo dyes by different advanced oxidation processes: Fenton, Fenton-like, photo-Fenton and photo-Fenton-like. *Journal of American Science*, 6(10), 128-142.
- Anliker, R. (1979). Ecotoxicology of dyestuffs—a joint effort by industry. *Ecotoxicology and Environmental Safety*, 3(1), 59-74. [https://doi.org/10.1016/0147-6513\(79\)90060-5](https://doi.org/10.1016/0147-6513(79)90060-5)
- Chacón, J. M., Leal, M. T., Sánchez, M., & Bandala, E. R. (2006). Solar photocatalytic degradation of azo-dyes by photo-Fenton process. *Dyes*

and pigments, 69(3), 144-150. <https://doi.org/10.1016/j.dyepig.2005.01.020>

- Dutta, K., Mukhopadhyay, S., Bhattacharjee, S., & Chaudhuri, B. (2001). Chemical oxidation of methylene blue using a Fenton-like reaction. *Journal of hazardous materials*, 84(1), 57-71. [https://doi.org/10.1016/S0304-3894\(01\)00202-3](https://doi.org/10.1016/S0304-3894(01)00202-3)
- Fenton, H. J. H. (1894). LXXIII.—Oxidation of tartaric acid in presence of iron. *Journal of the Chemical Society, Transactions*, 65, 899-910. <https://doi.org/10.1039/CT8946500899>
- Goldstein, S., Meyerstein, D., & Czapski, G. (1993). The fenton reagents. *Free radical biology and medicine*, 15(4), 435-445. [https://doi.org/10.1016/0891-5849\(93\)90043-T](https://doi.org/10.1016/0891-5849(93)90043-T)
- Hsueh, C. L., Huang, Y. H., Wang, C. C., & Chen, C. Y. (2005). Degradation of azo dyes using low iron concentration of Fenton and Fenton-like system. *Chemosphere*, 58(10), 1409-1414. <https://doi.org/10.1016/j.chemosphere.2004.09.091>
- Jiang, C., Pang, S., Ouyang, F., Ma, J., & Jiang, J. (2010). A new insight into Fenton and Fenton-like processes for water treatment. *Journal of hazardous materials*, 174(1-3), 813-817. <https://doi.org/10.1016/j.jhazmat.2009.09.125>
- Kidak, R., & Ince, N. H. (2006). Effects of operating parameters on sonochemical decomposition of phenol. *Journal of hazardous materials*, 137(3), 1453-1457. <https://doi.org/10.1016/j.jhazmat.2006.04.021>
- Kim, T. H., Park, C., Yang, J., & Kim, S. (2004). Comparison of disperse and reactive dye removals by chemical coagulation and Fenton oxidation. *Journal of hazardous materials*, 112(1-2), 95-103. <https://doi.org/10.1016/j.jhazmat.2004.04.008>
- Kumar, J. E., Mulai, T., Kharmawphlang, W., Sharan, R. N., & Sahoo, M. K. (2020). Decolourisation, mineralisation and detoxification of mixture of azo dyes using Fenton and Fenton-type advanced oxidation processes. *Chemical Papers*, 74(9), 3145-3159. <https://doi.org/10.1007/s11696-020-01147-9>
- Kuo, W. G. (1992). Decolorizing dye wastewater with Fenton's reagent. *Water Research*, 26(7), 881-886. [https://doi.org/10.1016/0043-1354\(92\)90192-7](https://doi.org/10.1016/0043-1354(92)90192-7)

- Kartal Temel, N., JOTCSB. (2024), 7(1), 77-86.
- Kushwaha^a, R., Garg, S., & Bajpai, S. (2019). Modeling and optimization of Nile blue sulfate mineralization by heterogeneous fenton oxidation. *Toxicological & Environmental Chemistry*, 101(1-2), 26-44. <https://doi.org/10.1080/02772248.2019.1621314>
- Kushwaha^b, R., Garg, S., & Bajpai, S. (2018). Modified generalized kinetic model and degradation mechanistic pathways for catalytic oxidation of NBS dye in Fenton-like oxidation process. *Research on Chemical Intermediates*, 44, 5759-5786. <https://doi.org/10.1007/s11164-018-3453-6>
- Liu, R., Chiu, H. M., Shiau, C. S., Yeh, R. Y. L., & Hung, Y. T. (2007). Degradation and sludge production of textile dyes by Fenton and photo-Fenton processes. *Dyes and Pigments*, 73(1), 1-6. <https://doi.org/10.1016/j.dyepig.2005.10.002>
- Liu, Y., Zhao, Y., & Wang, J. (2021). Fenton/Fenton-like processes with in-situ production of hydrogen peroxide/hydroxyl radical for degradation of emerging contaminants: Advances and prospects. *Journal of Hazardous Materials*, 404, 124191. <https://doi.org/10.1016/j.jhazmat.2020.124191>
- Neamtu, M., Yediler, A., Siminiceanu, I., & Kettrup, A. (2003). Oxidation of commercial reactive azo dye aqueous solutions by the photo-Fenton and Fenton-like processes. *Journal of Photochemistry and Photobiology A: Chemistry*, 161(1), 87-93. [https://doi.org/10.1016/S1010-6030\(03\)00270-3](https://doi.org/10.1016/S1010-6030(03)00270-3)
- Netpradit, S., Thiravetyan, P., & Towprayoon, S. (2003). Application of 'waste' metal hydroxide sludge for adsorption of azo reactive dyes. *Water Research*, 37(4), 763-772. [https://doi.org/10.1016/S0043-1354\(02\)00375-5](https://doi.org/10.1016/S0043-1354(02)00375-5)
- Neyens, E., & Baeyens, J. (2003). A review of classic Fenton's peroxidation as an advanced oxidation technique. *Journal of Hazardous materials*, 98(1-3), 33-50. [https://doi.org/10.1016/S0304-3894\(02\)00282-0](https://doi.org/10.1016/S0304-3894(02)00282-0)
- Nidheesh, P. V., Gandhimathi, R., & Ramesh, S. T. (2013). Degradation of dyes from aqueous solution by Fenton processes: a review. *Environmental Science and Pollution Research*, 20, 2099-2132. <https://doi.org/10.1007/s11356-012-1385-z>
- Ollis, D. F., Pelizzetti, E., & Serpone, N. (1991). Photocatalyzed destruction of water contaminants. *Environmental science & technology*, 25(9), 1522-1529.
- Pera-Titus, M., García-Molina, V., Baños, M. A., Giménez, J., & Esplugas, S. (2004). Degradation of chlorophenols by means of advanced oxidation processes: a general review. *Applied Catalysis B: Environmental*, 47(4), 219-256. <https://doi.org/10.1016/j.apcatb.2003.09.010>
- Perkins, W. S., Judkins Jr, J. F., & Perry, W. D. (1980). Renovation of Dyebath Water By Chlorination or Ozonation. *Textile Chemist & Colorist*, 12(8).
- Safarzadeh-Amiri, A., Bolton, J. R., & Cater, S. R. (1996). The use of iron in advanced oxidation processes. *Journal of Advanced Oxidation Technologies*, 1(1), 18-26. <https://doi.org/10.1515/jaots-1996-0105>
- Saien, J., Ardjmand, R. R., & Iloukhani, H. (2003). Photocatalytic decomposition of sodium dodecyl benzene sulfonate under aqueous media in the presence of TiO₂. *Physics and Chemistry of Liquids*, 41(5), 519-531. <https://doi.org/10.1080/00319100310001604849>
- Saleem, M. N., Shah, A., Ullah, N., Nisar, J., & Iftikhar, F. J. (2023). Detection and Degradation Studies of Nile Blue Sulphate Using Electrochemical and UV-Vis Spectroscopic Techniques. *catalysts*, 13(1), 141. <https://doi.org/10.3390/catal13010141>
- Singh, J., Kumar, V., Kim, K. H., & Rawat, M. (2019). Biogenic synthesis of copper oxide nanoparticles using plant extract and its prodigious potential for photocatalytic degradation of dyes. *Environmental research*, 177, 108569. <https://doi.org/10.1016/j.envres.2019.108569>
- Solozhenko, E. G., Soboleva, N. M., & Goncharuk, V. V. (1995). Decolourization of azodye solutions by Fenton's oxidation. *Water Research*, 29(9), 2206-2210. [https://doi.org/10.1016/0043-1354\(95\)00042-J](https://doi.org/10.1016/0043-1354(95)00042-J)
- Sökmen, M., Allen, D. W., Akkaş, F., Kartal, N., & Acar, F. (2001). Photo-degradation of some dyes using Ag-loaded titaniumdioxide. *Water, air, and soil pollution*, 132, 153-163. <https://doi.org/10.1023/A:1012069009633>
- Sökmen, M., Allen, D. W., Clench, M. R., & Hewson, A. T. (2002). GC-MS characterisation of products of oxidation of thiophenes using the Fenton and related reagents. *Journal of Advanced Oxidation Technologies*, 5(1), 11-21. <https://doi.org/10.1515/jaots-2002-0102>
- Sun, H., Liu, C., & Yao, Y. (2021). Degradation of Azo Dyes Using Natural Pyrite as Fenton-Like

- Kartal Temel, N., JOTCSB. (2024), 7(1), 77-86.
Reaction Catalyst. Environmental Engineering Science, 38(9), 854-866.
<https://doi.org/10.1089/ees.2020.0359>
- Temel, N. K., & Sökmen, M. (2011). New catalyst systems for the degradation of chlorophenols. Desalination, 281, 209-214.
<https://doi.org/10.1016/j.desal.2011.07.066>
- Wang, N., Zheng, T., Zhang, G., & Wang, P. (2016). A review on Fenton-like processes for organic wastewater treatment. Journal of Environmental Chemical Engineering, 4(1), 762-787.
<https://doi.org/10.1016/j.jece.2015.12.016>
- Woislawski, S. (1953). The spectrophotometric determination of ionization constants of basic dyes1. Journal of the American Chemical Society, 75(21), 5201-5203.
- Wu, T., Lin, T., Zhao, J., Hidaka, H., & Serpone, N. (1999). TiO₂-assisted photodegradation of dyes. 9. Photooxidation of a squarylium cyanine dye in aqueous dispersions under visible light irradiation. Environmental science & technology, 33(9), 1379-1387.
<https://doi.org/10.1021/es980923i>
- Xu, X. R., Li, H. B., Wang, W. H., & Gu, J. D. (2004). Degradation of dyes in aqueous solutions by the Fenton process. Chemosphere, 57(7), 595-600.
<https://doi.org/10.1016/j.chemosphere.2004.07.030>
- Yaseen, M., Humayun, M., Khan, A., Idrees, M., Shah, N., & Bibi, S. (2022). Photo- assisted removal of rhodamine B and Nile blue dyes from water using CuO-SiO₂ composite. Molecules, 27(16), 5343.
<https://doi.org/10.3390/molecules27165343>
- Yasmeen, S., Burratti, L., Duranti, L., Sgreccia, E., & Proposito, P. (2024). Photocatalytic Degradation of Organic Pollutants—Nile Blue, Methylene Blue, and Bentazon Herbicide—Using NiO-ZnO Nanocomposite. *Nanomaterials*, 14(5), 470.
<https://doi.org/10.3390/nano14050470>



Estimation and Optimization of the Radiant Field in Flat Plate Heterogeneous Photoreactors with the P1-approximation of the Radiative Transfer Equation (RTE)

Clovis Nchikou 

Universidad Autónoma de Nuevo León, Facultad de Ciencias Químicas, San Nicolás De Los Garza, 6645, México.

Abstract: In this work, the P1-approximation of the radiative transfer equation (RTE) was used for the description and optimization of the radiant field in a flat plate photoreactor under solar radiation with three commercial brands of titanium dioxide photocatalysts. The boundary layer of photon absorption ($[\delta_{\text{abs}}]$), the average volumetric rate of photon absorption (V_{RPA}), and a new apparent optical thickness (ζ_{app1}) were used as design parameters for optimization. A simple mathematical expression for the calculation of δ_{abs} also called the best reactor thickness was formulated. For the three catalysts, varying the reactor height (L) resulted in a decrease in the local volumetric rate of photon absorption (L_{VRPA}) from the top side to the bottom of the reactor for any value of the catalyst loading (C_{cat}). It was also observed that when C_{cat} increases the V_{RPA} increases exponentially until a fixed value where it remains almost constant. With $L = 1$ cm, the optimum C_{cat} ($C_{\text{cat-op}}$) was 0.2 g/L in 0.85 cm of thickness, 0.3 g/L in 0.82 cm of thickness, and 0.4 g/L in 0.89 cm of thickness for the photocatalysts Catalyst D P-25, Catalyst A, and Catalyst H, respectively. The optimum apparent optical thickness ($\zeta_{\text{app1,op}}$) was 4.87, 4.62, and 3.7 for the photocatalysts Catalyst D P-25, Catalyst A, and Catalyst H, respectively. These results are in good agreement with the literature. Results found in this work give predictions on radiation absorption in flat plate photocatalytic reactors with different heights.

Keywords: Flat plate reactor, Boundary layer, L_{VRPA} , Titanium dioxide, P1-approximation.

Submitted: March 12, 2024. **Accepted:** May 04, 2024.

Cite this: Nchikou, C. (2024). Estimation and Optimization of the Radiant Field in Flat Plate Heterogeneous Photoreactors with the P1-approximation of the Radiative Transfer Equation (RTE). *Journal of the Turkish Chemical Society, Section B: Chemical Engineering*, 7(1), 87–104. <https://doi.org/10.58692/jotcsb.1450662>

Corresponding author. E-mail: clovis.nchikou@uanl.edu.mx.

1. INTRODUCTION

Water pollution is one of the major global issues, primarily affecting developing countries. Several approaches have been put out to address this situation. For many decades now, heterogeneous photocatalysis has been considered a potential oxidation method for disinfecting and decontaminating water (He et al., 2021; Li et al., 2022; Nair & Jagadeesh Babu, 2017). It is an advanced oxidation technology based on the photo-excitation of photocatalysts with solar or artificial radiation. The activation of a semiconductor with an energy equal to or greater than its band gap energy generates electron-hole pairs, which in contact with charge carriers (H_2O , OH^- , O_2 , etc) produce radical oxidative species such as hydroxyl radicals. These radicals are transitory compounds that attack contaminants present in the fluid phase through oxidative or reductive reaction pathways (Li Puma et al., 2020). Research on solar photocatalysis as a clean technology for producing hydrogen and solar fuels, as well as a sustainable alternative to treating industrial wastewater and removing organic pollutants, dyes, pesticides, and emerging contaminants, has increased dramatically as a result of the ongoing concern

about water remediation (Rizzo et al., 2019; Vaya & Surolia, 2020). Because mathematical modeling is crucial to the design, assessment, optimization, and efficiency estimation of photoreactors at various sizes, it has become more and more relevant in this field (Wang et al., 2021). The mathematical modeling of photocatalysis processes is composed of a sequence of sub-models including the modeling of the radiant field (Ochoa-Gutiérrez et al., 2018). This sub-model includes the solar emission model and the absorption-scattering model for the quantification of the *LVRPA*, one of the key parameters of the intrinsic kinetic equation (Colina-Márquez et al., 2015). The *LVRPA* depends on the geometry, radiation source, catalyst loading, and type of photocatalyst, in some cases on the pollutant if this presents absorption of radiant energy. For its determination, one should solve the RTE which remains a challenging task due to its integro-differential form (Illi et al., 2019). Eq. (1) traduces the steady-state and non-temperature-dependence of the RTE, which describes the different phenomena that occur on the light when it traverses a medium, such as absorption, in-scattering, and out-scattering as represented in Eq. (1).

$$\frac{dI_\lambda(S, \Omega)}{ds} = -K I_\lambda(S, \Omega) - \sigma_\lambda I_\lambda(S, \Omega) + \frac{\sigma_\lambda}{4\pi} \int_{\Omega=4\pi} P(\Omega' \rightarrow \Omega) I_\lambda(S, \Omega') d\Omega' \quad (1)$$

where I_λ is the photon irradiance (W/m^2), K_λ the absorption coefficient (m^2/kg), σ_λ the scattering coefficient (m^2/kg), $P(\Omega' \rightarrow \Omega)$ the scattering phase function, λ the wavelength (m), S the spatial coordinate (m) and Ω the directional solid angle (Steradian) (Fujii et al., 2022; Ghafoori et al., 2020; Howell et al., 2021).

The RTE gives an account of how light is dispersed or absorbed within a specific medium. Numerous numerical techniques, such as the discrete ordinate methods (DOM) and the Monte Carlo model, were employed to solve the RTE; nevertheless, these methods are time-consuming and need significant processing resources (Acosta-Herazo et al., 2020; Moreno-SanSegundo et al., 2020; Peralta Muniz Moreira & Li Puma,

2021). Alternative analytic methods such as the n-flux or the Pn approximation models (n is a strictly positive integer) have been used to solve the RTE, to describe and quantify satisfactorily the radiant field in various types of photocatalytic reactors (Arancibia-Bulnes et al., 2009; Cuevas et al., 2007). The P1-approximation is the lowest order of the spherical harmonics method (also known as the Pn-approximation), i.e., keeps only the first two terms of the Pn-approximation (Akdemir et al., 2022; Christenson et al., 2018; Harel et al., 2021). It is more versatile than two and four-flux models because it lends itself more easily to different geometries (Arancibia-Bulnes et al., 2009). It has been used to solve the RTE in one dimension in flat plate photoreactors and two dimensions in cylindrical photoreactors (Arancibia-Bulnes et al., 2009; Cuevas & Arancibia-Bulnes, s. f.). The P1 approximation

saves computational time and effort by reducing the mathematical complexity of the RTE to an analytical equation (Arancibia-Bulnes et al., 2009; Cuevas et al., 2007; Cuevas & Arancibia-Bulnes, s. f.). Flat plate reactors can be scaled up and can be used with solar radiation, so they are very attractive and also provide an excellent configuration for efficient activation of the photocatalyst TiO₂ (Li Puma, 2005). Their modeling requires a complex analysis of the radiation field inside the photoreactor (Cassano et al., 1995).

In this paper, the P1 approximation was used to model radiant fields and to find the optimum operational conditions in flat plate heterogeneous photoreactors under solar radiation. Three commercial brands of titanium dioxide photocatalysts (Catalyst D, Catalyst A, and Catalyst H) were used and some comparisons were made between them. Design parameters such as the *VRPA*, the best reactor thickness δ_{abs} , and a new apparent optical thickness ζ_{app1} were used. ζ_{app1} was formulated with the P1 approximation approach. Kinetic models of pollution degradation and hydrogen production could benefit from the information provided. In kinetic models of pollution degradation and hydrogen production, determining the local volumetric rate of photon absorption might help to improve understanding of the relevant processes. It makes it possible to calculate reaction rates, energy transfer, and overall efficiency precisely, which improves environmental results and leads to optimal systems.

2. MATERIALS AND METHODS

2. 1. Radiant field

The radiant field was estimated by solving the RTE in one dimension in rectangular coordinates, and then the *LVRPA* was deduced. Eq. (2) is the governing equation of the P1 approximation or the so-called Helmholtz's equation which will be solved later in one dimension with suitable boundary conditions.

$$\Delta G_{\lambda} = k_{d,\lambda}^2 G_{\lambda} \quad (2)$$

where,

$$k_{d,\lambda} = \beta_{\lambda} \sqrt{3(1-\omega_{\lambda})(1-g_{\lambda} \frac{\omega_{\lambda}}{3})} \quad (3)$$

where g_{λ} is the asymmetry Henyey-Greenstein phase function factor corresponding to the monochromatic radiation of wavelength λ and which is proper to each catalyst, β_{λ} is the monochromatic extinction coefficient being the sum of κ_{λ} and σ_{λ} which are the monochromatic absorption and scattering coefficients respectively defined as,

$$\beta_{\lambda} = \kappa_{\lambda} + \sigma_{\lambda} \quad (4)$$

All of these coefficients depend on catalyst particle concentration in a linear fashion as,

$$\beta_{\lambda} = \beta_{\lambda}^* C_{cat}, \kappa_{\lambda} = \kappa_{\lambda}^* C_{cat}, \sigma_{\lambda} = \sigma_{\lambda}^* C_{cat} \quad (5)$$

where C_{cat} is the catalyst concentration, β_{λ}^* , κ_{λ}^* and σ_{λ}^* are specific coefficients, independent of this concentration (for values in the usual ranges for photocatalysis).

ω_{λ} is the scattering albedo which gives the probability that a photon is scattered when colliding with a particle defined as,

$$\omega_{\lambda} = \frac{\sigma_{\lambda}}{\beta_{\lambda}} \quad (6)$$

Instead of using the monochromatic parameters, one should use their average values in a defined wavelength interval $[\lambda_{min}, \lambda_{max}]$ using the following equation,

$$\Gamma^* = \frac{\int_{\lambda_{min}}^{\lambda_{max}} \Gamma_{\lambda} I(\lambda) d\lambda}{\int_{\lambda_{min}}^{\lambda_{max}} I(\lambda) d\lambda} \quad (7)$$

where Γ_{λ} can be one of the parameters κ_{λ} , σ_{λ} , β_{λ} or g_{λ} and $\lambda_{min} = 280$ nm, $\lambda_{max} = 395$ nm given by the interception of solar emission spectrum and titanium dioxide absorption spectrum; $I(\lambda)$ is the spectrum of solar emission power (Tourasse & Dumortier, 2014).

G_λ is the local radiation which corresponds to the integration of the irradiance I_λ all over the solid angle Ω . After finding the expression of G_λ , one can easily deduce the local volumetric rate of photon absorption (LVRPA) from Eq. (8); this parameter is very important for the determination of the intrinsic kinetic rate of the photocatalytic reaction in a given reaction system.

$$LVRPA = k_\lambda G_\lambda \quad (8)$$

In this paper, the concept of the boundary layer of photon absorption introduced yet in the literature (Otálvaro-Marín et al., 2014) and which allows the determination of the best thickness has been discussed with the P1 approximation approach. Figure 1 represents a flat plate reactor with thickness L , located perpendicularly to the

source, where I_0 represents the constant incident radiation intensity. The region where there is a gradient of energy absorption has been called the boundary layer of photon absorption, and its thickness δ_{abs} which can be understood as the reactor thickness measured from the irradiated surface where 99% of total energy is absorbed. Then δ_{abs} is defined as x -value which satisfies the following equation:

$$\int_0^{\delta_{abs}} LVRPA(x) dx = 0.99 \int_0^L LVRPA(x) dx \quad (9)$$

This definition of boundary layer thickness for transport phenomena and absorption of radiant energy is analogous to the definition of thickness of hydrodynamic, thermal, and concentration boundary layer on a flat plate (Incropera, s. f.; Otálvaro-Marín et al., 2014).

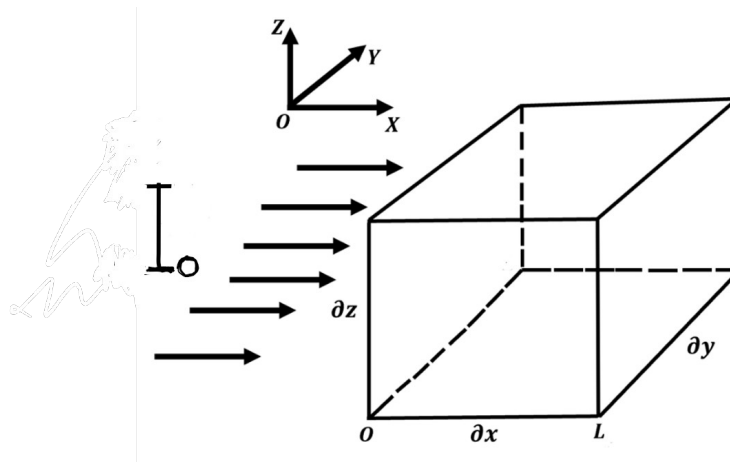


Figure 1. Collimated incident radiation on a slab reactor.

Oversizing the reactor thickness could lead to the formation of a dark sublayer with very little photon absorption. As a result, while choosing the ideal thickness for flat plate reactors, the boundary layer thickness becomes a design parameter (Otálvaro-Marín et al., 2014). It can be used as a geometrical parameter that is equivalent to the optimal reactor thickness, depending on the type and loading of the catalyst. It is worth mentioning that the new apparent optical thickness was also formulated

here with the P1 approximation approach and was used for a design purpose.

2. 2. Solution for the RTE in One Dimension Using the P1 Approximation Approach

Figure 1 shows a schematic representation of a flat plate reactor with thickness L , located perpendicularly to the source. The P1 approximation in one dimension in cartesian coordinates becomes:

$$\frac{\partial G_\lambda}{\partial x} = k_{d,\lambda}^2 G_\lambda \tag{10}$$

$$\xi_\lambda = \beta_\lambda \left(1 - g_\lambda \frac{\omega}{3}\right) \tag{14}$$

The general solution of Eq. 10 is:

$$G_\lambda = A e^{k_{d,\lambda} x} + B e^{-k_{d,\lambda} x} \tag{11}$$

where A and B are real constants to determine later.

2. 3. Boundary Conditions

For the determination of the constants A and B Marshak’s boundary conditions (Marshak, 1947) are considered in Eqs. (1-2), where I_0 represents the photon flux reaching perpendicularly the top side of the reactor and with the assumption that the photon flux does not reach the reactor bottom and that the inner reflectance of reactor glass is negligible.

$$G_\lambda(0) - \frac{2}{3\xi_\lambda} \frac{dG_\lambda(x)}{dx} \Big|_{x=0} = 4I_0 \tag{12}$$

$$G_\lambda(L) + \frac{2}{3\xi_\lambda} \frac{dG_\lambda(x)}{dx} \Big|_{x=L} = 0 \tag{13}$$

where ,

That leads to the following system of equations:

$$\left(1 - \frac{2k_{d,\lambda}}{3\xi_\lambda}\right) A + \left(1 + \frac{2k_{d,\lambda}}{3\xi_\lambda}\right) B = 4I_0 \tag{15}$$

$$\left(1 + \frac{2k_{d,\lambda}}{3\xi_\lambda}\right) e^{k_{d,\lambda} L} A + \left(1 - \frac{2k_{d,\lambda}}{3\xi_\lambda}\right) e^{-k_{d,\lambda} L} B = 0 \tag{16}$$

Which yields

$$A = \frac{4\left(1 - \frac{2k_{d,\lambda}}{3\xi_\lambda}\right) e^{-k_{d,\lambda} L} I_0}{\left(1 - \frac{2k_{d,\lambda}}{3\xi_\lambda}\right)^2 e^{-k_{d,\lambda} L} - \left(1 + \frac{2k_{d,\lambda}}{3\xi_\lambda}\right)^2 e^{k_{d,\lambda} L}} \tag{17}$$

$$B = \frac{-4\left(1 + \frac{2k_{d,\lambda}}{3\xi_\lambda}\right) e^{k_{d,\lambda} L} I_0}{\left(1 - \frac{2k_{d,\lambda}}{3\xi_\lambda}\right)^2 e^{-k_{d,\lambda} L} - \left(1 + \frac{2k_{d,\lambda}}{3\xi_\lambda}\right)^2 e^{k_{d,\lambda} L}} \tag{18}$$

Finally, one finds,

$$G_\lambda(x) = \frac{4\left(1 - \frac{2k_{d,\lambda}}{3\xi_\lambda}\right) e^{-k_{d,\lambda}(L-x)} - 4\left(1 + \frac{2k_{d,\lambda}}{3\xi_\lambda}\right) e^{k_{d,\lambda}(L-x)}}{\left(1 - \frac{2k_{d,\lambda}}{3\xi_\lambda}\right)^2 e^{-k_{d,\lambda} L} - \left(1 + \frac{2k_{d,\lambda}}{3\xi_\lambda}\right)^2 e^{k_{d,\lambda} L}} I_0 \tag{19}$$

The local volumetric rate of photon absorption will be then,

$$LVRPA(x) = \frac{4\kappa_\lambda \left(\left(1 - \frac{2k_{d,\lambda}}{3\xi_\lambda}\right) e^{-k_{d,\lambda}(L-x)} - \left(1 + \frac{2k_{d,\lambda}}{3\xi_\lambda}\right) e^{k_{d,\lambda}(L-x)} \right)}{\left(1 - \frac{2k_{d,\lambda}}{3\xi_\lambda}\right)^2 e^{-k_{d,\lambda}L} - \left(1 + \frac{2k_{d,\lambda}}{3\xi_\lambda}\right)^2 e^{k_{d,\lambda}L}} I_0 \quad (20)$$

2. 4. Parameters of the P1 Approximation

$\omega_{\lambda,mod}$, λ_{mod} and ζ_{app1} are defined here as the P1 approximation parameters, their equivalent are ω_{corr} , λ_{corr} and ζ_{app} for the six-flux model (SFM) respectively, ζ_{app1} is a design parameter as ζ_{app} is for the SFM (*mod* stands for *modified*). These parameters are defined as follows:

$$\lambda_0 = \frac{1}{\beta_\lambda} \quad (23)$$

ζ_{app1} is the apparent optimal thickness defined as

$$\omega_{\lambda,mod} = \sqrt{\omega_\lambda \left(1 + \frac{g_\lambda}{3} - \frac{g_\lambda}{3} \omega_\lambda\right)} \quad (21)$$

$$\zeta_{app1} = \zeta \sqrt{3(1 - \omega_{\lambda,mod}^2)} \quad (24)$$

where ζ is the optical thickness, for a flat plate reactor expressed as,

$$\lambda_{mod} = \frac{\lambda_0}{\sqrt{3(1 - \omega_{\lambda,mod}^2)}} \quad (22)$$

$$\zeta = \frac{L}{\lambda_0} \quad (25)$$

where λ_0 is the mean free path of photon defined as,

$$k_{d,\lambda} = \frac{1}{\lambda_{mod}} \quad (26)$$

$$LVRPA(x) = \frac{4\kappa_\lambda \left(\left(1 - \frac{2}{3\xi_\lambda}\right) e^{\frac{-L-x}{\lambda_{mod}}} - \left(1 + \frac{2}{3\xi_\lambda}\right) e^{\frac{L-x}{\lambda_{mod}}} \right)}{\left(1 - \frac{2}{3\xi_\lambda}\right)^2 e^{\frac{-L}{\lambda_{mod}}} - \left(1 + \frac{2}{3\xi_\lambda}\right)^2 e^{\frac{L}{\lambda_{mod}}}} I_0 \quad (27)$$

The unique solution for Eq. (9) is given by:

where,

$$\delta_{abs} = \lambda_{mod} \ln\left(\frac{\Sigma + \sqrt{\Sigma^2 + 4AB}}{2A}\right) \quad (28)$$

$$\Sigma = 0.99(A e^{\frac{L}{\lambda_{mod}}} - B e^{\frac{-L}{\lambda_{mod}}} - A + B) + A - B \quad (29)$$

where A and B are constants defined in Eqs. (17-18) respectively.

2. 5. Volumetric Rate of Photon Absorption, $VRPA$

$VRPA$ is defined as an average value of $LVRPA$ in the entire reactor volume. For a flat plate reactor, when the incident radiation intensity is constant along the reactor wall, the is expressed as:

$$VRPA = \frac{1}{L} \int_0^L LVRPA(x, C_{cat}) dx \quad (30)$$

$VRPA$ is a design parameter formulated and validated to determine the optimum catalyst loadings in photocatalytic processes (Brandi et al., 1996; Otálvaro-Marín et al., 2014).

3. RESULTS AND DISCUSSION

The simulation of the P1 approximation in a flat plate photoreactor was performed under solar radiation with three different brands of commercial titanium dioxide with their optical characteristics (albedo, modified albedo, scattering and absorption coefficient, asymmetry factor) reported in the literature (Acosta-Herazo et al., 2016; Otálvaro-Marín et al., 2014) and in Table 1. The reactor thickness L was considered to vary.

Table 1. Average optical properties of commercial photocatalysts based on titanium dioxide under solar radiation (Acosta-Herazo et al., 2016; Otálvaro-Marín et al., 2014), modified albedo, and asymmetry factor g .

Catalyst	$\sigma^* \times 10^{-4}$ ($cm^2 g^{-1}$)	$\kappa^* \times 10^{-3}$ ($cm^2 g^{-1}$)	$\beta^* \times 10^{-4}$ ($cm^2 g^{-1}$)	ω	ω_{mod}	g
Catalyst A	3.73	2.43	3.98	0.94	0.97	0.53
Catalyst D	5.42	2.87	5.71	0.95	0.99	0.53
Catalyst H	2.52	1.17	2.64	0.96	0.98	0.57

3.1. $LVRPA$

The local volumetric rate of photon absorption per unit of incoming radiant flux ($LVRPA/I_0$) in function of x-coordinate at different catalyst loads describes the distribution of the photon absorption inside the reactor for each of the catalysts Catalyst A, Catalyst D and Catalyst H as depicted in Figure 2 ($L=1$ cm). For each catalyst, the $LVRPA/I_0$ profile shows the decrease of the absorption from the top side (Maximum value of $LVRPA/I_0$) until the bottom of the reactor (minimum value of $LVRPA/I_0$) and that the absorption at the top side of the reactor increases exponentially with the increase of the

catalyst load due to the amount of surface-exposed catalyst and the back-scattering energy absorption from the internal layer inside the reactor. Near the irradiated surface, the change $LVRPA/I_0$ with respect to x is linked to extinction coefficients; a rise in catalyst concentration and high extinction coefficients quickly extinguish the total energy of the system. These observations are in good agreement with the literature (Nchikou et al., 2021; Otálvaro-Marín et al., 2014). It is also observed that the more the catalyst loading increases the more the absorption at the reactor bottom decreases. The $LVRPA/I_0$ is negligible at the reactor bottom for C_{cat} greater than 0.3 g/L for Catalyst A and Catalyst D, the same result was found by using

the SFM (Otálvaro-Marín et al., 2014) which was validated by comparing it to rigorous solution of

the RTE (Brandi et al., 1999; Zalazar et al., 2005).

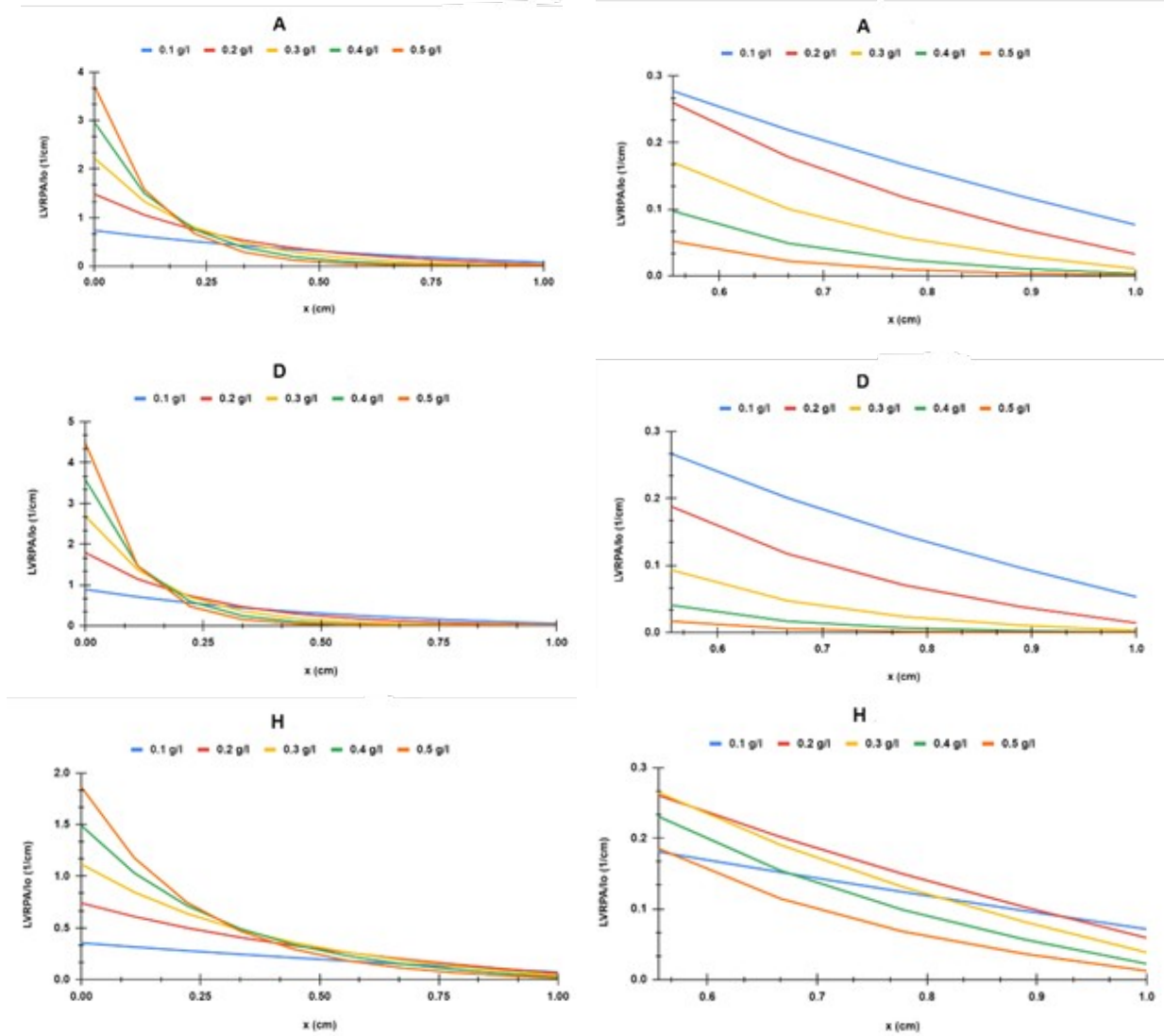


Figure 2. The $LVRPA$ per unit of light intensity vs x-axis with different C_{cat} , ($L=1$ cm)
 a) Catalyst A , b) Catalyst D, c) Catalyst H

The $LVRPA/I_0$ profile for each catalyst in Figure 3 shows a good uniformization of photon absorption for C_{cat} equal to 0.1 g/L (Figure 3 a, c, and e) but at 0.5 g/L (Figure 3 b, d, and f) of C_{cat} photon absorption decreases considerably at the inner zone of the reactor while increases significantly at the

zone around its wall. This could be explained by the fact that the cloudy effect starts which impedes the photon penetration in the inner part of the reactor due to the saturation of the absorption at the irradiated reactor surface (Colina-Márquez et al., 2010). With Catalyst H the clouding effect starts with C_{cat} greater than 0.5 g/L.

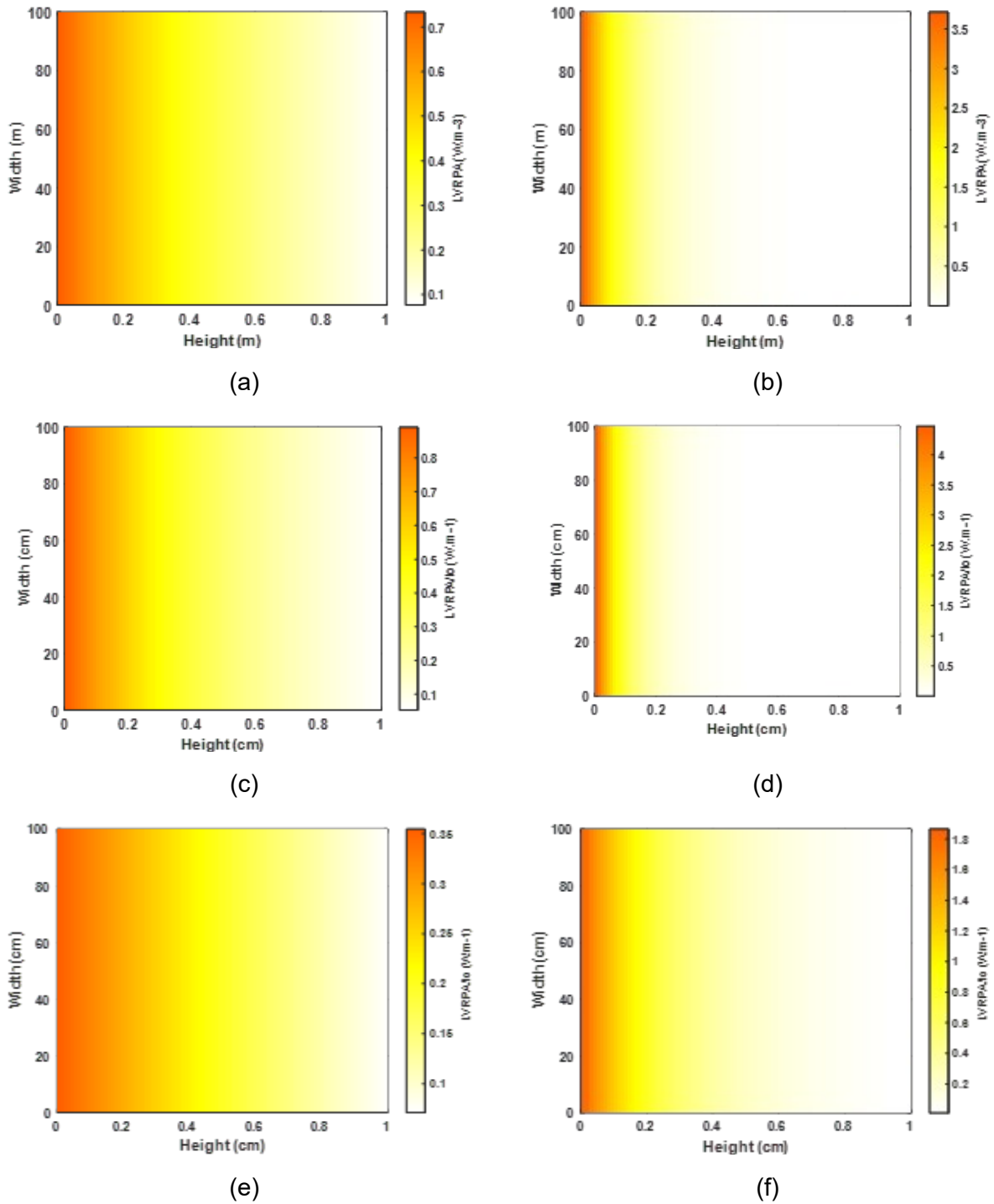


Figure 3. Absorption profile per unit of light intensity at 0.1 g/L of C_{cat} (a, c, e) for Catalyst A, Catalyst D, and Catalyst H respectively) and at 0.5 g/L of C_{cat} (b, d, f) for Catalyst A, Catalyst D, and Catalyst H respectively).

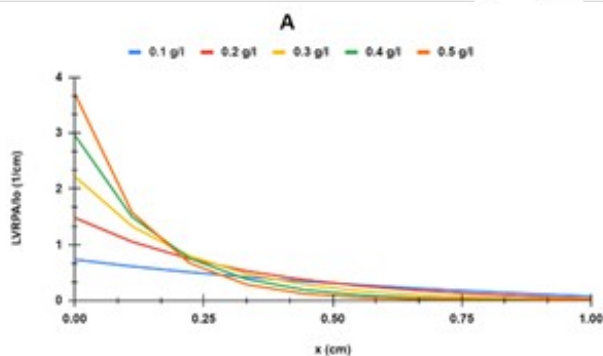
3. 2. Optimal Operating Conditions in a Flat Plate Photoreactor

3. 2. 1. VRPA

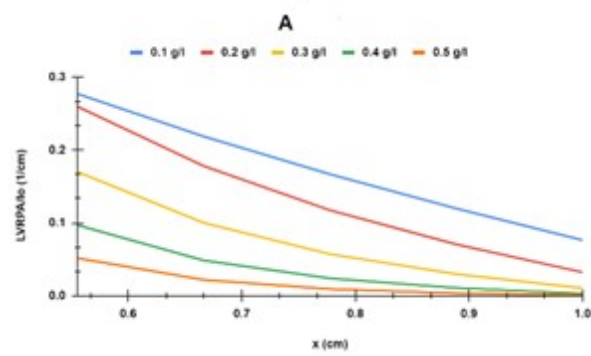
Based on the quantity of radiation absorbed by the catalyst, the $VRPA$ is crucial for assessing the quantum yield of photocatalytic reactions, it gives more significant information compared to the quantum efficiency, which depends on the incident photon flux. Additionally, it enables a suitable assessment of the activity of catalysts with various optical characteristics (Colina-Márquez et al., 2010). Figure 4 represents the $VRPA$ per unit of light intensity ($VRPA/I_0$) as a function of catalyst loading with different reactor depths for the three catalysts and different reactor heights. It shows how the $VRPA/I_0$ increases exponentially and reaches a value from where it remains almost constant due to the photon saturation at the upper side of the reactor. The $VRPA/I_0$ with Catalyst D is a little higher than with Catalyst A for C_{cat} less than 0.15 g/L approximately for $L=0.5$ cm and $L=1$ cm but above this value, the reverse is observed. For reactor height higher than unity, Catalyst A has the highest $VRPA/I_0$ (see Figure 4 a) and b)); meanwhile Catalyst H has the lowest $VRPA/I_0$ for C_{cat} less than 0.25 g/L and

almost coincides with Catalyst D in terms of absorption for C_{cat} greater than 0.25 g/L (see Figure 4 c) and d)).

In the case when $L=1$ cm, the $VRPA/I_0$ profiles present a weak absorption for C_{cat} less than 0.1 g/L and from 0.1 to 0.4 g/L an exponential increase; catalyst loading above 0.2, 0.3 and 0.4 g/L respectively for Catalyst D, Catalyst A and Catalyst H would be a catalyst waste since the $VRPA/I_0$ will no more increase significantly and high value of C_{cat} produces the clouding effect. The optimum values of C_{cat} are around 0.2, 0.3, and 0.4 g/L for Catalyst D, Catalyst A, and Catalyst H, respectively, which agree with the literature (Otálvaro-Marín et al., 2014). In comparison to the catalyst Catalyst D, the catalyst Catalyst A $VRPA$ maximum is approximately 12 % higher. A comparable pattern was observed, where Catalyst A is 19 % and 7 % more efficient than Catalyst D P-25 in the case of UV lamps used for polychromatic radiation and in the case of solar radiation using the SFM approach respectively (Brandi et al., 1999; Otálvaro-Marín et al., 2014). As it is shown in Figure 4, although the $VRPA/I_0$ increases with C_{cat} , it decreases with the increase of the reactor height. It drops to 80% approximately for each of the photocatalysts for reactor height varying from 0.5 to 3 cm.



(a)



(b)

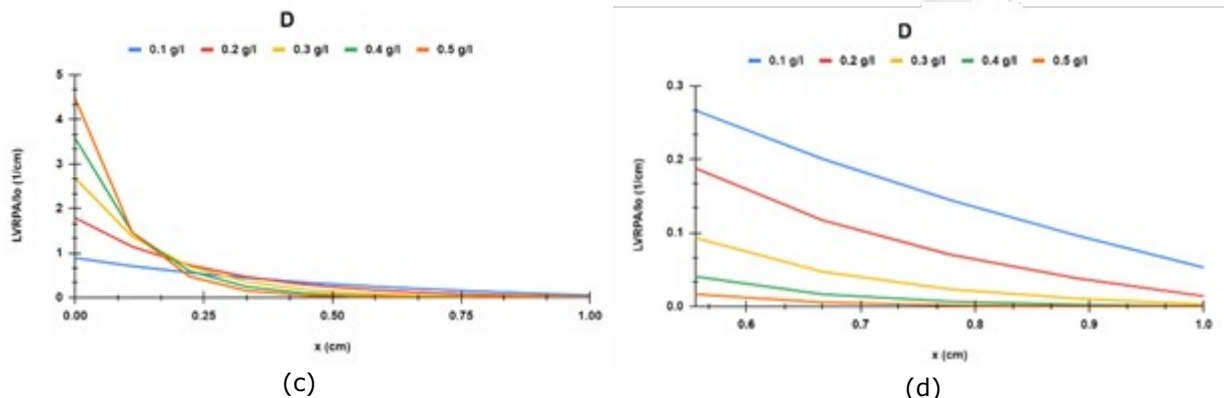
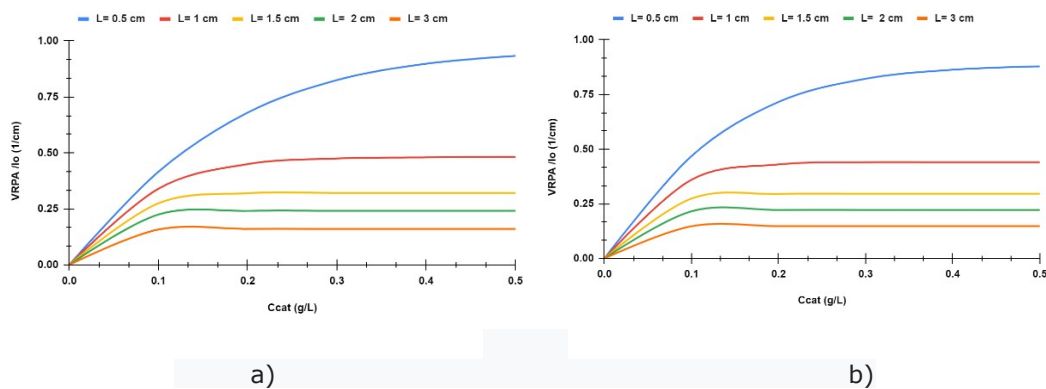


Figure 4. The $VRPA$ per unit of light intensity vs catalyst loading with different reactor depths for the three catalysts (a) $L=0.5$ cm, b) $L=1$ cm, c) $L=2$ cm, d) $L=3$ cm).

3. 2. 2. Impact of the reactor height on the $VRPA$

Figure 5 shows how the reactor height affects the $VRPA/I_0$ for the three catalysts. In this figure, the $VRPA/I_0$ decreases with the increase of the reactor height for each of the three catalysts. For both catalysts Catalyst A and Catalyst D, the $VRPA$ maximum ($VRPA_{max}/I_0$) is reduced to 50% when L increases from 0.5 to 1 cm and to 30% when L increases from 1 to 1.5 cm; over 2 cm the $VRPA_{max}/I_0$ does not vary too much. The same observation is made with the catalyst Catalyst H except that the $VRPA_{max}/I_0$ decreases to 40 % approximately when increasing L from 0.5 to 1 cm. These reductions

of the $VRPA_{max}/I_0$ could be explained by the fact that the more the reactor height increases the more the photon absorption uniformization decreases since the photon pathway becomes very long and it struggles to reach the inner part of the reactor. Moreover, for the catalysts Catalyst A and Catalyst D the optimum C_{cat} is about 0.15 g/L for $L > 1$ cm; meanwhile for Catalyst H, the optimum C_{cat} is about 0.15 g/L for $L \geq 3$ cm. Thus, for high values of L , the optimum C_{cat} is very low but unfortunately working with a very small amount of C_{cat} implies low production of oxidizing species. Then oversizing the reactor height reduces considerably the average value of the $LVRPA$ inside the reactor and therefore could disfavor the photocatalytic process.



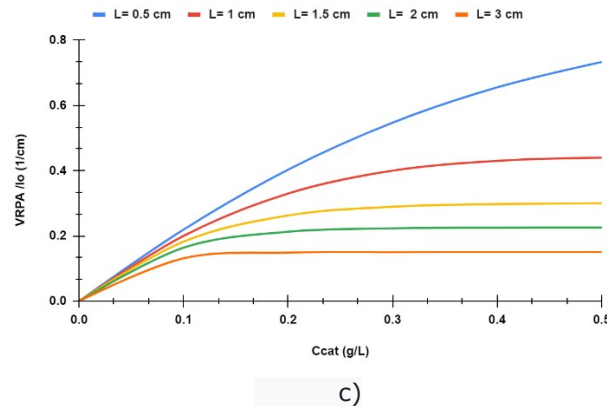


Figure 5. The $VRPA$ per unit of light intensity vs catalyst loading with different reactor depths, $L = 0.5$ cm in blue line, $L = 1$ cm in red line, $L = 1.5$ cm in yellow line, $L = 2$ cm in green line, $L = 3$ cm in orange line
 a) Catalyst A , b) Catalyst D, c) Catalyst H

4. REACTOR SIZING

4. 1. Boundary Layer

Eq. (28) establishes the boundary layer of photon absorption (δ_{abs}) dependence on the catalyst, catalyst loading, and the reactor thickness. Figure 6 shows how varies δ_{abs} with respect to C_{cat} and L for the catalysts Catalyst A, Catalyst D and Catalyst H. For any value of L , δ_{abs} decreases with the increase of C_{cat} since the more C_{cat} increases the more photons penetration to the inner part of the reactor becomes difficult. For low values of C_{cat} , δ_{abs} increases linearly with

L , probably because low C_{cat} means no saturation of catalyst particles, and therefore, photons can easily move and reach the reactor bottom and then be absorbed (δ_{abs} is almost equal to L). It is worth mentioning that the more the boundary layer approaches the reactor height the more the absorption is uniform inside the reactor. Finally, for high values of C_{cat} (greater than 0.5 g/L approximately), δ_{abs} increases linearly with L until a fixed value where it remains almost constant. This is obvious since in this case, the clouding effect occurs because of the presence of a high amount of catalyst particles at the reactor wall impeding photons penetration.

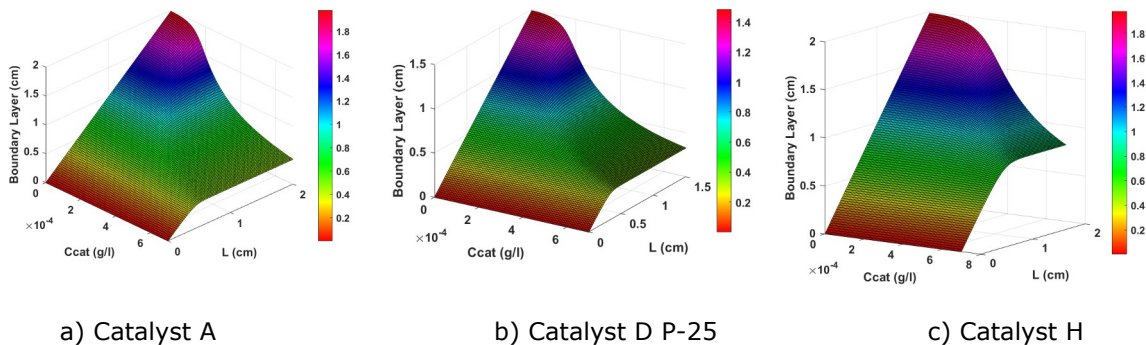


Figure 6. Boundary layer of photon absorption as a function of catalyst loading and reactor height for the three catalysts.

Figure 7 shows how the boundary layer of photon absorption varies as a function of catalyst loading ($L = 1$ cm). Combining Figures 4 and 7 one can find helpful details to specify the kind and amount of catalyst as well as the design thickness of a flat plate reactor. For each of the catalysts, for C_{cat} lower than 0.1 g/L, absorption takes place in almost the whole reactor but a very small value of the $VRPA$ is produced (δ_{abs} is almost equal to L). For C_{cat} from 0.1 to 0.2 g/L, photon absorption occurs over 85% of the entire reactor height while in the range 0.2-0.4 g/L of C_{cat} , the $VRPA$ maximum is obtained between 82 and 89% of the entire reactor thickness as shown in Table 2. This table summarizes the optimum catalyst loading, maximum energy absorbed, and design thickness

for different reactor thicknesses (0.5, 1, 2, and 3 cm). Comparisons have been made between the three catalysts in the literature using the SFM when $L = 1$ cm (Otálvaro-Marín et al., 2014), and the same observations were found here. As shown in Table 2, Catalyst D is the best catalyst since it needs only 0.2 g/L of C_{cat} to produce 0.43 (1/cm) of $VRPA/I_0$ over 86 % of the reactor thickness. It was also found in the literature that for a reactor height of 1 cm, the boundary layer of photon absorption is around 0.86 cm using different Catalyst D optical properties than those in this work (Acosta-Herazo et al., n. d.). Catalyst H comes in third position, it needs 0.4 g/L of C_{cat} to reach 0.43 (1/cm) of $VRPA/I_0$ even though it has the highest δ_{abs} (0.89). For reactor thickness equal to 0.5 cm, Catalyst A stands as the best photocatalyst and then Catalyst D.

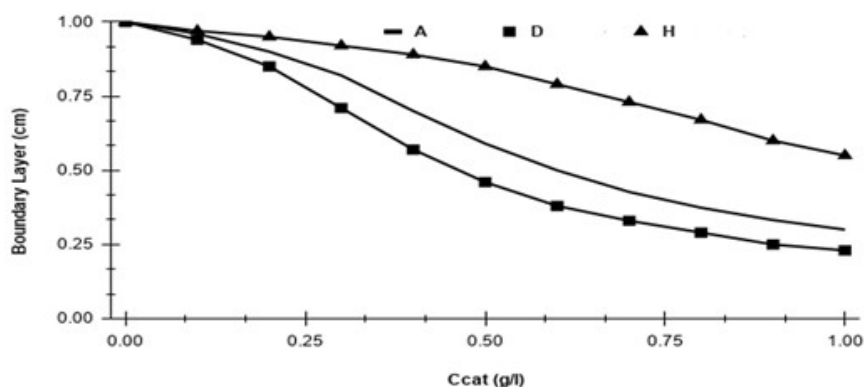


Figure 7. Boundary layer of photon absorption as a function of catalyst loading ($L = 1$ cm).

For $L = 3$ cm, all the catalysts produce almost the same $VRPA/I_0$ at the same optimum C_{cat} (0.15 g/L) but Catalyst H performs as the best

catalyst followed by Catalyst A since Catalyst H has the highest δ_{abs} (2.61 cm) and Catalyst D the lowest (1.52 cm).

Table 2. Optimum catalyst loading, maximum energy absorbed, and design thickness of flat plate reactor under solar radiation for different reactor heights (0.5, 1, 2, and 3 cm). The values in bracket in column 4 represent $\frac{\delta_{abs}}{L} \times 100$.

catalyst	C_{cat-op} (g/L)	$VRPA_{max}/I_0$ (1/cm)	Suggested thickness (cm)	Reactor height (cm)
Catalyst D	0.5	0.88	0.4 (80%)	0.5
	0.2	0.43	0.86 (86%)	1
	0.15	0.22	1.43 (72%)	2
	0.15	0.15	1.52 (51%)	3
Catalyst A	0.5	0.93	0.43 (86%)	0.5
	0.3	0.48	0.82 (82%)	1
	0.15	0.24	1.64 (82%)	2
	0.15	0.16	1.94 (65%)	3
Catalyst H	0.5	0.73	0.47 (94%)	0.5
	0.4	0.43	0.89 (89%)	1
	0.25	0.2	1.85 (93%)	2
	0.15	0.14	2.61 (87%)	3

4. 2. Apparent Optical Thickness

The volumetric rate of photon absorption per unit of reactor length $VRPA/H$ is another design parameter, it is obtained by integrating the $LVRPA$ over the reactor width and height. It can also be found by multiplying the $VRPA$ by the cross-sectional area of the reactor. In this work, the reactor width was supposed to be unity. For the optimization of the radiation absorption inside the flat plate reactor of any height, a new apparent optical thickness ζ_{app1} was introduced with the P1 approximation (see Eq. 24) as it was the case of ζ_{app} with the SFM approach in the literature (Colina-Márquez et al., 2010). This dimensionless design parameter removes the dependence of the optimum catalyst loading on the reactor height and catalyst albedo as it is proved in Figure 8. Figure 8 a) shows how the $VRPA/H$ per unit of light intensity (I_0) varies as a function of ζ_{app1} for different reactor heights with Catalyst D P25 catalyst properties taken from (Colina-Márquez et al., 2010). The optimum value of ζ_{app1} ($\zeta_{app1,op}$) remains almost the same (about 4.87) no matter the change in the reactor height. Figure 8 b) displays the variation

of the $VRPA/H$ as a function of ζ_{app1} at different catalyst albedo but with a fixed absorption coefficient ($\kappa = 2.87 \text{ cm}^2 \text{ g}^{-1}$) and $L=2$ cm. It was found almost the same $\zeta_{app1,op}$ for different albedo, about 4.87. ζ_{app1} keeps the same concept as the ζ_{app} with the SFM approach, therefore, reactors working at the same $\zeta_{app1,op}$ have the same behavior in terms of radiation absorption (Colina-Márquez et al., 2010; Otálvaro-Marín et al., 2014). To prove this affirmation, it was supposed a flat plate reactor working at $\zeta_{app1,op} = 4.87$ with 0.3 g/L of optimum C_{cat} and with $\omega=0.85$. In this case, the reactor height was found about 1.37 cm using Eq. (24). The corresponding $VRPA/H$ was established and for comparison purposes, its curve (curve in yellow in Figure 8 b) was drawn as a function of ζ_{app1} by taking $\omega=0.85$ and $\kappa = 2.87 \text{ cm}^2 \text{ g}^{-1}$ and it was found that it matches the curve in black (see Figure 8 b) $\omega=0.85$). This proves the independence of the optimum catalyst loading on the reactor height and catalyst albedo. $\zeta_{app1,op}$ values obtained were 4.62, 4.87, and 3.7 for Catalyst A, Catalyst D, and Catalyst H,

respectively, almost the same values of the optimum ζ_{app} obtained (4.39, 4.08, and 3.77) with reactor height taken 1 cm by using the features displayed in Table 1. The best design conditions for different catalyst loadings and reactor thicknesses are obtained by keeping

$\zeta_{app1,op}$ constant. For optimization purposes, it is recommended to use ζ_{app} when the reactor height is not near 1 cm, therefore, the same recommendation should be considered when using ζ_{app1} .

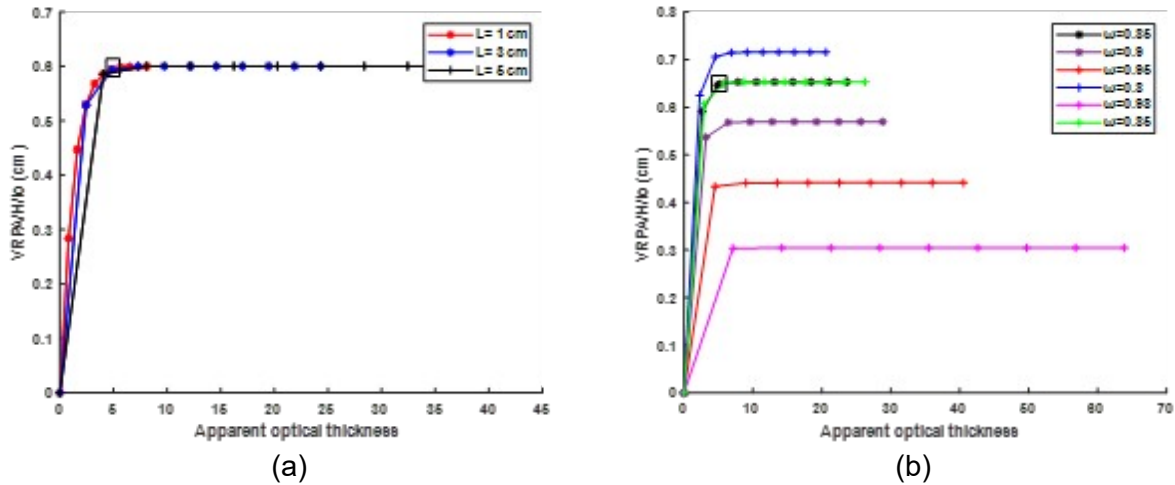


Figure 8. a) Effect of the apparent optical thicknesses ζ_{app1} on the $VRPA/H$ per unit of reactor length and per unit of light intensity with a fixed scattering albedo of the photocatalyst at three different reactor heights. Catalyst D P25 catalyst properties were taken from (Colina-Márquez et al., 2010) ($\omega=0.88$ and $\kappa=1.74 \text{ cm}^2 \text{ g}^{-1}$). The boxed point in the figure corresponds to $\zeta_{app1,op} = 4.87$ and $= 0.595 \text{ cm}$. b) Effect of the apparent optical thicknesses ζ_{app1} on the $VRPA/H$ per unit of reactor length and unit of light intensity as a function of the scattering albedo of the photocatalyst. The specific mass absorption coefficient was kept constant ($2.87 \text{ cm}^2 \text{ g}^{-1}$), and ω was varied, with reactor height equal to 2 cm. The yellow line refers to data of the VRPA obtained using $\zeta_{app1,op} = 4.87$ (the reactor height was found about 1.37 cm using Eq. (24)), $\omega=0.85$ and $\kappa=2.87 \text{ cm}^2 \text{ g}^{-1}$. The boxed point in the figure corresponds to $\zeta_{app1,op} = 4.87$ and $= 0.653 \text{ cm}$.

5. PERSPECTIVES

In future works, our attention will be focusing on extending this present work to flat plate photocatalytic reactors with incident radiation varying along the reactor width and this will imply solving the RTE in 2D using the P1 approximation.

6. CONCLUSION

In this study, it was demonstrated that the P1 approximation is a viable alternative approach for

characterizing the radiant field in a flat plate reactor with any kind of catalyst present in a high-scattering medium. The radiant field in a flat plate photocatalytic reactor was described and optimized using it. The $VRPA$, the boundary layer of photon absorption, and the new apparent optical thickness were established for optimization purposes. These design parameters were used to find the optimum operating conditions employing the catalysts Catalyst D, Catalyst A, and Catalyst H, and comparisons were made between the three catalysts as well.

While the new apparent optical thickness established with the P1 approximation approach eliminates the dependence of the optimum catalyst loading on the reactor height and catalyst albedo, the *VRPA* and the boundary layer of photon absorption help determine the optimal catalyst loading for any reactor height and reactor sizing, respectively. Findings are consistent with those obtained using the SFM and could help for scaling up. The significance of the information provided here for flat plate photoreactor design resides in its ability to remove the necessity for statistical analysis of experimental designs, which requires a major investment of time and resources. Establishing a rate equation to explain the kinetics of the photocatalytic degradation of different chemicals could also benefit from this.

7. ACKNOWLEDGMENTS

Dr. Clovis Nchikou dedicates this article to the memory of Dr. Juan-Antonio Rojas-Estrada.

8. COMPETING INTERESTS

The author declares that he has no known competing financial interests or personal relationships that could have appeared to influence the work reported in this article.

9. REFERENCES





- Acosta-Herazo, R., Cañaverel-Velásquez, B., Pérez-Giraldo, K., Mueses, M. A., Pinzón-Cárdenas, M. H., & Machuca-Martínez, F. (2020). A MATLAB-Based Application for Modeling and Simulation of Solar Slurry Photocatalytic Reactors for Environmental Applications. *Water*, *12*(8), 2196. <https://doi.org/10.3390/w12082196>
- Acosta-Herazo, R., Monterroza-Romero, J., Mueses, M. Á., Machuca-Martínez, F., & Li Puma, G. (2016). Coupling the Six Flux Absorption-Scattering Model to the Henyey-Greenstein scattering phase function: Evaluation and optimization of radiation absorption in solar heterogeneous photoreactors. *Chemical Engineering Journal*, *302*, 86-96. <https://doi.org/10.1016/j.cej.2016.04.127>
- Acosta-Herazo, R., Mueses, M. Á., Machuca-Martínez, F., & Li, G. (s. f.). *Layer of photon absorption and apparent optical thickness*.
- Akdemir, O., Lagendijk, A., & Vos, W. L. (2022). Breakdown of light transport models in photonic scattering slabs with strong absorption and anisotropy. *Physical Review A*, *105*(3), 033517. <https://doi.org/10.1103/PhysRevA.105.033517>
- Arancibia-Bulnes, C. A., Jiménez, A. E., & Estrada, C. A. (2009). Development and Modeling of Solar Photocatalytic Reactors. En *Advances in Chemical Engineering* (Vol. 36, pp. 185-227). Elsevier. [https://doi.org/10.1016/S0065-2377\(09\)00406-2](https://doi.org/10.1016/S0065-2377(09)00406-2)
- Brandi, R. J., Alfano, O. M., & Cassano, A. E. (1996). Modeling of radiation absorption in a flat plate photocatalytic reactor. *Chemical Engineering Science*, *51*(11), 3169-3174. [https://doi.org/10.1016/0009-2509\(96\)00215-1](https://doi.org/10.1016/0009-2509(96)00215-1)
- Brandi, R. J., Alfano, O. M., & Cassano, A. E. (1999). Rigorous model and experimental verification of the radiation field in a flat-plate solar collector simulator employed for photocatalytic reactions. *Chemical Engineering Science*.
- Cassano, A. E., Martin, C. A., Brandi, R. J., & Alfano, O. M. (1995). Photoreactor Analysis and Design: Fundamentals and Applications. *Industrial & Engineering Chemistry Research*, *34*(7), 2155-2201. <https://doi.org/10.1021/ie00046a001>
- Christenson, J. G., Austin, R. A., & Phillips, R. J. (2018). Comparison of approximate solutions to the phonon Boltzmann transport equation with the relaxation time approximation: Spherical harmonics expansions and the discrete ordinates method. *Journal of Applied Physics*, *123*(17), 174304. <https://doi.org/10.1063/1.5022182>
- Colina-Márquez, J., Machuca-Martínez, F., & Li Puma, G. (2015). Modeling the Photocatalytic Mineralization in Water of Commercial Formulation of Estrogens 17- β Estradiol (E2) and Noregestrol Acetate in Contraceptive Pills in a Solar Powered Compound Parabolic Collector. *Molecules*, *20*(7), 13354-13373. <https://doi.org/10.3390/molecules200713354>
- Colina-Márquez, J., Machuca-Martínez, F., & Puma, G. L. (2010). Radiation Absorption and Optimization of Solar Photocatalytic Reactors for Environmental Applications. *Environmental Science & Technology*, *44*(13), 5112-5120. <https://doi.org/10.1021/es100130h>
- Cuevas, S. A., & Arancibia-Bulnes, C. A. (s. f.). *Modeling UV radiation absorption in a flat-plate photocatalytic reactor*.
- Cuevas, S. A., Arancibia-Bulnes, C. A., & Serrano, B. (2007). Radiation Field in an Annular

- Photocatalytic Reactor by the P1 Approximation. *International Journal of Chemical Reactor Engineering*, 5(1). <https://doi.org/10.2202/1542-6580.1589>
- Fujii, H., Terabayashi, I., Aoki, T., Inoue, Y., Na, H., Kobayashi, K., & Watanabe, M. (2022). Numerical Study of Near-Infrared Light Propagation in Aqueous Alumina Suspensions Using the Steady-State Radiative Transfer Equation and Dependent Scattering Theory. *Applied Sciences*, 12(3), 1190. <https://doi.org/10.3390/app12031190>
- Ghafoori, S., Nasirian, M., Al-Jamal, R., Mallouh, F. A., & Mehrvar, M. (2020). Statistical parameter optimization and modeling of photodegradation of methyl orange using a composite photocatalyst prepared by thermal synthesis. *Environmental Science and Pollution Research*, 27(36), 45650-45660. <https://doi.org/10.1007/s11356-020-10301-5>
- Harel, R., Burov, S., & Heizler, S. I. (2021). Asymptotic P_N Approximation in Radiative Transfer Problems. *Journal of Computational and Theoretical Transport*, 50(5), 390-406. <https://doi.org/10.1080/23324309.2020.1845738>
- He, C., Clifton, O., Felker-Quinn, E., Fulgham, S. R., Juncosa Calahorrano, J. F., Lombardozzi, D., Purser, G., Riches, M., Schwantes, R., Tang, W., Poulter, B., & Steiner, A. L. (2021). Interactions between Air Pollution and Terrestrial Ecosystems: Perspectives on Challenges and Future Directions. *Bulletin of the American Meteorological Society*, 102(3), E525-E538. <https://doi.org/10.1175/BAMS-D-20-0066.1>
- Howell, J. R., Mengüç, M. P., Daun, K. J., & Siegel, R. (2021). *Thermal radiation heat transfer* (Seventh edition). CRC Press.
- Illi, E., Bouanani, F. E., Park, K.-H., Ayoub, F., & Alouini, M.-S. (2019). An Improved Accurate Solver for the Time-Dependent RTE in Underwater Optical Wireless Communications. *IEEE Access*, 7, 96478-96494. <https://doi.org/10.1109/ACCESS.2019.2929122>
- Incropera, F. P. (s. f.). [PDF] *Fundamentals Of Heat And Mass Transfer*.
- Li, J., Carlson, B. E., Yung, Y. L., Lv, D., Hansen, J., Penner, J. E., Liao, H., Ramaswamy, V., Kahn, R. A., Zhang, P., Dubovik, O., Ding, A., Lacis, A. A., Zhang, L., & Dong, Y. (2022). Scattering and absorbing aerosols in the climate system. *Nature Reviews Earth & Environment*, 3(6), 363-379. <https://doi.org/10.1038/s43017-022-00296-7>
- Li Puma, G. (2005). Dimensionless Analysis of Photocatalytic Reactors Using Suspended Solid Photocatalysts. *Chemical Engineering Research and Design*, 83(7), 820-826. <https://doi.org/10.1205/cherd.04336>
- Li Puma, G., Machuca-Martínez, F., Mueses, M., Colina-Márquez, J., & Bustillo-Lecompte, C. (2020). Scale-Up and Optimization for Slurry Photoreactors. En C. Bustillo-Lecompte (Ed.), *Advanced Oxidation Processes—Applications, Trends, and Prospects*. IntechOpen. <https://doi.org/10.5772/intechopen.91920>
- Moreno-SanSegundo, J., Casado, C., & Marugán, J. (2020). Enhanced numerical simulation of photocatalytic reactors with an improved solver for the radiative transfer equation. *Chemical Engineering Journal*, 388, 124183. <https://doi.org/10.1016/j.cej.2020.124183>
- Nair, A. K., & JagadeeshBabu, P. E. (2017). Ag-TiO₂ nanosheet embedded photocatalytic membrane for solar water treatment. *Journal of Environmental Chemical Engineering*, 5(4), 4128-4133. <https://doi.org/10.1016/j.jece.2017.07.046>
- Nchikou, C., Loredó-Medrano, J. Á., Hernández-Ramírez, A., Colina-Marquez, J. Á., & Mueses, M. Á. (2021). Estimation of the radiation field for CPC photocatalytic reactors using a novel six-flux model in two dimensions (SFM-2D). *Journal of Environmental Chemical Engineering*, 9(6), 106392. <https://doi.org/10.1016/j.jece.2021.106392>
- Ochoa-Gutiérrez, K. S., Tabares-Aguilar, E., Mueses, M. Á., Machuca-Martínez, F., & Li Puma, G. (2018). A Novel Prototype Offset Multi Tubular Photoreactor (OMTP) for solar photocatalytic degradation of water contaminants. *Chemical Engineering Journal*, 341, 628-638. <https://doi.org/10.1016/j.cej.2018.02.068>
- Otálvaro-Marín, H. L., Mueses, M. A., & Machuca-Martínez, F. (2014). Boundary Layer of Photon Absorption Applied to Heterogeneous Photocatalytic Solar Flat Plate Reactor Design. *International Journal of Photoenergy*, 2014, 1-8. <https://doi.org/10.1155/2014/930439>
- Peralta Muniz Moreira, R., & Li Puma, G. (2021). Multiphysics Computational Fluid-Dynamics (CFD) Modeling of Annular Photocatalytic Reactors by the Discrete Ordinates Method (DOM) and the Six-Flux Model (SFM) and Evaluation of the Contaminant Intrinsic Kinetics Constants. *Catalysis Today*, 361, 77-84. <https://doi.org/10.1016/j.cattod.2020.01.012>

- Rizzo, L., Malato, S., Antakyali, D., Beretsou, V. G., Đolić, M. B., Gernjak, W., Heath, E., Ivancev-Tumbas, I., Karaolia, P., Lado Ribeiro, A. R., Mascolo, G., McArdell, C. S., Schaar, H., Silva, A. M. T., & Fatta-Kassinos, D. (2019). Consolidated vs new advanced treatment methods for the removal of contaminants of emerging concern from urban wastewater. *Science of The Total Environment*, 655, 986-1008. <https://doi.org/10.1016/j.scitotenv.2018.11.265>
- Tourasse, G., & Dumortier, D. (2014). Development of a System Measuring the Solar Radiation Spectrum in 5 Planes for Daylight and PV Applications. *Energy Procedia*, 57, 1110-1119. <https://doi.org/10.1016/j.egypro.2014.10.071>
- Vaya, D., & Surolia, P. K. (2020). Semiconductor based photocatalytic degradation of pesticides: An overview. *Environmental Technology & Innovation*, 20, 101128. <https://doi.org/10.1016/j.eti.2020.101128>
- Wang, D., Mueses, M. A., Márquez, J. A. C., Machuca-Martínez, F., Grčić, I., Peralta Muniz Moreira, R., & Li Puma, G. (2021). Engineering and modeling perspectives on photocatalytic reactors for water treatment. *Water Research*, 202, 117421. <https://doi.org/10.1016/j.watres.2021.117421>
- Zalazar, C. S., Romero, R. L., Martín, C. A., & Cassano, A. E. (2005). Photocatalytic intrinsic reaction kinetics I: Mineralization of dichloroacetic acid. *Chemical Engineering Science*, 60(19), 5240-5254. <https://doi.org/10.1016/j.ces.2005.04.050>



Kinetics Analysis of Crystal Violet Adsorption from Aqueous Solution onto Flamboyant Pod Biochar

Azeez G. Akinyemi^{1,2*} , Abass O. Alade^{1,2,3} , Akeem O. Arinkoola¹ ,
Shukurat B. Olabiyi¹ .

¹Department of Chemical Engineering, Ladoké Akintola University of Technology, Ogbomosó, Nigeria

²Bioenvironmental, Water and Engineering Research Group (BWERG), Ladoké Akintola University of Technology, Ogbomosó, Nigeria

³Science and Engineering Research Group (SAERG), Ladoké Akintola University of Technology, Ogbomosó, Nigeria

Abstract: The increasing presence of persistent synthetic dyes, like crystal violet (CV), in wastewater poses a significant threat to aquatic ecosystems and human health due to its genotoxicity and carcinogenicity. Biochar derived from agricultural waste offers a promising, cost-effective, and eco-friendly approach for dye removal. This study explores the potential of flamboyant pod biochar (FPB) as a novel and sustainable adsorbent for CV removal. FPB offers a unique advantage as it utilizes readily available flamboyant pod waste, promoting waste valorization and a cost-effective approach. FPB was synthesized through a simple process involving milling, sun-drying, and pyrolyzing flamboyant pod waste at 300 °C. Batch adsorption experiments were conducted to evaluate the influence of contact time and initial dye concentration on removal efficiency. Kinetic modeling using pseudo-first-order and pseudo-second-order models explored the underlying mechanisms governing the adsorption process. The pseudo-second-order kinetic model exhibited a superior fit ($R^2 > 0.87$) compared to the pseudo-first-order model, suggesting a chemisorption mechanism governing the adsorption process. These findings demonstrate the potential of FPB as a low-cost, sustainable adsorbent for CV removal from wastewater.

Keywords: Adsorption, Biochar, Crystal Violet, Error Analysis, Kinetic Model.

Submitted: January 14, 2024. **Accepted:** May 06, 2024.

Cite this: Akinyemi, A. G., Alade, A. O., Arinkoola, A. O., & Olabiyi, S. B. (2024). Kinetics Analysis of Crystal Violet Adsorption from Aqueous Solution onto Flamboyant Pod Biochar. *Journal of the Turkish Chemical Society, Section B: Chemical Engineering*, 7(2), 105-122. <https://doi.org/10.58692/jotcsb.1414940>,

*Corresponding author. E-mail: azeezakinyemi61@gmail.com Tel: +2349060267570.

1. INTRODUCTION

Dyes, a ubiquitous group of synthetic aromatic compounds, find application across a vast spectrum of industries, including textiles, food, and pharmaceuticals. However, their recalcitrance towards biodegradation presents a significant environmental challenge. Effluent from the textile industry, a major source of dye contamination, is estimated to contain 10-20% of unused dyes. Adsorption has emerged as a promising strategy for the removal of these pollutants from wastewater due to its high efficiency, reusability, and

diverse range of adsorbent materials (Chahinez et al., 2020; Zamouche et al., 2020).

Crystal violet (CV), a commonly used cationic dye, was selected for this study due to its hazardous nature and strong adsorption properties. Cationic dyes like CV pose a greater threat to human health and the environment compared to their anionic counterparts. This is attributed to their strong affinity for negatively charged cell membranes. This electrostatic attraction allows CV to readily interact with and penetrate living cells, accumulating within

the cytoplasm (Zamouche *et al.*, 2020). CV exhibits cytotoxicity and genotoxicity, including mutagenic and carcinogenic properties (Abbasi *et al.*, 2020). Therefore, developing efficient methods for CV removal from wastewater is crucial.

Delonix regia pods, commonly known as flamboyant pods or flame tree pods, present a promising renewable feedstock for biochar production. These large, lignocellulosic pods are a byproduct of the flamboyant tree (*Delonix regia*), a popular ornamental species cultivated throughout tropical and subtropical regions. Following seed dispersal, the pods naturally detach from the tree and accumulate as a significant component of agricultural waste. Fortunately, flamboyant pods possess several characteristics that make them ideal biochar feedstock. Their abundance, cellulosic composition, and ease of collection and processing after falling from the tree contribute to their suitability. Moreover, utilizing flamboyant pods for biochar creation not only addresses agricultural waste management but also transforms this waste into a valuable product for environmental applications, promoting a sustainable waste valorization approach.

Biochar has emerged as a promising adsorbent for dye remediation due to its exceptional capacity. This stems from its high surface area, offering a multitude of binding sites for dye molecules, and the presence of diverse functional groups on its surface that can interact favorably with dyes. While traditional methods often boast high efficacy, their economic feasibility can be hindered by the vast array of dye structures. The adsorption capacity and specific interaction mechanisms between biochar and dye pollutants are influenced by a complex interplay of factors. These include the inherent characteristics of the dye itself, the properties of the biochar (such as surface chemistry and porosity), environmental conditions (pH, ionic strength), and even the aging process of the biochar (Vyavahare *et al.*, 2019). Understanding the impact of these key factors is crucial for optimizing biochar's application in dye removal.

In recent years, adsorption has emerged as a preferred method for dye removal from wastewater due to several advantages, including high efficiency, ease of operation, a vast array of applicable adsorbent materials, and cost-effectiveness (Loulidi *et al.*, 2020).

However, optimizing adsorption processes for maximum dye removal efficiency necessitates a thorough understanding of the various influencing parameters and their impact on adsorption capacity. Traditional optimization techniques often rely on a substantial number of experiments, which can be both expensive and time-consuming (Rosly *et al.*, 2021). Furthermore, these methods might not adequately capture the intricate interactions between process variables and their combined effects on the adsorption capacity (Rosly *et al.*, 2021).

This study addresses these limitations by investigating flamboyant pod biochar (FPB) as a novel, sustainable adsorbent for crystal violet removal. We explore the efficacy of FPB by examining the influence of key adsorption parameters such as dye concentration, contact time, and FPB dosage. Furthermore, equilibrium isotherms and error analysis are employed to elucidate the mechanism and correlation governing the adsorption process.

2. MATERIAL AND METHODS

2.1. Biochar Synthesis from Flamboyant Pod

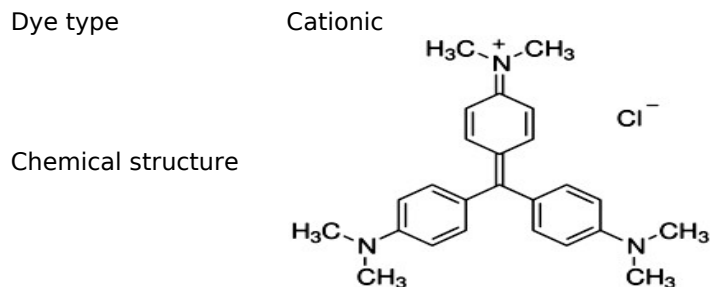
The acquired flamboyant pod sample was washed with distilled water to remove surface impurities, sun-dried for 48 hours to reduce moisture content, milled with PMG-100, power mortar grinder, and sieved using a 2 mm mesh sieve size to obtain uniform particle size. The resulting flamboyant pod sample was calcined at temperature (300 °C), particle size (2 mm), flamboyant pod moisture (10 %), and pyrolysis duration (30 minutes) in a muffle furnace to produce flamboyant pod biochar, referred to as FPB (Barber *et al.*, 2018).

2.2. Preparation of Adsorbate Solution

The Crystal Violet (CV) dye (chemical formula = $C_{25}H_{30}N_3Cl$, solubility in water 16 g/L at 25 °C, Molecular weight = 407.98 g/mol) with a purity of 99% was used in this study (structure shown in Table 1). A stock solution of 1000 mg/L CV was prepared by dissolving 1 g of the dye in 1 L of distilled water in a volumetric flask. The stock solution was stored in a dark environment to avoid depolarization. All working solutions with desired concentrations were prepared by diluting the stock solution with distilled water according to standard methods (APHA 1995).

Table 1: Characteristics and chemical properties of crystal violet.

Name	Crystal Violet
Chemical formula	$C_{25}H_{30}N_3Cl$
Molecular weight	407.98 g/mol
λ_{max} (nm)	590 nm



2.3 Batch Adsorption Experiment

All experiments were conducted in triplicate, and the reported values represent averages with associated standard deviations. Initial optimization experiments established the optimal range for initial dye concentration (50-250 mg/L) and contact time (10-225 minutes). For the adsorption experiments, 100 mL of dye solution with an initial concentration of 50 mg/L was added to 250 mL conical flask along with a 1 g of FPB. The mixture was agitated on a shaker (Bioshaker BR-23FH) at 150 rpm for the desired contact time (10-225 minutes). After agitation, the residual concentration of the dye solution were obtained using a UV-visible spectrophotometer, measuring absorbance at the maximum wavelength of CV ($\lambda_{max} = 590 \text{ nm}$).

$$\text{Removal Efficiency (\%)} (\text{RE}) = \frac{C_0 - C_e}{C_0} \times 100 \quad (1)$$

$$\text{Adsorption Capacity}_{(mg/g)} @ \text{equilibrium} (q_e) = (C_0 - C_e) \frac{M}{V} \quad (2)$$

$$\text{Adsorption Capacity}_{(mg/g)} @ \text{any time} (q_t) = (C_0 - C_t) \frac{M}{V} \quad (3)$$

Where C_0 and C_e are the initial and final concentration of the crystal violet and m and v is the mass of the biochar and volume of

the adsorbate utilized, while q_e and q_t are adsorption capacity (mg/g) at equilibrium and any time, respectively.

2.4. Analysis of Experimental Data

2.4.1. Adsorption kinetic model

Adsorption kinetics plays a pivotal role in determining the pace at which a solute is taken up, while influencing the duration of its interaction at the solid-solution interface. Therefore, it is essential to comprehend the reaction mechanism governing the sorption process for the effective design of sorption treatment facilities. If not adequately comprehended, the adsorption kinetics could present significant challenges in the development of treatment systems incorporating adsorbents. Furthermore, it serves as a tool to identify the rate-limiting step within an adsorption process. The insights derived from adsorption kinetics are invaluable to industry operators and planners, offering crucial guidance for the appropriate treatment of contaminated wastewater through adsorption. In practical or industrial settings, the rapid adsorption of solutes in an adsorption system is highly desirable. Kinetic parameters aid in predicting the adsorption rate and equilibrium time, providing essential information for the design and modeling of adsorption processes. The specific adsorption kinetics examined in this research are detailed below.

Table 2: Linear and non-linear forms of adsorption kinetic models (8).

Models	Non-linear	Equation
Zeroth order	NA	$q_t = k_0 t + q_0$
First order	NA	$\ln q_t = k_1 t + \ln q_0$
Second order	NA	$\frac{1}{q_t} = k_2 t + \frac{1}{q_0}$
Third order	NA	$\frac{1}{q_t^2} = k_3 t + q_0^2$
Pseudo-first order		
Type 1	$q_t = q_e (1 - e^{-k_1 t})$	$\log(q_e - q_t) - \log(q_e) = \frac{-k_1 t}{2.303}$

Type 2

Type 3

$$c_t = c_o e^{-k_1 t}$$

Type 4

$$\ln(q_e - q_t) - \ln(q_e) = -k_1 t$$

$$\ln\left(\frac{c_t}{c_o}\right) = -k_1 t$$

$$\ln\left(1 - \frac{c_o - c_t}{c_o - c_e}\right) = -k_1 t$$

Pseudo Second Order

Type 1

$$\frac{1}{q_t} = \frac{1}{k_2 q_e^2} + \frac{t}{q_e}$$

Type 2

$$\frac{1}{q_t} = \frac{1}{k_2 q_e^2} \frac{1}{t} + \frac{1}{q_e}$$

Type 3

$$\left(\frac{1}{q_t} - \frac{1}{q_e}\right) q_e^2 = \frac{1}{k_2 t}$$

Type 4

$$q_t = q_e \left[1 - \frac{1}{1 + k_2 t} \right]$$

$$q_t = q_e - \left(\frac{1}{k_2 q_e}\right) \frac{q_t}{t}$$

Type 5

$$(q_t - q_e) q_e = -\left(\frac{q_t}{k_2 t}\right)$$

Type 6

$$\frac{q_t}{t} = k_2 q_e^2 - k_2 q_e q_t$$

Type 7

$$\frac{1}{q_e - q_t} - \frac{1}{q_e} = k_2 t$$

Type 8

$$\frac{1}{t} = k_2 q_e^2 \left(\frac{1}{q_t}\right) - k_2 q_e$$

Type 9

$$\frac{q_e}{q_e - q_t} - 1 = k_2 t$$

Type 10

$$\frac{\Theta}{1 - \Theta} = k_2 t$$

Type 11

$$C_t - \frac{1}{C_0} = k_2 t$$

Type 12

$$\frac{1}{C_t} - \frac{1}{C_0} = k_2 t$$

Type 13

$$\frac{1}{C_0 - C_t} = k_2 t + b$$

Pseudo-third order

$$q_t = q_e \left[1 - \frac{1}{(1 + 2k_3 t)^{\frac{1}{2}}} \right]$$

Esquivel kinetic model

Type 1

$$\frac{1}{q_t} = \frac{K_E}{q_e t} + \frac{1}{q_e}$$

Type 2

$$q_t = q_e \left(\frac{t}{t + K_E} \right)$$

$$\left(\frac{1}{q_t} - \frac{1}{q_e}\right) q_e = \frac{K_E}{t}$$

Elovich kinetic model

Type 1

$$q_t = k_5 \ln(k_5 k_{eq}) + k_5 (\ln t)$$

Type 2	$q_t = \frac{-k_4}{k_5} t e^{-k_1 q_t}$	$q_t = \frac{1}{k_6} \ln(k_6 k_7) + \frac{1}{k_6} \ln t$
Avrami	$q_t = q_e - q_e \exp(-k t^n)$	$\ln \left(\ln \left(\frac{q_e}{q_e - q_t} \right) \right) = n \ln k + n \ln t$

2.4.2 Statistical Error Analysis

Over the years, error functions have found utility in the selection of the appropriate adsorption model. Their primary utility lies in quantifying the dispersion of the adsorbent, facilitating a rigorous quantitative analysis of the data, and, most significantly, confirming the consistency of the experimental results, which underpin the construction of the

adsorption model (Benmaamar *et al.*, 2017). In this process, the most suitable equation is derived by employing established special functions to quantify the error deviation between the experimentally observed data and the estimated values. The mathematical equations for these error functions are presented in Table 3.

Table 3: Mathematical equations of error analysis function.

Error function	Equation	Reference
Sum square error	$SSE = \sum_{i=1}^n (q_{\text{exp}} - q_{\text{obs}})^2$	(Batool <i>et al.</i> , 2018)
Hybrid function fractional error	$HYBRID = \frac{100}{p-n} \sum_{i=1}^p \left[\frac{(q_{e,\text{exp}} - q_{e,\text{cal}})^2}{q_{e,\text{exp}}} \right]$	(Sivarajasekar & Baskar, 2019)
Marquardt's percent standard deviation (MPSD)	$MPSD = 100 \sqrt{\frac{1}{n-p} \sum_{i=1}^n \left(1 - \frac{q_{e,\text{cal}}}{q_{e,\text{obs}}} \right)^2}$	(Olafadehan, 2021)
Sum of normalized errors	$SNE = \sum_{i=1}^n \frac{f_i}{f_{i,\text{max}}}$	(Adekunbi <i>et al.</i> , 2020)
Sum of absolute errors	$SAE = \sum_{i=1}^n q_{\text{exp}} - q_{\text{obs}} $	(Shojaei <i>et al.</i> , 2019)
Residual Sum of Squares	$RSS = \sum_{i=1}^n q_{\text{exp}} - q_{\text{obs}} ^2$	(Elmorsi <i>et al.</i> , 2022)
Nonlinear chi-square test	$X^2 = \sum_{i=1}^n \frac{(q_{e,\text{obs}} - q_{e,\text{cal}})^2}{q_{e,\text{obs}}}$	(Hami <i>et al.</i> , 2019)
Coefficient of determination (R2)	$R^2 = 1 - \frac{\sum_{i=1}^n (q_{e,\text{exp}} - q_{e,\text{cal}})^2}{\sum_{i=1}^n (q_{e,\text{cal}} - q_{e,\text{exp}})^2}$	(Popoola, 2019)
Average relative error (ARE)	$ARE = \frac{1}{n} \sum_{i=1}^n \left \frac{q_{e,\text{obs}} - q_{e,\text{cal}}}{q_{e,\text{obs}}} \right $	(Adekunbi <i>et al.</i> , 2020)
Standard deviation of relative error (SRE)	$SRE = \sqrt{\frac{1}{n} \sum_{i=1}^n [(q_{e,\text{obs}} - q_{e,\text{cal}}) - ARE]^2}$	(Popoola, 2019)
Residual Root Mean Squared Error (RMSE)	$RMSE = \frac{1}{n-2} \sqrt{\sum_{i=1}^n (q_{e,\text{obs}} - q_{e,\text{cal}})^2}$	(Elmorsi <i>et al.</i> , 2022)
ARED	$ARED = \frac{100}{n} \sum_{i=1}^n \left \frac{q_{e,\text{obs}} - q_{e,\text{cal}}}{q_{e,\text{obs}}} \right $	(Olafadehan, 2021)

$$\begin{aligned}
 \text{ARS} &= \sqrt{\frac{\sum_{i=1}^n \left[\frac{q_{e,obs} - q_{e,cal}}{q_{e,obs}} \right]^2}{n-1}} && \text{(Hami et al., 2019)} \\
 \text{MPSED} &= \sqrt{\frac{\sum_{i=1}^n \left[\frac{q_{e,obs} - q_{e,cal}}{q_{e,obs}} \right]^2}{n-p}} && \text{(Elmorsi et al., 2022)} \\
 \Delta q (\%) = 100 * \text{ARS} &= 100 \sqrt{\frac{\sum_{i=1}^n \left[\frac{q_{e,obs} - q_{e,cal}}{q_{e,obs}} \right]^2}{n-1}} && \text{(Shojaei et al., 2019)}
 \end{aligned}$$

In this study, several key parameters are employed to evaluate and analyze the adsorption of crystal violet onto FPB. The number of experimental data points, denoted as "n," plays a crucial role in shaping the analysis. Additionally, "q_{cal}" represents the calculated amount of crystal violet adsorbed onto FPB, while "q_{obs}" (or "q_{exp}") signifies the experimentally observed data. The variable "p" indicates the number of parameters utilized within each kinetic model, reflecting the model's complexity. Further, various metrics are utilized to assess the quality and accuracy of the analysis, including ARED, ARE, ARS, and the dimensionless parameter "HYBRID." Additionally, parameters such as SNE, MPSD, MPSED, SAE, SSE, and q(%) are all examples of normalized error metrics used to rigorously assess the adsorption process.

3. RESULTS AND DISCUSSION

3.1. Effect of Contact Time

The contact time has a major impact on the performance of the adsorption process. It helps to determine how long it takes for CV adsorption on FPB to attain equilibrium. An initial concentration of 100 mg/L, continual agitation of 150 rpm, a dose of 1 g of FPB, room temperature, and contact times between 30 and 225 minutes were applied in this experiment. Three steps of adsorption are visible in the result. Adsorption proceeds fast at stage 1 of the process, and dye molecules enter the process's huge pores on the adsorbent's surface instantly shortly. Stage 2 contains a slower intra-particle diffusion process when dye molecules penetrate the tiny pores of the adsorbent, and stage 3 is when equilibrium is attained. Further adsorption was minimal as a function of contact time after establishing equilibrium (Çoruh & Geyikçi, 2012). The FPB reaches saturation in roughly 66 minutes and has an adsorption capacity and removal efficiency that improve with time. There are several accessible active sites on the FPB adsorbent surface, which contributes to the first

increase in the rate of adsorption capacity. In contrast to the sluggish CV adsorption, which was created by the saturation of the binding sites, the slow adsorption of dye ions was caused by the repulsive forces between the dye ions and the ions already adsorbed on the adsorbent (Lairini et al., 2017).

The effect of contact time on CV adsorption by FPB was investigated. Experiments employed an initial CV concentration of 100 mg/L, continuous agitation at 150 rpm, a 1 g FPB dose, and room temperature, with contact times varying from 30 to 225 minutes. The results revealed a three-stage adsorption process. Stage 1 exhibited a rapid initial uptake as CV molecules readily occupied the abundant pores on the FPB surface, leading to a significant increase in both adsorption capacity and removal efficiency due to the presence of numerous active sites. Stage 2 involved a slower intra-particle diffusion process where dye molecules penetrated the smaller pores of the FPB, resulting in continued adsorption at a slower rate. Finally, Stage 3 represented the achievement of equilibrium, where further adsorption became minimal with increasing contact time (Çoruh & Geyikçi, 2012). FPB reached saturation around 66 minutes. This three-stage process highlights the interplay between available active sites and repulsive forces. The initial rapid adsorption and subsequent slowdown can be attributed to the depletion of active sites and the development of repulsive forces between incoming CV molecules and those already adsorbed on the FPB (Lairini et al., 2017).

3.2. Pareto Analysis of the Effect of Time on QE and RE

The Pareto analysis (Equation 4), also known as the 80/20 rule, is a valuable tool for identifying the factors with the most significant influence on a process. In this study, we employed Pareto analysis to assess the relative importance of contact time on the adsorption capacity (QE) and

removal efficiency (RE) of CV by FPB (Zarei et al., 2010):

$$P_i(\%) = \left[\frac{(b_i^2)}{\sum b_i^2} \right] \times 100 \quad (4)$$

The Pareto effect of each item in Equation 4 is represented in P_i , whereas B_i shows the regression coefficients from the regression equation in terms of coded values. As shown

in Figure 1, the contact time between 0 and 45 minutes has the greatest impact on the adsorption capacity and the removal efficiency of CV dye by the FPB adsorbent, with the first 45 minutes accounting for about 80% of the adsorbent's activity in the removal of dye, compared to the remaining of the 225 minutes, which account for only 20%. The bulk of CV dye adsorption happened within the first five minutes and over 80% of the dye was absorbed during the (30 mins) rapid adsorption phase.

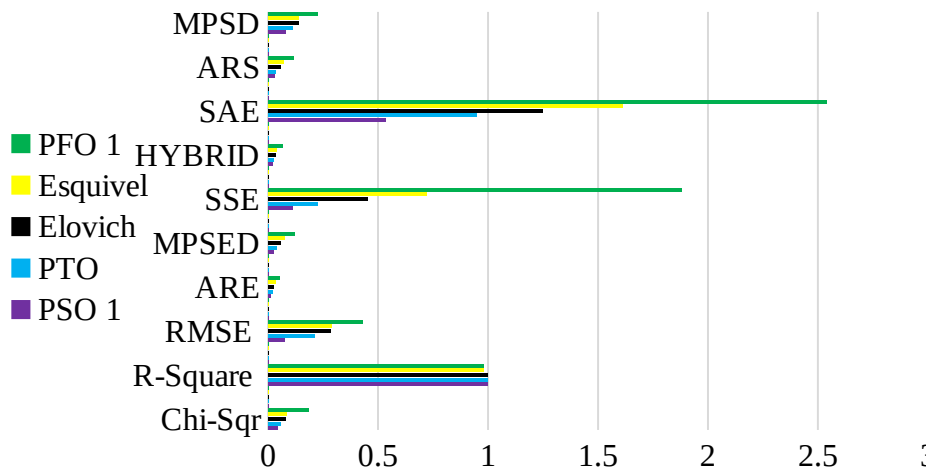
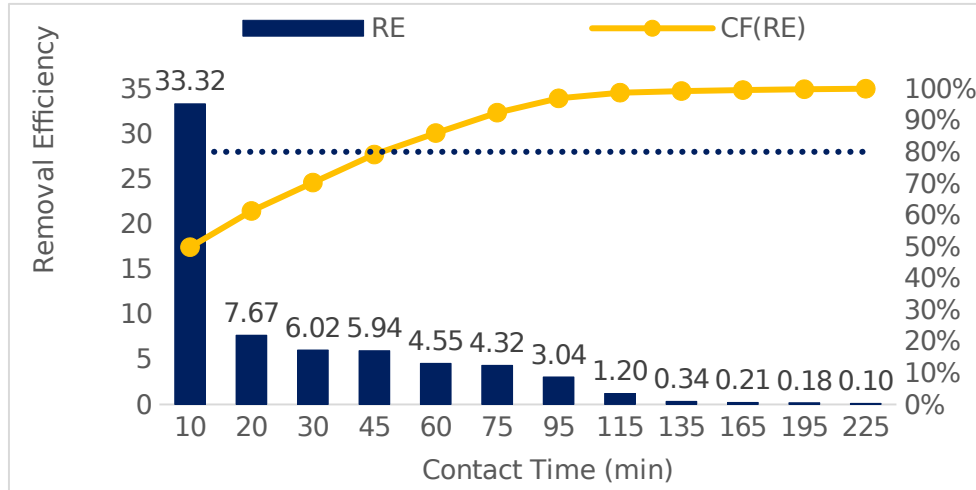


Figure 1: Pareto chart of (top) adsorption capacity (bottom) removal efficiency for the effect of contact time on CV dye.

3.3. Adsorption Kinetics

Several linear and nonlinear kinetic models were applied to investigate the adsorption kinetics of the experimental data of adsorption of crystal violet by FPB. Analyzing the kinetic parameters obtained from these models can provide valuable information for

estimating the adsorption rate and optimizing adsorption processes (Abbasi et al., 2020; Patil et al., 2020). The kinetic constants of each model studied in this inquiry are presented in Table 4-5 for linear and nonlinear appropriate.

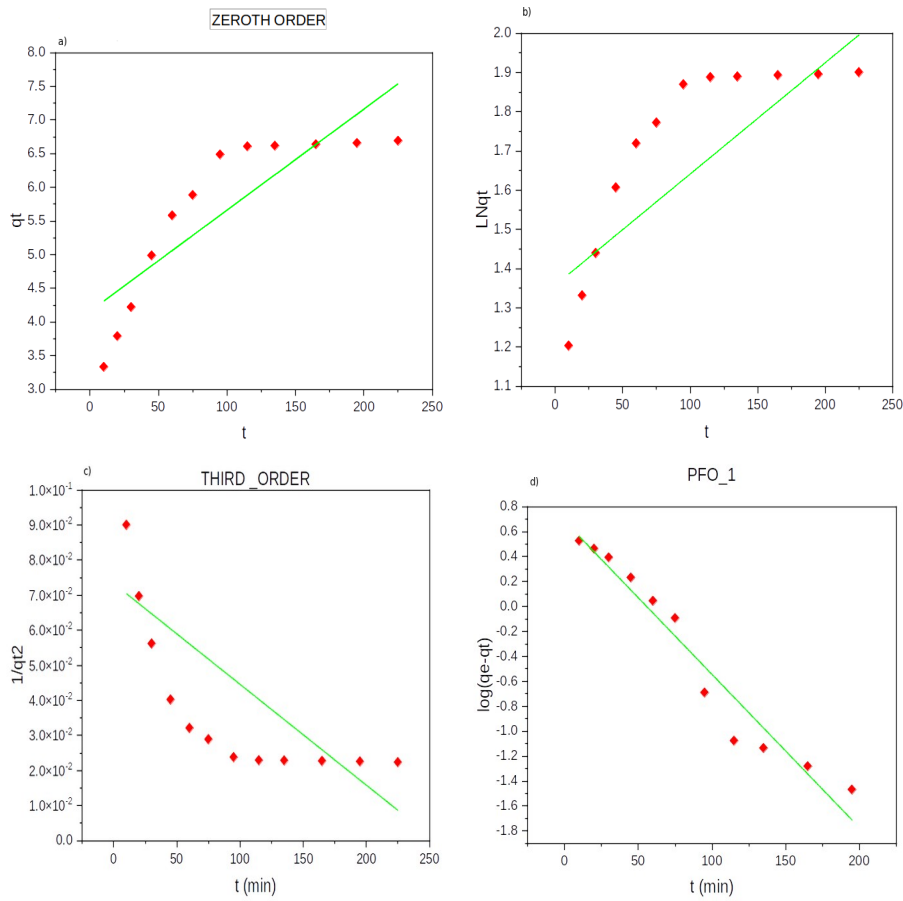
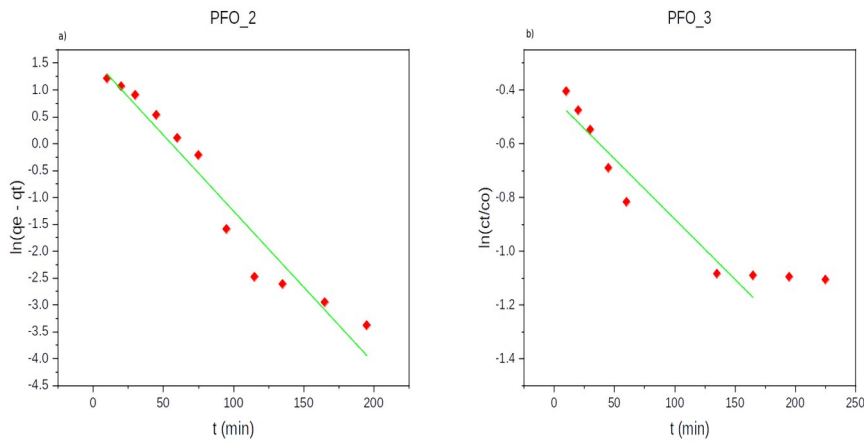


Figure 2: Graph of (a) Zeroth order (b) First Order (c) Second Order (d) Third Order Kinetic model.



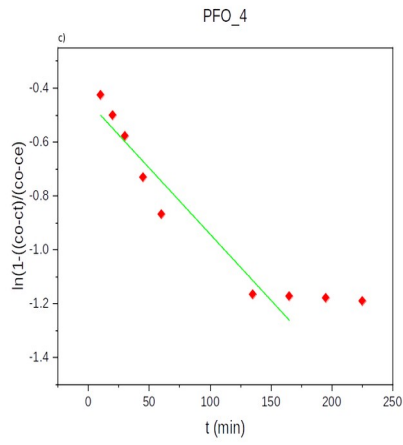
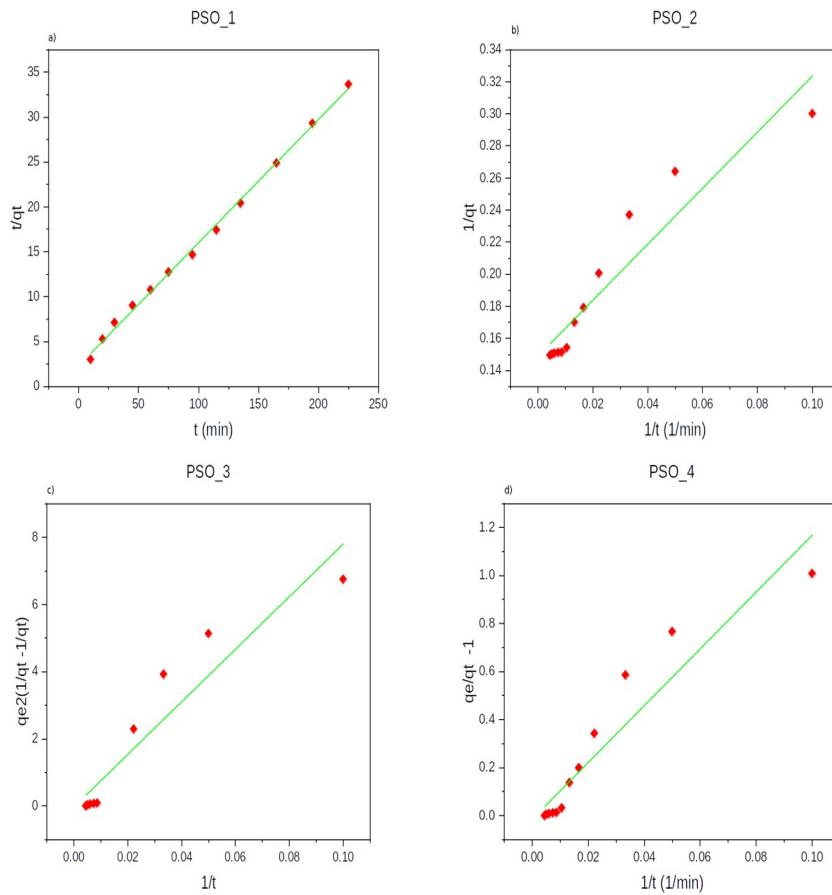
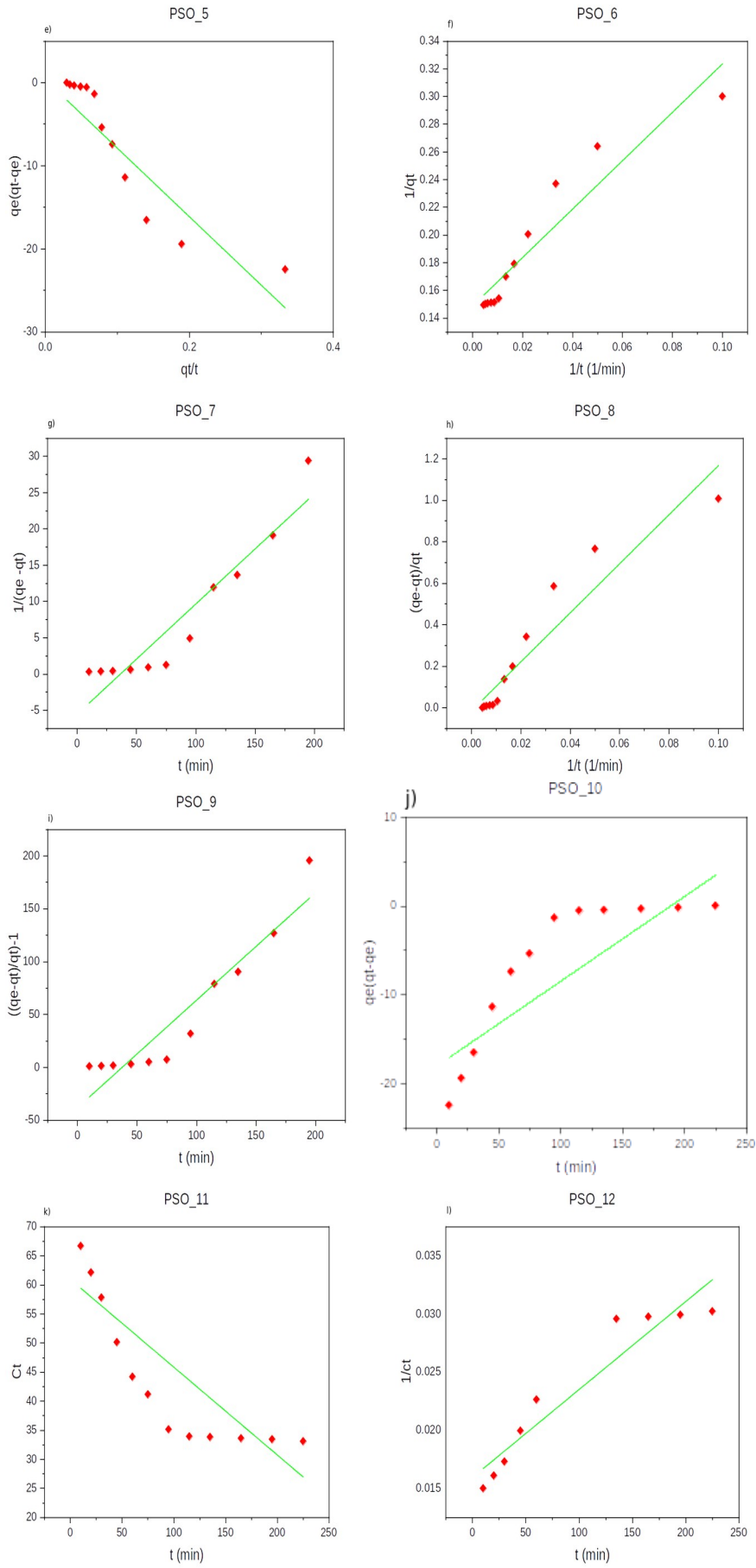


Figure 3: Graph of Pseudo First Order (a) Type 1, (b) Type 2, (c) Type 3





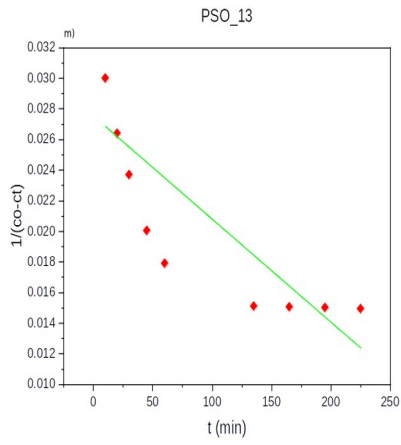


Figure 4: Graph of Pseudo Second Order (a) Type 1, (b) Type 2, (c) Type 3, (d) Type 4, (e) Type 5, (f) Type 6, (g) Type 7, (h) Type 8, (i) Type 9, (j) Type 10, (k) Type 11, (l) Type 12, (m) Type 13.

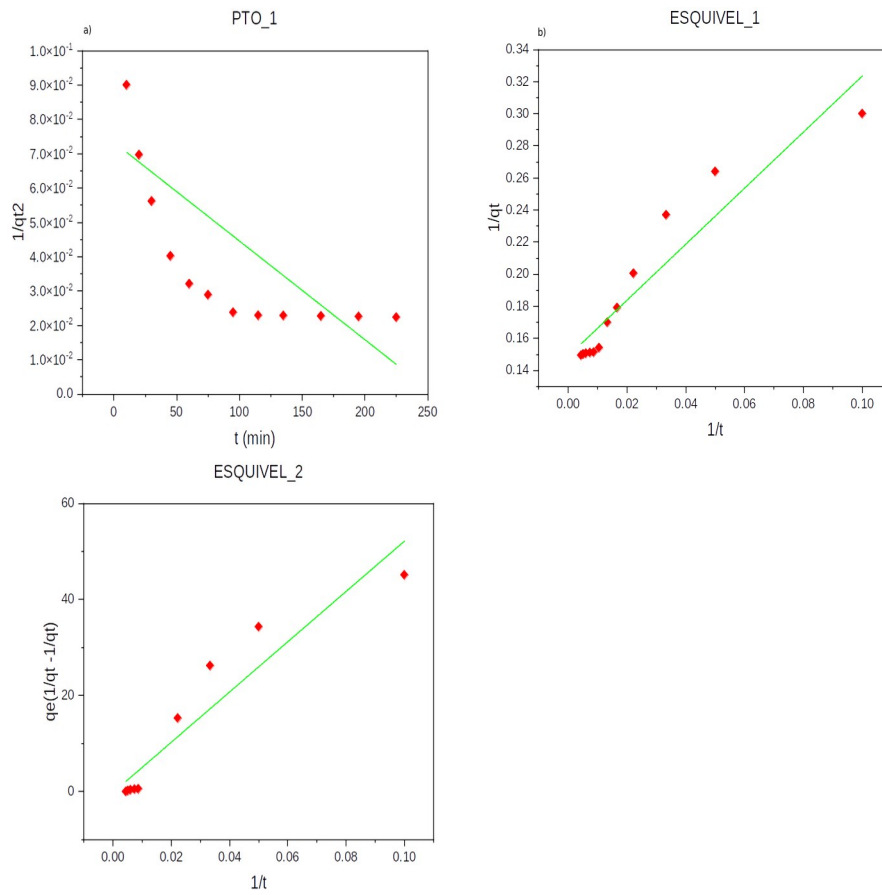


Figure 5: Graph of (a) Pseudo Third Order, (b) Esquivel Type 1, (c) Esquivel Type 2.

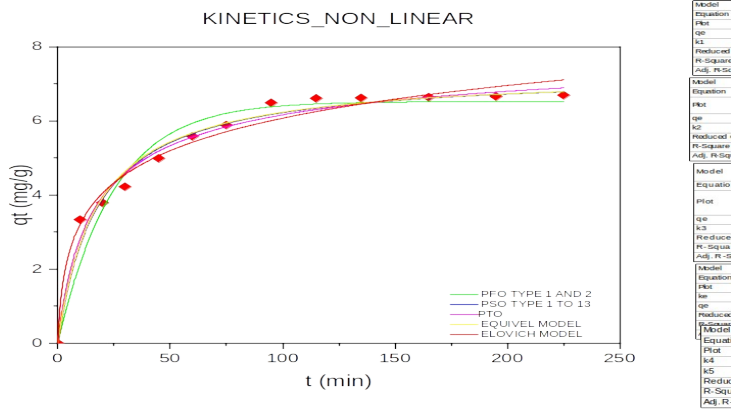


Figure 6: Graph of Non-linear Kinetic Models.

Table 4: Parameters of linear kinetic models.

Model	Parameter	Value	Model	Parameter	Value
Zeroth order	K_0	0.0150	PSO 7	K_2	0.1519
First order	K_0	0.0028	PSO 8	K_2	0.0126
Second order	K_0	-0.0006	PSO 9	K_2	1.0163
Third order	K_0	-0.0003	PSO 10	K_2	0.0956
PFO 1	K_1	0.0283	PSO 11	K_2	-0.1510
PFO 2	K_1	0.0283	PSO 12	K_2	7.56E-05
PFO 3	K_1	0.0045	PSO 13	K_2	-6.7E-05
PFO 4	K_1	0.0050	PTO	K_3	-2.8740
PSO 1	K_2	0.0598	Elovich 1	K_4	15.2137
PSO 2	K_2	0.0127		K_5	0.2327
PSO3	K_2	0.0128	Elovich 2	K_4	0.7961
PSO 4	K_2	0.0126		K_5	1.5877
PSO 5	K_2	0.0121	Esquivel 1	K_4	11.7437
PSO 6	K_2	0.0127	Esquivel 2	K_4	523.6213

Table 5: Parameters of non-linear kinetic models.

Kinetic Model	Parameter	Value
PFO 1	Q_E	6.5238
	K_1	0.0403
PSO 1	Q_E	7.3192
	K_2	0.0569
PTO	Q_E	8.4464
	K_3	0.0635
Elovich	K_4	1.4488
	K_5	0.7796
Esquivel	Q_E	7.3108
	K_5	0.5753

3.4. Error Analysis

As presented in Table 6, it is obvious that the non-linear Elovich kinetic model is the best

fitting model for the experimental data of the adsorption phenomenon studied with the lowest value of RSS, ARED, ARE, MPSED,

SSE, HYBRID, SAE=EABS, ARS, and Q = 100*ARS and the highest R², Adj. R² and (R-Value) values were found when modeling the experimental data using the pseudo-first-order model, pseudo-second-order, and pseudo-third-order model. The pseudo third-order model also displayed the lowest Reduced Chi-Sqr and RMSE values for the experimental data. The linear pseudo-second order type 2 proved to be the best fitting model for the adsorption experiment data as shown in Table 7 with the lowest ARED, MPSED, SSE, SAE=EABS, ARS, Q = 100*ARS, and MPSED values. The lowest value of RSS was attained by modeling pseudo-second-order model type 12 & 13 using the experimental data whereas the maximum values of R-Square, Adj. R² and Pearson's r were obtained by modeling Pseudo second-order kinetic model type 1. Esquivel Type 2 displayed the least value of ARE and SSE.

A swift comparison between linear and non-linear analyses was conducted to identify the most suitable error function(s) for each regression technique, employing the pseudo-second-order model as a case study. Our findings revealed that, in the context of

linear analysis, the regression coefficient (R²) attained the highest value (pseudo-second order type 1), making it the most acceptable error estimation tool for identifying the optimal kinetic model fit within a linear framework. Conversely, the other error functions (ARED, ARE, SAE, ARS, MPSED, Δq, SSE, MSPED, and HYBRID) exhibited superior suitability for non-linear analysis. It's important to note that the transition from non-linear to linear regression procedures introduces a shift in experimental error, presenting a unique challenge in error estimation that influences the validity of the chosen approach. Furthermore, the linear analysis technique implies that data points cluster around a Gaussian distribution, with error estimates remaining consistent at the equilibrium liquid-phase residual concentration value (X-axis) (Olaosebikan *et al.*, 2022). However, this behavior is inconsistent with equilibrium kinetic models, given their non-linear nature. Surprisingly, a non-linear regression approach mitigates such errors, rendering it the most suitable analytical method for obtaining more realistic isotherm parameters (Elmorsi *et al.*, 2022).

Table 6: Error analysis of the selected non-linear kinetic models.

Models	PFO 1	PSO 1	PTO	Elovich	Esquivel
R. Chi-Sqr	0.1863	0.0444	0.0558	0.0809	0.0823
R-Square	1.0000	1.0000	1.0000	0.9808	0.9804
Adj. R2	1.0000	1.0000	1.0000	0.9790	0.9786
RSS	2.0492	44.3303	5.7355	0.8895	0.9048
R-Value	1.0000	1.0000	1.0000	0.9903	0.9902
RMSE	0.4316	0.2108	0.4058	0.2844	0.2868
ARED	5.3477	0.1293	2.6956	1.8947	3.4189
ARE	0.0535	0.0129	0.0270	0.0189	0.0342
MPSED	0.1206	0.0237	0.0577	0.0387	0.0729
SSE	1.8788	0.1105	0.4518	0.2269	0.7189
HYBRID	0.0642	0.0195	0.0323	0.0253	0.0410
SAE=EABS	2.5371	0.5347	1.2482	0.9482	1.6139
ARS	0.1150	0.0303	0.0550	0.0350	0.0695
Q = 100*ARS	11.5034	3.0280	5.5042	3.5003	6.9474
MPSD	0.2273	0.1395	0.1103	0.0781	0.1390

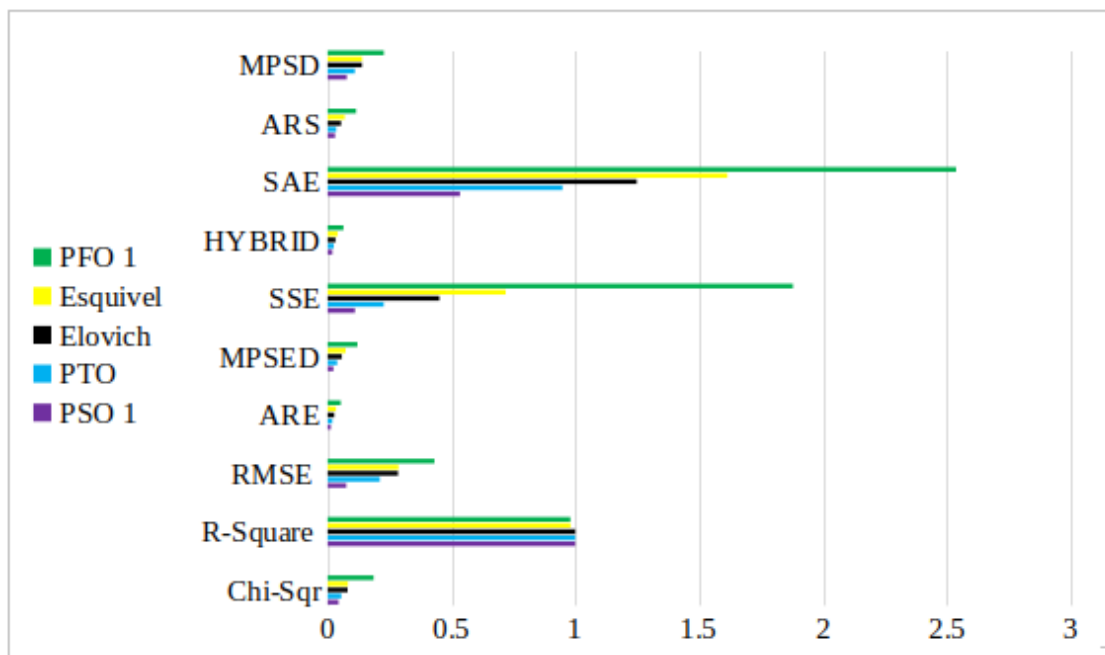


Figure 7: Plot of nonlinear kinetic error analysis.

Table 7: Error analysis of the selected linear kinetic models.

Kinetic Models	RSS	Pearson's r	R2	Adj. R2	ARED	ARE	MPSED	SSE	HYBRID	SAE=EABS	ARS	Q =100*ARS	MPSD
Zeroth	4.632	0.8530	0.7276	0.7004	10.777	0.1078	0.1355	4.6316	0.1176	6.6411	0.1355	13.5484	0.2898
First	0.105	0.8948	0.8006	0.7673	12.324	0.1232	0.147	7.8734	0.1345	8.3549	0.147	14.7029	0.3487
Second	0.006	-0.8746	0.7649	0.7313	14.646	0.1465	0.1717	11.7751	0.1598	10.2293	0.1717	17.1702	0.4184
Third	0.001	-0.8838	0.7811	0.7446	14.646	0.1465	0.1717	11.7751	0.1598	10.2293	0.177	17.7021	0.4184
PFO 1	0.301	-0.9742	0.9491	0.9434	133.84	1.3384	1.9908	1921.15	1.4601	103.419	1.9908	199.079	5.1277
PFO 2	1.597	-0.9742	0.9491	0.9434	100.97	1.0098	1.8471	996.53	1.1016	58.2284	1.8471	184.714	4.1776
PFO 3	0.033	-0.9641	0.9294	0.9153	108.97	1.0977	1.7144	996.53	1.1566	58.8367	1.8714	184.737	4.7561
PFO 4	0.037	-0.9658	0.9328	0.9194	122.97	1.0098	1.8471	996.53	1.1016	58.2284	1.8471	188.714	4.1561
PSO 1	2.739	0.9987	0.9974	0.9971	4.7003	0.047	0.0014	0.9097	0.0513	2.5987	0.0014	0.1374	0.1114
PSO 2	0.003	0.9468	0.8965	0.8817	7.800	0.078	0.0061	0.2561	0.078	0.506	0.0061	0.610	0.0395
PSO3	5.700	0.9468	0.8965	0.8817	17.63	0.1763	0.0311	1.3078	0.1763	1.1436	0.0311	3.114	0.2016
PSO 4	0.134	0.9477	0.8981	0.8879	63.737	0.6374	1.0589	209.26	0.6953	32.2491	1.0589	105.887	2.1296
PSO 5	90.555	-0.9215	0.8492	0.8276	69.1724	0.6917	1.3086	252.97	0.7546	32.6196	1.3086	130.856	2.4935
PSO 6	0.003	0.9468	0.896	0.882	1.E+04	1.7E+02	2.4E+02	1.6E+07	1.5E+02	7.7E+03	2.4E+02	2.4E+04	5.3E+02
PSO 7	103.6	0.945	0.892	0.880	25.215	0.252	0.455	32.555	0.275	12.054	0.455	45.554	0.881
PSO 8	0.134	0.948	0.898	0.888	1.7E+04	1.7E+02	4.5E+02	6.8E+07	1.9E+02	1.1E+04	4.5E+02	4.5E+04	1.1E+03
PSO 9	4638	0.945	0.892	0.880	21.162	0.212	0.378	22.861	0.231	10.170	0.378	37.774	0.734
PSO 10	117.4	0.897	0.804	0.777	14.919	0.149	0.289	17.415	0.163	7.872	0.289	28.893	0.601
PSO 11	239.7	-0.915	0.837	0.814	14.986	0.192	0.289	17.454	0.127	7.723	0.289	28.930	0.604
PSO 12	0.000	0.952	0.906	0.892	19.919	0.492	0.889	17.154	0.175	7.831	0.293	28.759	0.643
PSO 13	0.000	-0.923	0.862	0.850	19.189	0.419	0.893	17.164	0.151	7.308	0.230	28.759	0.631
PTO	0.001	-0.884	0.781	0.745	40.438	0.404	0.654	94.482	0.441	21.319	0.654	65.439	1.373
Elovich-1	0.882	0.974	0.948	0.943	31.432	0.314	0.533	57.184	0.377	16.574	0.508	50.869	1.120
Elovich-2	0.882	0.974	0.948	0.943	31.232	0.332	0.352	57.358	0.319	16.427	0.569	50.876	1.118
Esquivel-1	0.003	0.947	0.896	0.882	5.420	0.054	0.064	0.748	0.067	1.679	0.064	6.379	0.129
Esquivel-2	255.20	0.9468	0.896	0.882	5.052	0.050	0.069	0.762	0.061	1.695	0.069	6.363	0.126

4. CONCLUSION

The efficacy of synthetic FPB for the removal of crystal violet dye from an aqueous solution was investigated in this research. Three parallel sets of trials were conducted using RSM based on CCD to investigate the effects of various operational elements and their relationships and then to determine the optimal circumstances. According to the statistical analysis results, a quadratic regression model may successfully grasp the experimental data. The Pareto chart was utilized to show the effects of time on the dye adsorption capacity and removal efficacy by the FPB adsorbent, and it was discovered that over 80% of the adsorption occurred during the first 45 minutes. Contour and surface plots demonstrated that increasing the time and decreasing the particle size of the FPB adsorbent resulted in the best removal performance of crystal violet dye. The surface plot also revealed that reducing particle size can result in the maximum adsorption capacity of crystal violet dye, as temperature was shown to be ineffective in the removal of crystal violet from wastewater.

5. ACKNOWLEDGMENTS

The authors acknowledge the Bioenvironmental Water Engineering Research Group (BEWERG) and the "Departments of Chemical Engineering Ladoke Akintola University of Technology (LAUTECH)" for the usage of their laboratories.

6. CONFLICT OF INTEREST

The authors uphold that there are no conflicts of interest related to the publication of this article.

7. REFERENCES

- Abbasi, F., Tavakkoli Yarakhi, M., Farrokhnia, A., & Bamdad, M. (2020). Keratin nanoparticles obtained from human hair for removal of crystal violet from aqueous solution: Optimized by Taguchi method. *International Journal of Biological Macromolecules*, 143, 492-500. <https://doi.org/10.1016/j.ijbiomac.2019.12.065>
- Adekunbi, E. A., Babajide, J. O., Oloyede, H. O., Amoko, J. S., Obijole, O. A., & Oke, I. A. (2020). Evaluation of Microsoft Excel solver as a tool for adsorption kinetics determination. *Ife Journal of Science*, 21(3), 169. <https://doi.org/10.4314/ijfs.v21i3.14>
- Barber, S. T., Yin, J., Draper, K., & Trabold, T. A. (2018). Closing nutrient cycles with biochar- from filtration to fertilizer. *Journal of Cleaner Production*, 197, 1597-1606. <https://doi.org/10.1016/j.jclepro.2018.06.136>
- Batool, F., Akbar, J., Iqbal, S., Noreen, S., & Bukhari, S. N. A. (2018). Study of Isothermal, Kinetic, and Thermodynamic Parameters for Adsorption of Cadmium: An Overview of Linear and Nonlinear Approach and Error Analysis. *Bioinorganic Chemistry and Applications*, 2018, 1-11. <https://doi.org/10.1155/2018/3463724>
- Benmaamar et al. (2017). A batch study of adsorption equilibrium and kinetic for methylene blue onto synthesized zeolite. <http://www.jmaterenvironsci.com/>, 8(2), 539-550.
- Chahinez, H.-O., Abdelkader, O., Leila, Y., & Tran, H. N. (2020). One-stage preparation of palm petiole-derived biochar: Characterization and application for adsorption of crystal violet dye in water. *Environmental Technology & Innovation*, 19, 100872. <https://doi.org/10.1016/j.eti.2020.100872>
- Çoruh, S., & Geyikçi, F. (2012). Adsorption of copper (II) ions on montmorillonite and sepiolite clays: Equilibrium and kinetic studies. *Desalination and Water Treatment*, 45(1-3), 351-360. <https://doi.org/10.1080/19443994.2012.692058>
- Elmorsi, R. R., Abou-El-Sherbini, K. S., Shehab El-Dein, W. A., & Lotfy, H. R. (2022). Activated eco-waste of Posidonia oceanica rhizome as a potential adsorbent of methylene blue from saline water. *Biomass Conversion and Biorefinery*. <https://doi.org/10.1007/s13399-022-02709-5>
- Hami, H., Abbas, R., Jasim, A., Abdul Abass, D., Abed, M. A., & Maryoosh, A. A. (2019). Kinetics study of Removal Doxycycline drug from aqueous solution using Aluminum Oxide surface. *Egyptian Journal of Chemistry*, 0(0), 0-0. <https://doi.org/10.21608/ejchem.2019.5499.1483>
- Lairini, S.E, Mahtal, K, Miyah, Y, Tanji, K, Guissi, S, Boumchita, S, & Zerrouq F. (n.d.). Adsorption of Crystal violet from aqueous solution by using potato peels (*Solanum tuberosum*): Equilibrium and kinetic studies. *Journal of Materials and Environmental Sciences*, 8(9), 3252-3261.
- Loulidi, I., Boukhliji, F., Ouchabi, M., Amar, A., Jabri, M., Kali, A., Chraibi, S., Hadey, C., & Aziz, F. (2020). Adsorption of Crystal Violet onto an Agricultural Waste Residue: Kinetics, Isotherm, Thermodynamics, and Mechanism of Adsorption. *The Scientific World Journal*, 2020, 1-9. <https://doi.org/10.1155/2020/5873521>
- Olafadehan, O.A., (2021). Fundamentals of Adsorption Processes, ISBN: 978-620-3-30705-4, LAP Lambert Academic Publishing, Omni-Scriptum DUE GmbH.
- Olaosebikan, A. O., Victor, E. B., Kehinde, O. A., & Adebukola, M. B. (2022). Isotherms, kinetic and thermodynamic studies of methylene blue adsorption on chitosan flakes derived from African giant snail shell. *African Journal of Environmental Science and Technology*, 16(1), 37-70. <https://doi.org/10.5897/AJEST2021.3065>
- Patil, S. R., Sutar, S. S., & Jadhav, J. P. (2020). Sorption of crystal violet from aqueous solution using live roots of *Eichhornia crassipes*: Kinetic, isotherm, phyto and cyto-genotoxicity studies. *Environmental Technology & Innovation*, 18, 100648. <https://doi.org/10.1016/j.eti.2020.100648>
- Popoola, L. T. (2019). Characterization and adsorptive behaviour of snail shell-rice husk (SS-RH) calcined particles (CPs) towards cationic dye. *Heliyon*, 5(1), e01153. <https://doi.org/10.1016/j.heliyon.2019.e01153>

Akinyemi, A. G. et al., (2024). JOTCSB, 7(2), 105-122.

Rosly, N. Z., Abdullah, A. H., Ahmad Kamarudin, M., Ashari, S. E., & Alang Ahmad, S. A. (2021). Adsorption of Methylene Blue Dye by Calix[6]Arene-Modified Lead Sulphide (Pbs): Optimisation Using Response Surface Methodology. *International Journal of Environmental Research and Public Health*, 18(2), 397. <https://doi.org/10.3390/ijerph18020397>

Shojaei, S., Ahmadi, J., Davoodabadi Farahani, M., Mehdizadeh, B. and Pirkamali, M.R. (2019). Removal of crystal violet using nanozeolite-x from aqueous solution: Central composite design optimization study. *Journal of Water and Environmental Nanotechnology*, 4(1). <https://doi.org/10.22090/jwent.2019.01.004>

Sivarajasekar, N., & Baskar, R. (2019). Adsorption of Basic Magenta II onto H2SO4 activated immature Gossypium hirsutum seeds: Kinetics, isotherms, mass transfer, thermodynamics and process design. *Arabian Journal of Chemistry*, 12(7), 1322–1337. <https://doi.org/10.1016/j.arabjc.2014.10.040>

Vyavahare, G., Jadhav, P., Jadhav, J., Patil, R., Aware, C., Patil, D., Gophane, A., Yang, Y.-H., & Gurav, R. (2019). Strategies for crystal violet dye sorption on biochar derived from mango leaves and evaluation of residual dye toxicity. *Journal of Cleaner Production*, 207, 296–305. <https://doi.org/10.1016/j.jclepro.2018.09.193>

Zamouche, M., Habib, A., Saaidia, K., & Bencheikh Lehocine, M. (2020). Batch mode for adsorption of crystal violet by cedar cone forest waste. *SN Applied Sciences*, 2(2), 198. <https://doi.org/10.1007/s42452-020-1976-0>

Zarei, M., A., Niaei D., Salari A., & Khataee A. (2010). Application of Response Surface Methodology for Optimisation of Peroxi-Coagulation of Textile Dye Solution Using Carbon Nanotube-PTFE Cathode. *Journal Hazard Material*, 173, 544–551.



Heat Treatment Optimization and Nitriding Effects on Mechanical Properties of 32CrMoV12-10 Steel

Fatih DEMİR¹ , Muhammed Bora AKIN¹ , Ahmet YARTAŞI^{1*} 

¹Çankırı Karatekin University, Department of Chemical Engineering, Çankırı, 18100, Türkiye

Abstract: 32CrMoV12-10 steel is widely utilized in industries where high strength and toughness are crucial. This alloy is commonly used in manufacturing components like gun barrels, gears, and bearings, which demand exceptional mechanical properties. These parts typically undergo heat treatments, including hardening and surface enhancement techniques such as nitriding, to extend their fatigue life significantly. It is crucial to identify optimal heat treatment conditions to achieve desired material performance. In this study, commercial 32CrMoV12-10 steel was selected to investigate the impact of heat treatment parameters (temperature, duration time, and quenching media) on its mechanical properties. To analyse the effect of these parameters, the Technique for Order of Preference by Similarity to Ideal Solution (TOPSIS) and the Taguchi Method were employed, facilitating a systematic examination of the process stages and subsequent mechanical testing outcomes, including Charpy V-notch impact, hardness, and tensile strength assessments. An optimal heat treatment protocol was established based on these analyses, and the nitriding depth of the optimally treated sample was examined using a micro-Vickers hardness tester. For comparative analysis, another sample with closely related outcomes was also evaluated. Results indicated that the surface hardness of the optimally treated Sample 10 reached 870 HV, with a core hardness of 417 HV, compared to non-nitrided Sample 3, which showed a surface hardness of 860 HV and a core hardness of 415 HV. Despite the proximity in their values, Sample 10 exhibited slightly higher micro-Vickers hardness than Sample 3. However, while Sample 3 fails to meet the specified tensile stress and hardness criteria, Sample 10, produced through optimization, meets criteria, ranging from 970 to 1040 N/mm², underscoring the efficacy of the optimization process facilitated by TOPSIS. This optimization was notable for its minimal experimental requirements, proving effective in conserving time, energy, and resources while investigating the processed material.

Keywords: 32CrMoV12-10 steel, TOPSIS based Taguchi Method, Heat treatment, Nitriding, Mechanical properties.

Submitted: December 09, 2023. **Accepted:** June 06, 2024.

Cite this: Demir, F., Akın, Muhammed B., & Yartaşı, A. (2024). An Investigation into Different Heat Treatment Conditions on Mechanical Properties and Nitriding of 32CrMoV12-10 Steel. Journal of the Turkish Chemical Society, Section B: Chemical Engineering, 7(2), 123-140. <https://doi.org/10.58692/jotcsb.1402484>.

***Corresponding author. E-mail:** mbakin@karatekin.edu.tr.

1. INTRODUCTION

The application of various coatings (such as laser, chrome, etc.), production methods, and heat treatment techniques holds significant importance in conferring specific properties to steel materials. These processes aim to enhance the material's resistance to both corrosion and abrasion (Saklakoğlu et al., 2016). It has been reported that the parameters of the heat treatment process and the chosen production methods significantly impact

the material's behavior during manufacturing, influencing surface hardness and tension, regardless of whether machining is involved or not (Toktaş et al., 2017).

Advancements in weapon technology have observed significant progress. Throughout this developmental journey, a marked improvement has been witnessed in achieving high strength, toughness, enhanced wear resistance, and superior corrosion resistance. Consequently, gun barrels have become lighter and

have demonstrated superior properties concerning abrasion (GÖKSU, 2015).

Presently, the global arms market specifies an increase in the expected firing life for light, medium, and high-caliber barrels compared to standard requirements. The barrel's shot life, varying by caliber, stands at 50,000 shots for light weapons. However, this number decreases as the caliber size increases due to heightened pressure. Material composition, heat treatment methods, and coating types significantly influence the firing life of weapons (Rutci, 2019).

Research indicates that firearms experience high pressures and temperatures during operation. Upon the ammunition core's exit from the barrel, a considerable increase in temperature and pressure occurs in the barrel chamber. This phenomenon stems from the pressure exerted by gunpowder against the barrel walls, along with a rapid temperature surge within the barrel steel, leading to material stress. Therefore, the selection of materials should prioritize strength, durability, and high impact resistance to ensure extended life with superior dimensional stability (Karslı et al., 2021).

A study examining the effect of heat treatments on the mechanical properties of 42CrMo4, a steel known to be more expensive than 36CrB4, revealed that by adjusting the tempering temperature of 36CrM4 steel, similar mechanical properties to 42CrMo4 steel could be achieved, leading to cost savings (Karslı et al., 2021).

Furthermore, in another study, XRD (X-Ray Diffraction) results and hardness evaluations of X40CrMoV51 high alloy steel were conducted following ion nitriding post-tempering and quenching. The study noted that the nitrided surface exhibited twice the hardness compared to the quenched surface. The study highlighted that in applications where hardness is crucial, the material's high resistance to corrosion and wear significantly contributes to increased lifespan (Karslı et al., 2021).

Gas nitriding applied to 32CrMoV12-10 steel has been observed to provide a surface hardness at least 1.5 times higher than that achieved through quenching and tempering processes (Karslı et al., 2021).

Studies applying gas, plasma, and solid nitriding to AISI H13, N-8550, and AISI P20 steels reported an increase in surface hardness for these steels (Almeida et al., 2015).

In a separate study, plasma nitriding was performed on AISI 420, 416, 410NiMo, and 410 martensitic stainless steels at various temperatures, leading to an enhancement in the surface hardness of the martensitic stainless steels. However, an exception

was noted in the form of a reduced surface hardness, attributed to the precipitation of Cr alloy and CrN, which binds nitrogen. This was in contrast to the results at 450 °C, with the exception being the 410NiMo steel at 500 °C, where no decrease in hardness was observed (Ferreira et al., 2015).

Furthermore, it was found that the application of gas nitriding to DIN1.2344 hot work tool steel resulted in improved wear resistance (Bakdemir et al., 2020). To improve efficiency in the production process by reducing time, costs, and waste, the effectiveness of materials whether they pass or fail the quality control tests during nitriding is assessed (Perraki & Orfanoudaki, 2004; Roussel et al., 2010; Scholte et al., 1984).

The literature review highlights numerous studies focusing on the hardening of steels using diverse processes and methodologies. Nonetheless, there is a noticeable absence of research employing the TOPSIS-based Taguchi Method for optimizing the heat treatment process specifically aimed at hardening 32CrMoV12-10 steel. This study, therefore, addresses a significant gap in the current body of knowledge. In our approach, a three-factor, three-level experimental design was applied to 32CrMoV12-10 steel, which is typically supplied in either rolled or forged conditions for subsequent machining and forming operations. The decision to undertake machining on machine tools for this steel type was guided by the insights gained through the application of the TOPSIS-based Taguchi Method. This methodological choice aims to enhance the efficiency of the production process by reducing time, costs, and material waste, while also considering the outcomes of quality control checks, particularly focusing on the steel's performance post-nitriding treatment.

In this context, our study includes the application of various heat treatment regimes to 32CrMoV12-10 steel using the Taguchi method and subsequently evaluates the resulting mechanical properties to identify the most effective heat treatment conditions. The investigation extended to examining the influence of nitriding on steel exhibiting optimal mechanical strength characteristics. The findings suggest that the proposed optimization process not only fills a crucial gap in the literature but also demonstrates that significant process improvements are achievable with relative ease by adopting the suggested method.

2. EXPERIMENTAL SECTION

2.1. Materials

In this study, 32CrMoV12-10 steel suitable for hardening and tempering will be used. The chemical component analysis of 32CrMoV12-10 steel is given in Table 1 (SIJ GROUP 2020).

Table 1: Chemical analysis of 32CrMoV12-10 Steel (% wt.).

Chemical Compound	% Component
C	0.32
Cr	3
Mo	1
V	0.30
Si	Max. 0.35
Mn	Max. 0.60

Three cylindrical specimens of 32CrMoV12-10 steel, each measuring 100 mm x 70 mm (height x radius), were supplied for the experiments. These specimens were cut with a minimum wall thickness of 15 mm using a saw, as illustrated in Figure 1. Additionally,

each specimen was assigned a unique identification number.

After conducting the tensile, Charpy impact, and hardness measurement tests, the samples were subjected to the nitriding process. This process was determined based on two test conditions, one yielding the best results and the other the worst, within the desired value range according to the Taguchi Method. The nitriding capacity of the material and the depth of nitrogen penetration under two distinct test conditions were assessed and compared.

2.2. Sample Preparation and Testing for Heat Treatment

The steel test specimens, all with identical wall thicknesses for heat treatment, were cut into nine separate pieces measuring 12x12 cm². Figure 2 illustrates the specimens sliced into plates.

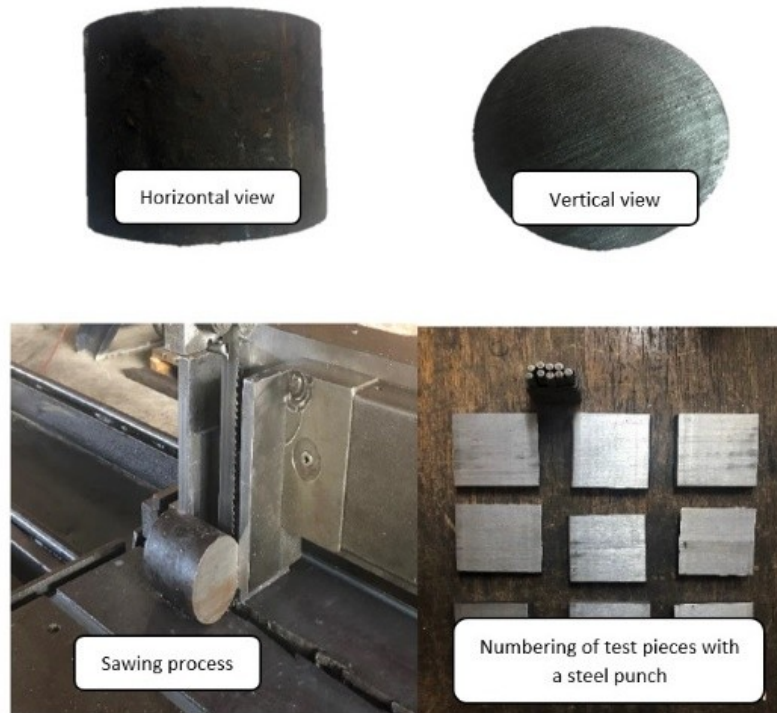


Figure 1: Preparation of 32CrMoV12-10 steel for heat treatment.

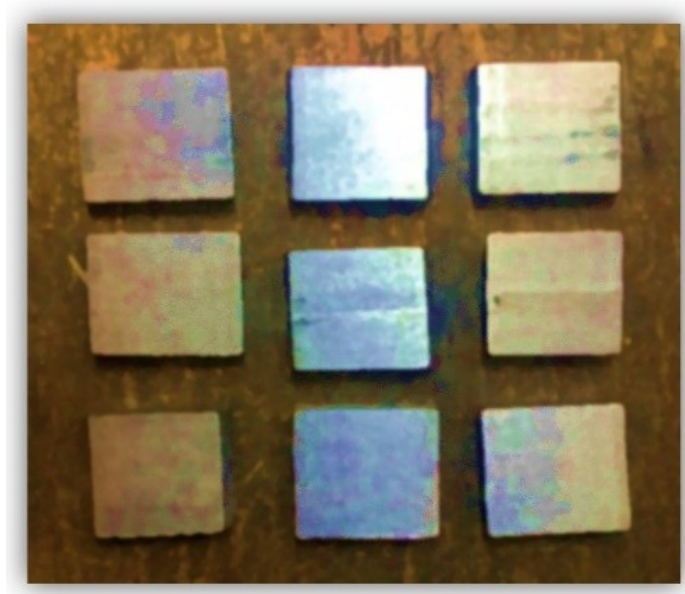


Figure 2: 32CrMoV12-10 steel specimens with equal wall thicknesses sliced and ready for heat treatment.

In determining the heat treatment parameters for commercial 32CrMoV12-10 steel, the decision was made based on the region where the highest impact notch value was observed, which was derived from the literature and technical documents provided by the manufacturer. The identification of the temperature and time parameters was guided by the temperature-time graphs provided for characteristic hardening. Similarly, the selection of the quenching media was informed by the literature

and technical documentation from the manufacturer (ARMAD, Tekin).

The experimental design followed the Taguchi L_9 Method, utilizing predefined factors and levels as outlined in Table 2. Table 3 details the experimental setup comprising three controllable variables (Factor A, Factor B, and Factor C) with three corresponding levels for each factor (Level 1, Level 2, and Level 3).

Table 2: The factors selected for the experimental design and their level values.

Factors	Level 1	Level 2	Level 3
A- Temperature (°C)	925	950	975
B- Duration Time (min)	45	60	75
C- Quenching Media	Water	Heat Treatment Oil	10% salt water

The graphs depicting the heat treatment process applied to the specimens are presented in Figure 3. In this graph, the initial stage involves preheating, intended to mitigate abrupt cooling effects, enhancing temperature penetration within the material and facilitating the formation of a more

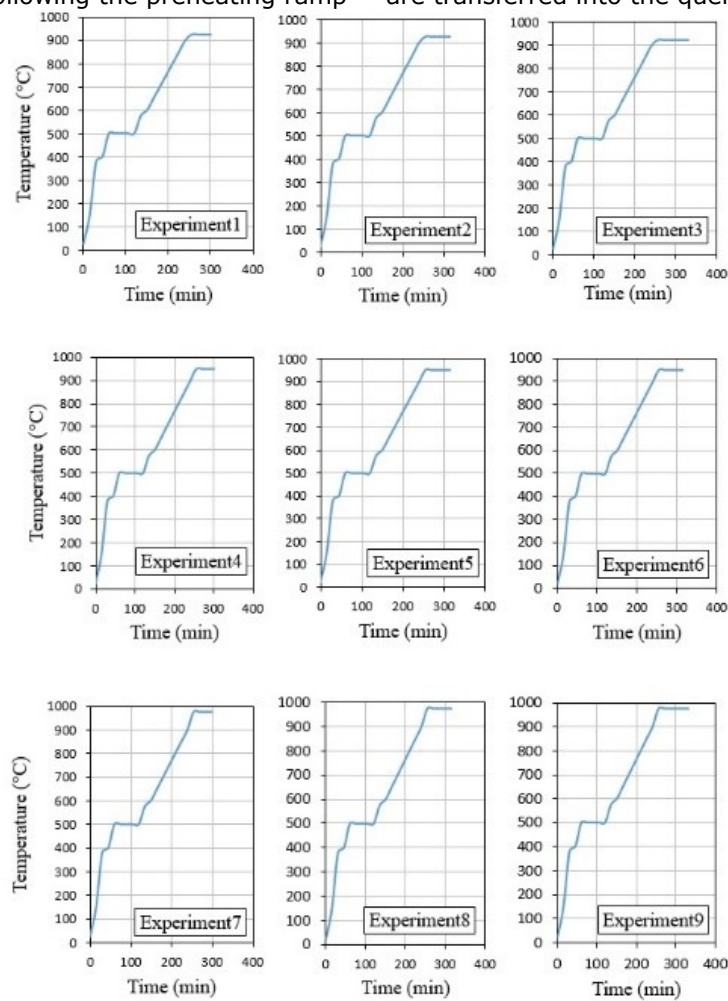
ductile grain structure, namely pearlitic, within the heat-affected zone. Subsequently, the material is heated to the specified treatment temperature, and once the specimens reach the austenitizing temperature, they are quenched after a defined time interval to harden the material.

Table 3: Experimental setup determined by the L9 orthogonal array.

Exp. No	Factors		
	A	B	C
1	1	1	1
2	1	2	2
3	1	3	3
4	2	1	2
5	2	2	3
6	2	3	1
7	3	1	3
8	3	2	1
9	3	3	2

The heat treatment process is initiated within the retort, depicted in Figure 4, adhering to the assigned variables and levels according to the L9 orthogonal sequence. Following the preheating ramp

of the furnace temperature and stabilization at the set soak temperature for a specific duration, the specimens undergo the hardening process as they are transferred into the quenching media.

**Figure 3:** Heat treatment program applied for the specimens in the experiments.

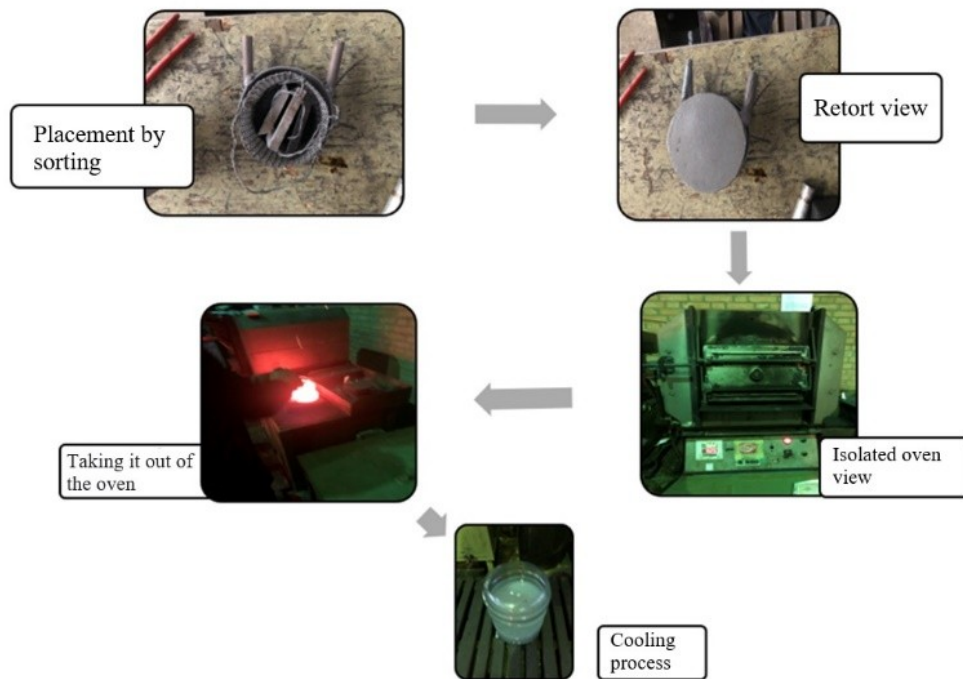


Figure 4: Heat treatment and quenching stages in the experimental.

As depicted in Figure 3, the heat treatment procedure extends up to a maximum duration of 330 minutes. Subsequent to the quenching process, illustrated in Figure 4, the specimens undergo tempering (held at 550 °C for 300 minutes) with the aim of enhancing material toughness.

The heat-treated specimens, illustrated in Figure 5a, were subjected to blasting using S170 steel shot to prepare them for entry into the testing environment, as shown in Figure 5b. This sandblasting process effectively removes surface oil, rust, and metal residue, thereby ensuring the surface of the material is suitably prepared for laboratory conditions.

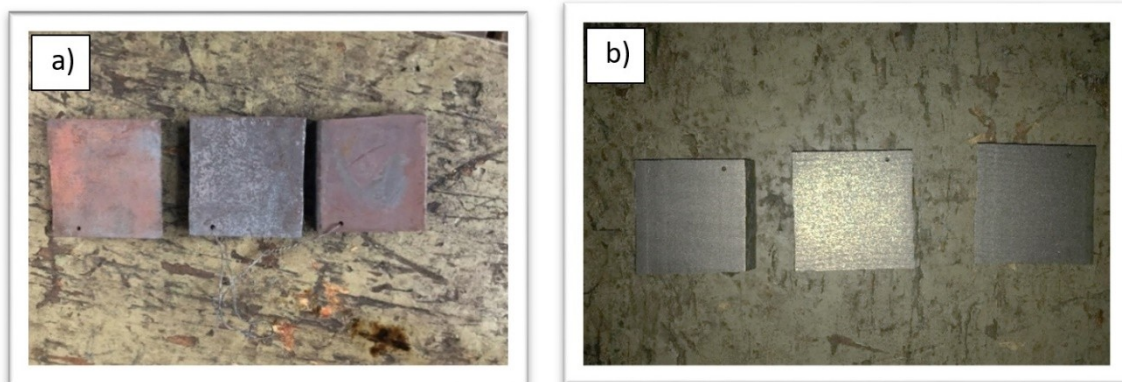


Figure 5: (a) Crusted surface after heat treatment and (b) surface after blasting (S170).

2.2.1. Specimen preparation for Charpy impact V-notch test

After the heat treatment process, materials measuring 12x100 mm were processed using a

milling machine to create Charpy impact test specimens following the guidelines outlined in the ISO 148-1 standard (Figure 6). Subsequently, the notches were precisely formed on the milling machine, rendering the material ready for testing.

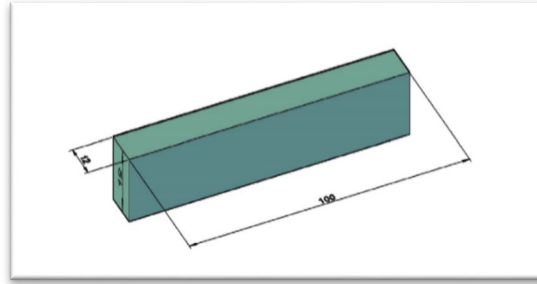


Figure 6: Schematic representation of specimen conforming to ISO 148-1 standard for Charpy impact V-notch test.

For the Charpy impact V-notch test, a notch, 9 mm wide and 2 mm deep, was created at the center of each specimen, conforming to the specifications defined in the ISO 148-1 standard.

2.2.2. Application of the Charpy impact V-notch test

The Charpy impact test aims to measure the energy, recorded in joules, at the moment of initial impact when breaking a test piece. This is achieved by using a hammer capable of circular motion within

a protective enclosure, as depicted in the schematic diagram in Figure 7a.

The Charpy impact tester, illustrated in Figure 7b, comprises an internal mechanism with a hammer moving in circular motion, a mechanism to hold the hammer in place, an anvil to position the specimen, and an outer casing encompassing the entire system with wire mesh to safeguard the specimen from potential splintering or damage due to the impact of the hammer.

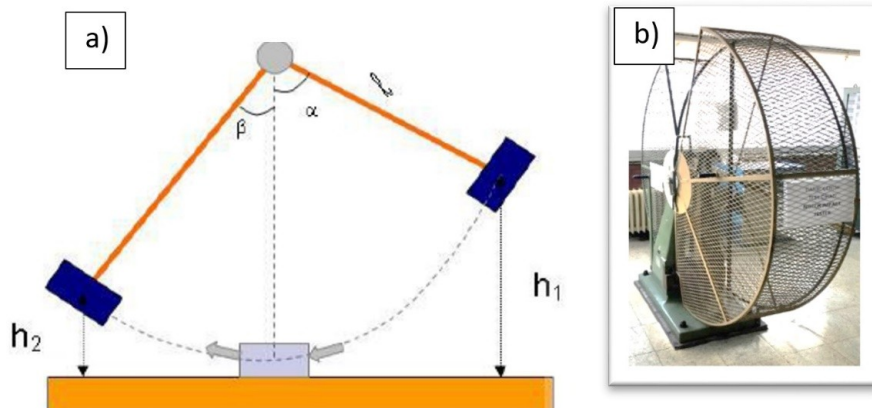


Figure 7: (a) Schematic illustration displaying the internal mechanisms of the Charpy impact tester, and outlining the operational principles of the device, and (b) Charpy impact test device.

In the Charpy impact test following the ISO 148-1 standard, the test specimen is placed on the anvil with the notch facing inward. Upon releasing the hammer from a specific height "h" behind the V-notch, the specimens, positioned both vertically and

horizontally, assume their final orientation. Figure 8 illustrates the functionality of the impact notch test mechanism and the resulting specimens from the experiment.

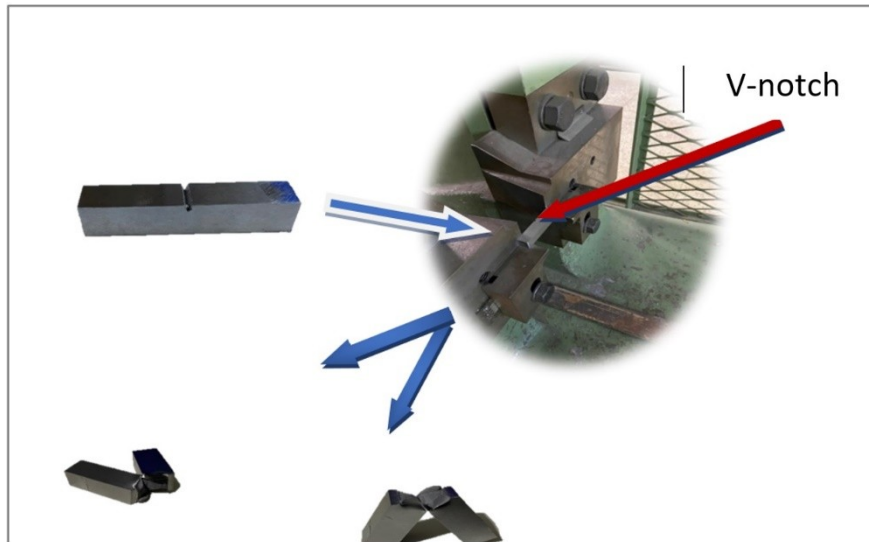


Figure 8: Images of the specimens before and after undergoing the Charpy impact test.

2.2.3. Tensile test specimen preparation

After undergoing heat treatment, the specimens were machined using a universal lathe in compliance with the TS EN ISO 10002-1 standard to prepare

them for the tensile test. M10 threads were drilled on both ends of the specimens using the lathe. The dimensions of the specimens are illustrated in Figure 9.

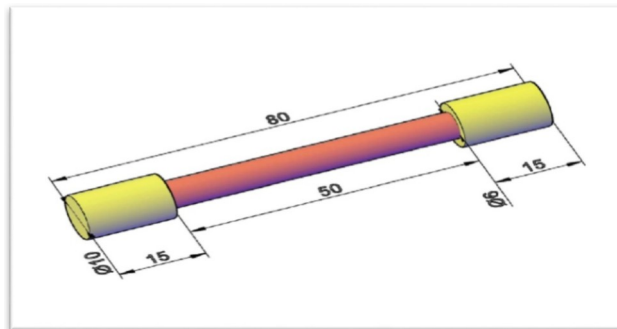


Figure 9: Dimensions of the tensile test bar specimen in millimeters along with a schematic representation.

2.2.4. Tensile Test Procedure

The 20-ton Galdabini brand tensile testing machine was utilized to measure the yield strength, ultimate tensile strength, and percentage of elongation of the samples. The specimen is affixed to the tester's jaws in accordance with the drilled thread diameter for the part under examination. The tester applies an incremental upward and downward force "F" to the fixed portion. The maximum tensile force is derived from the resulting graph plotted by the tensile tester, correlating "F" force with plastic deformation.

Figure 10 displays the tensile test bar connected between the two jaws, emphasizing the region denoted by the red ellipse indicating a specific elongation, signifying the material's transition into

plastic deformation. Additionally, the figure illustrates the outcome of the tensile test leading to the rupture of this material.

2.2.5. Brinell Hardness Testing Procedure

The measurements were conducted using a Wolpert brand hardness tester, and the results were evaluated and recorded in duplicate reports.

Hardness measurements were carried out in the laboratory environment using the Wolpert device. The process involved placing the material on the lower table and applying pressure to crush the material by releasing the load. The hardness result was determined by manually measuring the diameter of the impression with the aid of a ruler and under proper lighting conditions.

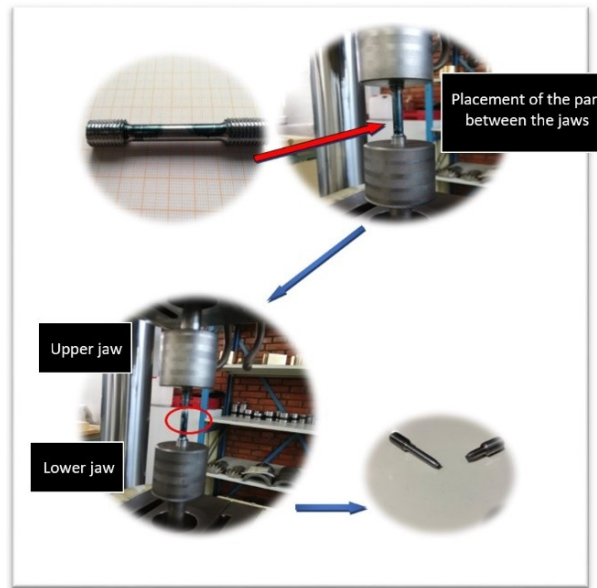


Figure 10: Images of the tensile test specimen: before and after testing.

2.2.6. Microhardness Measurements

For the microhardness measurements, the samples were encased in bakelite and compressed, as

depicted in Figure 11a. Subsequently, they underwent a polishing process, as shown in Figure 11b.

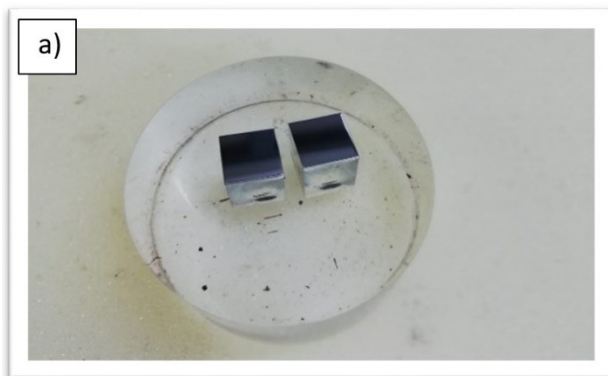


Figure 11: (a) Samples taken on bakelite, and (b) surface cleaning of samples before analysis.

Using the Ness brand device, the nitration penetration and core hardness of the samples within the prepared bakelites were measured. The results regarding nitrogen diffusion were obtained from the software integrated with the device.

Following the calibration of the Ness brand microhardness analyser, the samples were positioned. Upon activation of the device, the lenses detected the positions, and data were collected after approximately 20 minutes of scanning, employing 100x and 1000x magnification for measuring the initial trace and subsequently the opened trace.

2.3. Calculations for TOPSIS method

In the study, responses obtained through the Taguchi method are processed, and the TOPSIS (Technique for Order Preference by Similarity to the Ideal Solution) method is applied. Naturally, the

targeted values are intended to be optimized either to their minimum or maximum levels. Through the TOPSIS method, values aimed at minimization are brought to the lowest possible level, and those aimed at maximization are elevated to the highest possible level. This process thus simplifies reaching the most ideal solution in terms of proximity. After forming the decision matrix, it is necessary to normalize the target values and determine their weights to obtain standardized measurement units (Hwang and Yoon, 1981).

The initial step in the TOPSIS calculation of the study is to use the responses derived from the Taguchi method to create a standard decision matrix. This standard decision matrix is generally expressed as Equation 1, and with the utilization of the results, the standard decision matrix as outlined in Equation 2 is obtained.

$$R_{ij} = \frac{a_{ij}}{\sqrt{\sum_{k=1}^m a_{kj}^2}} \quad (1)$$

$$R_{ij} = \begin{bmatrix} r_{11} & r_{12} & \dots & r_{1n} \\ r_{21} & r_{22} & \dots & r_{2n} \\ \cdot & \cdot & \cdot & \cdot \\ \cdot & \cdot & \cdot & \cdot \\ r_{m1} & r_{m2} & \dots & r_{mn} \end{bmatrix} \quad (2)$$

The formation of the weighted standard decision matrix constitutes the initial step. In the calculations, the total of the weighted values for the evaluation criteria is determined as illustrated in Equation 3 (Şimşek, 2014).

$$\sum_{i=1}^n w_i = 1 \quad (3)$$

Following the establishment of the weighted standard decision matrix, the next step involves multiplying each value in the columns of the standard decision matrix by the corresponding weight value (w_i) to construct the weighted standard decision matrix as demonstrated in Equation 4 (Şimşek, 2014).

$$V_{ij} = \begin{bmatrix} w_1 r_{11} & w_2 r_{12} & \dots & w_n r_{1n} \\ w_1 r_{21} & w_2 r_{22} & \dots & w_n r_{2n} \\ \cdot & \cdot & \cdot & \cdot \\ \cdot & \cdot & \cdot & \cdot \\ w_1 r_{m1} & w_2 r_{m2} & \dots & w_n r_{mn} \end{bmatrix} \quad (4)$$

Subsequently, the formation of the ideal (A^*) and the negative ideal (A^-) solutions is undertaken. To generate the ideal solution set, the largest values for the standardized criteria within the weighted standard decision matrix are selected. The formula for constructing the positive ideal solution set is given in Equation 5.

$$A^* = \max_i V_{ij} | j \in J \quad \min_i V_{ij} | j \in J' \quad (5)$$

Through Equation 5, the calculated set is expressed as $A^* = \{v_1^*, v_2^*, \dots, v_n^*\}$.

Conversely, when identifying the negative ideal solution set, the smallest values for the normalized criteria within the weighted standard decision matrix

are chosen. The equation used to find the negative ideal solution set is presented in Equation 6 (Şimşek 2014).

$$A^- = \min_i V_{ij} | j \in J \quad \max_i V_{ij} | j \in J' \quad (6)$$

Using Equation 6, the set calculated is expressed as $A^- = \{v_1^-, v_2^-, \dots, v_n^-\}$.

In both equations, the two expressions represent J as the benefit (goal is maximum) and J' as the cost (goal is minimum) values. It is observed that either the positive or negative ideal solution set consists of n elements, corresponding to the number of evaluation factors.

Upon reaching the Calculation of Separation Measures step, determining the deviations from the ideal and negative ideal solution sets necessitates establishing the deviation values for the decision points. These values emerge as the positive ideal separation and negative ideal separation, respectively denoted as Equation 7 and Equation 8 (Şimşek 2014).

$$S_i^* = \sqrt{\sum_{j=1}^n (v_{ij} - v_j^*)^2} \quad (7)$$

$$S_i^- = \sqrt{\sum_{j=1}^n (v_{ij} - v_j^-)^2} \quad (8)$$

The numbers S_i^* and S_i^- to be calculated will be as many as the response numbers in the experimental design (Şimşek 2014).

In the final step, calculating the distance of the decision points from the ideal solution utilizes S_i^* and S_i^- values. The relative closeness to the ideal solution is the ratio of the S_i^- value to the sum of the S_i^* and S_i^- values (Equation 9) (Şimşek 2014).

$$C_i^* = \frac{S_i^-}{S_i^* + S_i^-} \quad (9)$$

Values calculated with Equation 9 will naturally range between 0 and 1 ($0 \leq C_i^* \leq 1$). When considered independently, the highest C_i^* value is selected. However, in the TOPSIS-based Taguchi method, C_i^* values are further assessed using the Taguchi method, thereby achieving the final optimization results.

2.4. Nitriding process

Following the optimization of the heat treatment process with the Taguchi method, Sample 10 was produced. Subsequently, Sample 10 underwent a nitriding process. Gas nitriding was applied for 72 hours at 540 °C. After nitriding, comparisons were made between Sample 3, which had the best test results, and the nitrided Sample 10.

3. RESULTS AND DISCUSSION

The experimental design was completed using the levels automatically assigned to the factors in the L9 orthogonal array. The duplicate results from the tensile strength, impact notch, and hardness tests are presented in Table 4. The experimental data were processed utilizing the Taguchi Method within the Minitab program.

Table 4: According to the L₉ Taguchi Method, the results of the experiment.

Exp. No	Tensile (N/mm ²)	Strength*	Impact (J)	Notch**	Hardness* (N/mm ²)	
1	874	877	181	178	930	965
2	940	945	180	175	965	995
3	1049	1035	133	138	1125	1120
4	929	935	180	177	965	962
5	976	983	150	149	1060	1045
6	1135	1129	124	127	1190	1155
7	1137	1142	124	123	1118	1155
8	997	986	153	150	1060	1045
9	1003	989	156	159	1060	1048

* It is desired to be in the range of 970-1040 N/mm²

**It is desired to be greater than 40 J.

3.1. Optimizing Material Testing Outcomes Using Taguchi Method and TOPSIS Analysis

The analysis of duplicate results from the tensile test, impact notch test, and hardness measurement experiment was conducted following the Taguchi Method, employing both the "larger is better" and "nominal is best" criteria as applicable. This method was chosen to identify the highest achievable values considering various factors (Factor A, Factor B, and Factor C) and their levels (Level 1, Level 2, Level 3) across the experiments. In the figures corresponding to each test (Figures 12, 13, and 14), factors are illustrated with green circles, levels with

yellow circles, and the optimal values targeted are marked with red circles. The objective was to pinpoint the maximum value achievable based on the defined factors and levels for each type of test. The Minitab software package was utilized to document the outcomes of these analyses. The insights from the data points, particularly those underscored by the red circles in the figures, were harnessed to synthesize the dataset into a singular result using the TOPSIS method, thereby streamlining the analysis process and enhancing the efficiency of identifying optimal conditions across different types of material tests.

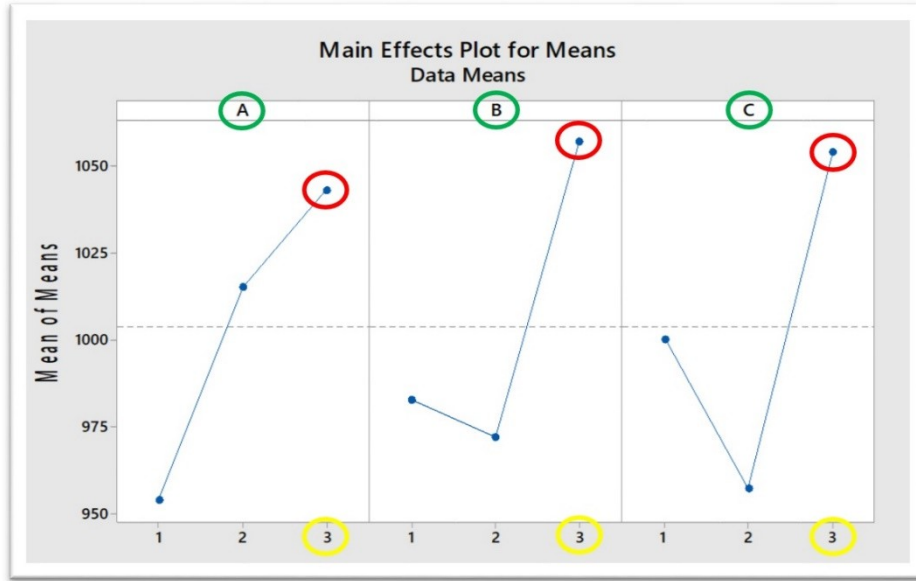


Figure 12: "Larger is better" recommendation for tensile experiment according to Taguchi Method.

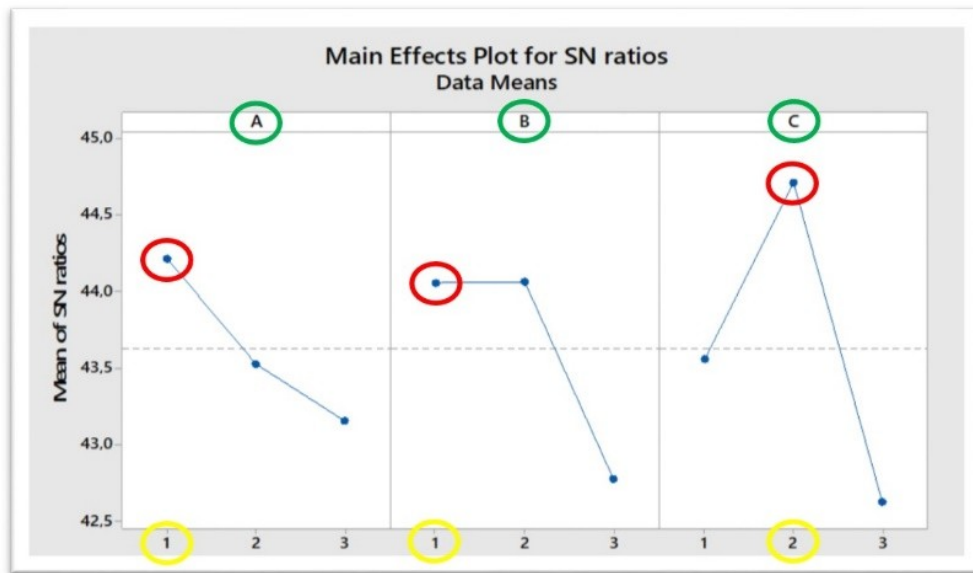


Figure 13: S/N ratios of impact notch test according to Taguchi Method.

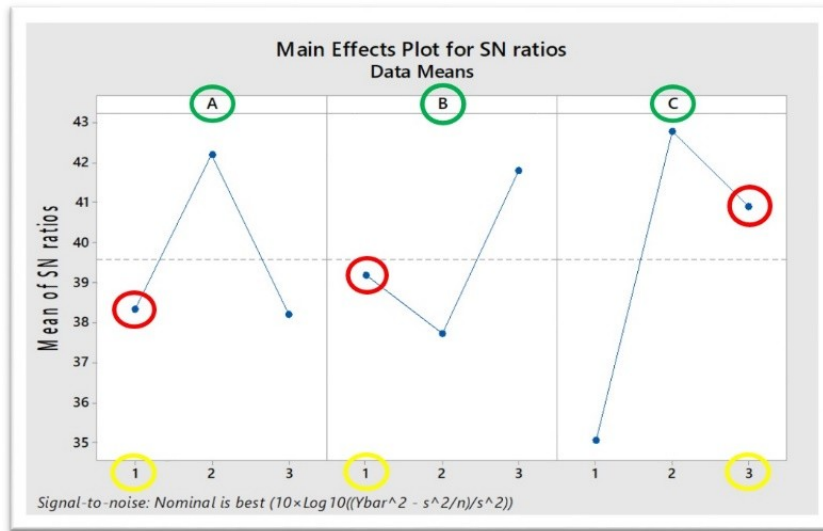


Figure 14: S/N ratios of hardness test according to Taguchi Method.

3.2. TOPSIS Based Taguchi Method Results

The replicated results of the tensile, V-notch, and hardness measurement tests underwent analysis using the variable of “nominal is better” or “larger is better” according to the Taguchi method, as illustrated in Figure 12, Figure 13, and Figure 14. The distribution variation of three factors across different levels was examined. As the values highlighted with the red circle influence strength, fracture, and toughness interdependently, optimal values were selected for the best experimental design utilizing the TOPSIS method.

results closest to the optimum desired values are shown in Table 5.

The data derived from the TOPSIS method were subsequently integrated back into the Taguchi Method, employing the “larger is better” approach to enhance strength and toughness within the experimental design, and an analysis was conducted. In the results depicted in Figure 15, green circles indicate the factors, yellow circles represent the levels, and red circles signify the maximum values to be attained based on the factors and levels.

The data obtained after the application of the Taguchi and TOPSIS methods and the duplicate

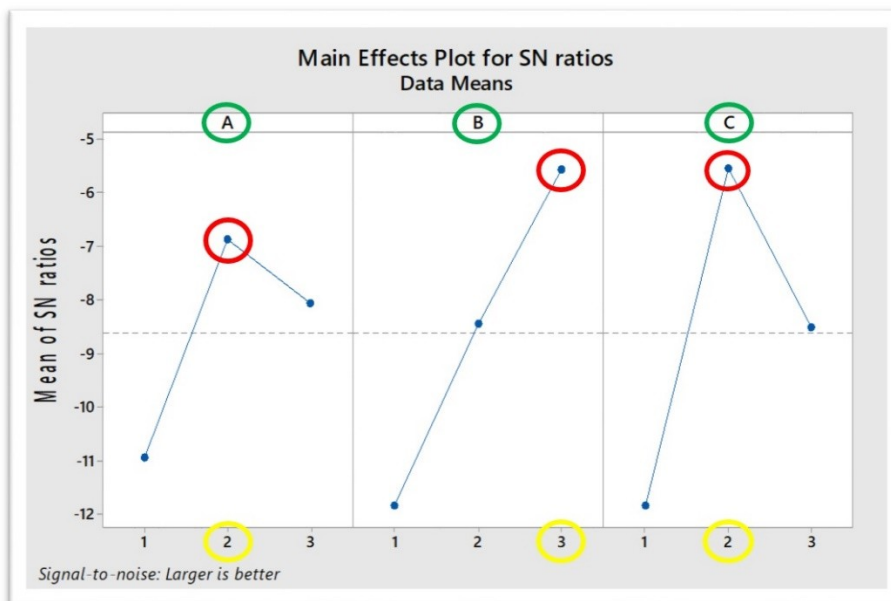


Figure 15: TOPSIS based Taguchi Method “larger is better”.

The results obtained from the Minitab software, utilizing the Taguchi method, were integrated into a cohesive outcome through the application of the TOPSIS Method, as detailed in Table 5. The optimal experiment, as determined by this analysis, was

performed at a temperature setting of 950°C (A2), with a heat treatment duration of 75 minutes (B3) and employing a quenching process that uses heat treatment oil (C2), as illustrated in Figure 16.

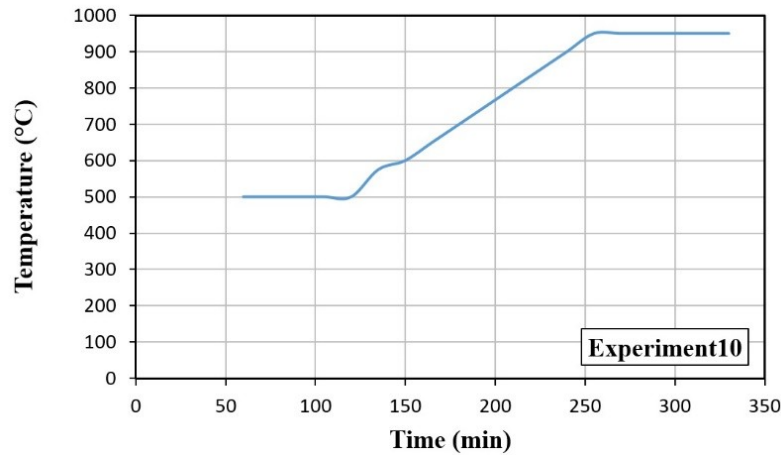


Figure 16: Heat treatment program based on optimization results.

The targeted range for the tensile test is 970-1040 N/mm². Upon conducting the tensile test, strength parameters such as elastic modulus, yield value, breaking strength, as well as ductility factors like elongation at break, shrinkage at break, and toughness, were determined. The material's ductility and toughness falling within the specified range affirm the suitability of the temperature, duration time, and quenching media selected during the heat treatment process. Table 6 presents the values for sample number 10, which underwent a 72-hour nitration process at 540 °C.

The impact notch test is conducted to assess the fracture behavior of metals, offering insight into their mechanical properties, particularly under conditions conducive to brittle fracture. As per literature, impact notch tests should yield results of ≥ 40 J. Table 6 indicates that, based on the experimental design applied, values falling within the "larger is better" criteria range from 154 to 157. Brittle fracture occurs when the sample breaks before undergoing plastic deformation. However, as evidenced by these test results, plastic deformation often occurs before fracture. Under applied force, besides normal (perpendicular) stress, there is an additional shear stress at approximately 45°. Once this shear stress surpasses the material's shear strength (critical shear), elastic deformation

transitions into plastic deformation, followed by fracture. This process, known as ductile fracture, results in an uneven and fibrous fracture surface, as depicted in Figure 10. Consequently, the experimental design aligns with literature expectations based on these findings.

The Brinell hardness measurement method involves determining the diameter of an indentation created by applying a specific load over a set period using a hardened ball of known diameter on the material's surface. Results obtained from the experiment fell within the range of 880-1030 N/mm², aligning with literature standards. This range ensures that the material maintains an optimal balance: it is neither excessively hard, risking brittleness and breakage, nor too soft, ensuring maximum wear resistance. Consequently, the material's hardness is maintained at an ideal point, delivering the desired outcome in the experiment.

The area under the elongation curve of a material signifies its toughness, which differs significantly between brittle and ductile materials. However, it's crucial to note that this area illustrates the extent of plastic deformation the material can withstand before fracture, rather than strictly representing toughness against sudden impacts and forces.

Table 5: TOPSIS Method application using S/N ratios with weighted application for heat treatment experiments.

Decision Matrix (S/N Ratios)				Weight Normalized Decision Matrix			S_i^*	S_i^-	C_i^*	
Responses	R_1	R_2	R_3		V_{i1}	V_{i2}	V_{i3}			
Weights	0.333	0.333	0.333							
R1	54.11	45.13	31.66	→	0.13^b	0.11	0.09	0.05^c	0,01^d	0,14^e
R2	49.34	45.06	33.29	→	0.12	0.11	0.09	0.05	0,01	0,22
R3	40.59	42.44	50.03	→	0.10	0.11	0.14	0.02	0,06	0,75
R4	47.27	45.13	53.14	→	0.11	0.11	0.15	0.01	0,06	0,83
R5	45.88	43.52	39.93	→	0.11	0.11	0.11	0.03	0,03	0,48
R6	48.21	41.94	33.51	→	0.11	0.11	0.09	0.05	0,01	0,24
R7	50.80	41.90	32.76	→	0.12	0.11	0.09	0.05	0,01	0,15
R8	42.09	43.61	39.93	→	0.10	0.11	0.11	0.03	0,03	0,52
R9	40.13	43.94	41.88	→	0.10	0.11	0.12	0.04	0,19	0,82
-	140.13^a	130.94	120.74	$A^*=$	0.11	0.11	0.14	-	-	-
-	-	-	-	A^-	0.13	0.11	0.09	-	-	-

The expressions a,b,c,d,e indicate sample calculations made in matrices using the relevant equations.

^a The sum of the squares of each element in the columns

^b Equation 1 → $v_{1,1}=0.333*[(54.11/140.13)]=0.13$

^c Equation 7 → $S_1^*=\{[(0.13-0.11+...+[(0.09-0.14)]]\}^{1/2}=0.05$

^d Equation 8 → $S_1^-=\{[(0.13-0.13+...+[(0.09-0.09)]]\}^{1/2}=0.01$

Equation 9 → $C_1^*=0.01/(0.01+0.05)=0.14$

Table 6: Experimental results determined according to Taguchi and TOPSIS methods (sample 10) and determined for comparison (sample 3).

• Sample No	Required Values					
	Tensile Strength		Impact Notch		Hardness	
	970-1040 N/mm ²		≥ 40 J		970-1040 N/mm ²	
• 10	1006	1009	154	151	1030	1028
• 3	1049	1035	133	138	1125	1120

The data derived from the Taguchi Method demonstrates an algorithm that enables factors (Factor A, Factor B, and Factor C) to yield an optimal result based on their interdependence. Two explanatory test results reflecting these outcomes as mechanical properties are presented in Table 5. Experiment number 10 aligns with

literature standards, providing data that reflects the outcomes obtained by executing the experiment according to the specified factor and level suggested by Taguchi. The performance values of these test conditions in nitration are shown in Table 7.

Table 7: Microvickers test results for Sample 3 and Nitrided Sample 10

Nitriding Process	Top Surface Hardness ≥ 700 HV	Core Hardness ≥ 300 HV	Nitriding Depth ≥ 0,1 mm
Sample 10	870	417	0.10
Sample 3	860	415	0.10

The results from the Microvickers, Tensile Strength, Impact Notch, and Hardness analyses reveal that Sample 10 is the only material that meets all the desired criteria. This result highlights the significance of the study. The production of materials with desired values through the TOPSIS-based Taguchi method has resulted in savings of time, materials, and energy.

4. CONCLUSION

The method emphasizes the relationship between various factors (A, B, and C) to achieve an optimized outcome in terms of mechanical properties, yielding successful results in revealing the connection between the TOPSIS-Based Taguchi Method and factors. The optimization results obtained are significant as the first study in the literature to use the TOPSIS-based Taguchi method. Besides, the results stand out by providing detailed statistical outcomes regarding the optimization of the process conducted with nitriding.

The analysis conducted in the study presents the two most influential test results indicating these outcomes concerning mechanical properties and shows effective results, notably displaying that the trials of Sample 10 are in alignment with the literature standards for mechanical properties.

Sample 5, Sample 8, Sample 9, and Sample 10 are within the targeted tensile strength test range (970-1040 N/mm²), demonstrating satisfactory performance.

Results obtained from the Impact Notch Resistance Test exceeded the expected level (>40 J), indicating a positive performance.

The findings derived from the application of the Taguchi method were systematically synthesized into a coherent outcome utilizing the TOPSIS Method. This statistical analysis identified the conditions for the optimal experiment as a temperature setting of 950 °C, a heat treatment duration of 75 minutes, and the use of oil as the quenching medium. This optimized process led to the successful production of a material characterized by superior performance metrics post-nitration.

In the Hardness Test, Sample 3 and Sample 10 met the specified hardness level (970-1040 N/mm²) and exhibited the desired properties.

The results obtained from the conducted study appear to be better in comparison with the study by Karslı et al. (2021). The surface hardness obtained in the mentioned study is reported as 800 HV and the core hardness at a depth of 0.1 mm is reported as 368 HV. The values obtained with Sample 10, produced through optimization, and Sample 3, selected as a comparison sample, are superior (Table 7).

5. CONFLICT OF INTEREST

The authors declare that there is no conflict of interest.

6. REFERENCES

- ARMAD - <https://www.aubertduval.com> [Accessed 5th June 2022].
- Almeida EAD, Costa CE, & Milan JCG. Study of the nitrided layer obtained by different nitriding methods. *Matéria (Rio de Janeiro)*. 2015;20(2): 465.
- Bakdemir SA, Özkan D, Türküz MC, Uzun E, & Salman S. Effect of the nitriding process in the wear behaviour of DIN 1.2344 hot work steel. *Journal of Naval Sciences and Engineering*. 2020;16(1): 45-70.
- Callister WD & Rethwisch DG. *Materials Science and Engineering: An Introduction*, 8th ed.: John Wiley & Sons; 2009.
- Cengiz M. Hardox 400 Çelik Yüzeyinin Plazma Transferli Ark Kaynak Yöntemiyle Aşımlandırılması ve Taguchi Metoduyla Değerlendirilmesi. *Dicle University Journal of Engineering (DUJE)*. 2019;10(3): 969-979.
- Du H, Somers MAJ, & Agren J. Microstructural and compositional Evolution of Compound Layers during Gaseous Nitrocarburizing. *Metallurgical and Materials Transactions A: Physical Metallurgy and Materials Science*. 2000;31A: 195-211.
- Canıyılmaz E, & Kutay F. Taguchi Metodunda Varyans Analizine Alternatif Bir Yaklaşım. *Gazi Üniversitesi Mühendislik Mimarlık Fakültesi Dergisi*. 2003;18(3): 51-63.
- Ferreira L, Brunatto SF, & Cardoso RP. Martensitic Stainless Steels Low Temperature Nitriding: Dependence of Substrate Composition. *Materials research*. 2015;18: 622-627.
- Friehling PB, & Somers MAJ. Growth Kinetics of the Compound Layer on Gaseous Nitriding of Iron: The Effect of the Surface Reaction in Mass and Charge Transport in Inorganic Devices: *Fundamentals to Devices (Part B)*. Techna Srl; 2000.
- GÖKSU (2015). Web site. <https://www.otuken.com.tr>. [Accessed 3th January 2022]
- Gür AK & Kaya S. Abrasive Wear Resistance Optimization of Three Different Carbide Coatings by The Taguchi Method. *Mater. Test*. 2017;595: 450-455.
- HASCOMETAL - <http://www.hascometal.com/teknik-bilgiler.aspx?ID=68> [Accessed 1st October 2021]
- HASÇELİK - <https://hascelik.com/celik-hakkinda-genel-bilgiler/celik-nedir> [Accessed 1st May 2022]
- Haefer R & Ilschner B. *Oberflächen- und Dünnschicht-Technologie*. Springer Verlag; 1991.
- Hwang CL & Yoon P. *Multiple Attribute Decision Making In: Lecture Notes In Economics And Mathematical Systems*. Springer Verlag; 1981.
- Joseph, R. *Heat Treatments of Steels*, 10th edition, ASM.: 91. 465 pages, American Society for Metals; 1973.
- Karslı M, Kemikoğlu U & Yavuz S. Tabanca Namlu Malzemesi 32CrMoV12-10 Aşımına Uygulanan Gaz Nitrasyon ve Su Verme İşlemlerinin Darbe Dayanımına Etkisinin İncelenmesi. *Gümüşhane University Journal of Science and Technology*, 2021;11(4), 1198-1207.
- Kaya S. Yüzeyi Modifiye Edilmiş Ferritik Paslanmaz Çeliğin Aşınma Direncinin Taguchi Metoduyla Optimizasyonu. Master Thesis, Fırat University, Graduate School of Natural and Applied Sciences, 105 pages, Elazığ; 2017.
- Phadke M. *Quality Engineering Using Robust Design Book*, Library of Congress Cataloging AT & T Bell Laboratories, New Jersey, USA; 1989.
- Şirvancı M. Kalite için deney tasarımı, Taguchi Yaklaşımı. *Literatür Publications*, 112 pages, İstanbul; 2011.
- Özay Ç. Teğetsel tornalama-frezeleme yönteminde işleme parametrelerinin teorik ve deneysel olarak araştırılması. PhD Thesis, Fırat University, Graduate School of Natural and Applied Sciences, Elazığ; 2009.
- Ross PJ. *Taguchi Techniques for Quality Engineering, Loss Fuction, Orthogonal Exp. Param. Toler. Des.*, 279 pages., Mcgraw-Hill; 1998.
- Rutci AT. Development of Barrel Material Used in Light Weapons and Investigations of Manufacturing Process Parameters. Master Thesis, Sakarya University, Institute of Natural Sciences, Sakarya; 2019.
- Saklakoğlu N, Gençalp İrizalp S, İldaş G & Demirok S. Microstructure and wear properties of Fe-based hardfacing alloy / Fe esaslı sert kaplama aşımının mikroyapı ve aşınma özelliklerinin incelenmesi. *Celal Bayar University Journal of Science*. 2016;12(3): 517-523.
- SIJ GROUP - <https://www.sij.si/en/sij-brands/sinox/> [Accessed 1st October 2021].
- Şimşek B. Hazır Betonun Optimal Karışım Oranlarının Belirlenmesi İçin Bir Çok Yanıtlı Modelleme ve En İyi Uygulaması: Topsis Tabanlı Taguchi Yaklaşımı İle Cevap Yüzey Yöntemi. PhD Thesis, Ankara University, Graduate School of Natural and Applied Sciences, Ankara; 2014.
- Tekin A. *Çelik ve Isıl İşlemi Bofors El Kitabı*. Hakan Ofset Publications, 616 pages, İstanbul; 1984.
- Toktaş G & Toktaş A & Duran, M. Investigating The Wear Behaviour of Induction Hardened 100Cr6 Steel. *Sakarya University Journal of Science*. 2018;225:1174-1180.
- Topbaş AM. *Çelik ve Isıl İşlem El Kitabı*. Ekim Ofset Publications, 553 pages, İstanbul; 1998.
- Uzkut M & Özdemir İ. Farklı Çeliklere Uygulanan Değişen Isıtma Hızlarının Mekanik Özelliklere Etkisinin İncelenmesi. *Dokuz Eylül Üniversitesi Mühendislik*

Demir, F., Akın, M. B., Yartaşı, A., (2024), JOTCSB, 7(2), 121-138.

RESEARCH ARTICLE

Fakültesi Fen Ve Mühendislik Dergisi, c. 2001:3(3): 65-73.

Weststrate CJ. Hydrocarbon and Ammonia Chemistry on Noble Metal Surfaces. PhD Thesis, Leiden Universty Leiden Institute of Chemistry LIC, Faculty of Science, Leiden/Holland; 2006.

Yang M. Nitriding- Fundamentals, modeling and process optimization. PhD Thesis, Worcester Polytechnic University, Material Science and Engineering, Worchester/USA; 2012.



Hydrochar and Value-Added Chemical Production Through Hydrothermal Carbonisation of Woody Biomass

Fatih Güleç^{1,2} * 

¹Low Carbon Energy and Resources Technologies research group, Faculty of Engineering, University of Nottingham, Nottingham, NG7 2TU, United Kingdom.

²Advanced Materials Research Group, Faculty of Engineering, University of Nottingham, Nottingham, NG7 2RD, United Kingdom.

Abstract: This study investigates the optimisation of hydrothermal carbonisation (HTC) parameters for transforming Whitewood biomass into hydrochar, focusing on bioenergy production and valuable chemical extraction as by-products. The optimal carbonisation was achieved at a process temperature of 240 -260 °C, which optimised the higher heating value of the hydrochar to 27-30 kJ/g and ensured a structural integrity similar to lignite coal. Increasing the temperature beyond 260 °C did not significantly enhance the energy content or quality of the hydrochar, establishing 260 °C as the practical upper limit for the HTC process. Residence times between 30 to 60 min were found to have minimal impact on the yield and quality of hydrochar, suggesting significant operational flexibility and the potential to double throughput without increasing energy consumption. The study also revealed that the process water by-product is rich in furan compounds, particularly furfural and hydroxymethyl furfural, with their highest concentration (125 mg/g of feedstock) occurring at 220 °C. The implementation of these findings could facilitate the development of a large-scale HTC facility, significantly reducing reliance on fossil fuels and enhancing economic viability by producing high-energy-density biofuels and high-value chemical by-products.

Keywords: Hydrothermal carbonisation, Biomass valorisation, Hydrochar, Value-added chemicals, Sustainable energy.

Submitted: May 15, 2024. **Accepted:** June 22, 2024.

Cite this: Güleç, F. (2024). Hydrochar and Value-Added Chemical Production Through Hydrothermal Carbonisation of Woody Biomass. *Journal of the Turkish Chemical Society, Section B: Chemical Engineering*, 7(2), 141-154. <https://doi.org/10.58692/jotcsb.1484204>.

***Corresponding author. E-mails:** Fatih.Gulec1@nottingham.ac.uk; Gulec.Fatih@outlook.com.

1. INTRODUCTION

The need for renewable energy sources has never been more critical. With an estimated 37.55 billion metric tonnes of CO₂ released into the atmosphere in 2023 (Tiseo, 2024). A rapid increase in global warming over the past few decades has brought the need for innovative, clean energy solutions. Many countries have been setting new policies and laws to reduce their Carbon Emissions and undo the near-irreversible consequences of global warming (Global CCS Institute, 2018). In 2019, the UK Government committed to achieve net zero by 2050. To meet this target, the UK signed an agreement at COP26 to end investments in new coal power generation (Smith et al., 2022; WHO, 2021). This follows the key policies in the Net Zero Strategy stating by 2035 the UK will be powered entirely by clean energy, subject to the security of supply (UK-Government, 2021).

The undeniable potential of biomass and bioenergy to replace fossil fuels in existing processes to produce heat, electricity, and fuel for transportation makes it an attractive and promising energy resource (Güleç, Samson, et al., 2022; Güleç, Williams, Kostas, Samson, et al., 2022). In order to valorise the biomass sources, there are many thermochemical processes such as hydrothermal conversion, pyrolysis, gasification and combustion. Hydrothermal Carbonisation (HTC) is an emerging thermochemical process that could be used in the bioenergy sector through the conversion of biomass into hydrochar (Sharma et al., 2020; Shen, 2020). Compared to other thermal conversion technologies i.e. pyrolysis or gasification, HTC is favourable (Bevan et al., 2021) as it does not require drying of the feedstock, which is highly energy-intensive and expensive.

The desired water content of the HTC feed is 75-90% (Kumar & Ankaram, 2019). Hydrochar obtained from HTC has been identified as a potential biofuel (Oumabady et al., 2020), contributing to this shift towards renewable energies and giving a major reason industries cite for not readily adopting biofuels is non-compatibility with existing equipment (Singh et al., 2022). Therefore, if it can be commercialised, HTC of biomass offers an attractive way to produce cleaner fuel for major industries, with the global biofuels arena growing at a rate of over 8% annually (Powell, 2022) and expected to surpass US\$200 billion in value by 2030. HTC can therefore provide an effective waste management system, and no ethical concerns arise from using second-generation biomass waste (Phang et al., 2023). Furthermore, hydrothermal conversion technologies including carbonisation, liquefaction, and gasification align well with Sustainable Development Goals (SDG7, SDG9, and SDG12) fostering cleaner energy solutions and promoting sustainable industrialisation and innovation (Welfle et al., 2023).

The selection of biomass feedstock and the parameters of the HTC process are crucial in ensuring that the resulting hydrochar meets the necessary specifications for its use as an industrial fuel. The presence of high-ash fuels can significantly increase fouling and slagging in combustion equipment, while alkaline metals in the ash may catalyse the combustion of hydrochars, altering their combustion characteristics compared to fossil coal (Stirling et al., 2018). Consequently, the ash content of the hydrochar must remain below 12 wt.% to meet industrial standards use (Agency, 2016). Due to their relatively low ash content and widespread availability, woody biomasses are particularly attractive feedstocks for HTC processes (Daskin et al., 2024). These woody feedstocks can be efficiently converted into hydrochar through HTC, making them a promising component in the production of green energy. Their global abundance and sustainable nature further enhance their appeal, as they help reduce reliance on non-renewable energy sources and contribute to the mitigation of environmental impacts associated with energy production.

This study focuses on the valorisation of Whitewood (WW) biomass using a lab-scale HTC reactor, aiming to produce sustainable hydrochar and value-added chemicals. Operating under a range of conditions, with temperatures between 200-280 °C and residence times from 30 to 180 min, the research includes a thorough characterisation of the solid, liquid, and gaseous products generated during the HTC process. The novelty of this research lies in its comprehensive evaluation of Whitewood biomass in the HTC process, assessing its applicability as a feedstock and identifying potential value-added products, including biochemicals, biogas, and hydrochar. Specifically, this paper presents the chemical composition and thermal properties of hydrochar to determine its suitability for bioenergy applications.

Additionally, it investigates the potential for extracting value-added chemicals from the liquid by-products through advanced chemical analyses. The study also assesses the gaseous products to understand their environmental impact and practical implications, thereby contributing comprehensive insights into the effectiveness and sustainability of the HTC process.

2. EXPERIMENTAL SECTION

A Whitewood (WW) Northern Ireland, supplied by Wolseley, was used as the biomass feedstock for the HTC process. The WW came in pellets formed from sawdust residues. The material was chosen due to its abundance and having been produced in the United Kingdom. To ensure the particle size was below 1 mm, the WW was milled in a Ball Mill for 2 min at 600 rpm. The milling process ensures homogeneity of the particles. Particle size can play a major role in heat and mass transfer within the HTC process. Larger particle sizes lead to slower reaction rates and incomplete conversion of the biomass. Smaller particle sizes are exposed to more water and heat, promoting hydrolysis and dehydration reactions.

2.1. Hydrothermal Carbonisation of Whitewood

The HTC experiments were carried out using a batch High-Pressure Autoclave Reactor System. WW sample (4.00 ± 0.01 g) was loaded into the vessel along with distilled water (26.00 ± 0.01 g) and mixed thoroughly to ensure homogeneity. The reactor vessel was sealed and flushed with nitrogen ensuring no air was present in the vessel, before being pressurised to 5 bar. A fluidised sand bed was then heated to the carbonisation temperature of 200 °C - 280 °C using compressed air entering at the bottom of the bed. When the sand-bed reach the set temperature, the autoclave was placed in the sand bed and kept at the isothermal temperature for a residence time of 30 min, 60 min, and 180 min. The temperature was monitored using an additional K-type thermocouple. Following the carbonisation, the reactor was moved to a separate cold fluidised sand bed maintained at 20 °C for 1 h to allow the vessel to cool down. After the elapsed hour a gas syringe was used to collect gaseous products whilst liquid and solid hydrochar was separated using a vacuum filtration unit. The primary products (solid, liquid, and gas) yields are calculated using Eq1-Eq3 (Güleç et al., 2021; Koechermann et al., 2018). Furthermore, hydrochar yield (Eq-4) is determined as the fixed carbon yield of the process. This is calculated by multiplying the fixed carbon content by the dry solid yield. Specifically, it involves assessing the proportion of fixed carbon in the hydrochar relative to the initial dry biomass, providing a clear measure of the efficiency and effectiveness of the hydrothermal carbonisation process in converting biomass to carbon-rich solid fuel.

$$\text{Solid yield (wt. \%)} = \frac{m_{\text{drychar}}}{m_{\text{ww},0}} * 100 \quad (1)$$

$$\text{Gas yield (wt. \%)} = \frac{m_{\text{gas}}}{m_{\text{ww},0}} * 100 \quad (2)$$

$$\text{Liquid yield (wt. \%)} = 100 - \text{Solid yield} - \text{Gas yield} \quad (3)$$

$$\text{Hydrochar yield (wt. \%)} = \left[\frac{m_{\text{drychar}}}{m_{\text{ww},0}} * 100 \right] * FC \quad (4)$$

Where, m_{drychar} ; represents the dry mass of solid char collected following the HTC process, $m_{\text{ww},0}$; represents the initial dry mass of feedstocks (ww), m_{gas} ; is the mass of the gas product collected following the HTC process (as determined by GC-MS analysis), FC is the fixed carbon content of hydrochar in wt.%.

2.2. Characterisation of Solid Hydrochar

2.2.1. Proximate analysis and thermal decomposition

Proximate analysis were performed by thermogravimetric analysis (TGA) using a TA-Q500 using a slow pyrolysis procedure presented before (Güleç et al., 2021; Lester et al., 2007). This method provides proximate analysis and enables further information regarding the changes in the composition of hydrochar by identification of displacement level. Approximately 30 mg of hydrochar was placed in a platinum pan of a model Q500 TGA. Samples were then heated from ambient temperature to 900 °C, at a heating rate of 5 °C/min, under a nitrogen flow of 100 mL/min. It was then held isothermally for 10 min to ensure total devolatilisation before changing the gas flow to 100 mL/min of air for 15 min to combust the fixed carbon. The temperature was then ramped down to 35 °C at a rate of 30 °C/min (Güleç et al., 2021; Lester et al., 2007). The mass loss before 110 °C was assumed to be moisture as the temperature is above the boiling point of water but below the temperature range for the thermal decomposition of hemicellulose, cellulose, and lignin. Mass loss from 110 °C up to 900 °C was considered volatile matter (VM) as the sample was under an inert nitrogen atmosphere. The rest of the mass loss was under airflow and considered as fixed carbon (FC). The remaining mass represented the ash content of the hydrochar. Three samples of feedstock and three hydrochars produced at the same process conditions were analysed to reduce systematic error.

2.2.2. Displacement

A novel characterisation property, suggested by (Lester et al., 2007), called "Displacement" has

been utilised to quantify the degree of hydrochar upgrade in HTC process using Eq 5. This dimensionless quantity provides a method to quantitatively compare the effectiveness of the hydrothermal treatment. It has been calculated from the absolute difference between the derivative weight loss from the feedstocks and the derivative weight loss from the hydrochar at each temperature, T.

$$\text{Displacement} = \sum_{T_i}^{T_f} \left(\left| \left(\frac{dw}{dt} \right)_{bf,T} \right| - \left(\frac{dw}{dt} \right)_{hc,T} \right) \quad (5)$$

Where, T_i and T_f are the temperature limits of the devolatilisation; 110°C and 900°C respectively. The higher the magnitude of displacement, the more structural decomposition has occurred during HTC process.

2.2.3. Ultimate Analysis

Ultimate (elemental) analysis was carried out for each hydrochar and feedstock using a Leco CHN628 and utilising helium as the carrier gas. Multiple pure standards of BBOT were used for calibration. Approximately 75 mg of sample was used per analysis. The oxygen content was determined by difference, assuming the total remaining was wholly elemental oxygen. The elemental analysis was triplicated to eliminate experimental error.

2.2.4. Fuel Characteristics

The higher heating value (HHV) of the hydrochars was estimated by a correlation with the ultimate analysis data (Callejón-Ferre et al., 2011). This particular correlation (Eq 6) was chosen based on a comprehensive analysis by (Daskin et al., 2024; Güleç, Williams, Kostas, Samson, et al., 2022) which showed that it had the lowest standard deviation from experimental data of 11 different theoretical correlations for the same feedstock.

$$\text{HHV} = -3.440 + 0.517(C+N) - 0.433(H+N) \quad (6)$$

Where, HHV is the higher heating value, C, N, and H are the elemental composition of Carbon, Nitrogen, and Hydrogen, respectively.

2.3. Characterisation of Process Liquid

Dichloromethane (DCM) was selected as the solvent to extract organic compounds for analysis from the process water by liquid-liquid extraction. It has mid-range polarity, meaning most organics will dissolve into it, plus DCM is immiscible with the water phase and denser, so can be easily drained off from a separating flask. Additionally, DCM is highly volatile, so it readily evaporates leaving behind the extracted compounds of interest. Extraction was performed by making 6 mL process water up to 15 mL volume with deionised water, then mixing with 15 mL DCM and settling for 5 min before draining off the solvent. This was repeated 3 times to extract maximum organics. The DCM was left to evaporate overnight, and a standard solution of squalane was prepared and 100 µL added to each sample. Squalane is a hydrocarbon not found in the process liquid, so its peak in the gas chromatography (GC) output was used as a reference point to enable the quantification of all other compounds. The organic compounds were analysed on a 6850 Agilent HP GC connected to a 5975 Agilent HP quadrupole mass spectrometer (MS), (EI mode, 70 eV). GCMS was equipped with an autosampler and a split/splitless injector. Compounds were separated by a DB-1701 MS fused silica capillary column (60 m × 0.25 mm i.d. × 0.5 µm film thickness) with helium as the carrier gas, and an oven program of 50 °C (held for 2 min) to 280 °C (held for 25 min), heated at a rate of 4 °C/min. MS is used for qualitative analysis, with compounds determined according to the NIST Mass Spectral Library from the National Institute of Standards and Technology, Maryland, USA. Compounds were then quantified with a Flame ionisation detector (FID). FID was used for quantification over MS as outputs are more reproducible and represent the composition of a mixture more reliably (St Gelais, 2014). This is because MS detects ions of fragmented compounds, with fragmentation and ionisation potential varying between compounds (Cicchetti et al., 2008), so is not suited to accurately measure the composition of a mixture. FID is inherently more quantitative as it works on the principle of detecting ions formed during the combustion of organic compounds.

2.4. Characterisation of Gas Products

Gas products were collected in an airtight bag and immediately analysed using Clarus 580 gas chromatography (GC) fitted with a Flame ionisation detector (FID) and thermal conductivity detector (TCD) operating at 200 °C. The gas samples were analysed by injecting 100 µL of each gas sample (split ratio 10:1) into the GC at 250 °C with separation performed on an alumina plot fused silica 30 m × 0.32 mm × 10 µm column, with helium as the carrier gas. The FID detector was used to analyse the hydrocarbon compounds and

TCD detector was used to analyse nonhydrocarbon compounds. The oven temperature was programmed from 60 °C (13 min hold) to 180 °C (10 min hold) at 10 °C/min.

3. RESULTS AND DISCUSSION

3.1. Hydrothermal Carbonisation of Whitewood

Figure 1 presents the yields of solid, liquid, gaseous primary products and hydrochar as functions of the hydrothermal carbonisation (HTC) process parameters: temperature (200 °C to 280 °C), residence time (30 to 180 min), and autogenous pressure, using biomass to water mass ratio of 1:6.5. The solid hydrochar product is generated through the decomposition and carbonisation of the major structural components of biomass—namely hemicellulose, cellulose, and lignin—which undergo hydrolysis, dehydration, and decarboxylation reactions. Specifically, the temperatures required to decompose these components range broadly, with hemicellulose starting to decompose at temperatures as low as 220 °C, cellulose at around 280 °C, and lignin between 160 °C and 900 °C (Güleç, Samson, et al., 2022; Güleç, Williams, Kostas, Samson, et al., 2022).

At lower temperatures (200–220 °C), the HTC process has a limited effect on the yield of solid hydrochar. The hydrochars produced at these temperatures exhibit only partial carbonisation, characterised by a light brown colour and large particle structure, similar to the original WW feedstock. These conditions result in less than 37 wt.% of the biomass being converted into gaseous and liquid products, indicating an incomplete carbonisation process. This is akin to findings by (Musa et al., 2022), where low temperatures were insufficient for the complete decomposition of major biomass components, such as Pine Kraft Lignin, leading to a higher yield of hydrochar. As the HTC temperature increases from 220 °C to 240 °C, there is a notable reduction in the yield of hydrochar from 64 wt.% to 49 wt.%, accompanied by an increase in the production of gaseous and liquid products. The hydrochars obtained at 240 °C are transformed into a homogeneous, blackish, coal-like solid structure. This decrease in hydrochar yield can be attributed to the major decomposition and carbonisation of hemicellulose within the feedstock, as this temperature range is ideal for hemicellulose breakdown but still below the decomposition temperatures for cellulose and lignin. Regarding residence time, Figure 1 shows a slight decrease in hydrochar yield from 65 wt.% to 59 wt.% as residence time increases from 30 to 180 min. Concurrently, the gas yield increases from 1 wt.% to 8 wt.%, corroborating findings by (Musa et al., 2022). (Ghanim et al., 2016) suggests that the increase in gas and liquid products at longer residence times could be explained by the degradation of soluble hemicellulose, cellulose, and lignin fragments in the aqueous phase.

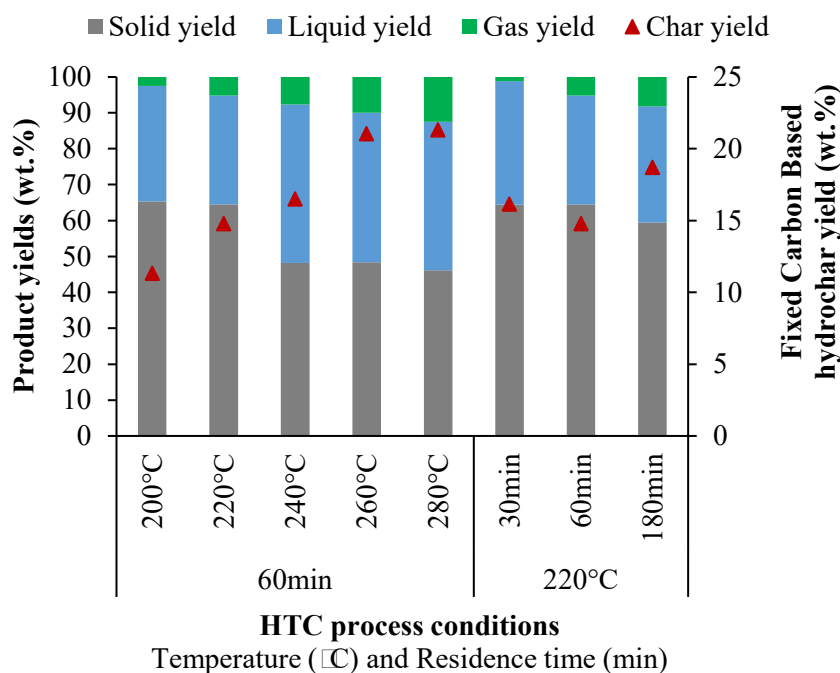


Figure 1. Solid (grey bar), liquid (blue bar), gaseous (green bar) and hydrochar (red triangle) product yields as a function of HTC process temperature (200 °C–280 °C), residence time (30–180 min) and autogenous pressure using biomass to water mass ratio of 1:6.5.

The linear increase in gas product yield across the experimental temperature range from 2.5 wt.% at 200 °C to 12.5 wt.% at 280 °C highlights a strong correlation between process temperature and gas yield. Although liquid product yield also increases from 30.3 wt.% to 49.6 wt.% as the temperature rises from 220 to 240 °C, further temperature increases do not significantly alter liquid yield, indicating that the majority of solid biomass decomposes primarily through liquefaction at these critical temperatures (220–240 °C). Figure 1 also shows that the fixed carbon-based hydrochar yield increases with rising process temperatures and residence times. For instance, at a constant residence time of 60 min, increasing the temperature from 200 °C to 260 °C results in a progressive increase in char yield from 11 wt.% to 21 wt.%. This indicates that higher temperatures facilitate the conversion of biomass into hydrochar, enhancing the carbon content. At 220 °C, increasing the residence time from 30 min to 180 min leads to a slight increase in hydrochar yield from 16 wt.% to 19 wt.%. This suggests that longer exposure to the HTC conditions promotes further carbonisation of the biomass, although the effect is less pronounced compared to temperature changes.

3.2. Fuel Characteristics of Hydrochars

3.2.1. Proximate analysis, Ultimate analysis, and HHV

Figure 2a illustrates the proximate analyses of feedstock and hydrochars. The fixed carbon ratio shows a notable increase from 17 wt.% to 44 wt.% as the hydrothermal temperature is raised from 200 °C to 280 °C. This increase in fixed carbon content correlates with a significant decrease in

volatile matter, which drops from 80 wt.% to 50 wt.%. While residence time does affect carbonisation, with fixed carbon increasing from 25 wt.% to 31 wt.% as residence time extends from 30 min to 180 min, the impact of residence time is substantially less significant than that of temperature (Güleç, Williams, Kostas, Samson, et al., 2022; Musa et al., 2022). The ultimate analysis results, as shown in Figure 2b, indicate that the carbon content of the biomass increases due to hydrothermal carbonisation. The increase in carbon content from 47 wt.% to 70 wt.% is more pronounced with higher process temperatures at 280 °C. Similarly, an increase in residence time also leads to a slight rise in carbon content from 54 wt.% to 60 wt.%, further emphasising the influence of temperature and residence time on the carbon yield in the hydrothermal carbonisation process.

Similar to the fixed carbon-based hydrochar yield (Figure 1), the HHV of solid products, as calculated and shown in Figure 2a, shows a considerable increase from 18 kJ/g to 30 kJ/g with the escalation of process temperature from 200 °C to 260 °C. In contrast, increasing the residence time from 30 min to 180 min at a constant temperature of 220 °C results in a smaller increase in HHV, from 22 kJ/g to 25 kJ/g. This suggests that temperature is a more critical factor than residence time in enhancing the energy content of hydrochars. Both hydrochar yield and HHV propose that optimising the temperature during the HTC process is crucial for maximising both the yield and energy content of hydrochar. Adjusting the residence time can further fine-tune these outcomes, but its effects are secondary to those of temperature.

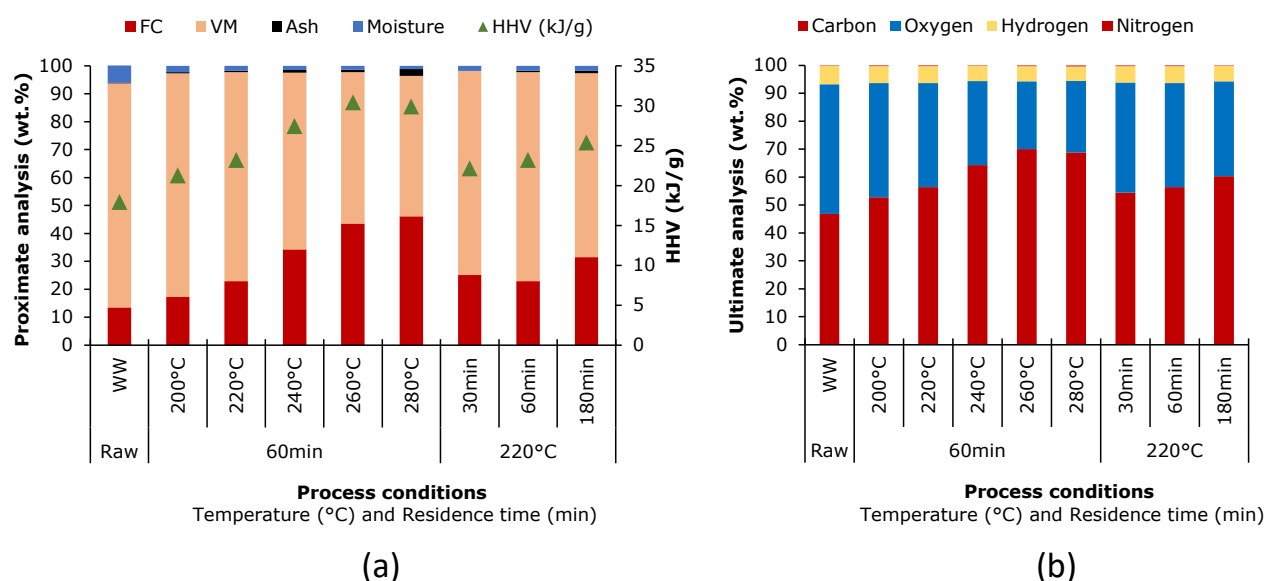


Figure 2. a) Proximate analysis and b) Ultimate analysis results of raw feedstocks and hydrochars produced with HTC (200°C–280°C, 30-180 min and autogenous pressure).

Additionally, ash content is a vital parameter for determining the suitability of hydrochar in energy production. Initial measurements showed the ash content in feedstock to be 0.23 wt.%. However, the hydrochars exhibited higher ash contents than the original feedstocks; this increase is due to a reduction in solid yield rather than an absolute increase in ash mass. Specifically, hydrochar produced at 200 °C had an ash content of 0.42 wt. %, which escalated to 2.42 wt.% at 280 °C, with a standard error of $\pm 0.32\%$. The HTC process tends to leech organic compounds into the process water, increasing the relative ash proportion in the solid residue, although the inorganic material is somewhat removed from the biomass (Hansen et al., 2020). Despite these increases, all samples

maintained an ash content well below the 12 wt.% thresholds considered acceptable for bioenergy applications, affirming that hydrochars produced from WW are suitable for use as fuel in green energy generation. The hydrochars in this study were produced in a batch process, which, compared to a semi-continuous HTC process involving WW, tends to result in 50 wt.% lower ash content (Güleç, Williams, Kostas, Smon, et al., 2022). This suggests that allowing process water to interact with the hydrochars during the reaction facilitates the transfer of inorganic material to the liquid phase, a crucial consideration for feedstocks intended for semi-continuous processing where slightly higher ash content might still be acceptable for combustion in industrial boilers.

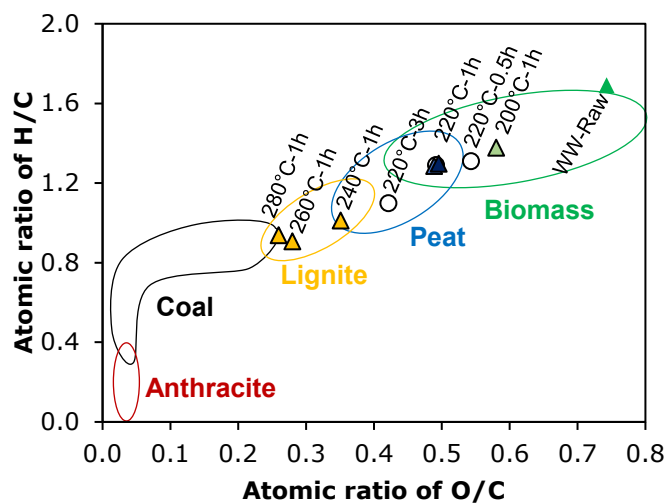


Figure 3. Van Krevelen diagram for raw biomass feedstocks (WW-Raw) and hydrochars produced as under HTC process conditions; 200°C–280°C, 30-180 min and autogenous pressure.

The Van Krevelen diagram (Figure 3), which plots the atomic ratio of H/C versus O/C, provides detailed insights into the fuel characteristics of produced hydrochars relative to conventional fuels such as peat, lignite, coal, and anthracite. The diagram shows the results of complex reactions including dehydration, demethylation, and decarboxylation, as noted by Güleç et al. (Güleç, Samson, et al., 2022; Güleç, Williams, Kostas, Samson, et al., 2022). Figure 3 indicates the trends, which is characterised by an increase in carbon content, leading to reduced atomic O/C and H/C ratios. This trend is a consistent dehydration pattern as both temperature and residence time increase. The dehydration process provides lower hydrogen and oxygen content within the hydrochar (Funke & Ziegler, 2010). The hydrochars produced at 200 and 220 °C are categorised within the Biomass zone, while those at 240 °C align with the Peat-Lignite zone, and those at 280 °C approach the border between Lignite-Coal. This progression demonstrates how increases in temperature progressively enhance the structure of the hydrochar, fostering a coal-like structure by carbonising biomass.

0.0.1. Thermal Decomposition and Displacement

Figure 4 shows the thermal decomposition and derivative weight changes during the slow pyrolysis of WW and hydrochars produced from WW. This analysis provides further details about the chemical composition of hydrochars following specific HTC processes. The degradation temperatures of biomass constituents are known as hemicellulose decomposes between 220-315 °C, cellulose between 315-400 °C, and lignin over a broad range of 160-900 °C (Yang et al., 2007).

The hydrous nature of HTC plays a crucial role in the process. Hydrolysis reactions, which predominantly involve the splitting of ester and ether bonds in biopolymers, lead to their breakdown into oligomers and monomers (Funke & Ziegler, 2010; Güleç et al., 2023). For instance, the disappearance of the hemicellulose shoulder in the raw WW observed in Figures 4b indicates that the hemicellulose structure can decompose at temperatures above 200 °C, a process that begins as low as 180 °C (Funke & Ziegler, 2010).

Significant peaks (260-340 °C) representing the cellulose-lignin structure remain in the hydrochars produced at 200 and 220°C. However, further carbonisation at higher temperatures, such as 240°C, leads to the breakdown of cellulose, as evidenced by the decrease in the cellulose-lignin peak shown in Figure 4b. Increasing the temperature further to 260 °C and 280 °C results in almost complete disappearance of this peak, indicating significant cellulose decomposition (Güleç et al., 2021). At the highest investigated temperatures, a new peak emerges at approximately 390-450 °C, correlating with the concentration of lignin remaining in the solid product.

The devolatilisation profiles of hydrochars produced at residence times of 30 and 180 min show more carbonisation than those processed for 60 min (Figure 4d). Interestingly, while the increased carbonisation at 180 min aligns with expectations due to prolonged reaction time, the similar profile at 30 min contradicts other studies that suggest longer times lead to more carbonisation (Cao et al., 2021; Reza et al., 2015; Smith & Ross, 2019). The unexpected trend in hydrochar produced at the residence time of 30 min and 60 min can be attributed to the cooling time. In these experiments, the cooling period lasts approximately one hour, which is longer than the actual residence times of 30 min and equal to 60 min, resulting in a total process time of 90-120 minutes from heating to cooling. This prolonged cooling period effectively extends the carbonisation process, reducing the differences between hydrochars produced at these shorter residence times. Given that the impact of residence time has shown minimal enhancement in the hydrochar (Figure 1-3), it is likely that the differences observed between the 30 min and 60 min conditions are due to the short residence time of the process rather than a consistent experimental trend. (Smith & Ross, 2019) found that temperature has a more significant impact on hydrochar characteristics than residence time. In order to enhance the understanding of short residence time, further investigation into the thermal dynamics and reaction kinetics during the cooling phase could provide deeper insights.

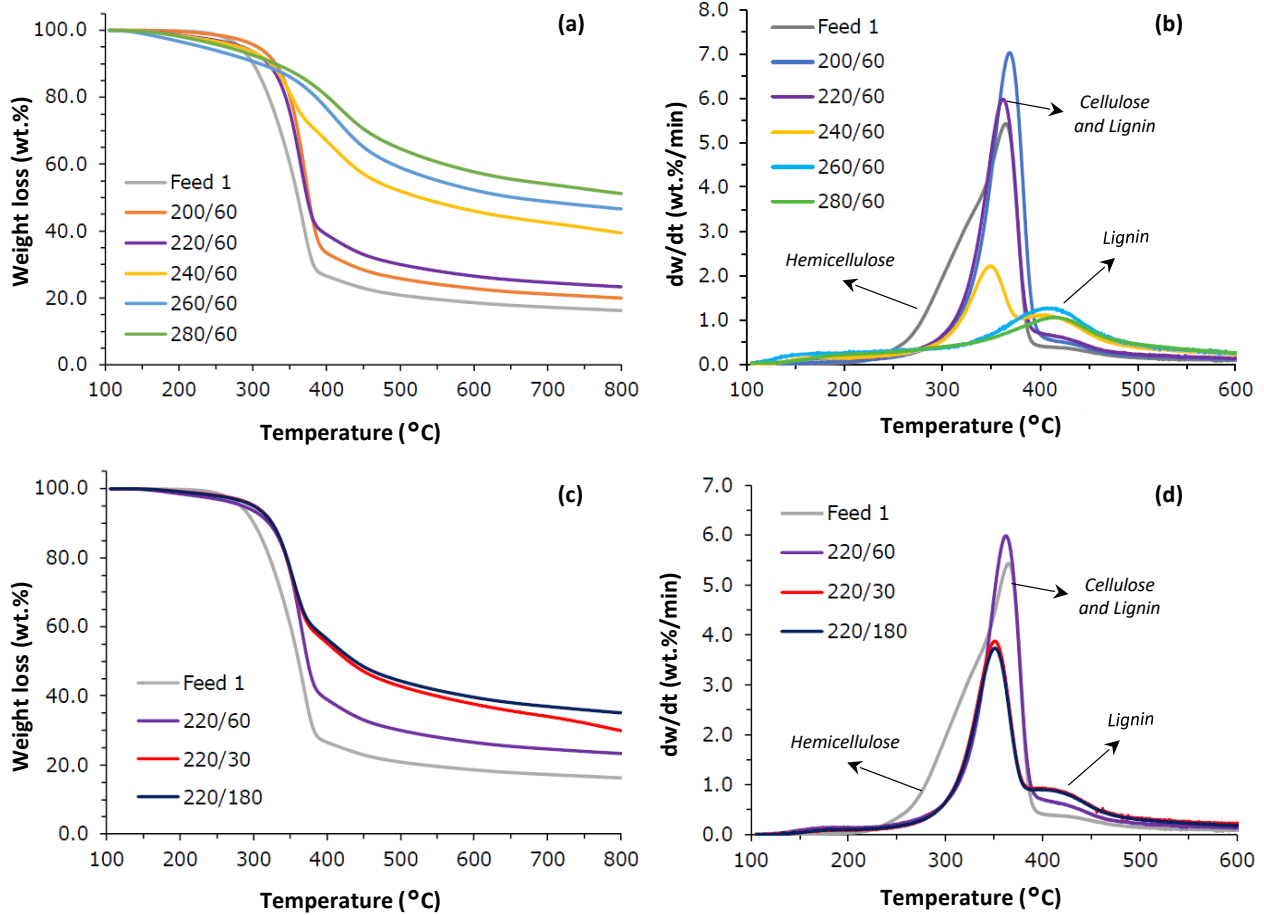


Figure 4. Thermal decomposition of WW and hydrochars under slow pyrolysis conditions (5 °C/min) and derivative weight change by temperature for a-b) hydrochars produced at different temperatures (200-280 °C) and c-d) hydrochars produced by different residence time (30-180 min).

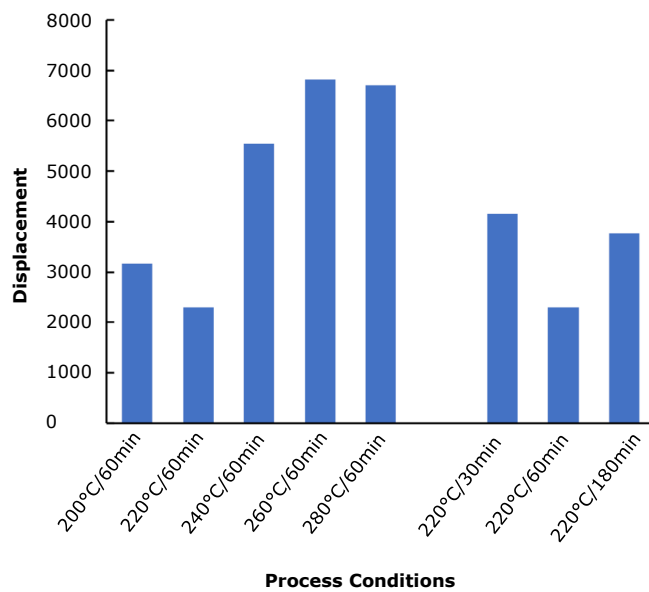


Figure 5. Displacement level of hydrochars produced at different temperatures (200-280 °C) and residence times (30-180 min).

Figure 5 shows the displacement levels of hydrochars across various temperatures and residence times. At elevated temperatures of 240 °C, 260 °C, and 280 °C, the displacement levels were notably high, ranging from 6000 to 7000, in stark contrast to the significantly lower

displacements of 2000 to 3000 recorded at 200 °C and 220 °C. These substantial displacements at higher temperatures correspond with the notable absence of hemicellulose and cellulose in the devolatilisation profiles, which significantly contribute to the deviation in mass loss from the feedstock. However, it is interesting to note that the displacements at 220 °C were unexpectedly lower than those at 200 °C. Although higher displacement is generally favorable for achieving a better hydrochar structure, this is not always the case, particularly when biomass decomposes completely during the hydrothermal process. For instance, during hydrothermal gasification, biomass may transform into inorganic compounds, resulting in no char formation at the end of the reaction. This process might theoretically yield the maximum displacement, yet it does not necessarily indicate that the resulting material has desirable fuel properties. This suggests that displacement cannot be directly correlated with fuel quality based solely on displacement measurements.

3.3. Value-added Chemicals in Liquid Products

Figure 6 illustrates the various compounds present in the process water and the relative amounts between samples from HTC runs under varying conditions. It is seen that the largest peak at 19 min residence time, a furan compound, is only present in process liquid from HTC at the lowest temperatures of 200 °C and 220 °C, and is also not present in the liquid when residence time was only

30 min. The next most intense peak at 39 min is not present at all in the liquid from the hottest HTC run at 280 °C, and is noticeably less intense at 260 °C, whilst several other compounds are detected in these two samples which are not present in the process liquids from HTC runs at reduced temperatures.

The chemicals identified in the process liquid were categorised into four groups: Acids, Aldehydes & Ketones, Furans, and Phenols. Table 1 shows that the organic group generally present in the highest quantity in the process water is furans. Across all samples, the total amount of organics in the process water is highest for the HTC run at 220 °C and a 60 min residence time. Furans are the most prominent chemical group found in the process water by-product when HTC is carried out at 240 °C and below, and residence time is seen to have minimal impact on the quantities of furans present. Within this group, the main compounds are furfural and hydroxymethyl furfural (HMF). Furfural is typically generated from lignocellulosic biomass such as WW (Zhang et al., 2022). The high furfural content seen in liquid from lower temperature hydrochars supports later findings in this research that HTC does not decompose cellulose structures when the reaction occurs below 240 °C. Higher hydrochar processing temperatures likely caused furfurals to be decomposed into other molecules (Diaz Perez et al., 2023), as is seen by the numerous peaks representing compounds only present in the liquid from HTC at 280 °C.

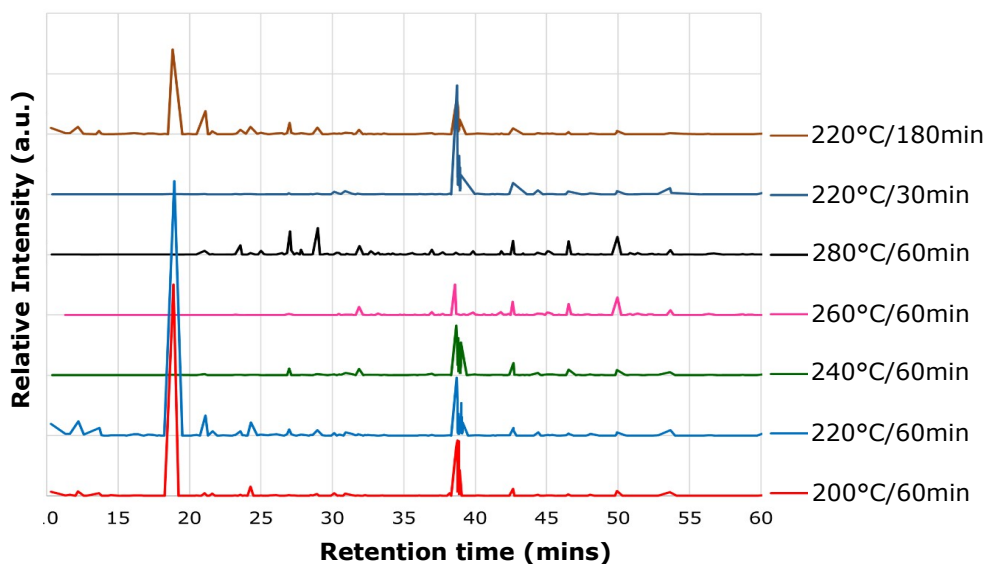


Figure 6. Relative peak intensities for liquid samples of the HTC process at different temperatures (200-280 °C) and residence times (30-180 min) (detailed peak definition is provided in Appendix A).

Table 1. Comparison of process liquid from HTC runs under varying temperatures and residence time.

Value-added chemical compounds	Liquid Samples*						220°C 180mi n
	200° C	220° C	240° C	260° C	280° C	220° C 30mi n	
	60min (mg/g Biomass Feedstock ±0.19 mg/g)						
Acids							
Acetic Acid	0.00	1.91	0.00	0.00	0.00	0.00	1.16
Aldehydes & Ketones							
Acetol	0.57	2.36	0.00	0.00	0.00	0.00	1.40
Acetoin	0.34	1.26	0.00	0.00	0.05	0.00	0.58
Butanone	0.30	3.37	0.19	0.00	0.59	0.00	4.42
Hexanedione (Diacetyethane)	0.00	0.70	0.00	0.00	1.40	0.00	0.81
Corylone (Hydroxy Methyl Cyclopentenone)	0.00	1.00	1.06	0.17	3.47	0.179	2.15
Vanillin (Hydroxy Methoxy Benzaldehyde)	0.87	2.11	1.92	1.83	2.07	1.696	1.11
Total Aldehydes & Ketones	2.08	10.80	3.17	2.00	7.57	1.87	10.48
Furans							
Furfural	26.49	42.39	0.00	0.00	0.05	0.00	16.36
Ethanone (Furanyl)	0.26	0.70	0.00	0.00	0.09	0.00	0.52
Methyl Furaldeyde	1.13	2.16	0.00	0.00	0.23	0.00	1.40
Furyl Hydroxy Methyl Ketone	0.34	0.40	0.14	0.17	0.32	0.40	0.12
Furandicarboxaldehyde	0.26	1.00	0.34	0.00	0.00	0.49	0.23
Hydroxymethyl Furfural	34.39	78.86	53.84	4.43	0.32	60.87	36.79
		125.5					
Total Furans	62.89	2	54.32	4.60	0.99	61.77	55.42
Phenols							
Methoxy Phenol	0.00	0.90	0.19	0.00	3.96	0.00	1.22
Methoxy Propyl Phenol	0.15	0.55	0.38	0.21	0.32	0.58	0.00
Hydroxy Methoxy Phenyl Propanone	0.19	0.65	0.86	1.53	1.98	0.45	0.76
Hydroxy Methoxy Phenyl Butanone	0.11	0.25	0.14	0.00	0.00	0.18	0.00
Hydroxy Methoxy Phenyl Propanol	0.60	0.90	0.82	2.47	2.66	0.80	0.99
Hydroxy Methoxy Phenyl Propanal	0.87	0.90	0.48	0.68	0.68	0.94	0.00
Total Phenols	1.93	4.17	2.88	4.90	9.60	2.95	2.97

*Amounts of organic compounds are presented in milligrams per gram of WW feedstock. Error is calculated from the standard deviation of analysis results repeated for the 220°C 1 hour liquid sample and is found to be ± 0.19 mg/g, giving high confidence in the results.

Furfural has been used as a chemical feedstock in synthesising plastics, solvents, and resins, and it has been proven that furfural and HMF can be generated from biomass in high quantities at low cost (Siddarth H. Krishna, 2018). The global furfural market is valued around US\$600 million in 2023 (Statista, 2023) and is growing due to rising demand for sustainably produced chemical feedstocks for plastics. The combination of HTC conditions producing the highest quantity of furans in the process liquid at 125 mg per gram of WW feedstock is 220°C and 60 min residence time. This translates to 1 g of furans (primarily furfural and HMF) in the process liquid for every 8 g of WW that undergoes HTC. This relatively large amount of furfural and HMF is a key finding with major impacts to HTC process economics, given furfural can be expected to sell for US\$1000/tonne (Siddarth H. Krishna, 2018).

The next most prevalent chemical group is phenols. These are present in small quantities of <10 mg/g feedstock, and changes to HTC process conditions are not seen to correlate with a large change in phenolics, suggesting quantities are

more dependent on the biomass chosen for HTC rather than process parameters. Studies have shown HTC can be integrated with anaerobic digestors producing biogas (Brown et al., 2020) by using the process liquid as feedstock, however, phenols inhibit methane production when present in quantities greater than 1.5mg/L (Poirier & Chapleur, 2018). The process liquid from WW HTC is also suitable for use as a feedstock to anaerobic digestors, as total phenol levels are far below inhibiting limits, as shown in Table 1.

3.4. Gas Products

Figure 7 shows the composition of gaseous products generated during HTC at temperatures of 220 °C and 240 °C. Gas chromatography analysis reveals that the predominant component of the gaseous products at both temperatures is CO₂. Specifically, at 220 °C, three repeated gas analyses yielded an average CO₂ composition of 98 \pm 2.5 vol. %, with a 95% confidence interval. As the temperature of the HTC process increases, the volume fraction of CO₂ in the gas slightly decreases, while there is a noticeable increase in carbon monoxide (CO) production. At 240 °C, CO₂

and CO account for 92 vol.% and 7.11 vol.%, respectively. Additionally, there are minor increases in methane (0.1 vol.%), hydrogen (0.3 vol.%), and trace quantities of light hydrocarbons such as ethene and butene. This finding aligns with and is supported by results from a study by (Musa et al., 2022), which identified that the primary component of the gaseous phase product from HTC is CO₂, accompanied by some CO and trace amounts of hydrocarbon gases. Further quantitative comparisons can be made with a study by Basso et al., which provides additional insights into the composition of these gases (Basso et al., 2018).

While the gaseous products from HTC are not typically considered high-value, modifications to

the facility design could leverage these by-products effectively. For instance, recycling the gases produced back into the HTC reactor vessel could gradually increase the concentration of the gas product, resulting in a stream rich in CO₂, CO, H₂, and hydrocarbons. This enriched stream presents some utilisation options such as fuel source or carbon capture. If the concentration of hydrocarbons is sufficiently high, this stream could potentially be used as a fuel source, thereby reducing the energy demands of the HTC facility. Predominantly consisting of CO₂, this stream could be purified into a highly concentrated CO₂ stream, which could then be used in carbon capture and storage applications, contributing to the creation of carbon-negative bioenergy fuel.

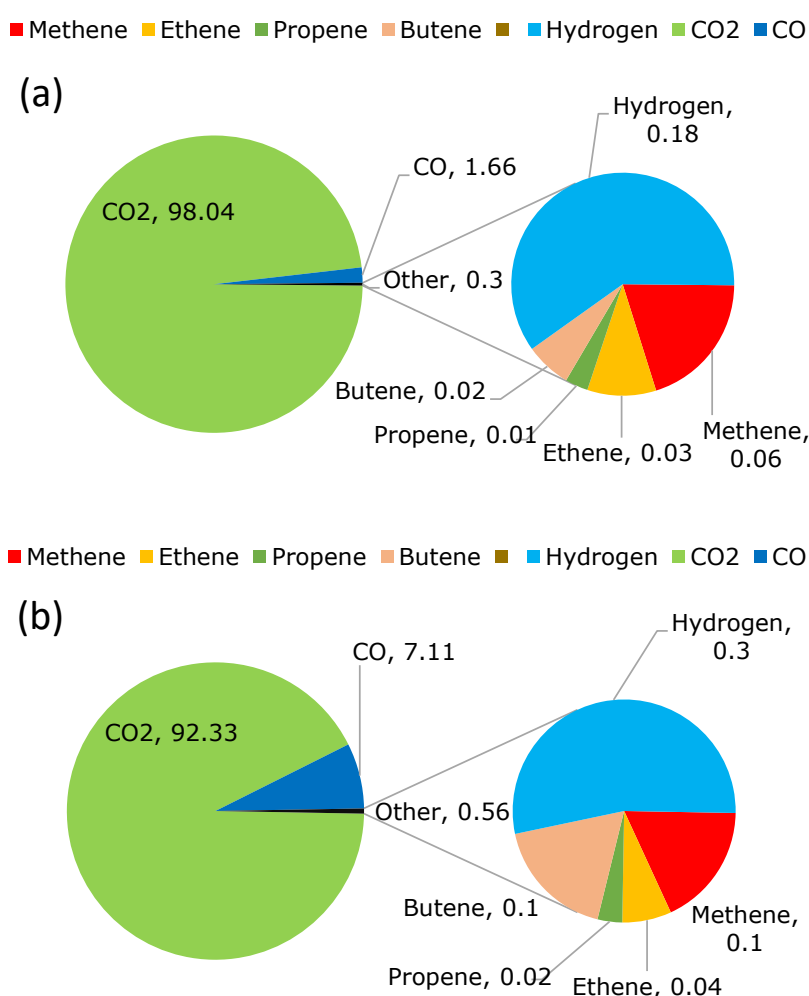


Figure 7. Gas composition (vol%) within the gaseous products of HTC process at the temperatures of a) 220°C and 60 min and b) 240°C and 60min.

4. CONCLUSION

This study systematically evaluated the optimisation of hydrothermal carbonisation (HTC) parameters for the production of hydrochar from woody biomass (whitewood), aimed at enhancing its suitability for bioenergy and value-added chemical applications. The findings show that a process temperature of 240-260 °C is optimal for

achieving effective carbonisation, maximising the higher heating value (27-30 kJ/g), and ensuring the structural integrity of the hydrochar similar to lignite-coal structure. Temperatures exceeding 260 °C do not yield significant improvements in the energy content or quality of the hydrochar, indicating that 260 °C is the upper limit for process temperature. Residence time has a minimal impact

on the yield and quality of hydrochar between 30 min to 60 min, allowing for operational flexibility and increased throughput without additional energy costs. The study also highlighted the importance of managing residence times to balance energy use with production efficiency. The process water by-product contains substantial quantities of furan compounds, specifically furfural and hydroxymethyl furfural. These compounds are most abundant when the HTC process is conducted at temperatures of 240 °C or lower. Optimal production of furans, reaching as high as 125 mg/g of feedstock, occurs at a temperature of 220 °C. Implementing the findings from this study could lead to the development of a large-scale HTC facility that not only contributes to reducing dependency on fossil fuels but also supports the economic viability through the production of both high-energy-density biofuels and valuable chemical by-products. This aligns with Sustainable Development Goals (SDG7, SDG9, and SDG12) fostering cleaner energy solutions and promoting sustainable industrialisation and innovation.

5. CONFLICT OF INTEREST

The authors have no conflict of interest.

6. ACKNOWLEDGMENTS

This research was partially funded and supported by the EPSRC, BBSRC and UK SuperGen Bioenergy Hub [Grant number EP/S000771/1], the University of Nottingham FPVC Research Acceleration Fund (Dr Fatih Gulec).

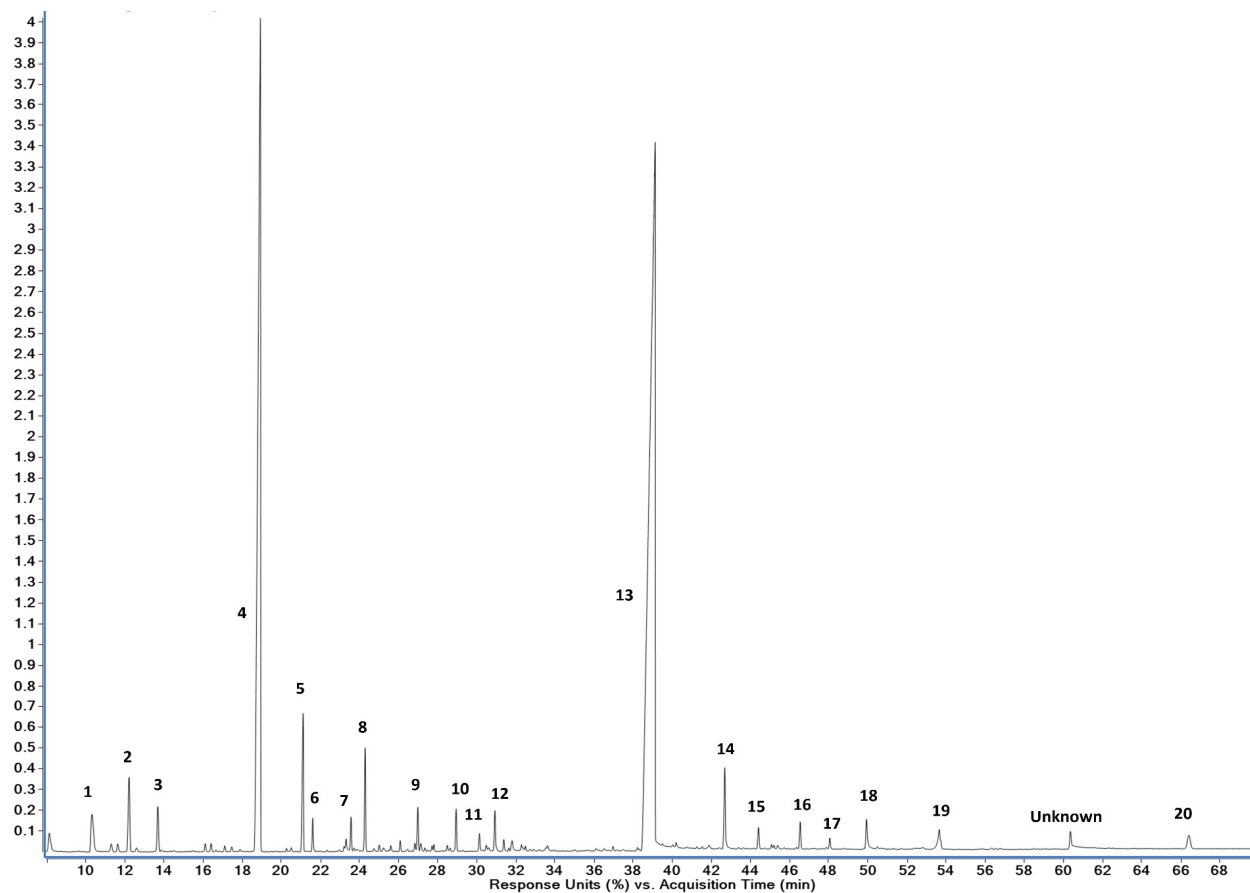
7. REFERENCES

- Agency, E. (2016). Material comparators for end-of-waste decisions.
- Basso, D., Weiss-Hortala, E., Patuzzi, F., Baratieri, M., & Fiori, L. (2018). In deep analysis on the behavior of grape marc constituents during hydrothermal carbonization. *Energies*, 11(6), 1379.
- Bevan, E., Fu, J., Luberti, M., & Zheng, Y. (2021). Challenges and opportunities of hydrothermal carbonisation in the UK; case study in Chirnside. *RSC advances*, 11(55), 34870-34897.
- Brown, A. E., Finnerty, G. L., Camargo-Valero, M. A., & Ross, A. B. (2020). Valorisation of macroalgae via the integration of hydrothermal carbonisation and anaerobic digestion. *Bioresource Technology*, 312, 123539.
- Callejón-Ferre, A., Velázquez-Martí, B., López-Martínez, J., & Manzano-Agugliaro, F. (2011). Greenhouse crop residues: Energy potential and models for the prediction of their higher heating value. *Renewable and Sustainable Energy Reviews*, 15(2), 948-955.
- Cao, Z., Hülsemann, B., Wüst, D., Oechsner, H., Lautenbach, A., & Kruse, A. (2021). Effect of residence time during hydrothermal carbonization of biogas digestate on the combustion characteristics of hydrochar and the biogas production of process water. *Bioresource technology*, 333, 125110.
- Cicchetti, E., Merle, P., & Chaintreau, A. (2008). Quantitation in gas chromatography: usual practices and performances of a response factor database. *Flavour and fragrance journal*, 23(6), 450-459.
- Daskin, M., Erdoğan, A., Güleç, F., & Okolie, J. A. (2024). Generalizability of empirical correlations for predicting higher heating values of biomass. *Energy Sources, Part A: Recovery, Utilization, and Environmental Effects*, 46(1), 5434-5450.
- Diaz Perez, N., Lindfors, C., A. M. van den Broek, L., van der Putten, J., Meredith, W., & Robinson, J. (2023). Comparison of bio-oils derived from crop digestate treated through conventional and microwave pyrolysis as an alternative route for further waste valorization. *Biomass Conversion and Biorefinery*, pp.1-16.
- Funke, A., & Ziegler, F. (2010). Hydrothermal carbonization of biomass: A summary and discussion of chemical mechanisms for process engineering. *Biofuels, Bioproducts and Biorefining*, 4(2), 160-177.
- Ghanim, B. M., Pandey, D. S., Kwapinski, W., & Leahy, J. J. (2016). Hydrothermal carbonisation of poultry litter: Effects of treatment temperature and residence time on yields and chemical properties of hydrochars. *Bioresource technology*, 216, 373-380.
- Global CCS Institute. (2018). The global status of CCS. <https://www.globalccsinstitute.com/resources/global-status-report/>
- Güleç, F., Parthiban, A., Umenweke, G. C., Musa, U., Williams, O., Mortezaei, Y., Suk-Oh, H., Lester, E., Ogbaga, C. C., & Gunes, B. (2023). Progress in lignocellulosic biomass valorization for biofuels and value-added chemical production in the EU: A focus on thermochemical conversion processes. *Biofuels, Bioproducts and Biorefining*, 18(3), 755-781.
- Güleç, F., Riesco, L. M. G., Williams, O., Kostas, E. T., Samson, A., & Lester, E. (2021). Hydrothermal conversion of different lignocellulosic biomass feedstocks–Effect of the process conditions on hydrochar structures. *Fuel*, 302, 121166.
- Güleç, F., Samson, A., Williams, O., Kostas, E. T., & Lester, E. (2022). Biofuel characteristics of chars produced from rapeseed, whitewood, and seaweed via thermal conversion technologies–Impacts of feedstocks and process conditions. *Fuel Processing Technology*, 238, 107492.
- Güleç, F., Williams, O., Kostas, E. T., Samson, A., & Lester, E. (2022). A comprehensive comparative study on the energy application of chars produced from different biomass feedstocks via hydrothermal conversion, pyrolysis, and torrefaction. *Energy Conversion and Management*, 270, 116260.
- Güleç, F., Williams, O., Kostas, E. T., Smon, A., & Lester, E. (2022). A comprehensive comparative study on the energy application of chars produced from different biomass feedstocks via hydrothermal conversion, pyrolysis, and torrefaction. *Energy Conversion and Management*, 270, 116260.

- Hansen, L. J., Fendt, S., & Spliethoff, H. (2020). Impact of hydrothermal carbonization on combustion properties of residual biomass. *Biomass Conversion and Biorefinery*, 12(7), 2541-2552.
- Koechermann, J., Goersch, K., Wirth, B., Muehlenberg, J., & Klemm, M. (2018). Hydrothermal carbonization: Temperature influence on hydrochar and aqueous phase composition during process water recirculation. *Journal of Environmental Chemical Engineering*, 6(4), 5481-5487.
- Kumar, S., & Ankaram, S. (2019). Waste-to-energy model/tool presentation. In *Current developments in biotechnology and bioengineering* (pp. 239-258). Elsevier.
- Lester, E., Gong, M., & Thompson, A. (2007). A method for source apportionment in biomass/coal blends using thermogravimetric analysis. *Journal of Analytical and Applied Pyrolysis*, 80(1), 111-117.
- Musa, U., Castro-Díaz, M., Uguna, C. N., & Snape, C. E. (2022). Effect of process variables on producing biocoals by hydrothermal carbonisation of pine Kraft lignin at low temperatures. *Fuel*, 325, 124784.
- Oumabady, S., Kamaludeen, S., Ramasamy, M., Kalaiselvi, P., & Parameswari, E. (2020). Preparation and Characterization of Optimized Hydrochar from Paper Board Mill Sludge. *Scientific reports*, 10(1), 773.
- Phang, F. J. F., Soh, M., Khaerudini, D. S., Timuda, G. E., Chew, J. J., How, B. S., Loh, S. K., Yusup, S., & Sunarso, J. (2023). Catalytic wet torrefaction of lignocellulosic biomass: An overview with emphasis on fuel application. *South African Journal of Chemical Engineering*, 43(1), 162-189.
- Poirier, S., & Chapleur, O. (2018). Inhibition of anaerobic digestion by phenol and ammonia: Effect on degradation performances and microbial dynamics. *Data in brief*, 19, 2235-2239.
- Powell, H. (2022). Biofuels market size to surpass \$201.21 billion by 2030. *Connected Energy Solutions*. <https://connectedenergysolutions.co.uk/biofuels-market-size-to-surpass-201-21-billion-by-2030/>
- Reza, M. T., Mumme, J., & Ebert, A. (2015). Characterization of hydrochar obtained from hydrothermal carbonization of wheat straw digestate. *Biomass Conversion and Biorefinery*, 5, 425-435.
- Sharma, R., Jasrotia, K., Singh, N., Ghosh, P., Sharma, N. R., Singh, J., Kanwar, R., & Kumar, A. (2020). A comprehensive review on hydrothermal carbonization of biomass and its applications. *Chemistry Africa*, 3(1), 1-19.
- Shen, Y. (2020). A review on hydrothermal carbonization of biomass and plastic wastes to energy products. *Biomass and Bioenergy*, 134, 105479.
- Siddarth H. Krishna, K. H., Kevin J. Barnett, Jiayue He, Christos T. Maravelias, James A. Dumesic, George W. Huber, Mario De bruyn, Bert M. Weckhuysen. (2018). Oxygenated commodity chemicals from chemo-catalytic conversion of biomass derived heterocycles. Department of Chemical and Biological Engineering, University of Wisconsin-Madison.
- Singh, A., Gill, A., Lim, D. L. K., Kasmaruddin, A., Miri, T., Chakrabarty, A., Chai, H. H., Selvarajoo, A., Massawe, F., Abakr, Y. A., & al., e. (2022). Feasibility of Bio-Coal Production from Hydrothermal Carbonization (HTC) Technology Using Food Waste in Malaysia. *Sustainability*, 14(8), 4534.
- Smith, A. M., & Ross, A. B. (2019). The influence of residence time during hydrothermal carbonisation of miscanthus on bio-coal combustion chemistry. *Energies*, 12(3), 523.
- Smith, P., Beaumont, L., Bernacchi, C. J., Byrne, M., Cheung, W., Conant, R. T., Cotrufo, F., Feng, X., Janssens, I., & Jones, H. (2022). Essential outcomes for COP26.
- St Gelais, A. (2014). GC Analysis – Part V. FID or MS for Essential Oils? Laboratoire PhytoChemia. <https://phytochemia.com/en/2014/09/02/gc-analysis-part-v-fid-or-ms-for-essential-oils/#:~:text=In%20general%2C%20the%20MS%20should,compound%20in%20an%20essential%20oil>
- Statista. (2023). Market value of furfural worldwide from 2015 to 2021, with a forecast for 2022 to 2029. <https://www.statista.com/statistics/1310467/furfural-market-value-worldwide/#:~:text=In%202021%2C%20the%20market%20of,566%20million%20U.S.%20dollars%20worldwide>
- Stirling, R. J., Snape, C. E., & Meredith, W. (2018). The impact of hydrothermal carbonisation on the char reactivity of biomass. *Fuel processing technology*, 177, 152-158.
- Tiseo, I. (2024). Annual carbon dioxide (CO₂) emissions worldwide from 1940 to 2023. Retrieved 13/05/2024 from <https://www.statista.com/statistics/276629/global-co2-emissions/>
- UK-Government. (2021). Net Zero Strategy: Build Back Greener.
- Welfle, A. J., Almena, A., Arshad, M. N., Banks, S. W., Butnar, I., Chong, K. J., Cooper, S. G., Daly, H., Freitas, S. G., & Güleç, F. (2023). Sustainability of bioenergy-Mapping the risks & benefits to inform future bioenergy systems. *Biomass and Bioenergy*, 177, 106919.
- WHO. (2021). COP26 special report on climate change and health: the health argument for climate action. World Health Organization.
- Yang, H., Yan, R., Chen, H., Lee, D. H., & Zheng, C. (2007). Characteristics of hemicellulose, cellulose and lignin pyrolysis. *Fuel*, 86(12-13), 1781-1788.
- Zhang, X., Zhu, P., Li, Q., & Xia, H. (2022). Recent Advances in the Catalytic Conversion of Biomass to Furfural in Deep Eutectic Solvents. *Frontiers in Chemistry*, 10, 911674.

APPENDICES

Appendix A: Labelled FID spectra with 20 main peaks identified in the table.



Peak No	Molecular Mass (g/mol)	Compound Group	Compound Name
1	60	Carboxylic Acid	Acetic Acid
2	74	Ketone	Acetol
3	88	Ketone	Acetoin
4	96	Furan	Furfural
5	72	Ketone	Butanone
6	110	Furan	Ethanone (Furanyl)
7	114	Ketone	Hexanedione (Diacetyethane)
8	110	Furan	Methyl Furaldeyde
9	112	Ketone	Corylone (Hydroxy Methyl Cyclopentenone)
10	124	Phenol	Methoxy Phenol
11	126	Furan	Furyl Hydroxy Methyl Ketone
12	124	Furan	Furandicarboxaldehyde
13	126	Furan	Hydroxy Methyl Furfural
14	152	Aldehyde	Vanillin (Hydroxy Methoxy Benzaldehyde)
15	166	Phenol	Methoxy Propyl Phenol
16	180	Phenol	Hydroxy Methoxy Phenyl Propanone
17	194	Phenol	Butyrovanilone (Hydroxy Methoxy Phenyl Butanone)
18	182	Phenol	Hydroxy Methoxy Phenyl Propanol
19	178	Phenol	Hydroxy Methoxy Phenyl Propanal
20	196	Alkane	Squalane (Reference Compound)



Eco-friendly and low-cost phytodyeing for wool, cotton and polyester textile materials using *Parthenocissus Quinquefolia* L. Fruit Extracts

Adem Önal , Sedanur Gökçe 

Tokat Gaziosmanpaşa University, Türkiye

Abstract: This study investigates the extraction of natural colorant from fresh fruits of *Parthenocissus quinquefolia* L. and the application of the extracted dye to wool yarn, cotton, and polyester fabrics in the presence and absence of various mordants. The effect of mordant type on the dyeing quality with different mordanting methods was examined. Iron sulfate, tin chloride, alum, copper sulfate, and potassium dichromate were used as mordant. The effects of these mordants on the color of the dyed samples were investigated in terms of CIELab (L^* , a^* , b^*) and K/S values. The light, washing and rubbing fastness of the dyed samples were evaluated according to ISO standards. While dyeing wool yarn without mordant produces reddish brown, and dyeing with mordant produces a wide range of colors from green to purple, blue and lilac tones are obtained in cotton fabric dyeing, and green, purple and brown tones are obtained in polyester fabric dyeing. While polyester fabrics are dyed with synthetic dyes at 130 °C, in this study they were dyed with natural dyes at 90 °C. As a result of dyeing, colors with high fastness are generally obtained.

Keywords: Natural dyes, *Parthenocissus quinquefolia* L., cotton fabric, wool yarn, polyester, fastness.

Submitted: February 27, 2024. **Accepted:** July 02, 2024.

Cite this: Önal, A., & Gökce, S. (2024). Eco-friendly and low-cost phytodyeing for wool, cotton and polyester textile materials using *Parthenocissus Quinquefolia* L. Journal of the Turkish Chemical Society, Section B: Chemical Engineering, 7(2), 155-166. <https://doi.org/10.58692/jotcsb.1443924>

*Corresponding author. E-mail: adem.onal@gop.edu.tr

1. INTRODUCTION

Dyes are generally used in textile, paper, cosmetic, food, pharmaceutical, and leather industries (Chiou et al., 2002; Banat et al., 1996). Water pollution due to discharge of non-biodegradable colored effluents from textile dye manufacturing and textile-dyeing still is one of the major environmental concerns in the world today. Strong colors transferred by synthetic dyes to the receiving aquatic ecosystems poses aesthetic and serious ecological problems such as inhibition of benthic photosynthesis and carcinogenicity (Forgacs et al., 2004; Robinson et al., 2001). Textile industry uses high amounts of water, its wastewater being the main way by which dyes are discharged into the environment. Textile wastes are characterized by prominent color and high concentrations of organic and inorganic compounds caused by residual dyes that were not fixed to the fibers during the dyeing process (Cooper et al., 1995). These environmental problems of public health concern related to colored wastewaters containing synthetic dyes have diverted researchers urgently to look for eco-friendly

products. For this reason, there has been a rapid return to natural dyes in the world (Tawfik et al., 2002).

The colorants of natural dyes that are obtained from animal or vegetable matter without chemical processing. Coloring agents of plants are derived from roots, leaves, barks, and trunks or fruits. Henna, madder, pomegranate, turmeric, walnut etc. are well-known examples of natural dyes. The introduction of natural dyes in textile dye houses is coupled to several requirements which have to be fulfilled, i.e., adaptation of traditional processes on modern equipment, and selection of material leading to product with acceptable fastness properties (Bechtold et al., 2003). However, natural dyes possess some limitations such as lesser availability, poor color yield, complexity of bond process and non-reproduce ability of shades. They offer much more advantages including renewable sources, minimal health hazard, no disposal problems and harmonization with nature (Adeel et al., 2009).

Parthenocissus quinquefolia L., is a deciduous climbing plant belonging to the Vitaceae family, native to North America and can be found in South Africa and Australia (Adel et al., 2021). This plant is a very widely known ivy and ornamental plant and its fruits are quite poisonous to humans. It can be said that there are many flavonoids such as anthocyanin groups and many other substances in the chemical structure of the plant. *Parthenocissus quinquefolia* L., is used for many different purposes today. While the plant itself is used to prevent erosion of the soil, it is known that in traditional medicine, some parts of it are used as an expectorant, its fruits are used to relieve rheumatism pain, its roots are used as a diuretic, and its bark and branches are used as cough syrup. It is also grown as an ornamental plant due to its pleasant appearance and perfect covering of fences and garden walls. (Benli, 2017).

In the literature, the dyestuff properties of extracts obtained from various parts of *Parthenocissus quinquefolia* L. have been investigated. Ticha et al. investigated a new phyto-dyeing process of natural fibers such as cotton, wool and silk using the natural aqueous extract of *Parthenocissus quinquefolia* L. (Ticha et al., 2017). In the study, anthocyanins, the main coloring components of the dye extract, were characterized by HPLC-MS analysis. Menten Çolak et al. dyed wool yarns using the pre-mordanting method with *Parthenocissus quinquefolia* L. leaves (Çolak et al., 2020). The authors reported that matte colors were obtained from iron and copper salts, and light and bright colors were obtained from dyeings without alum and mordant. It has been reported in the literature that quinquefolia contains anthocyanin pigment as a natural dye.

In this article, it was investigated in detail whether the ripe purple fruits of *Parthenocissus quinquefolia* L. could be a source of natural dye. For this purpose, the dyeing properties of wool yarn, cotton fabric and polyester fabric types were examined. Dyeing was carried out according to non-mordanting (additive-free) and mordanting (pre-, meta-, post-mordanting) methods. The fastness of the colors, K/S values and Pantone color codes were determined and interpreted comparatively. According to literature research, the dye substance in *Parthenocissus quinquefolia* L. was identified as cyaniding (Benli, 2019) (Figure 1).

2. EXPERIMENTAL SECTION

2.1. Materials and chemicals

2.1.1. Plant material

Parthenocissus quinquefolia L. fruits were harvested in Tokat (Türkiye) in November 2023. The ripe purple fruits of the plant were refluxed in the Soxhlet device 2 hours after collection and purple solution was obtained (w/V, 50 g/500 mL). The resulting colored solution was used in the dyeing process.

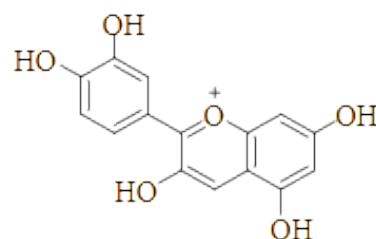


Figure 1: The chemical structure of cyanidine.

2.1.2. Textile materials

Prescourd wool yarn (2 nM) were obtained commercially from Tokat (Türkiye). Before use, it was bleached with a solution containing 200 mL of hydrogen peroxide and 50 mL of ammonia (30%) at 50 °C for 60 minutes at a liquor ratio of 100:6. Then, the obtained material was neutralized with formic acid solution, washed thoroughly with distilled water and dried at room temperature for 48 hours.

The bleached cotton (235 g/m²) was commercially obtained from Toga Tekstil company, Tokat-Türkiye. The recommended process consists of preparing the fabric in a pre-bath containing a certain amount of cationizing agent at 50 °C for 30 minutes. Then the cotton was dried at room temperature.

The polyester fabric (185 g/m²) was purchased from Toga textile company, Tokat-Türkiye.

2.1.3. Precationizing of cotton fabric

The recommended process consists of preparing the fabric in a pre-bath containing a certain amount of cationizing agent at 50 °C for 30 minutes. Then the cotton was dried at room temperature and the bleached cotton was commercially obtained from Tokat Toga Tekstil company.

2.1.4. Chemicals and instrument

Mordants (Iron sulfate, tin chloride, alum, copper sulfate, and potassium dichromate) were obtained from Merck. Extraction was performed using Soxhlet apparatus. The color properties of the dyed samples were evaluated by Premier Colorscan SS 6200A Spectrophotometer in terms of CIE Lab values (L^* , a^* , b^* , C^*) and color strength (K/S) values. Color codes were determined using Color Index numbers. Light fastness (Atlas weather-ometer), washing fastness (Lauder-meter) and rubbing fastness (255 model crock-meter) of all dyed samples, determined according to ISO 105-C06 and CIS, were tested.

2.1.5. Extraction of dyestuff solution from *P. quinquefolia* L. fruit

50 g of fresh *Parthenocissus quinquefolia* L. fruit was refluxed using distilled water (500 mL) and became colorless in the Soxhlet apparatus. This process was continued until a total of 4 liters of colored extract was obtained, and finally, the extracts were collected when a stable color tone was obtained.

2.1.6. Plant dyeing method without mordant

Woolen yarns, cotton fabrics and polyester fabrics were dyed at a ratio of 50:1. The dyeing bath was kept at medium pH (6.55). The dyeing temperature was maintained at 85 °C for 45 min. The dyed samples were then rinsed with water. Finally, the fabrics were washed thoroughly with cold water, pressed and dried at room temperature.

2.1.7. Mordanting methods

Mordanting methods (Iron sulfate, tin chloride, alum, copper sulfate, and potassium dichromate) were performed as we have previously reported in the literature (Önal et al., 2021; Önal et al., 2023).

Pre-mordanting method

The textile products (5 g) were heated in 0.1 M mordant solution (100 mL) for 1 h at 90 °C. It was heated in 0.1 M mordant solution (100 mL) for 1 h at 90 °C. After cooling it was rinsed with distilled water and put into dye-bath solution (100 mL). It was heated at 90 °C for 1 h. The dyed samples were rinsed with distilled water and dried.

Meta-mordanting method

0.1 M mordant solution, dyestuff solution and textile materials were heated in the flask and heated at 90 °C for 1 h. After cooling, it was rinsed and dried.

Post-mordanting method

The textile products (5 g) were firstly treated with the dyestuff solution at 90 °C for 1 h. After cooling, it was rinsed with distilled water and put into 0.1 M mordant solution (100 mL) and heated for 1h at 90 °C. The dyed samples were rinsed with distilled water and dried.

The dyeing diagram for all samples is given in Figure 2. In meta-mordanting, solid mordant corresponding to 0.1 M 100 mL concentration value was added to the dyestuff solution extracted from *P. Quinquefolia* L fruits, and a Flotte ratio of 1:100 was applied. The dyeing process was carried out for 60 minutes at 90 °C with a temperature increase of 1.5-2 °C per minute. At the end of the dyeing period, after it was left to cool to room temperature and filtered, washed with distilled water, rinsed and dried.

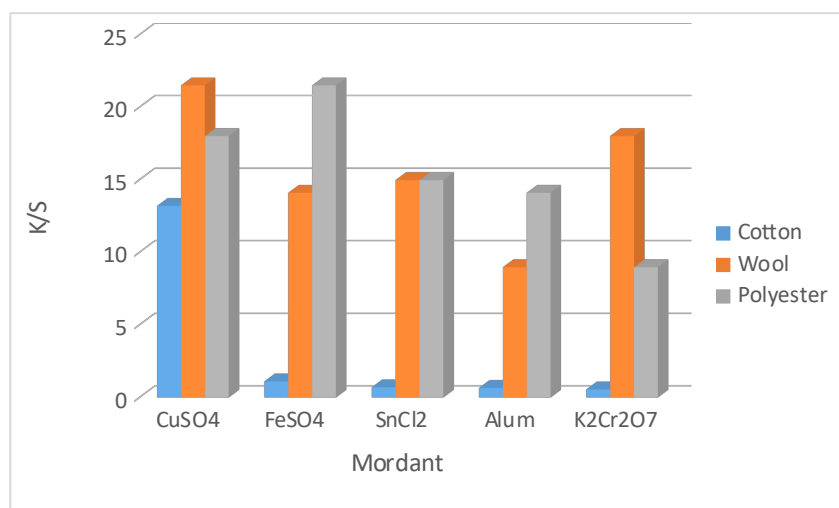


Figure 2: Dyeing temperature.

3. RESULTS AND DISCUSSION

Fastness values and color codes of dyed wool yarns, cotton fabrics, and polyester fabrics are presented in Table 1, Table 2 and Table 3, respectively.

When Table 1 is examined, the highest score in washing fastness in the final mordanting with iron sulfate was found to be 5, wet fastness as 4, dry fastness as 4-5, and light fastness as 4. Washing, wet, dry rubbing and light fastness values obtained with copper sulfate are close to 5. Dry rubbing fastness in all three mordanting methods is 5. Light

fastness is on average 4-5 and is higher than iron sulfate. In pre-mordanting with alum, the washing fastness is 4-5, and the dry and wet rubbing fastness for the three mordanting methods is 5. Light fastness is 4 in pre- and meta-mordanting and 3-4 in post-mordanting. The washing, dry and wet rubbing fastnesses obtained with alum are higher than copper sulfate and iron sulfate, but are slightly lower in terms of light fastness. In dyeing with $K_2Cr_2O_7$, the fastness to washing, wet and dry rubbing is 5 for all three mordanting methods, and the fastness to light is 3-4.

Table 1: Fastness values and color codes of dyed cotton fabrics.

Method	Mordant	Wash fastness ^a	Rubbing fastness ^b (wet-dry)	Light fastness ^c	Color code (Pantone)
Pre-	FeSO ₄	4 - 5	4 - 4/5	3 - 4	7529CS
Meta-	FeSO ₄	4 - 5	4 - 4/5	4	401 CS
Post-	FeSO ₄	5	4/5 - 5	4	4675CS
Pre-	CuSO ₄	5	5 - 4/5	4 - 5	7530 CS
Meta-	CuSO ₄	4 - 5	5 - 5	4 - 5	413 CS
Post-	CuSO ₄	4 - 5	5 - 5	4 - 5	726 CS
Pre-	KAl(SO ₄) ₂	4 - 5	5 - 5	4	406 CS
Meta-	KAl(SO ₄) ₂	5	5 - 5	4	454 CS
Post-	KAl(SO ₄) ₂	5	5 - 5	3/4	5527 CS
Pre-	K ₂ Cr ₂ O ₇	5	5 - 5	4	155 CS
Meta-	K ₂ Cr ₂ O ₇	5	5 - 5	3/4	474 CS
Post-	K ₂ Cr ₂ O ₇	5	5 - 5	3/4	473 CS
Pre-	SnCl ₂	5	5 - 5	4	7437 CS
Meta-	SnCl ₂	5	5 - 5	4	7436 CS
Post-	SnCl ₂	5	5 - 5	3/4	434 CS
	unmordant	3 - 4	5 - 5	2 - 3	686 CS

^aWash and ^brubbing fastness 1 = poor, 2 = moderate, 3 = fairly good, 4 = good, 5 = very good, ^cLight fastness 1 = very poor, 2 = poor, 3 = moderate, 4 = fairly good, 5 = good, 6 = very good, 7 = excellent, 8 = outstanding.

In dyeing with SnCl₂, the washing, wet and dry rubbing fastnesses for all three mordanting methods are 5, and the light fastness value is approximately the same as the K₂Cr₂O₇ mordant.

In dyeing without mordant, washing fastness was determined as 3/4, dry and wet rubbing fastness was determined as 5, and light fastness was determined as 2-3. Ranking according to the fastness values of mordants:

CuSO₄ > Kal(SO₄)₂ > SnCl₂ > K₂Cr₂O₇ > FeSO₄.

Ranking mordanting methods according to their effectiveness:

Pre-mordanting > Meta-mordanting > Post mordanting > No mordanting

In dyeing cotton fabrics without mordant, washing fastness was determined as 3-4 (medium), dry and wet rubbing fastness was determined as 5 (very good), and light fastness was determined as 1-2 (poor). Higher values were found in mordant dyeings. This result proves that the use of mordant increases fastness.

In the dyeing of cotton fabric; green, light brown color tones with copper sulfate; gray, lilac light brown color tones with iron sulfate; light lilac, beige color tones with alum, cream tones with potassium dichromate; dark lilac and light lilac color tones were obtained with stannous chloride, while a matte gray color tone were obtained in dyeing without mordant.

Table 2: Fastness values and color codes of dyed wool yarn.

Method	Mordant	Wash fastness ^a	Rubbing fastness ^b (wet-dry)	Light fastness ^c	Color code (Pantone)
Pre-	FeSO ₄	4/5	3/4 - 3	2/3	444 CS
Meta-	FeSO ₄	4	3/4 - 4	3	425 CS
Post-	FeSO ₄	4	4/5 - 4/5	3	404 CS
Pre-	CuSO ₄	5	4/5 - 4/5	3/4	416 CS
Meta-	CuSO ₄	5	3/4 - 4	2/3	446 CS
Post-	CuSO ₄	4/5	4/5 - 4/5	2/3	3995 CS
Pre-	KAl(SO ₄) ₂	4/5	5 - 5	3	WmGy 4CS
Meta-	KAl(SO ₄) ₂	4/5	5 - 5	3	402 CS
Post-	KAl(SO ₄) ₂	4/5	5 - 5	2/3	WmGy 5CS
Pre-	K ₂ Cr ₂ O ₇	5	4 - 5	3 - 4	7502 CS
Meta-	K ₂ Cr ₂ O ₇	5	4 - 5	3 - 4	7509 CS
Post-	K ₂ Cr ₂ O ₇	5	4 - 4/5	3 - 4	7511 CS
Pre-	SnCl ₂	2/3	3 - 4	3	431 CS
Meta-	SnCl ₂	3	3 - 3	3 - 4	451 CS
Post-	SnCl ₂	5	5 - 5	3	4495 CS
	unmordant	2/3	4/5 - 5	1/2	WmGy 2CS

^aWash and ^brubbing fastness 1 = poor, 2 = moderate, 3 = fairly good, 4 = good, 5 = very good, ^cLight fastness 1 = very poor, 2 = poor, 3 = moderate, 4 = fairly good, 5 = good, 6 = very good, 7 = excellent, 8 = outstanding.

Table 2 reveals that, the washing fastnesses for wool yarn dyeing with iron sulfate are 4-4/5 for pre- and post- mordanting methods, while it is 4 points for meta-mordanting. However, wet rubbing fastness is lower than dry rubbing fastness (3/4).

The washing fastness values (5) of wool yarn samples dyed using CuSO₄ mordant are slightly higher than the washing fastness values of FeSO₄. In dyeing with CuSO₄ mordant, the wet and dry rubbing fastnesses are 4 in meta- mordanting and 4/5 in pre- and post-mordanting methods. Light fastness is 2/3 for all three mordants.

The washing, wet and dry rubbing fastnesses obtained in all three mordanting methods with alum mordant are on average 4-4/5 and are higher than other mordants. The light fastness was found to be approximately 3.

The washing fastness (5), wet rubbing fastness (4), dry rubbing fastness (4/5), and light fastness (3-3/4) were found of wool yarns mordanted with K₂Cr₂O₇ mordant. In wool yarn dyeing using SnCl₂ mordant, fastness values were found to be 2/3 in pre-mordanting, 3 in meta-mordanting and 5 in post-mordanting method. Light fastness is very close to other mordants in all three mordanting methods.

According to the no mordanting dyeing method, the washing fastness of wool yarn dyeing was found to be 2/3, while the dry rubbing fastness was found to be 5 and the wet rubbing fastness was found to be 2/3.

In dyeing with wool yarn without mordant, washing fastness was determined as 2-3 (moderate), dry and wet rubbing fastness was determined as 4-5 (very good), light fastness was determined as 1-2 (poor). Higher values were found in mordanted dyeings. This result shows that the use of mordant increases the fastness.

If we were to rank them in terms of fastness values; we can write it as:



If we were to rank the mordanting method in terms of its effectiveness; we can write it as:

Pre-mordanting > Meta-mordanting > Post mordanting > No mordanting

In wool yarn dyeing with *P. Quinquefolia* extract, green and purplish green; bluish green with iron sulfate; gray and light green with alum; brown with potassium dichromate; Bluish green, dark green and light brown color tones were obtained with stannous chloride.

Table 3: Fastness values and color codes of dyed polyester fabric.

Method	Mordant	Wash fastness ^a	Rubbing fastness ^b (wet-dry)	Light fastness ^c	Color code (Pantone)
Pre-	FeSO ₄	3/4	5 - 5	2/3	719 CS
Meta-	FeSO ₄	4/5	4/5 - 4/5	4	Cl Gy 5 CS
Post-	FeSO ₄	4/5	5 - 5	4	406 CS
Pre-	CuSO ₄	3/4	5 - 5	3/4	Wm Gy5CS
Meta-	CuSO ₄	3/4	5 - 5	4/5	Wm Gy3CS
Post-	CuSO ₄	5	5 - 5	4/5	Wm Gy1CS
Pre-	KAl(SO ₄) ₂	4/5	5 - 5	4	Cl Gy 1CS
Meta-	KAl(SO ₄) ₂	4/5	5 - 5	4	Wm Gy4CS
Post-	KAl(SO ₄) ₂	4/5	5 - 5	4/5	664 CS
Pre-	K ₂ Cr ₂ O ₇	4/5	4/5 - 5	3 - 4	4685 CS
Meta-	K ₂ Cr ₂ O ₇	4/5	4/5 - 5	3 - 4	489 CS
Post-	K ₂ Cr ₂ O ₇	4/5	4/5 - 5	3 - 4	474 CS
Pre-	SnCl ₂	4	5 - 5	3 - 4	503 CS
Meta-	SnCl ₂	4/5	5 - 5	3 - 4	4755 CS
Post-	SnCl ₂	4/5	5 - 5	3	482 CS
	unmordant	1/2	3/4 - 4	1/2	727 CS

^aWash and ^brubbing fastness 1 = poor, 2 = moderate, 3 = fairly good, 4 = good, 5 = very good, ^cLight fastness 1 = very poor, 2 = poor, 3 = moderate, 4 = fairly good, 5 = good, 6 = very good, 7 = excellent, 8 = outstanding.

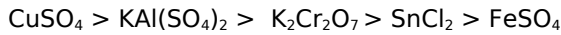
Based on Table 3, while the washing fastness with iron sulfate mordant in polyester fabric dyeing with *P. Quinquefolia* fruit extract was found to be 4/5 for all three mordanting methods, wet and dry rubbing fastnesses were determined to be close to each other (4/5-5). Light fastness was determined in pre-mordanting (2/3), meta-and in the post- mordanting (4).

The fastness values found with copper sulfate are very close to those of iron sulfate.

Washing fastnesses obtained with alum for all three mordanting methods are (4/5), wet and dry rubbing fastnesses are (5), and light fastnesses are approximately (4). As a result of dyeing with K₂Cr₂O₇, washing fastness (4/5), wet and dry

fastness (4/5) and light fastness (3/4) were measured.

If we were to rank them in terms of fastness values, we can write it as:



If we were to rank the mordanting method in terms of its effectiveness we can write as:

Pre-mordanting > Meta-mordanting > Post mordanting > No mordanting

In dyeing of polyester fabric without mordant, washing fastness was determined as 1-2 (poor), dry and wet rubbing fastness was determined as 3-4 (moderate), and light fastness was determined as 1-2 (poor). Higher values were found in mordant dyeings. This result evidences that the use of mordant increase the fastness.

As a result, according to Tables 1, 2 and 3, it can be deduced also that mordanting improved wash,

rubbing, and light fastness properties of dyed cotton, polyester fabric and wool yarn.

Colors obtained from polyester fabric dyeings; metallic light green- metallic light brown with copper sulfate; metallic light brown - coffee with iron sulfate; metallic light lilac with alum; bright light brown with potassium dichromate; the color tones ranging from dark lilac to light lilac were obtained with stannous chlororide.

3.1. Determination of color performance

The pre-, meta- and post- mordanting dyed samples were investigated for fastness properties. The spectral reflectance measurements of the naturally dyed samples were determined using a spectrophotometer (Konica Minolta 3600d). Color strength was determined as K/S values of the dyed samples using the Kubelka-Munk equation (Džimbeg-Malčić et al., 2011) . K/S and L^* , a^* , b^* values of cotton fabrics, wool yarn, and polyester fabrics are given in Tables 4, 5, and 6, respectively.

Table 4: K/S and L^* a^* b^* values of cotton fabrics.

Fabric	Mordant/Method	L^*	a^*	b^*	K/S
Cotton	FeSO ₄ (pre-)	61.88	-1.22	3.96	1.10
	FeSO ₄ (meta-)	60.86	-1.86	3.61	1.11
	FeSO ₄ (post)	68.64	0.16	12.44	1.05
	CuSO ₄ (pre-)	63.11	-3.17	9.38	13.20
	CuSO ₄ (meta-)	64.79	-3.97	8.16	1.15
	CuSO ₄ (post-)	67.85	-0.71	15.29	1.27
	KAl(SO ₄) ₂ (pre-)	72.63	-1.75	2.62	0.50
	KAl(SO ₄) ₂ (meta-)	72.98	-3.10	8.47	0.66
	KAl(SO ₄) ₂ (post-)	78.63	0.51	6.88	0.40
	K ₂ Cr ₂ O ₇ (pre-)	77.47	-0.13	11.84	0.52
	K ₂ Cr ₂ O ₇ (post-)	79.09	-1.47	13.19	0.55
	K ₂ Cr ₂ O ₇ (pre-)	79.34	0.15	12.50	0.48
	SnCl ₂ (pre-)	66.78	0.54	-4.93	0.70
	SnCl ₂ (meta-)	70.55	-0.34	-2.65	0.50
	SnCl ₂ (post-)	76.60	-1.43	-2.94	0.34
Non - mordant		71.68	-2.59	8.26	0.74

Table 5: K/S and L* a* b* values of wool yarn.

Fabric	Mordant/Method	L*	a*	b*	K/S
Wool	FeSO ₄ (pre-)	38.02	-2.56	6.64	7.02
	FeSO ₄ (meta-)	27.52	-1.89	5.51	14.10
	FeSO ₄ (post)	35.15	-2.24	6.54	8.33
	CuSO ₄ (pre-)	41.27	-3.12	17.62	10.00
	CuSO ₄ (meta-)	29.89	-4.14	7.54	13.01
	CuSO ₄ (post-)	31.34	1.43	17.74	21.50
	KAl(SO ₄) ₂ (pre-)	38.65	-1.61	9.39	8.97
	KAl(SO ₄) ₂ (meta-)	42.18	-0.15	9.33	6.95
	KAl(SO ₄) ₂ (post-)	43.04	-2.85	7.55	5.25
	K ₂ Cr ₂ O ₇ (pre-)	56.88	1.77	23.04	4.20
	K ₂ Cr ₂ O ₇ (post-)	52.78	1.39	26.00	7.00
	K ₂ Cr ₂ O ₇ (pre-)	42.37	8.10	32.01	18.02
	SnCl ₂ (pre-)	33.05	-3.75	3.93	13.15
	SnCl ₂ (meta-)	36.43	-2.08	16.78	14.98
	SnCl ₂ (post-)	45.42	0.37	22.56	7.95
	Non - mordant	51.06	5.76	12.49	4.00

Table 6: K/S and L* a* b* values of polyester fabrics.

Fabric	Mordant/Method	L*	a*	b*	K/S
Polyester	FeSO ₄ (pre-)	72.23	1.68	8.72	0.70
	FeSO ₄ (meta-)	59.95	-1.08	0.99	1.11
	FeSO ₄ (post)	69.20	-0.19	7.61	0.77
	CuSO ₄ (pre-)	73.81	-2.63	3.73	0.50
	CuSO ₄ (meta-)	67.47	-0.48	6.64	0.86
	CuSO ₄ (post-)	70.41	-0.66	7.11	0.75
	KAl(SO ₄) ₂ (pre-)	73.39	-0.94	1.98	0.61
	KAl(SO ₄) ₂ (meta-)	68.90	-1.28	2.10	0.60
	KAl(SO ₄) ₂ (post-)	70.47	-0.58	2.43	0.52
	K ₂ Cr ₂ O ₇ (pre-)	73.85	-0.13	4.35	0.57
	K ₂ Cr ₂ O ₇ (post-)	59.95	-1.08	0.99	0.42
	K ₂ Cr ₂ O ₇ (pre-)	78.49	-0.10	8.43	0.51
	SnCl ₂ (pre-)	73.19	-0.55	0.15	0.42
	SnCl ₂ (meta-)	68.86	-2.08	0.38	0.65
	SnCl ₂ (post-)	72.15	-1.02	0.35	0.55
	Non - mordant	75.66	-3.13	8.83	0.55

Table 4 reveals that mordanting for cotton fabrics relatively increases color strength, especially in the case of CuSO₄ mordanted fabrics.

The color strength (K/S) of cotton samples decreased in the following order: CuSO₄ > FeSO₄ > SnCl₂ > K₂Cr₂O₇ > alum

Table 5 reveals that mordanting for wool yarn relatively increases color strength, especially in fabrics mordanted with CuSO₄. Dyeing performances of wool fabrics increase especially depending on color strength (K/S) values as follows: CuSO₄ > FeSO₄ > K₂Cr₂O₇ > SnCl₂ > alum

According to Table 6, mordanting relatively increased the color strength, especially in the case of polyester fabrics mordanted with FeSO₄ mordanting.

Dyeing performances of polyester fabrics increase especially depending on color strength (K/S) values as follows: CuSO₄ > FeSO₄ > K₂Cr₂O₇ > alum > SnCl₂

The highest K/S values for cotton, wool and polyester fabrics are given in Figure 3.

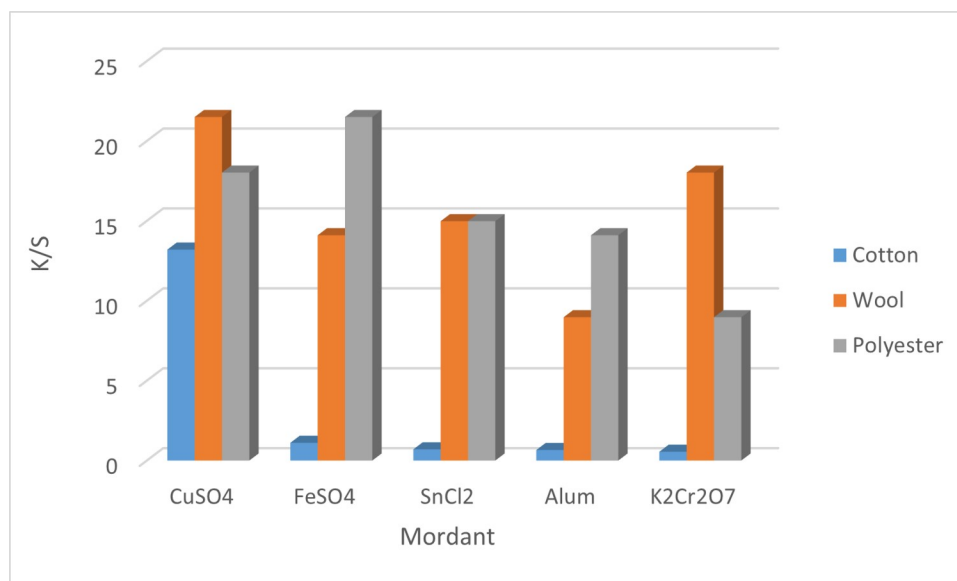


Figure 3: The highest K/S values for cotton, wool and polyester fabrics.

Figure 3 shows the highest K/S values for dyed cotton fabrics. While the highest value in the chart is 13.20, obtained in pre-mordanting with CuSO₄ mordant, these values are 1.11 in meta-mordanting with FeSO₄, 0.70 in pre-mordanting with SnCl₂, 0.66 for alum, 0.66 for K₂Cr₂O₇. Figure 3 shows the highest K/S value for dyed wool yarns. While the highest value of 21.50 was obtained in pre-mordanting with CuSO₄ mordant, these values were 18.02 in pre-mordanting with K₂Cr₂O₇, 14.98 in co-mordanting with SnCl₂, 14.10 in meta-mordanting for FeSO₄, and 8.97 in pre-mordanting for alum. Figure 3 shows the highest K/S value for dyed polyester fabrics. While the highest value of 1.11 was obtained in mordanting with FeSO₄ mordant, these values were 0.86 in pre-mordanting for CuSO₄, 0.65 in pre-mordanting with SnCl₂, 0.61 in pre-mordanting for alum, and 0.51 in pre-mordanting for K₂Cr₂O₇.

When the K/S values of cotton fabric, wool yarn and polyester fabrics are compared, the following order is given:

wool yarn > cotton fabric > polyester fabric

When compared in terms of K/S values, it is understood that the meta mordanting method is more effective than the pre- and post-mordanting method.

Samples of cotton fabrics, wool yarn, and polyester fabrics dyed with *Parthenocissus quinquefolia* L. fruit extract are shown in Figure 4.

3.2. Proposed Dyeing Mechanism

Mordant means fixative. It ensures better binding of the dye to the fiber or fabric and also increases the fastness of the dyed fiber. As mentioned before, copper sulfate, iron sulfate, alum, tin chloride, and potassium dichromate were used as mordant in this study. According to the results, it is clear that the best colorations are achieved by meta- and post-mordanting with FeSO₄, which can be explained by its good binding ability with anthocyanins and functional groups of fibers. Additionally, ferrous sulfate has the capacity to form coordination complexes and easily chelate with the dye molecule. From a mechanistic perspective and considering the length of the bonds, only Cyanidin, which has hydroxyl groups in the ortho position on the ring, is capable of chelating with the iron atom. As a result, the structure of the dye-mordant complex with Cyanidin and FeSO₄ is proposed in Figure 5. Since ferrous sulfate coordination numbers are equal to 6, some coordination sites will remain vacant during their interaction. Functional groups of the fibers can then occupy these regions. In this way, the metal can form a ternary complex in which one region binds to the fiber and the other region binds to the dye. The wool yarn dyeing mechanism is given in

Figure 3, the cotton fabric dyeing mechanism is given in Figure 6, and the polyester fabric dyeing mechanism is given in Figure 7. Mordant means fixative. It provides better bonding of the dyestuff to the fiber or fabric, and also increases the fastness of

dyed fiber. As mentioned before, in this study, copper sulfate, ferrous sulfate, alum, stannous chloride and potassium dichromate were used as mordant.



Figure 4: Samples of cotton, wool yarn and polyester fabric dyed with *Parthenocissus quinquefolia* L. fruit extract.

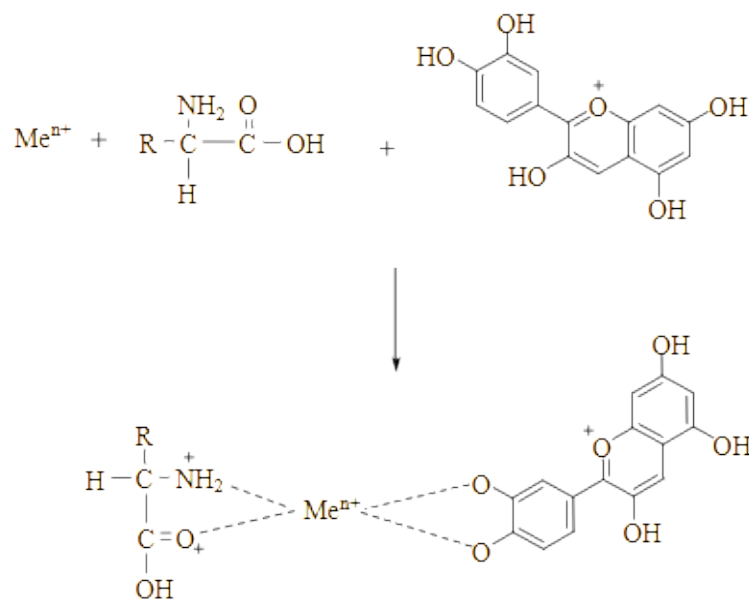


Figure 5: The proposed dyeing mechanism of wool yarn with cyanidine (Meⁿ⁺ : mordant cation).

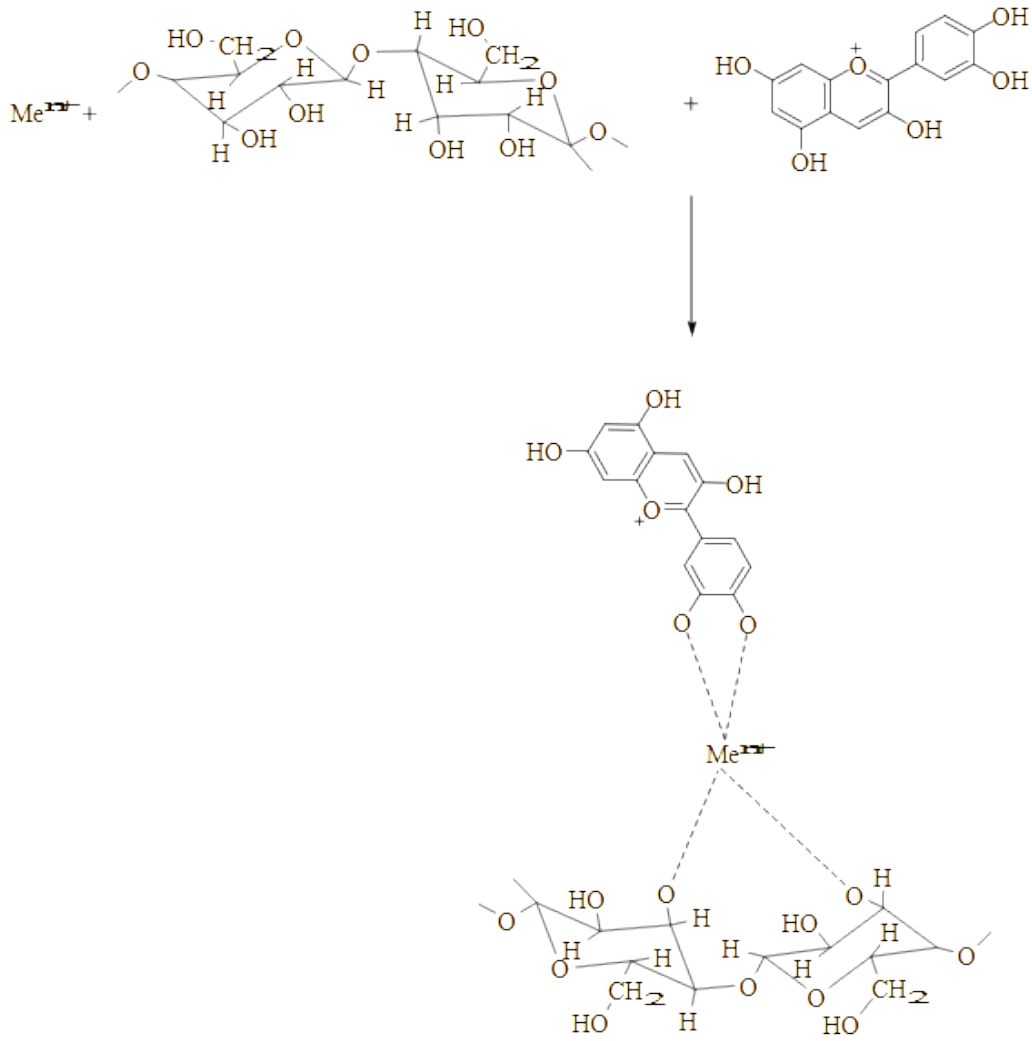


Figure 6: The proposed dyeing mechanism of cotton fabric with cyanidine (Me^{n+} : mordant cation).

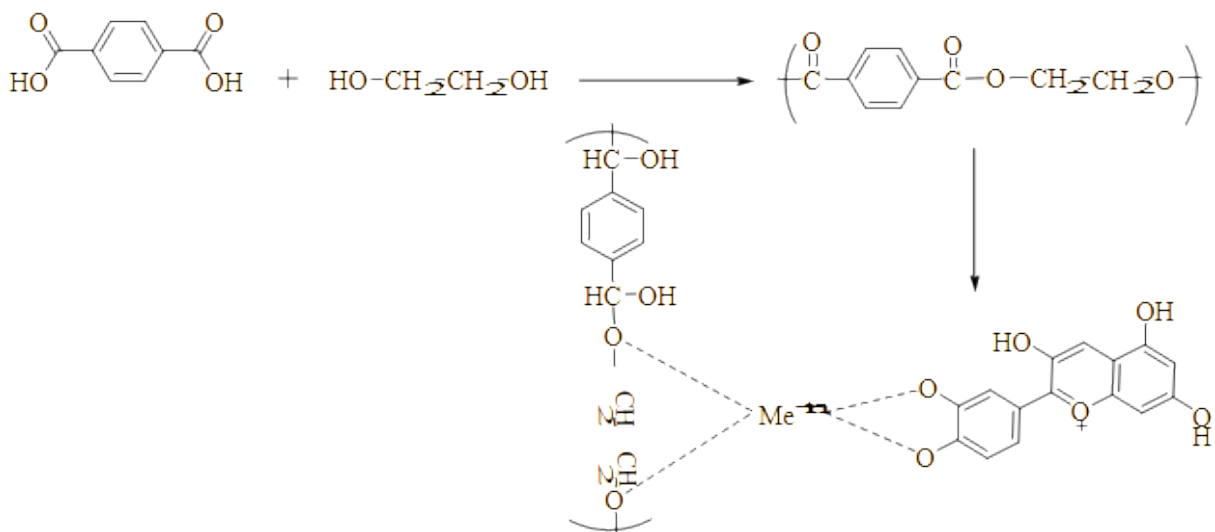


Figure 7: The proposed dyeing mechanism of cotton fabric with cyanidine (Me^{n+} : mordant cation).

4. CONCLUSION

In this study, the extract of fresh fruits of *Parthenocissus quinquefolia* L. was used in dyeing cotton fabric, wool yarn, and polyester fabric. The washing, dry and wet rubbing fastness of the dyed samples gave good results. Light fastness is medium to below average. With the use of mordant, the fastness properties of cotton, wool, and polyester fabrics are improved. Considering that natural dyes generally have poor fastness, it can be stated that the solidity properties of various dyed samples in this study can be considered good. However, although polyester fabrics are dyed at 130 °C in the industrial process, they can also be dyed below 100 °C. This result will also save energy and provide a significant advantage in dyeing synthetic materials. When all the results obtained are evaluated, it is clearly seen that *Parthenocissus quinquefolia* L. fresh fruits can be used in biomelecular wool yarn, cotton fabric and polyester fabric dyeing.

5. CONFLICT OF INTEREST

The authors declare no conflict of interest.

6. REFERENCES

- Abd El Aty, A. A., El-Bassyouni, G. T., Abdel-Zaher, N. A., & Guirguis, O. W. (2018). Experimental study on antimicrobial activity of silk fabric treated with natural dye extract from neem (*Azadirachta indica*) leaves. *Fibers and Polymers*, 19, 1880-1886.
- Adeel, S., Zia, K. M., Azeem, M., Kiran, S., Zuber, M., Irfan, M., & Qayyum, M. A. (2019). Microwave-supported green dyeing of mordanted wool fabric with arjun bark extracts. *Journal of Natural Fibers*, 18, 136-150.
- Adeel, S., Ali, S., Bhatti, I. A., & Zsila, F. (2009). Dyeing of cotton fabric using pomegranate (*Punica granatum*) aqueous extract. *Asian Journal of Chemistry*, 21(5), 3493.
- Banat, I. M., Nigam, P., Singh, D., & Marchant, R. (1996). Microbial decolorization of textile-dyecontaining effluents: a review. *Bioresource technology*, 58(3), 217-227.
- Baaka, N. (2022). Sustainable dyeing of wool fabric using kermes oak (*Quercus Coccifera* L) as source of natural colorant. *Journal of Natural Fibers*, 19(1), 37-45.
- Bechtold, T., Turcanu, A., Ganglberger, E., & Geissler, S. (2003). Natural dyes in modern textile dyehouses—how to combine experiences of two centuries to meet the demands of the future?. *Journal of Cleaner Production*, 11(5), 499-509.
- Benli, H. (2019). Amerikan sarmaşığı (*Parthenocissus quinquefolia* L.) bitkisinin yünü boyama özelliklerinin araştırılması. *Tekstil ve Mühendis*, 24(106), 54-61.
- Bukhari, M. N., Shabbir, M., Rather, L. J., Shahid, M., Singh, U., Khan, M. A., & Mohammad, F. (2017). Dyeing studies and fastness properties of brown naphthoquinone colorant extracted from *Juglans regia* L on natural protein fiber using different metal salt mordants. *Textiles and Clothing Sustainability*, 3, 1-9.
- Chiou, M. S., & Li, H. Y. (2002). Equilibrium and kinetic modeling of adsorption of reactive dye on cross-linked chitosan beads. *Journal of hazardous materials*, 93(2), 233-248.
- Cooper, P. (1995). Color in Dye House Effluent. *Bradford. Society of dyers and colorists*. 1, 10-15.
- Çolak, S., Kaygusuz, M., & Arğun, F. N. (2020). Dyeing of Wool Yarns with *Parthenocissus quinquefolia* L. Leaves Extract. In " *Theory and Research in Engineering*", Ed. A. Hayaloğlu, Gece kitablığı, Ankara.
- Džimbeg-Malčić, V., Barbarić-Mikočević, Ž., & Itrić, K. (2011). Kubelka-Munk theory in describing optical properties of paper (I). *Tehnički vjesnik*, 18(1), 117-124.
- Forgacs, E., Cserhádi, T., & Oros, G. (2004). Removal of synthetic dyes from wastewaters: a review. *Environment international*, 30(7), 953-971.
- Önal, A., Özbek, O., Tombul, K. C., & Nached, S. (2021). Investigation of the dyeing properties of cotton fabrics and wool yarns using *Prunus persica* leaf extract. *Journal of the Indian Chemical Society*, 98(7), 100092.
- Önal, A., Özbek, O., Düzgün, P., & Nached, S. Eco-friendly dyeing of fabric and wool yarn samples with *Morus nigra* leaf extracts. *Journal of the Turkish Chemical Society Section A: Chemistry*, 10(3), 819-826.
- Sharma, C. M., & Khanduri, V. P. (2007). Vegetative and reproductive phenophases in *Aesculus indica* Colebr. at two different altitudes in Himalayan forests. *Current Science*, 216-225.
- Rather, L. J., Shahid, M., Khan, M. A., & Mohammad, F. (2014). Study the effect of ammonia post-treatment on color characteristics of annatto-dyed textile substrate using reflectance spectrophotometry. *Industrial Crops and Products*, 59, 337-342.
- Robinson, T., McMullan, G., Marchant, R., & Nigam, P. (2001). Remediation of dyes in textile effluent: a critical review on current treatment technologies with a proposed alternative. *Bioresource technology*, 77(3), 247-255.
- Ticha, M. B., Meksi, N., Attia, H. E., Haddar, W., Guesmi, A., Jannet, H. B., & Mhenni, M. F. (2017). Ultrasonic extraction of *Parthenocissus quinquefolia* colorants: Extract identification by HPLC-MS analysis and cleaner application on the phytodyeing of natural fibres. *Dyes and Pigments*, 141, 103-111.
- Zhou, Y., Zhang, J., Tang, R. C., & Zhang, J. (2015). Simultaneous dyeing and functionalization of silk with three natural yellow dyes. *Industrial crops and products*, 64, 224-232.



Synthesis and Characterization of CL-PA Ionic Liquid

Ali Tuğrul Albayrak* 

*Istanbul University-Cerrahpaşa, Faculty of Engineering, Department of Chemical Engineering, Istanbul, Avcılar, 34320, Türkiye

Abstract: Caprolactam is most commonly used in the production of Nylon 6 in industry and is generally produced from cyclohexanone by the Beckmann rearrangement. Orthophosphoric acid is generally used in fertilizer production and is produced through two processes: wet and dry. In this study, detailed characterization of CL-PA was carried out by synthesizing CL-PA ionic liquid from orthophosphoric acid (PA) and caprolactam (CL). FTIR, Raman and UV-Vis spectroscopic analyses reveal that a bond is formed between CL and PA. The thermal behavior of CL-PA ionic liquid was inspected by TGA and DSC. It has been observed that the decomposition temperature of CL-PA ionic liquid is different from that of the starting materials (CL and PA). It was disclosed by DSC analysis that CL-PA ionic liquid only has a glass transition temperature. The room-temperature CL-PA ionic liquid synthesized from solid CL with melting point of 70.34 °C and 85 wt.% PA did not show any melting or freezing point and the glass transition temperature was found to be -27 °C. It was revealed that CL-PA ionic liquid was more thermally stable than CL which alone almost completely evaporated at about 197 °C. As a result of FTIR analysis of CL-PA ionic liquid and its constituents, it was demonstrated that -NH peaks of CL disappeared in the CL-PA spectrum and the peak of C=O group shifted to a lower frequency (i.e., 1604 cm⁻¹). In the Raman analysis of CL-PA and its constituents, it was observed that the asymmetric C=O bending vibration and C=O stretching vibration of CL disappeared in the CL-PA spectrum. In the UV spectrum, it was observed that the maximum absorbance of CL-PA ionic liquid varied with respect to that of CL.

Keywords: Ionic Liquid, Deep Eutectic Solvent, TGA, Glass Transition Temperature.

Submitted: April 26, 2024. **Accepted:** August 1, 2024.

Cite this: Albayrak, A. T. (2024). Synthesis and Characterization of CL-PA Ionic Liquid. *Journal of the Turkish Chemical Society, Section B: Chemical Engineering*, 7(2), 167–176.
<https://doi.org/10.58692/jotcsb.1473115>

*Corresponding author. E-mail: albayrak@iuc.edu.tr

1. INTRODUCTION

ϵ -Caprolactam is a water-soluble lactam (Kalinová et al., 2016) with a molecular formula of C₆H₁₁NO (Cherkasova et al., 2009) and a melting point of 69 °C (Kabo et al., 1992). Caprolactam is produced mostly from cyclohexanone by using NH₂OH and then H₂SO₄ (Beckmann Rearrangement) (McGraw-Hill Concise Encyclopedia of Science & Technology, 2005). However, the Beckmann rearrangement has disadvantages such as corrosion of the reactor by sulfuric acid and the formation of large amounts of ammonium sulfate as waste product (You et al., 2008). Therefore, alternative methods for the Beckmann Rearrangement have been proposed. In a study (S. Sun et al., 2022) in which the deep eutectic solvent Choline Chloride-Trifluoromethanesulphonic Acid [ChCl][TfOH]₃ was synthesized as catalyst and reaction medium, ϵ -caprolactam was obtained with

98.8% yield and 100% conversion of cyclohexanone oxime at the end of a 2-hour Beckmann rearrangement at 100 °C in the presence of [ChCl][TfOH]₃ and it has been reported that the [ChCl][TfOH]₃ recovered after the reaction can be reused consecutive seven times without significantly losing its activity (the caprolactam yield obtained after the 7th reuse is up to 98%). In another study (Ren et al., 2023), Bronsted acidic caprolactam-methanesulfonic acid [CPL][2MSA] ionic liquid was synthesized as a catalyst, and as a result of a 2-hour liquid phase Beckmann rearrangement at 90 °C, caprolactam was obtained with 100% conversion and 95% selectivity and it has been reported that under optimal conditions, [CPL][2MSA] can be reused ten times for CL synthesis. A review on the use of zeolite catalysts for the environmentally friendly manufacturing process of CL has also been published (H. Wang et al., 2023). Caprolactam is generally used in the production of Nylon 6 (Mather & Wardman,

2015). The previously mentioned and other CL synthesis methods, including their advantages and disadvantages, are briefly summarized in Table 1. As can be seen from the table, in addition to the importance of high conversion and high selectivity for the reaction, low temperatures and low pressures are particularly more favorable in terms of cost.

Orthophosphoric acid is usually available as 85 wt.% viscous aqueous solutions (House, 2020). Orthophosphoric acid has three different pK_a values ($pK_{a1} = 2.15$, $pK_{a2} = 7.21$ and $pK_{a3} = 12.36$) in water (Lange & Speight, 2005). Pure orthophosphoric acid is an inorganic acid with a melting point of 42.35 °C (Ashurst, 2016). H_3PO_4 is produced by two methods: wet process (Benvenuto & Plaumann, 2021), which involves the reaction of phosphate-containing

minerals with sulfuric acid, and dry process (L. K. Wang, 2006), which involves the reaction of diphosphorus pentoxide with water. Orthophosphoric acid is generally used in fertilizer production (Gilmour, 2014). Biochars are chemically activated with orthophosphoric acid to increase their adsorption capacity (Chu et al., 2018). In a study (Chen et al., 2019) in which biochar prepared using chicken feathers was activated with orthophosphoric acid, it was reported that the adsorption of Cd^{2+} and Pb^{2+} ions was further increased by orthophosphoric acid-modified biochar. There are also other applications of orthophosphoric acid, such as the use of orthophosphoric acid in fuel cells (Q. Sun et al., 2021).

Table 1: Some synthesis methods of caprolactam.

Materials	Reaction Conditions	Advantages	Disadvantages	Reference
Cyclohexanone Oxime, [ChCl][TfOH] ₃ as DES	100 °C, 2 hours	Reusability of DES, low reaction time, easy recovery of DES, high CL yield (98.8%), 100% conversion of cyclohexanone oxime, No (NH ₄) ₂ SO ₄		(S. Sun et al., 2022)
Cyclohexanone Oxime, [CPL][2MSA] as Ionic Liquid	90 °C, 2 hours	High conversion (100%) and high CL selectivity (95%), Reusability of Ionic Liquid, No (NH ₄) ₂ SO ₄ , environmentally friendly ionic liquid catalyst		(Ren et al., 2023)
Cyclohexanone Oxime, MFI zeolite catalyst	280 – 400 °C	High CL conversion, high CL selectivity, no (NH ₄) ₂ SO ₄	High temperature, catalyst requirement with high thermal stability	(Ichihashi et al., 2003; W.-C. Li et al., 2005)
Aqueous solution of cyclohexanone oxime, Supercritical Water	673 K and 40 MPa	CL yield > 80% CL selectivity of 100% No (NH ₄) ₂ SO ₄	High temperature and high pressure	(Sato et al., 2005)
SNIA viscosa Process, toluene as starting materials, air, hydrogen, nitrosyl sulfuric acid in the presence of oleum	The first step: Co catalyst, 160-170 °C, 8–10 bar The second step: Pd-on-graphite catalyst, 170 °C, 10–17 bar The third step: 80 °C	72% CL yield 90% CL selectivity ammonium sulfate-free synthesis	High temperature and high pressure in the first two consecutive steps	(Maxwell, 2005)

In addition to the application areas of orthophosphoric acid and caprolactam on their own, they have also been used in the preparation of deep eutectic solvents and ionic liquids. Deep eutectic solvents, consisting of a hydrogen bond donor and a

hydrogen bond acceptor, and ionic liquids, composed of an organic cation and an inorganic or organic anion (Płotka-Wasyłka et al., 2020), have many advantages (Bajpai, 2021) such as low volatility, wide liquid range, high thermal stability and the

capacity to dissolve inorganic and organic substances.

CL-based ionic liquids have been used in the removal of H₂S (Guo et al., 2011), absorption of SO₂ (Liu et al., 2013), oxidative desulfurization (Yang et al., 2016), and lipid recovery from microalgae (Naiyl et al., 2022). CL-based deep eutectic solvents have applications such as oxidative desulfurization of diesel fuel (Hao et al., 2018), natural gas desulfurization (Karibayev & Shah, 2020), extractive desulfurization of diesel fuel (L. Xu et al., 2022), use as electrolyte in energy storage systems (S. Wang et al., 2024; C. Xu et al., 2019), and isolation and recovery of valuable metals such as lithium and cobalt from waste lithium-ion batteries (Cao et al., 2023). Besides, in a study (Celik et al., 2021) in which caprolactam-glycine was synthesized, it was

2. EXPERIMENTAL SECTION

2.1. Materials

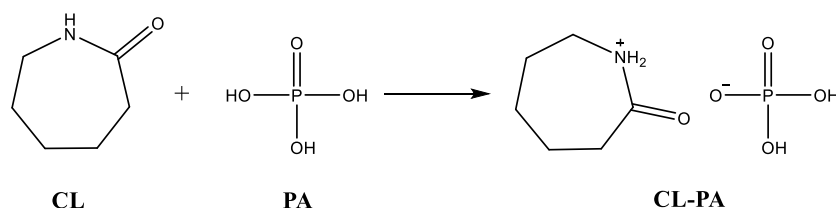
85 wt.% orthophosphoric acid aqueous solution from Balmumcu Kimya, 99 wt.% caprolactam and ≥ 99 wt.% dichloromethane (as solvent) from Sigma-Aldrich were provided.

2.2. Synthesis

0.25 mol of caprolactam was placed in a 250-mL conical flask and dissolved in 50 mL of

dichloromethane. 0.25 mol of orthophosphoric acid was added dropwise to the caprolactam solution in the flask immersed in a salt water bath below 0 °C and stirring was continued for 30 min below 0 °C. Then, stirring was carried out at room temperature for 24 h. Dichloromethane and water were removed from the ionic liquid at 60 °C and 40 mbar under vacuum using a rotary evaporator. A transparent and colorless viscous ionic liquid was obtained at room temperature. The synthesis reaction of CL-PA is shown in Scheme 1.

In this study, CL-PA ionic liquid was synthesized and its characterization was inspected in detail.



Scheme 1. Synthesis of CL-PA ionic liquid.

3. RESULTS AND DISCUSSION

3.1. DSC (Differential Scanning Calorimetry) Analysis

Thermal analysis was performed by Mettler Toledo DSC 3+. To observe the thermal behavior, CL-PA ionic liquid was cooled from 150 to -100 °C at a rate of 10 °C/min under nitrogen flow and then heated from -100 to 150 °C at the same rate. As a result of the DSC analysis, as seen in Figure 1, no freezing point was observed in the ionic liquid and the glass transition temperature from the heating cycle was determined as -27 °C.

Thermal analysis of CL was performed by TA Instruments DSC250. CL was first heated from 20 to 150 °C at a rate of 5 °C/min under nitrogen flow, and then cooled from 150 to 0 °C at the same rate. As seen in Figure 2, the melting point taken as the peak temperature on the heating cycle was determined as

70.34 °C, and 41.44 °C, taken as the peak temperature on the cooling cycle, was possibly considered the crystallization temperature.

3.2. TGA (Thermogravimetric Analysis)

Thermogravimetric analysis of CL-PA ionic liquid and CL was performed by Mettler Toledo DSC 3+. The ionic liquid was heated from 25 to 700 °C at a rate of 10 °C/min under nitrogen atmosphere. In Figure 3, in the first region up to 163 °C, the remaining water in CL-PA ionic liquid completely evaporated and CL also started to separate from the ionic liquid (Fang et al., 2018). In the second region between 163-217 °C, CL was completely separated and orthophosphoric acid began to decompose into pyrophosphoric acid (Yankova & Tankov, 2021). In the third region at 217-420 °C, thermal degradation of orthophosphoric acid to pyrophosphoric acid is completed.

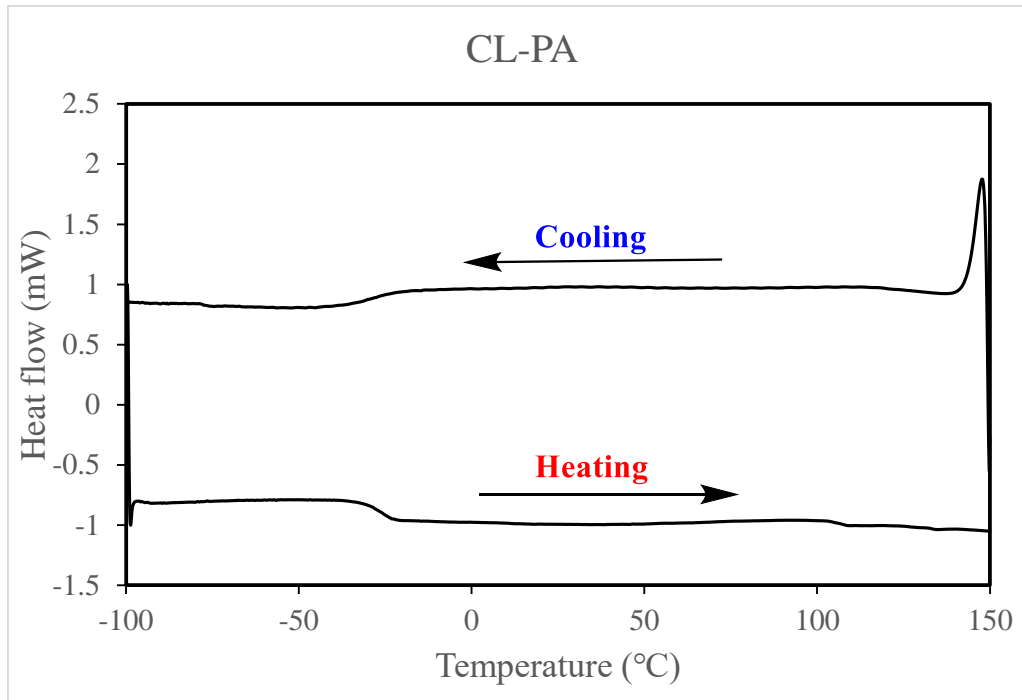


Figure 1. DSC thermal analysis of CL-PA ionic liquid.

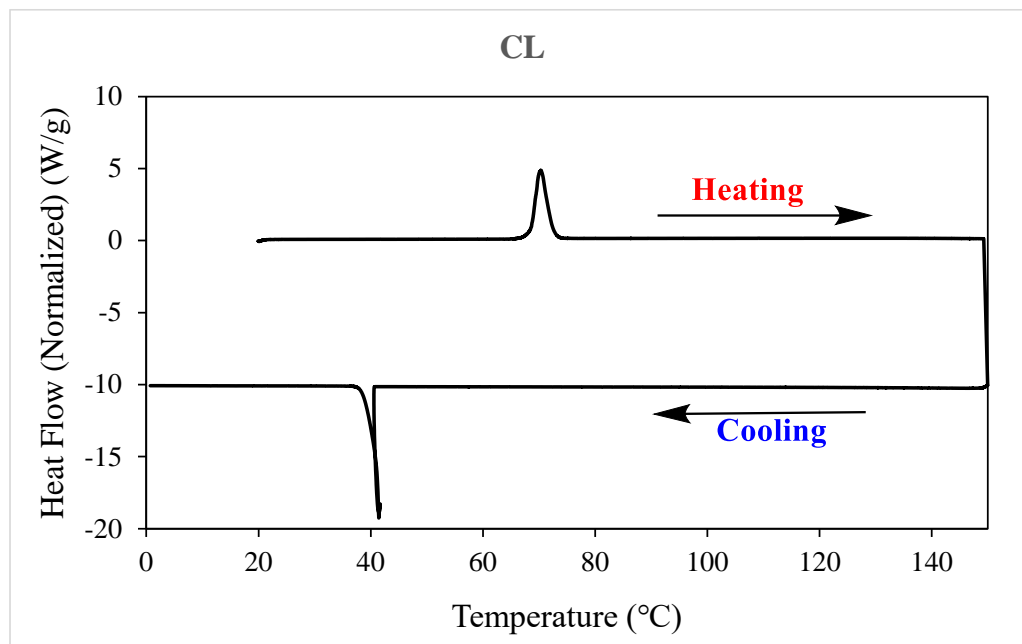


Figure 2. DSC thermal analysis of CL.

3.3. FTIR (Fourier Transform Infrared) Analysis

FTIR analysis of CL-PA ionic liquid was carried out by JASCO FT/IR-4700 in the range of $4000\text{--}400\text{ cm}^{-1}$. The resolution and the number of scans as FTIR operating parameters is 4 cm^{-1} and 16, respectively. When the spectrum of 85 wt% orthophosphoric acid aqueous solution is examined in Figure 4, the peaks at 2777 , 1635 , 1111 , 952 and 875 cm^{-1} are assigned to the intermolecular hydrogen bonding interaction of H_3PO_4 , the bending vibration of the --OH bond, the stretching vibration of P=O bond, the asymmetric

stretching vibration of P--OH bond, and the symmetric stretching vibration of P--OH bond, respectively (Wei et al., 2020). The peak at 3550 cm^{-1} indicates the presence of water (Malek & Chong, 2000). In the CL spectrum, the peaks at 3295 , 3194 and 3070 cm^{-1} belong to the --NH group, while the peak at 1652 cm^{-1} belongs to the C=O group (Zhou et al., 2020). It can be seen from the spectrum of CL-PA ionic liquid that the --NH group peaks of CL disappeared and the carbonyl peak of CL at 1652 cm^{-1} shifted to a lower frequency, that is, 1604 cm^{-1} , due to the bonding of a hydrogen of PA to the

nitrogen in CL (Naiyl et al., 2021). In the ionic liquid structure, the characteristic peaks of PA appear to be preserved.

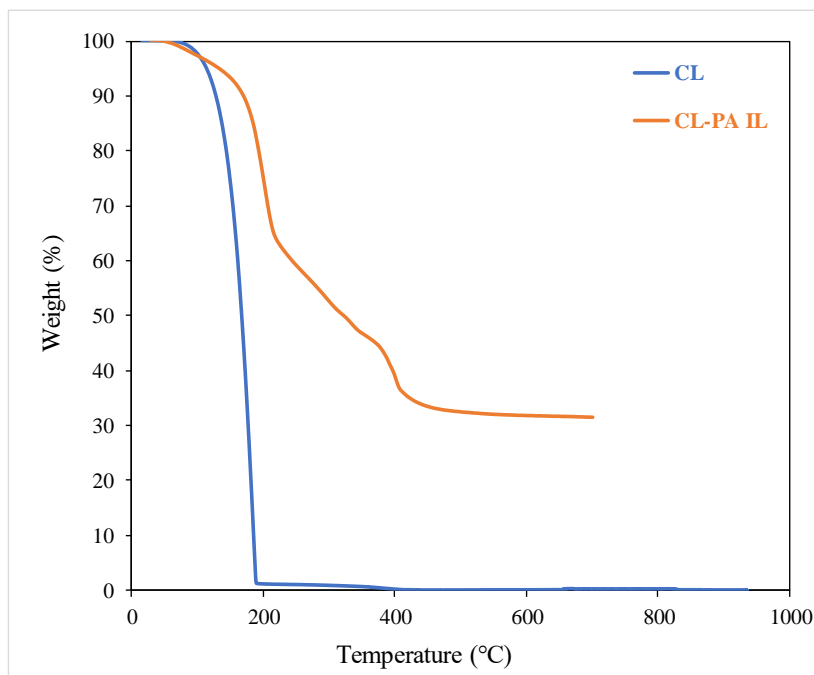


Figure 3. Thermal stability of CL-PA ionic liquid and CL.

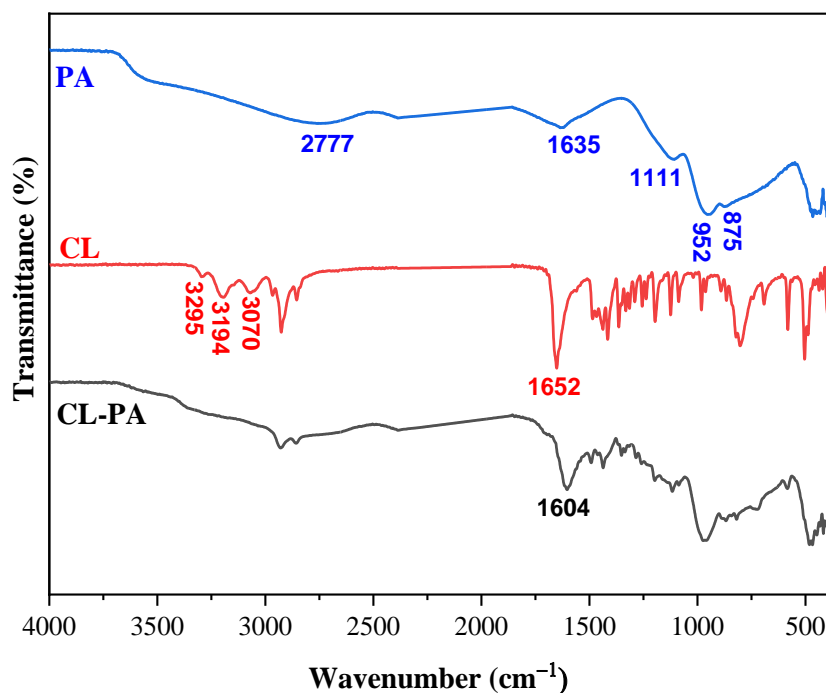


Figure 4. FTIR spectrum of PA, CL and CL-PA ionic liquid.

3.4. Raman Analysis

Raman analysis of CL-PA ionic liquid was carried out using a Renishaw In Via Qontor model spectrometer in the range of 4000-100 cm^{-1} . In Figure 5, in the PA spectrum, the sharp and strong band at 913 cm^{-1} (P=O) and the weak and broad bands at 354 and 491 cm^{-1} are the characteristic bands belonging to concentrated orthophosphoric acid (J. Li et al., 2011). The weak band at 1312 cm^{-1} belongs to the

phosphoryl group (stretching vibration of P=O) (Cheremisina et al., 2015; Larkin, 2011) and the band at 1603 cm^{-1} belongs to the H-OH bending vibration, indicating the presence of water (Frost et al., 2013). In the CL spectrum, the bands at 584, 701, 1495 and 1641 cm^{-1} are assigned to the asymmetric C=O bending vibration, N-H stretching vibration, C-N stretching vibration and C=O stretching vibration, respectively (Naiyl et al., 2021).

When the spectrum of CL-PA ionic liquid was examined, the wavenumbers and the peak intensities (consequently, peak areas) of the relevant peaks belonging to 85% PA solution and CL changed. In addition, the bands at 584 and 1641 cm^{-1} belonging

to CL do not appear in CL-PA ionic liquid. All these changes are an indication of the formation of a bond between CL and PA.

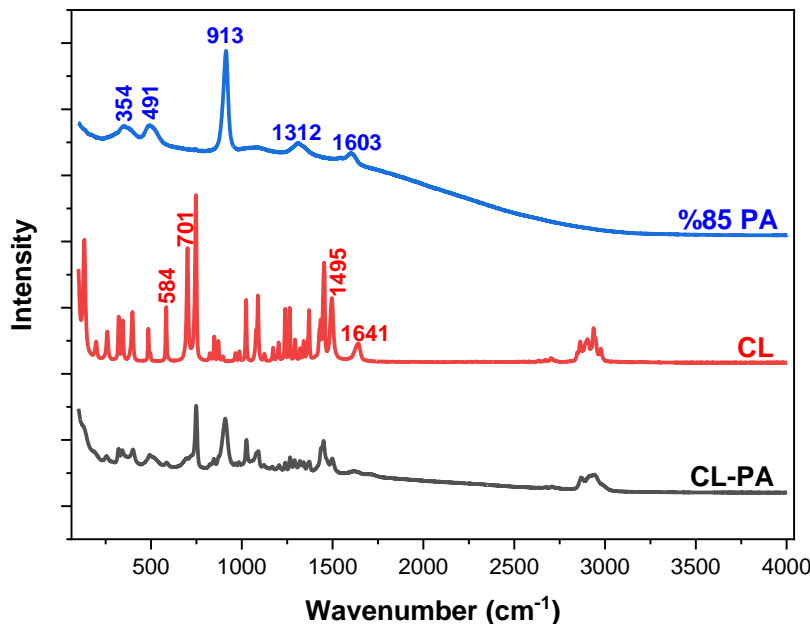


Figure 5. Raman spectrum of PA, CL and CL-PA ionic liquid.

3.5. UV-Vis Spectroscopy

UV-Vis spectra of CL-PA ionic liquid and CL were obtained in the wavelength range of 190-1100 nm using deuterium and tungsten lamps by Perkin-Elmer Lambda 35 UV-Vis spectrophotometer. For UV-Vis spectrum, CL and CL-PA were dissolved in water to

be 0.5 mM. As shown in Figure 6, CL gave a maximum absorbance at 200 nm. In the spectrum of CL-PA ionic liquid, the maximum absorbance of CL at 200 nm shifted to a shorter wavelength (197 nm) due to the decrease in the electron density of the CL molecule.

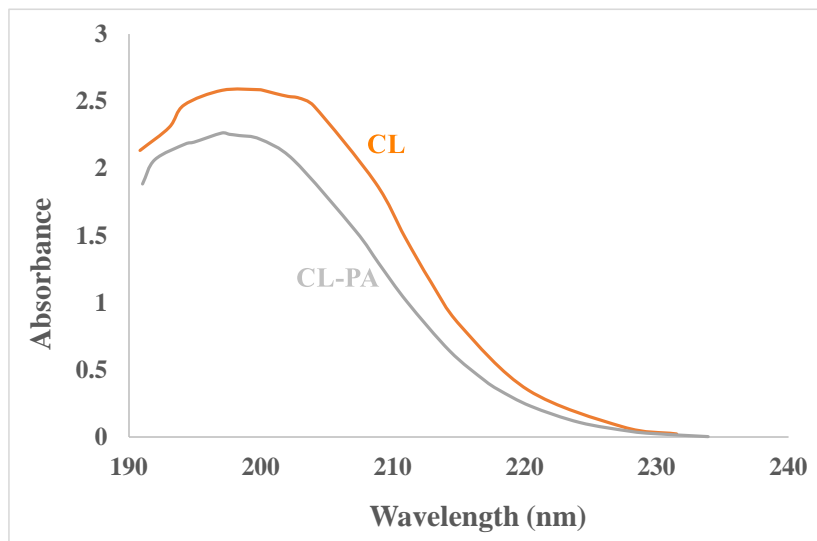


Figure 6. UV-Vis spectrum of CL-PA ionic liquid and CL.

4. OUTLOOK

Protic ionic liquids are formed by a neutralization reaction between acid and base through proton transfer (Shiflett, 2020) and therefore CL-PA is a protic ionic liquid. This water-soluble ionic liquid can

be used in the removal of sulfur from fuels and the absorption of acidic flue gases. Particularly in heterogeneous reactions, mass transfer is important for reaction conversion and high viscosity at relatively low temperatures can cause trouble. For this reason, accelerating mass transfer by increasing

the reaction temperature may favor the reaction conversion. On the other hand, when increasing the temperature, it is necessary to consider the decomposition temperature of the reactants and whether the reaction is exothermic or endothermic. The reusability of the ionic liquid after reactions is also of great importance in terms of cost. It should be evaluated how many times the ionic liquid can be reused in reactions without losing its effectiveness. Moreover, ionic liquid should not dissolve in the other phase, thus leading to loss of ionic liquid. The protic ionic liquid to be used should be stored in tightly closed, leak-proof containers as it may be sensitive to air and moisture. Ionic liquid can also be used as an antimicrobial agent, but its toxic effect must be evaluated. Besides, ionic liquids with high biodegradability and low toxicity can be preferred to minimize waste from an environmental perspective. Protic ionic liquids (PILs) can be used in four main applications (Bailey et al., 2024): Catalytic transformations (due to their ability to act as solvents and catalysts and their easy separation after reactions), biomass processing (due to their power to fractionate and dissolve biomass), energy storage and conversion (due to their negligible volatility unlike that of organic solvents, high thermal stability, and high ionic conductivity), and electrocatalysis (due to the efficient modulation of electrochemical reactivity of PIL electrolytes by changing anion and cation of PIL). CL-PA ionic liquid may have the potential to be used in the above-mentioned applications of protic ionic liquids. Based on its thermal stability, it may be used as catalyst in reactions, a thermal transfer fluid, and an electrolyte in fuel cells, at temperatures below about 163 °C.

5. CONCLUSION

It was observed that the synthesized CL-PA ionic liquid was stable in liquid state at room temperature, and the glass transition temperature was determined to be -27 °C from DSC analysis. Additionally, it was revealed that the thermal decomposition of protic ionic liquid CL-PA occurred in three stages. Therefore, CL-PA ionic liquid has different physicochemical properties from the starting materials CL and PA. To prove the formation of ionic liquid, UV-Vis, Raman and FTIR analyzes were performed. The three spectroscopic analyses demonstrate that a bond was formed between CL and PA according to the inspected spectra. The synthesized CL-PA protic ionic liquid may have many potential applications, such as recovery of valuable metals from waste batteries, use as electrolyte and catalyst in reactions and use as an extractant.

6. CONFLICT OF INTEREST

There is no conflict of interest to declare.

7. REFERENCES

- Ashurst, P. R. (Ed.). (2016). *Chemistry and Technology of Soft Drinks and Fruit Juices*. Wiley.
<https://doi.org/10.1002/9781118634943>
- Bailey, J., Byrne, E. L., Goodrich, P., Kavanagh, P. and Swadźba-Kwaśny, M. (2024). Protic ionic liquids for sustainable uses. *Green Chem.*, 26(3), 1092–1131.
<https://doi.org/10.1039/D3GC03297C>
- Bajpai, P. (2021). *Deep Eutectic Solvents for Pretreatment of Lignocellulosic Biomass*. Springer Singapore.
<https://doi.org/10.1007/978-981-16-4013-1>
- Cao, S., Ma, Y., Yang, L., Lin, L., Wang, J., Xing, Y., Lu, F., Cao, T., Zhao, Z. and Liu, D. (2023). Designing Low-Cost, Green, and Recyclable Deep Eutectic Solvents for Selective Separation and Recovery of Valuable Metals from Spent Li-Ion Batteries. *ACS Sustain. Chem. Eng.*, 11(48), 16984–16994.
<https://doi.org/10.1021/acssuschemeng.3c04802>
- Celik, S., Albayrak, A. T., Akyuz, S., Ozel, A. E. and Sigirci, B. D. (2021). Synthesis, antimicrobial activity, molecular docking and ADMET study of a caprolactam-glycine cluster. *J Biomol. Struct. Dyn.*, 39(7), 2376–2386.
<https://doi.org/10.1080/07391102.2020.1748112>
- Chen, H., Li, W., Wang, J., Xu, H., Liu, Y., Zhang, Z., Li, Y. and Zhang, Y. (2019). Adsorption of cadmium and lead ions by phosphoric acid-modified biochar generated from chicken feather: Selective adsorption and influence of dissolved organic matter. *Bioresour. Technol.*, 292.
<https://doi.org/10.1016/j.biortech.2019.121948>
- Cheremisina, O. V., Sergeev, V. V., Chirkst, D. E. and Litvinova, T. E. (2015). Thermodynamic investigation into extraction of cerium(III) by tributyl phosphate from phosphoric acid solutions. *Russ. J. Non-ferrous Metals*, 56(6), 615–621.
<https://doi.org/10.3103/S1067821215060036>
- Cherkasova, E. V., Patrakov, Y. F., Tryasunov, B. G., Cherkasova, T. G. and Tatarinova, E. S. (2009). Thermal analysis of rare-earth metal(III) hexa(isothiocyanato)chromate(III) complexes with ε-caprolactam. *Russ. J. Inorg. Chem.*, 54(10), 1625–1629. <https://doi.org/10.1134/S0036023609100192>
- Chu, G., Zhao, J., Huang, Y., Zhou, D., Liu, Y., Wu, M., Peng, H., Zhao, Q., Pan, B. and Steinberg, C. E. W. (2018). Phosphoric acid pretreatment enhances the specific surface areas of biochars by generation of micropores. *Environ. Pollut.*, 240, 1–9.
<https://doi.org/10.1016/j.envpol.2018.04.003>
- Fang, X., Wyatt, T., Shi, J. and Yao, D. (2018). Fabrication of high-strength polyoxymethylene fibers by gel spinning. *J. Mater. Sci.*, 53(16), 11901–11916.
<https://doi.org/10.1007/s10853-018-2410-5>
- Frost, R. L., Xi, Y., Scholz, R., Belotti, F. M. and Cândido Filho, M. (2013). Infrared and Raman spectroscopic characterization of the borate mineral colemanite – CaB₃O₄(OH)₃·H₂O – implications for the molecular structure. *J. Mol. Struct.*, 1037, 23–28.
<https://doi.org/10.1016/j.molstruc.2012.11.047>
- Gilmour, R. (2014). *Phosphoric Acid: Purification, Uses, Technology, and Economics*. CRC Press.
<https://doi.org/10.1201/b16187>
- Guo, B., Duan, E., Zhong, Y., Gao, L., Zhang, X. and Zhao, D. (2011). Absorption and oxidation of H₂S in caprolactam tetrabutyl ammonium bromide ionic liquid. *Energ. Fuel.*, 25(1), 159–161.
<https://doi.org/10.1021/ef1012006>

- Hao, L., Su, T., Hao, D., Deng, C., Ren, W. and Lü, H. (2018). Oxidative desulfurization of diesel fuel with caprolactam-based acidic deep eutectic solvents: Tailoring the reactivity of DESs by adjusting the composition. *Cuihua Xuebao/Chinese J. Catal.*, 39(9), 1552–1559. [https://doi.org/10.1016/S1872-2067\(18\)63091-8](https://doi.org/10.1016/S1872-2067(18)63091-8)
- House, J. E. (2020). *Inorganic chemistry*. Academic Press.
- Ichihashi, H., Ishida, M., Shiga, A., Kitamura, M., Suzuki, T., Suenobu, K. and Sugita, K. (2003). The Catalysis of Vapor-Phase Beckmann Rearrangement for the Production of ϵ -Caprolactam. *Catal. Surv. Asia*, 7(4), 261–270. <https://doi.org/10.1023/B:CATS.0000008165.80991.05>
- Kabo, G. J., Kozyro, A. A., Krouk, V. S., Sevruc, V. M., Yursha, I. A., Simirsky, V. V and Gogolinsky, V. I. (1992). Thermodynamic properties of 6-aminohexanoic lactam (ϵ -caprolactam). *J. Chem. Thermodyn.*, 24(1), 1-13. [https://doi.org/10.1016/S0021-9614\(05\)80249-6](https://doi.org/10.1016/S0021-9614(05)80249-6)
- Kalinová, J. P., Tříška, J., Vrchotová, N. and Novák, J. (2016). Uptake of caprolactam and its influence on growth and oxygen production of *Desmodesmus quadricauda* algae. *Environ. Pollut.*, 213, 518–523. <https://doi.org/10.1016/j.envpol.2016.03.024>
- Karibayev, M. and Shah, D. (2020). Comprehensive Computational Analysis Exploring the Formation of Caprolactam-Based Deep Eutectic Solvents and Their Applications in Natural Gas Desulfurization. *Energ. Fuel.*, 34(8), 9894–9902. <https://doi.org/10.1021/acs.energyfuels.0c01721>
- Lange, N. A. and Speight, J. G. (2005). *Lange's handbook of chemistry*. McGraw-Hill.
- Larkin, P. (2011). *Infrared and Raman Spectroscopy*. Elsevier. <https://doi.org/10.1016/C2010-0-68479-3>
- Li, J., Zhang, C. and Luo, J. (2011). Superlubricity behavior with phosphoric acid-water network induced by rubbing. *Langmuir*, 27(15), 9413–9417. <https://doi.org/10.1021/la201535x>
- Li, W.-C., Lu, A.-H., Palkovits, R., Schmidt, W., Spliethoff, B. and Schüth, F. (2005). Hierarchically Structured Monolithic Silicalite-1 Consisting of Crystallized Nanoparticles and Its Performance in the Beckmann Rearrangement of Cyclohexanone Oxime. *J. Am. Chem. Soc.*, 127(36), 12595–12600. <https://doi.org/10.1021/ja052693v>
- Liu, B., Zhao, J. and Wei, F. (2013). Characterization of caprolactam based eutectic ionic liquids and their application in SO₂ absorption. *J. Mol. Liq.*, 180, 19–25. <https://doi.org/10.1016/j.molliq.2012.12.024>
- Malek, M. A. and Chong, C. S. (2000). FTIR study of H₂O in polyallyl diglycol carbonate. *Vib. Spectrosc.*, 24, 181-184. [https://doi.org/10.1016/S0924-2031\(00\)00071-0](https://doi.org/10.1016/S0924-2031(00)00071-0)
- Benvenuto, M. A. and Plaumann, H. (2021). *Industrial Catalysis*. Walter de Gruyter GmbH, Berlin/Boston.
- Mather, R. R. and Wardman, R. H. (2015). *The chemistry of textile fibres*, 2nd Edition, The Royal Society of Chemistry. <https://doi.org/10.1039/9781782626534>
- Maxwell, G. R. (2005). *Synthetic Nitrogen Products*. Kluwer Academic Publishers. <https://doi.org/10.1007/b106641>
- McGraw-Hill Concise Encyclopedia of Science and Technology FIFTH EDITION. (2005). McGraw-Hill Companies, Inc.
- Naiyl, R. A., Kengara, F. O., Kiriamiti, K. H. and Ragab, Y. A. (2021). Synthesis and Characterization of Caprolactam- based Ionic Liquids as Green Solvents. *Asian J. Appl. Chem. Res.*, 74–87. <https://doi.org/10.9734/ajacr/2021/v8i430201>
- Naiyl, R. A., Kengara, F. O., Kiriamiti, K. H. and Ragab, Y. A. (2022). Lipid extraction from microalgae using pure caprolactam-based ionic liquids and with organic co-solvent. *PeerJ Anal. Chem.*, 4, e13. <https://doi.org/10.7717/peerj-achem.13>
- Plotka-Wasyłka, J., de la Guardia, M., Andruch, V. and Vilková, M. (2020). Deep eutectic solvents vs ionic liquids: Similarities and differences. *Microchem. J.*, 159, 105539. <https://doi.org/10.1016/j.microc.2020.105539>
- Ren, C., Wang, Z., Gao, Q., Li, J., Jiang, S., Huang, Q., Yang, Y., Zhang, J., Wang, Y., Hu, Y., Liu, Z. and Guo, X. (2023). Novel Brønsted Acidic Ionic Liquids as High Efficiency Catalysts for Liquid-Phase Beckmann Rearrangement. *Catalysts*, 13(6). <https://doi.org/10.3390/catal13060978>
- Sato, M., Ikushima, Y., Hatakeda, K. and Ikeshoji, T. (2005). Acceleration of Chemical Reactions Using a Supercritical Water Microreaction System. *Int. J. Chem. React. Eng.*, 3(1). <https://doi.org/10.2202/1542-6580.1294>
- Shiflett, M. B. (Ed.). (2020). *Commercial Applications of Ionic Liquids*. Springer International Publishing. <https://doi.org/10.1007/978-3-030-35245-5>
- Sun, Q., Lin, D., Khayatnezhad, M. and Taghavi, M. (2021). Investigation of phosphoric acid fuel cell, linear Fresnel solar reflector and Organic Rankine Cycle polygeneration energy system in different climatic conditions. *Process Saf. Environ.*, 147, 993–1008. <https://doi.org/10.1016/j.psep.2021.01.035>
- Sun, S., Liu, S., Yu, F., Zhang, J., Xing, W. and Yu, S. (2022). Reusable Deep Eutectic Solvents for Clean ϵ -Caprolactam Synthesis under Mild Conditions. *ACS Sustain. Chem. Eng.*, 10(4), 1675–1688. <https://doi.org/10.1021/acssuschemeng.1c07613>
- Wang, H., Qin, M., Wu, Q., Cheng, D. G., Meng, X., Wang, L. and Xiao, F. S. (2023). Zeolite Catalysts for Green Production of Caprolactam. *Ind. Eng. Chem. Res.*, 62(5), 2217–2224. <https://doi.org/10.1021/acs.iecr.2c01693>
- Wang, L. K. (2006). *Waste treatment in the process industries*. CRC/Taylor and Francis.
- Wang, S., Liu, G., Wan, W., Li, X., Li, J. and Wang, C. (2024). Acetamide-Caprolactam Deep Eutectic Solvent-Based Electrolyte for Stable Zn-Metal Batteries. *Adv. Mater.*, 36(5). <https://doi.org/10.1002/adma.202306546>
- Wei, H., Wang, T., Zhang, Q., Jiang, Y. and Mo, C. (2020). Study of composition and structure of aluminum phosphate binder. *J. Chin. Chem. Soc.*, 67(1), 116–124. <https://doi.org/10.1002/jccs.201900008>

- Xu, C., Zhang, W., Li, P., Zhao, S., Du, Y., Jin, H., Zhang, Y., Wang, Z. and Zhang, J. (2019). High-performance aluminum-ion batteries based on AlCl₃/caprolactam electrolytes. *Sustain. Energ. Fuels*, 4(1), 121–127. <https://doi.org/10.1039/c9se00941h>
- Xu, L., Yin, J., Luo, Y., Liu, H., Li, H., Zhu, L., He, J., Jiang, W., Zhu, W. and Li, H. (2022). Rational Design of Caprolactam-Based Deep Eutectic Solvents for Extractive Desulfurization of Diesel Fuel and Mechanism Study. *ACS Sustain. Chem. Eng.*, 10(14), 4551–4560. <https://doi.org/10.1021/acssuschemeng.1c08413>
- Yang, H., Jiang, B., Sun, Y., Hao, L., Huang, Z. and Zhang, L. (2016). Synthesis and oxidative desulfurization of novel lactam-based Brønsted-Lewis acidic ionic liquids. *Chem. Eng. J.*, 306, 131–138. <https://doi.org/10.1016/j.cej.2016.07.044>
- Yankova, R. and Tankov, I. (2021). Hydrogen bonding effect on the thermal behavior of acidic ionic liquids. *J. Mol. Struct.*, 1238, 130416. <https://doi.org/10.1016/j.molstruc.2021.130416>
- You, K., Mao, L., Yin, D., Liu, P. and Luo, H. (2008). Beckmann rearrangement of cyclohexanone oxime to ϵ -caprolactam catalyzed by sulfonic acid resin in DMSO. *Catal. Commun.*, 9(6), 1521–1526. <https://doi.org/10.1016/j.catcom.2008.01.011>
- Zhang, Y., Cui, P., Luo, G., Chen, L., Li, X., Chao, Y. and Zhu, W. (2023). One-step selective separation and efficient recovery of valuable metals from spent lithium batteries by phosphoric acid-based deep eutectic solvent. *Green Chem. Eng.*, 5(3), 390–398. <https://doi.org/10.1016/j.gce.2023.10.002>
- Zhou, Q., Yu, Y., Liu, Q., Zhuang, Y., Lv, Y., Song, N. and Ni, L. (2020). Morphology evolution and thermodynamic behavior of the “soft core hard shell” structure formed by reactive amino triblock in epoxy resin. *J. Mater. Sci.*, 55(35), 16846–16859. <https://doi.org/10.1007/s10853-020-05258-2>
- Zhu, Z., Luo, X., Sokolov, A. P., Sokolov, A. P. and Paddison, S. J. (2020). Proton Transfer in Phosphoric Acid-Based Protic Ionic Liquids: Effects of the Base. *J. Phys. Chem. A*, 124(20), 4141–4149. <https://doi.org/10.1021/acs.jpca.0c02863>



EFFECT OF BORIC ACID ADDITION ON ANTIBACTERIAL DYE PRODUCTION

Numan Yurtalan , Feza Geyikçi , Gediz Uğuz 

Ondokuz Mayıs University, Department of Chemical Engineering, 55139, Samsun, TURKEY

Abstract: In this study, the use of interior dyes with antibacterial properties was examined. Boric acid (H_3BO_3), which is a cheap and easily obtainable boron compound from our country's resources, has an antibacterial effect. Within the scope of the study, firstly, boric acid mixtures were prepared in appropriate concentrations and antibacterial dye production studies were carried out by adding them to indoor dyes. The antibacterial properties of the obtained dye were investigated through the inhibition effect on *E. coli* bacteria and its antibacterial activity was tested, and then the brightness, density, film thickness, scorching, pencil hardness and drying time tests of the dyes and the suitability of their characteristics to TS 5808/2012 and the applicability of these dyes were evaluated. The results showed that the antibacterial effect of boric acid did not have a negative effect on the dye quality, but maintained the standard values of the dye.

Keywords: Waste marble powder, Boric acid, Antibacterial material.

Submitted: June 21, 2024. **Accepted:** August 26, 2024.

Cite this: Yurtalan, N., Geyikçi, F., & Uğuz, G. (2024). Effect of boric acid addition on antibacterial dye production. *Journal of the Turkish Chemical Society, Section B: Chemical Engineering*, 7(2), 177–184. <https://doi.org/10.58692/jotcsb.1503140>

*Corresponding author. E-mail: numanyurtalan23@gmail.com.

1. INTRODUCTION

Boron and its compounds are frequently used in many industries. Due to the technology and its abundance, its applications are spreading over a wide area recently. Dyes are building materials that protect the surface of the material, provide an aesthetic appearance, and at the same time prevent factors such as rusting, contamination, corrosion, etc. It is a colored liquid material formed by the combination of metallic, organic, and plastic-based pigment, thinner and binding agents (Özkan, 2013).

Boric acid (H_3BO_3) is one of the most widely used boron compounds in industry as a source of B_2O_3 and is used in the preparation of many boron-containing chemicals such as boron carbide and boron esters.

Additionally, it is used in antiseptics, boron alloys, fire retardants, nylon production, photography, textile industry, glass and glass fiber production, enamel, and glaze. In recent years, it has also found use as a super slider.

Boric acid has a molecular weight 61.83 g/mol, B_2O_3 content of 56.3%, melting point of 171 °C, specific gravity of 1.44 g/cm³ is a crystalline substance with a temperature of formation of -1089 kJ/mol and a temperature of dissolution of +22.2 kJ/mol. Although its solubility in water is low at room temperature, its solubility increases significantly as the temperature rises. For this reason, it is generally considered sufficient to cool the saturated solution from 80 °C to 40 °C to crystallize boric acid in industry (Sarı, 2008; Kuru & Yarat, 2017).

The antibacterial property is sterilization and minimization of microbial action. Disinfectant materials are generally used to prevent this effect.

Disinfectants are chemicals used for places where pathogenic microorganisms exist or are likely to exist, and for devices or materials that may be a source of contamination. The pollution status of the environment in which the disinfectant will be used depending on many factors such as the type of microorganism, the surface to be disinfected, and the characteristics of the equipment, the characteristics of the disinfectant, and the cost (Abbasoğlu, 2007).

Microorganisms are creatures that can be found everywhere and reproduce rapidly if suitable conditions are provided. An adequate supply of moisture, temperature, and nutrients is necessary for bacteria to reproduce. The optimal growth temperature of bacteria is between 30-37 °C, while for fungi this temperature is 25-30 °C. Regional temperature changes in the body are among the factors that trigger the proliferation of bacteria (Akaydin & Kalkançı, 2014).

Ensuring indoor air quality and removing surface contamination by using antibacterial materials are frequently applied. However, it does not provide assurance about decontamination due to reasons such as the use of water, detergents, and disinfectants creating difficulties. In reaching every area and the inability of the applied substances to provide a permanent effect. For this reason, coating large surfaces with antimicrobial materials are seen as a more permanent option to prevent cross-contamination caused by microorganisms such as objects, devices or walls that are at risk (Bal & Şanlı, 2020).

Boric acid is a hydrophobic element that is considered to be non-toxic if it does not reach systemically significant amounts in studies, especially useful for various systems. Especially, boric acid shows antibacterial, anticandidal, and antifungal activity. It has been shown in various studies to be an active antibacterial agent against bacteria such as *Staphylococcus aureus*, *Klebsiella pneumoniae*, *Candida albicans*, *Aspergillus Niger*, *Escherichia coli*, and *Pseudomonas aeruginosa* (Kapukaya & Külahçı, 2020; Zer, Karabacak, & Manay, 2022).

In different parts of the world, the research and development of new antibacterial agents effective against bacteria continues rapidly. Some researchers have focused on assessing the antibacterial effect of boric acid in this process (Haesebrouck et al. 2009; Concia et al. 2016).

It has been reported that the solution, which is formed by mixing 2% boric acid and 2% acetic acid in equal proportions, inactivates *S. pseudintermedius* in the amount of 5×10^7 CFU/mL in 30 minutes when diluted at 1/2 and 1/4 ratios. It is stated that this effectiveness is increased more by the use of boric acid together with acetic acid. In a study conducted on humans in our country, it was reported that boric acid solution applied to the oral tract had strong antibacterial effects on *Enterococcus faecalis* (Zan et al. 2013)

Dyes can be divided according to their place of use and the type of binder in their content. Decorative dyes, construction dyes, industrial and corrosion dyes, furniture dyes, auto dyes, peelable dyes and food dyes are included in this classification (Çalışkan, 2019).

Especially in the Covid-19 pandemic we are experiencing, it has become clear how important hygiene is in public environment. Microorganisms can survive on surfaces for long periods of time, and contact with these surfaces can cause cross-infections. This is especially important in places such as food processing plants, offices, and hospitals (Bal & Şanlı, 2020).

In the selection of wall materials in hospital interiors, surfaces that do not emit dust, chemicals and vapors should be preferred. If the materials are fragmented, they should be used in large pieces and should not have a porous structure. In addition, it is recommended that the materials are easy to clean and have antibacterial properties (Kırbaş, 2012).

The use of antibacterial materials has been important in environments where the public can be found collectively such as indoor spaces, schools and hospitals, and where the microbial load is high. Antibacterial dyes and coatings have gained importance in order to prevent the growth and spread of these bacteria on surfaces such as walls, door handles, and tables. The production of antibacterial dye with boric acid, which is not harmful to human health, shows its usability in every possible environment. The emergence of products by using boric acid, which is abundantly available in our country, and our own resources can be considered as a national gain.

2. MATERIALS AND METHODS

2.1. Materials

Boric acid (H_3BO_3) was supplied by Eti Mining Enterprises. The contents of boric acid were represented in Table 1. Interior dye was supplied by Betek Dye and Chemical Industry Co. Inc. The features of interior dye were determined as 20 000410-TSE-115/01 standard and also were shown in Table 2. Antibacterial test kits supplied from (Hytech Slide) DiaTek Diagnostic Products Tech. Comp. Hytech Slide is a product that can perform analysis by taking samples from personnel, equipment, solid and liquid surfaces from all surfaces for microbiological analysis.

The storage temperature is 10 – 25 °C and the shelf life is 5-6 months. Each surface is divided into 10 areas, each area being 1 cm². Thus, the results can be given as the number of colonies in a total surface area of 10 cm².

Table 1. The contents of boric acid.

B ₂ O ₃	SO ₄ ²⁻	Cl ⁻	Fe ²⁺
%59.25 min	500 ppm max	10 ppm max	7 ppm max

Table 2. Features of interior dye (20 000410-TSE-115/01).

Parameters	TS 5808
Brightness	Checkmate
Particle Size	Thin
Coating Power	Class 2 (7 m ² /L)
Wet Scrubbing Resistance	Class 3

2.2. Methods

2.2.1. Preparation of dye

Firstly, boric acid solutions were prepared in different concentrations (3%, 4%, and 5%). 85 mL of water-based dye was taken and diluted with 15 mL of pure water in three different experimental setups. 85 mL of the diluted dyes were taken and 15 mL of 3%, 4%, and 5% boric acid solutions were added to them. 100 mL boric acid added dyes were obtained by volume (%v/v).

2.3 Characteristic Dye Analyses

2.3.1 Antibacterial test

Water-based dye mixtures were prepared as 3%, 4%, and 5% boric acid solutions with distilled water and the antibacterial properties of mixtures were tested. 10 mL of homogenized dye and boric acid mixtures were taken and spread over a certain area and left to dry for 48 hours at room temperature. Similarly, only 10 mL of the reference sample, which is the dye, was taken and left to dry. The drying antibacterial dye is stained with 10⁸ Kob/g *E. coli* bacteria. The stained antibacterial dye samples were placed in the incubator to continue the bacterial activity.

The antibacterial properties of the surfaces were determined by taking tests with antibacterial test kits containing *E. coli* medium.

2.3.2 Brightness analysis

Luminance is a property related to the reflection of light falling on a surface, and the degree of luminance refers to the clarity of the image created on the surface by the rays from a source. Gloss measurement is carried out using photoelectric devices. The gloss depends on the number of binders and fillers of the dye, the particle size of the fillers (Uğuz, 2019).

2.3.3 Density analysis

. In addition to being an important parameter for calculating dye consumption, dye density is also important during the packaging of the product. Density measurement is generally carried out with TS EN ISO 2811-1 standard methods.

2.3.4 Film thickness analysis

1 gram of dye samples was applied on the aluminum surface (150 μm) and the thickness of the dye film samples was measured with the Loyka-5202-25 brand film thickness measuring device.

2.3.5 Adhesion analysis

The scanning method (squaring) is used. Areas of 1 cm² are marked and divided into 100 equal parts by drawing 10 horizontal and 10 vertical lines that intersect each other perpendicularly with an interval

of 1 mm. It is adhered on an area of 1 cm² using adhesive tape. The tape is drawn perpendicular to the surface and the scorching dye areas are calculated as a percentage.

2.3.6 Pencil hardness analysis

It is used to determine the hardness of dye surfaces. In pencil hardness analysis, pencils from soft to hard are used: 5B, 4B, 2B, B, HB, 3H, 5H. With sandpaper, the tip of the pens is shaped into a square section. The degree of hardness, which is one level softer than the softest pencil that leaves a permanent mark on the dye surface by scratching the dye surfaces with pencils, is determined as the pen hardness of the film (Uğuz, 2019).

2.3.7 Drying time analysis

Samples are applied on the aluminum surface. 5, 10, 15, respectively. After minutes, the drying time is checked every 15 minutes for up to 4 hours, every 30 minutes after 4 hours, up to 8 hours and up to 24, 48 hours. First of all, it was tested whether the film sticks to our hands by touching our fingers, and after this stage, 1. For the degree of drying, a glass bead with a diameter of 0.2 mm was left on the dye surface from 5 cm above and it was checked whether it adhered to the surface. If it does not stick, the dye is 1. It has reached the degree of drying. Rounds 2 and 3 for drying degrees, the dye surfaces are covered with Kraft paper and masses of 0.05 N and 0.5 N, respectively, are applied for 1 minute and if the dye does not stick to the paper surface, the dye is 2 and 3. It has reached drying degrees. Rounds 4 and 5 at drying degrees, after the Kraft paper is placed on the dye surface, force is applied with masses of 5 N for 1 minute, if there is no adhesion but leaves a trace, the dye is 4. It reaches the degree of drying. If there are no traces and adhesions, the dye is 5. It reaches the degree of drying. Rounds 6 and 7 by applying the same processes within the drying degrees, a force weighing only 50 N is applied (Uğuz, 2019).

3. RESULTS AND DISCUSSION

3.1 Antibacterial Test

The obtained results showed that the effects of antibacterial dyes prepared at 3% and 4% concentrations on *E. coli* bacteria was less effective than the antibacterial dye prepared with 5% concentration. Since the percentage of boric acid will have a toxic effect after a certain concentration, optimum results have been obtained by keeping it at a concentration of 5%. In the boric acid dye mixture prepared with a concentration of 5%, the possibility of bacteria to survive on the surface decreased over time, and the antibacterial effect

decreased the number of *E. coli* over time. The surface of the test kits was divided into 10 areas of 1 cm², and the number of bacteria on these areas was counted at the end of t=0, t=1, and t=2 hours, respectively. As a result of the count, it was seen that the number of live bacteria was active in 3 units of the 10-unit area divided. Antibacterial tests were carried out with the help of kits that tested the expected hygiene environment on the surfaces.

It is known that bacteria and disease-causing microorganisms are found in public areas. The fact of hygiene comes to the fore, especially during the Covid-19 period. The development of projects to prevent the spread of microorganisms are

important, which is necessary for public health. In this reason, antibacterial dye using has been prioritized among the issues that need to be investigated. The low-cost antibacterial dye manufactured within the scope of the study can be easily applied to all areas (home, hospital, public transportation, etc.). It is envisaged that hygiene will be ensured indoors (especially in toilets). As can be seen in Figure 1, the antibacterial properties increase over time and the number of bacteria decreases.

In Figure 1, in the reference sample, bacteria are present in every 1 cm² area and continue their activities.

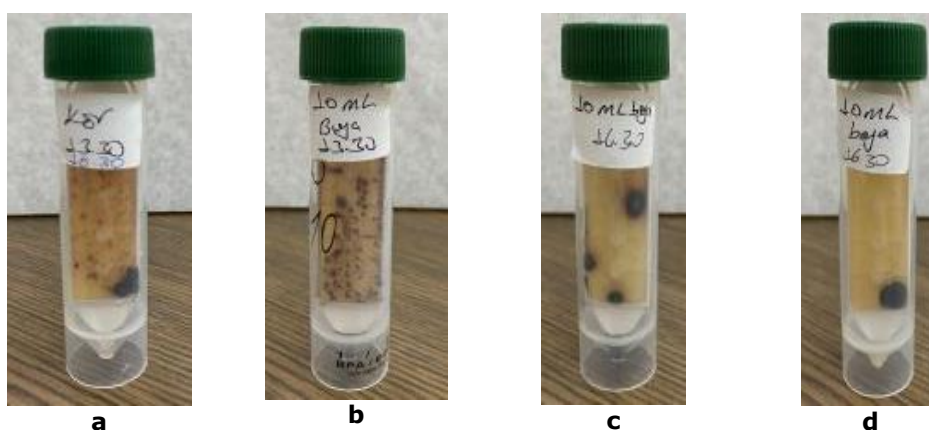


Figure 1. Antibacterial test results of samples (a) reference (b) 0 hour (c)1 hour (d)2 hours.

3.2 Analysis of Brightness

The results of the gloss analysis are given in Table 3. It is seen that the gloss values decrease with dilution and the contribution of boric acid.

Table 3. Change of gloss values in dyes.

Samples	20°	60°	85°
Reference Dye	0.5 gloss	2.0 gloss	4.9 gloss
Diluted Dye	0.5 gloss	2.0 gloss	3.6 gloss
Boric Acid-Added Antibacterial Dye	0.4 gloss	1.9 gloss	3.1 gloss

3.3 Density Analysis

The results of the density analysis are given in Table 4. It is seen that the density values decrease with dilution and the contribution of boric acid.

Table 4: Change of density values in dyes.

Samples	Density (g/cm ³)
Reference Dye	1.6268 g/cm ³
Diluted Dye	1.5568 g/cm ³
Boric Acid Added Antibacterial Dye	1.4768 g/cm ³

3.4 Film Thickness Analysis

The film thickness of the paints was measured with Loyka 5202-25 model micrometer. The results are given in Table 5.

Table 5: Change of film thickness values in dyes.

Samples	Thickness (mm)
Reference Dye	1.27 mm
Diluted Dye	1.48 mm
Boric Acid Added Antibacterial Dye	1.55 mm

3.5 Adhesion Analysis

The results of the adhesion analysis for the dyes on the floor, which are given in Figure 2, are given in

Table 6. Our dye samples (0) showed excellent adhesion by roasting.



Figure 2. Adhesion analysis experiment set.

Table 6. Change of roast values in dyes.

Roasting Degree	Blank Frames/ Total Frames
Reference Dye	0/100
Boric Acid-Added Antibacterial Dye	0/100
Diluted Dye	0/100

3.6 Pencil Hardness Analysis

The pencil hardness test set is given in Figure 3 and the analysis results are given in Table 7. There was no difference in film thicknesses.

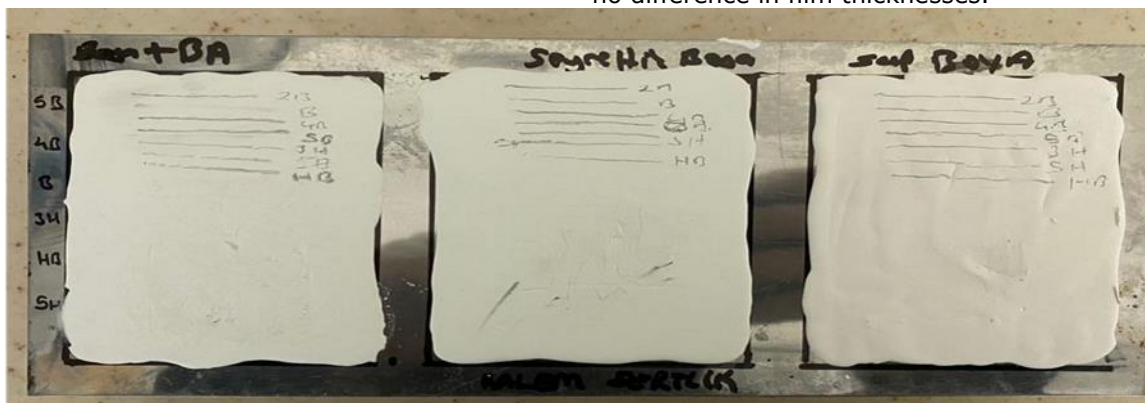


Figure 3. Pencil hardness analysis experiment set.

Table 7. Change of pencil hardness values in dyes.

Samples	Degree of Hardness (g)
Reference Dye	5B
Diluted Dye	5B
Boric Acid Added Antibacterial Dye	5B

3.7 Drying Time Analysis

Drying time analysis results are given in Table 8. Drying degrees can be listed as Antibacterial dye <

Dilute dye < Reference dye, respectively. The admixture of boric acid had little effect on drying.

Table 8. Change of drying time values in dyes.

Samples	2 h	4 h	8 h	24 h	48 h
Reference Dye	Sticks to the hand	Sticks to the hand	Grade 1	7th degree	7th degree
Dilute Dye	Sticks to the hand	Sticks to the hand	Sticks to the hand	Grade 5	7th degree
Boric Acid-Added Antibacterial Dye	Sticks to the hand	Sticks to the hand	Sticks to the hand	Grade 5	7th degree

4. CONCLUSIONS

Boron-based antibacterial dye was manufactured and the antibacterial activities of the dye samples were investigated. Traditional dye tests such as the degree of drying of the dye films, film thickness, gloss, and degree of spalling (adhesion) were carried out. The antibacterial dye properties produced are no different from the properties of the standard dye. Obtained results from characterization tests showed that the antibacterial dye did not lose its properties. There was no difference between standard dye and antibacterial dye in the drying degree, film thickness, gloss, roasting degree, density analysis. These dyes containing boric acid, which are generally used to dye the walls of hospitals, schools or crowded areas due to conditions that require hygiene, have gained antibacterial effectiveness from domestic and national resources and are promising for the dye market. It is predicted that the studies carried out are original within the scope of this information and will contribute to the antibacterial dye market and the literature.

5. ACKNOWLEDGEMENTS

This study were supported by Ondokuz Mayıs University BAP Unit with PYO.MUH.1908.22.059 Project Number. The authors are thankful for Dr. Nilgün ÖZDEMİR in Ondokuz Mayıs University Food Engineering Department for Antibacterial Analysis.

6. REFERENCES

- Abbasoğlu, U. (2007). Tests measuring the effectiveness of disinfectants on microorganisms. *5th National Sterilization Disinfection Congress*, (pp. 41-62). Ankara.
- Akaydın, M., & Kalkanlı, M. (2014). A study on the antibacterial properties of fabrics used as hospital garments. *Süleyman Demirel University Faculty of Arts and Science Journal of Science*, 9(1), 20-34.
- Bal, Ş., & Şanlı, N. O. (2020). Evaluation of the effectiveness of antibacterial wall dye in increasing indoor hygiene conditions. *Journal of Gazi University Faculty of Engineering and Architecture*, 35(4), 1913-1922.
- Caliskan, V. (2019). *Investigation of Attachments on the Properties of Temporary Coatings of*

Different Plasticizers. M.Sc. Thesis, Kocaeli University, Institute of Natural and Applied Sciences, Department of Chemical Engineering, Kocaeli, Turkey.

- Concia E, Mazzaferri F, Cordioli M (2016). New antibiotic development: Barriers and opportunities. *Ital J Med*, 10, 255-271.
- Ekin, İ. H., & Gülaydın, Ö. (2019). Antimicrobial Activity of Boric Acid Solution Against *Listeria monocytogenes* and *Staphylococcus aureus*. *Van Veterinary Journal*, 163-166.
- Uğuz, G. (2019). Investigation Of The Effects Of Different Dienophiles On Dye Properties. Hitit University, Department of Chemical Engineering. Çorum: Institute of Natural and Applied Sciences.
- Haesebrouck F, Baele M, De Keyser H, Hermans K, Pasmans F (2009). Antimicrobial activity of an acetic and boric acid solution against *Staphylococcus pseudintermedius*. *Vlaams Diergeneeskundig Tijdschrift*, 78 (2), 89-90.
- Kapukaya, R., & Külahçı, Ö. (2020). Treatment of Wounds with Tissue Defects with Polyurethane Sponge Containing Boric Acid. *Journal Of Boron*, 5(2), 83-90.
- Kırbaş, C. (2012, FEBRUARY). Architectural-Mechanical Project Design and Application Principles in Hospitals. *Installation Engineering (TMMOB Teseat Engineering (TMMOB Chamber of Mechanical Engineers)(127)*, 15-30.
- Kuru, R., & Yarat, A. (2017, September 15). An Updated Look at Boron and Its Effects on Our Health. *Clinical and Experimental Health Sciences*. *dergipark.org.tr*, 7(3), 107-115.
- Ozkan, E. (2013). *Determination of the Structural Properties of the Conductive Dye to be Applied on the New Generation Ceramics*. M.Sc. Thesis, Yıldız Technical University, Institute of Natural and Applied Sciences, Department of Chemical Engineering, Istanbul.
- Sari, M. (2008). The kinetics of dissolution of different minerals in boric acid solutions. M.Sc. Thesis, Istanbul Technical University,

Yurtalan, N., Geyikçi, F., Uğuz, G. (2024) 7(2), 177-184.

Institute of Natural and Applied Sciences,
Department of Chemical Engineering,
Istanbul.

Zan R, Hubbezoglu I, Ozdemir AK, Tunç T, Sumer Z, Alici O (2013). Antibacterial effect of different concentration of boric acid against *Enterococcus faecalis* biofilms in root canal. *Marmara Dental J*, 1 (2), 76-80

Zer, Y., Karabacak, F. N., & Manay, A. B. (2022). Investigation of disinfectant effectiveness of boric acid. *Turkish Journal of Hygiene and Experimental Biology*, 79(1), 145-152.



Evaluation of the Nitrogen Release Properties of Chitosan-Bentonite Beads

Dilşad Dolunay ESLEK KOYUNCU* , Müjgan OKUR , Birsen TEMUÇİN ,
Selin Meliha ŞEN , Esra ŞAHBAZ , Şule EROĞLU , Zeynep Sıla AKIN ,
Gonca TOPALOĞLU 

Gazi University, Chemical Engineering, Ankara, 06570, Türkiye.

Abstract: In this study, chitosan-bentonite beads were prepared by using bentonite and chitosan as fertilizer carrier materials and urea as fertilizer components. The prepared samples were named BUC0.2, BUC0.4 and BUC0.6 based on the bentonite ratios of 0.2%, 0.4% and 0.6% (weight/volume). In the FT-IR and XRD results, it was seen that the characteristic peaks of the bentonite structure became evident in the BUC0.6 sample, while chitosan peaks were dominant in the BUC0.2 sample, as expected. As the amount of bentonite increased, the swelling ratio generally increased from 31.6% to 48.6. In the nitrogen release experiments, a very rapid nitrogen release occurred in the first hours of release. It was thought to be due to the rapid dissolution of urea in water. The cumulative release percentage showed a slightly decreasing trend in the days following the release experiment. When nitrogen release profiles of the samples containing different amounts of bentonite were compared, it was observed that the nitrogen release curves were quite close to each other due to the lower bentonite ratio. Release percentages of the samples containing different amounts of bentonite were obtained between 61.2-67.7. Observations supported the efficient degradation of fertilizers in the soil environment. As a result, it was evaluated that the prepared materials were promising as environmentally friendly nitrogen fertilizer.

Keywords: Bentonite, chitosan, urea, fertilizer, biodegradation

Submitted: February 10, 2024. **Accepted:** September 05, 2024.

Cite this: Eselek Koyuncu, D. D., Okur, M., Temuçin, B., Şen, S. M., Şahbaz, E., Eroğlu, Ş., Akın, Z. S., & Topaloğlu, G. (2024). Evaluation of the Nitrogen Release Properties of Chitosan-Bentonite Beads. *Journal of the Turkish Chemical Society, Section B: Chemical Engineering*, 7(2), 185–194.

<https://doi.org/10.58692/jotcsb.1434727>

*Corresponding author. E-mail: deslek@gazi.edu.tr

1. INTRODUCTION

The increasing population increases the need for food in our country and in the world. However, land degradation occurs due to industrialization, urbanization, desertification, and floods, and as a result, arable land areas are decreasing day by day (Azeem et al., 2014). The necessity of increasing agricultural productivity to meet the increasing food demand necessitates the implementation of technological applications in the agricultural industry. Agricultural efficiency can be briefly defined as obtaining more product from less area. Some techniques are applied to increase agricultural efficiency. The most well-known of these methods include using high-quality seeds, leaving the soil fallow, ensuring that plant residues decompose in

the soil without burning, and fertilizing (Azeem et al., 2014; Katip, 2020). These techniques vary depending on land characteristics and soil type, and not every method can be applied to every land. Fertilization is one of the most practical and oldest known methods (Liu et al., 2019).

All natural or artificial substances containing the components plants need for their development are defined as fertilizers. The purpose of fertilization is not only to provide nutrients to the plant but also to maintain productivity by preserving the soil's physical, chemical, and biological properties. Fertilizers also prevent diseases and root pests and support the plant in taking nutrients from the soil. Fertilizers generally contain phosphate, nitrate, ammonium, and potassium salts, the components the soil needs most, and can be found in solid,

liquid, and gas forms (Katip, 2020). Plants absorb approximately 90 different elements from air, water, and soil. About 20% of these elements are essential for the growth and development of the plant, while others contribute to growth and development. It is known that each element contributes to different functions of the plant. Figure 1 shows the classification of essential nutritional elements that must be present in the plant. Elements found in plants are classified as "macro"

and "micro" nutrients according to their abundance. Of these elements, carbon, hydrogen, and oxygen, which constitute approximately 95% of the plant, can be taken from air and water in sufficient quantities, while other elements can be taken as anions, cations, or molecules. Apart from the elements given in Figure 1, Al, Co, Na, Si, and V elements must also be present in some plants (Bolat and Kara, 2017).

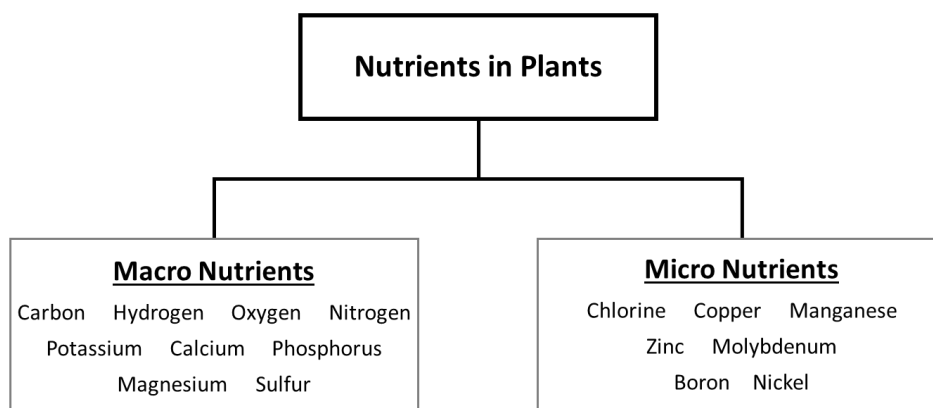


Figure 1: Classification of essential nutritional elements in plant.

Nitrogen (N), the primary nutrient required for plant growth, plays a role in the synthesis of protein and chlorophyll in the plant. Nitrogen, which is the basic building block of the plant cell wall, is also responsible for accelerating growth, stimulating roots, improving the quality of fruits, timely flowering, fruit formation, and seed formation (Bolat and Kara, 2017; Jayanudin *et al.*, 2021). Nitrogen is transferred to the soil by the breakdown of organic matter in the soil over time, and in this way, plants can benefit from nitrogen. However, most of the world's soil is poor in nitrogen (Bolat and Kara, 2017).

The most crucial problem in increasing agricultural efficiency is the unsensible use of fertilizer. Although the use of fertilizer is an effective method to increase agricultural productivity, excessive use of fertilizer causes pollution of the environment and water resources. As a result of unsensible fertilization, the soil's salt content increases, the microorganisms' activity decreases, and as a result, product quality and productivity decrease. The long-term disadvantages of unsensible fertilization are significant environmental effects such as pollution of groundwater, increase in the amount of nitrate in water, erosion of the soil surface, increase in the amount of phosphate in streams and rivers, and the spread of nitrogen oxide into the atmosphere (Mushtaq *et al.*, 2018).

With the development of controlled-release technology, efforts to reduce the adverse effects of traditional fertilization have gained importance in recent years. The controlled release provides a component's slow and long-term release into the desired environment. In recent years, this technology has shown promise in medicine,

pharmacy, chemistry, agriculture, and veterinary. Controlled-release fertilizers are fertilizers prepared by coating plant nutrients with a slow-release ingredient. Synthetic organic polymers (acrylic resin, polysulfone, polyurethane, polyolefin, etc.), natural organic biopolymers (lignin, starch, cellulose, etc.), and inorganic components (silicas, phosphates, sulfur, etc.) can be used as coating materials (Mann *et al.*, 2019; Tian *et al.*, 2019). These fertilizers have attracted attention in recent years due to their advantages, such as reducing the accumulation of traditional fertilizer-derived components in the soil, reducing fertilizer consumption, and minimizing the harmful effects of chemical fertilizers on the ecosystem (Rahman *et al.*, 2021). Controlled-release fertilizers provide slow release of nutrients into the soil, thus preventing nutrient leaching and nutrient loss. Since these fertilizers dissolve slowly in water, they also prevent groundwater contamination, especially in case of heavy rains and floods. In addition, their use on sloping, erosion-prone, and flow-prone lands provides significant benefits. Due to these advantages, controlled-release fertilizer production has accelerated in recent years. Studies have focused on fertilizer production with more environmentally friendly and lower-cost components.

The literature has determined that clays, hydroxyapatite materials, polymeric materials, and zeolites are used as support materials in controlled fertilizer release. Clays include double-layer hydroxides (Ureña-Amate *et al.*, 2011; Berber and Hafez 2018; Bernardo *et al.*, 2018), montmorillonite (Santos *et al.*, 2015; França *et al.*, 2018), kaolin (Liang *et al.*, 2007; Mushtaq *et al.*, 2018), bentonite (Daitx *et al.*, 2019; Liu *et al.*, 2019; Sarkar *et al.*,

2021; Umar *et al.*, 2022) are noteworthy. As polymeric materials, chitosan, which is a low-cost, non-toxic, natural, biodegradable biopolymer with swelling properties (Santos *et al.*, 2015; França *et al.*, 2018), cellulose (França *et al.*, 2021), starch (Han *et al.*, 2009; Perez and Francois, 2016; Giroto *et al.*, 2020) are the most frequently used components.

There are a few studies in the literature using bentonite. Liu *et al.* (2019) prepared biochar fertilizers loaded with urea by hydrothermal method for controlled release using bentonite and polyvinyl alcohol. After 28 days of incubation in water, 61.3% was released, and after 98 days of incubation in soil, 54.6% was released. It has been evaluated that the water retention ability of the soil increases thanks to the water absorption properties of biochar and bentonite (Liu *et al.*, 2019). In another study (Sarkar *et al.*, 2021), diammonium phosphate fertilizer was prepared using starch, polyvinyl alcohol, and bentonite. Starch is an essential component used in encapsulated controlled-release fertilizers due to its adequate hydroxyl content, ease of access, biodegradability, and reactive compatibility with other molecules. It was stated that as the bentonite content increased, the relative crystallinity and density increased. It has also been stated that high bentonite content stabilizes the fertilizer structure, and encapsulation slows down N and P release. There are only a few studies in the literature on the preparation of fertilizer with chitosan and bentonite components. Haseena *et al.* (2016), bentonite-chitosan films were prepared and immersed in ammonium chloride solution, and their ability to retain $\text{NH}_4^+\text{-N}$ was tested. As a result, it has been stated that these materials can be used as fertilizer (Haseena *et al.*, 2016). Hamid *et al.* (2013) carried out water absorption, soil degradation, DSC, and FTIR analyses of urea fertilizers prepared using chitosan and bentonite. In the study, the effect of changing the chitosan ratio on the properties of the fertilizer by keeping the amount of urea constant was evaluated. As a result, it was stated that chitosan can be used in fertilizer as a biodegradable material (Hamid *et al.*, 2013). Qudus *et al.* (2021) used vinasse and bentonite-chitosan matrix to prepare slow-release organomineral fertilizer. In the conducted study, vinasse was used as an NPK source. As a result, it was evaluated that the chitosan-bentonite matrix provides slow release effectively (Qudus *et al.*, 2021). In another study (Piluharto *et al.*, 2017), phosphate fertilizer was prepared with chitosan-bentonite beads, and low, medium, and high molecular weight types of chitosan were used. The release behavior of fertilizer materials was evaluated in different pH (3, 7, and 10) environments. It has been stated that chitosan polymer increases the water absorption capacity of fertilizer, and the most significant increase is observed with chitosan with high molecular weight. In addition, they have reported that the phosphate release decreased at decreasing pH values. There are no fertilizer studies in the literature that include chitosan, bentonite, and urea

together. In this study, bentonite and chitosan were used as controlled-release fertilizer carrier materials and urea (nitrogen source) was used as the fertilizer component. Fertilizers were prepared in different bentonite contents (0.2%, 0.4% and 0.6% weight/volume). Prepared samples were characterized by FT-IR and XRD analyses. Swelling percentages of fertilizers, urea release behavior in water, and biodegradation in soil were determined.

2. EXPERIMENTAL

2.1. Preparation of the Chitosan-Bentonite Beads

In this study, bentonite and chitosan were used as controlled-release fertilizer carrier materials and urea (nitrogen source) was used as the fertilizer component. First, bentonite was added to 400 mL of distilled water at 0.2%, 0.4%, and 0.6% weight/volume ratios. Urea (Sigma-Aldrich, >99%, CAS No.: 57-13-6), a nitrogen source, was added in a ratio of 4% weight/volume and stirred at room temperature for 24 hours. Chitosan (medium molecular weight, Sigma-Aldrich, CAS No.: 9012-76-4) was added to the urea-bentonite mixture at a ratio of 2% weight/volume. Since the dissolution of chitosan requires acidic conditions, acetic acid (glacial, >99.5%, Isolab, CAS No.: 64-19-7) was added to the mixture at 2% (volume/volume). The mixture was stirred at room temperature for 20 hours until chitosan dissolved. Using a Pasteur pipette, macro spheres were formed by dropping the prepared fertilizer mixture into a beaker containing 0.1 M sodium tripolyphosphate (ZAG, 94%). The materials prepared in this way were named BUC0.2, BUC0.4, and BUC0.6 based on the bentonite ratios of 0.2%, 0.4%, and 0.6%, respectively.

2.2. Characterization Studies

2.2.1. X-ray Diffraction (XRD)

X-ray diffraction patterns (XRD) were performed to determine the crystallite phase of the prepared spheres using a Rigaku Ultima-IV diffractometer (Cu K α radiation with a wavelength of $\lambda=0.15406$ nm, at 40 kV and 30 mA) at a scanning rate of 2°/min.

2.2.2. Fourier Transform Infrared Spectrometry (FT-IR)

Fourier transform infrared spectrometry (FT-IR) analyses were carried out in a Jasco 4700 ATR/FT-IR spectrometer (in the medium infrared region of 4000-400 cm^{-1} with 4 cm^{-1} resolution, 128 scans) to evaluate chemical structures and structural bonds of the fertilizers.

2.2.3. Swelling Percentage

Exactly weighed spheres were soaked in distilled water for 48 hours until sufficiently swollen. It was then taken out, excess water removed, and the swollen spheres weighed to calculate swelling percentage (Eq.1).

$$\text{Swelling \%} = \frac{w_t - w_i}{w_i} \quad (1)$$

Here, w_t and w_i were the weight of the swollen sphere at time "t" and the initial dried sphere, respectively.

2.3. Nitrogen Release in Distilled Water

A certain amount of fertilizers was taken, put into the flask, and added 50 mL of pure water. The flasks were placed in a water bath at 30°C. 5 mL samples were drawn at certain time intervals, and the same amount of purified water was added. Nitrogen analysis was performed for the samples taken to determine cumulative release. In the nitrogen release analysis, the reagent solutions were first prepared as follows.

0.01 g of $\text{FeCl}_3 \cdot 4\text{H}_2\text{O}$ was placed into a 100 mL volumetric flask. 30 mL of pure water was added and mixed until dissolved. 10 mL of H_3PO_4 and 30 mL of H_2SO_4 were added, mixed thoroughly, and

waited to cool (*Reagent 1*). 0.25 g diacetyl monoxime (DAM, Supelco, >99%) and 0.005 g thiosemicarbazide (TSC, Sigma-Aldrich, 99%) were weighed and placed in another volumetric flask. 50 mL of pure water was added and dissolved thoroughly (*Reagent 2*).

Then, 2 mL of *Reagent 1* and 1 mL of *Reagent 2* were added to 0.1 mL of the sample, shaken, and boiled for 5 minutes. It was cooled down to room temperature. Absorbance was measured at the wavelength of 526 nm in a UV spectrophotometer.

Each experiment was carried out in duplicate, and the cumulative nitrogen release percentage was calculated using the following equation (Eq.2) (Altunkaynak et al., 2022).

$$\text{Cumulative release \%} = \frac{(V_0 C_n + \sum_{i=1}^{n-1} C_i V_i)}{W_0} * 100 \quad (2)$$

Here, V_0 is the initial volume of the release solution in mL, V_i is the sample volume in mL, C_n and C_i are the nitrogen concentration (mg/L) at i and n sample times, and W_0 is the weight of total fertilizer in the release medium.

2.4. Degradation in Soil

Approximately 50 mg of fertilizer sample was placed 3 cm below the soil surface in two different soil environments: Infertile garden soil (Soil1) and commercial soil (Soil2). The biodegradation behavior of fertilizers was observed by maintaining soil's moisture for 15 days.

3. RESULTS AND DISCUSSION

In this study, chitosan/bentonite beads containing urea were prepared and the urea-nitrogen release properties of these beads were examined. The FT-IR analysis results of the bentonite, chitosan, and prepared samples are given in Figure 2. In the FT-IR spectra of pure bentonite, the peaks at 445, 523, 790, and 1120 cm^{-1} were attributed to the presence of quartz in the bentonite structure (Chang et al., 2020; Atkovska et al., 2016). A high-intensity peak at 1009 cm^{-1} and a small peak that appeared at 1626 cm^{-1} were related to the amorphous SiO_2 . A small shoulder at 619 cm^{-1} and a small peak at 672 cm^{-1} corresponded to the Al-O-Si-O bond (Zaitan et al., 2008; Atkovska et al., 2016). The presence of -OH groups was confirmed by the peaks at 912 (Al-Al-OH), 3410 (Si-OH) and 3608 cm^{-1} (Al-OH) (Chang et al., 2020; Atkovska et al., 2016). In addition, the peak at 1626 cm^{-1} was the indication of H-O-H bending and stretching vibrations of O-H bonds of water molecules in the silicate matrix (Elgarhy et al., 2022; Chang et al., 2020).

In the FTIR spectra of pure chitosan, the broad peak at 3200-3600 cm^{-1} indicated the stretching of -OH-groups. In this region, the -OH band and N-H stretching band overlapped. In the literature, the peaks at 3289 cm^{-1} and 3351 cm^{-1} were related to the N-H and O-H stretching and intramolecular hydrogen bonds. The peak at 2873 cm^{-1} belonged to the aliphatic C-H stretching. The peaks overlapped at 1593 and 1655 cm^{-1} and were assigned to the N-H bending of primary amine and C=O stretching of amide I, respectively. A small shoulder at 1327 cm^{-1} indicated the C-N stretching of amide III. At this region, bending vibrations of CH_2 (1417 cm^{-1}) and the symmetrical deformation peak of CH_3 (1374 cm^{-1}) were overlapped. The asymmetric stretching of C-O-C was observed at 1150 cm^{-1} . High-intensity peaks that overlapped at 1030 cm^{-1} and 1059 cm^{-1} were the indication of C-O stretching (Altunkaynak et al., 2022; Queiroz et al., 2015). In the BUC0.2, BUC0.4, and BUC0.6 samples, the characteristic peaks related to chitosan and bentonite structures were observed. It is seen in Figure 2-c that the characteristic peaks of the bentonite structure became evident in the BUC0.6 sample, which has a high bentonite ratio, while chitosan peaks were dominant in the BUC0.2 sample, as expected. It has been observed that the peaks belonging to SiO_2 and -CH in the chitosan/bentonite structure have shifted to high wavenumbers. In the studies conducted, it has been stated that the vibration bands of the interlayer Si-O groups of bentonite in the chitosan/bentonite structure and the vibration bands of -CH in the - CH_2 and - CH_3 groups at 2888 cm^{-1} and 2942 cm^{-1} , have shifted to high wavenumbers, meaning that the reactive groups of chitosan interact with bentonite, respectively (Abdelkrim et al., 2020).

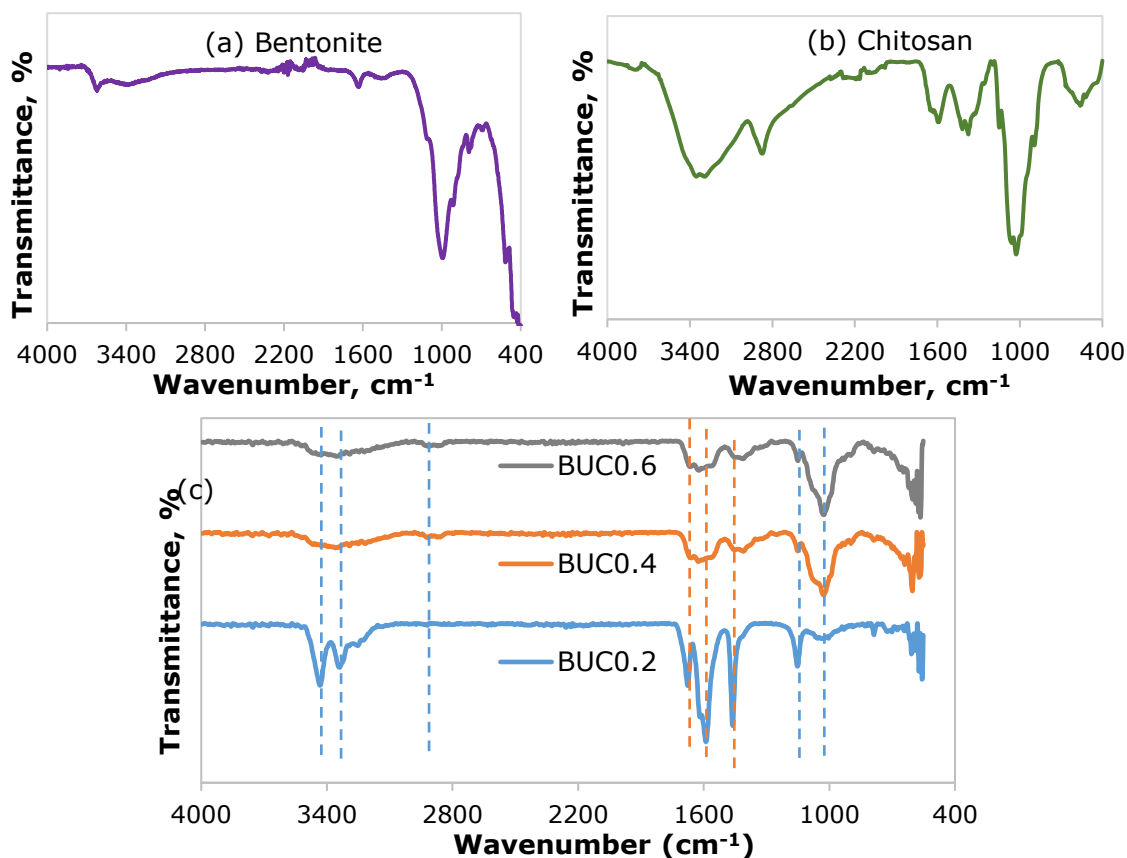


Figure 2: FT-IR spectra of (a) bentonite, (b) chitosan, and (c) prepared fertilizer samples.

The presence of bentonite and chitosan in the structure was also confirmed by the XRD patterns. XRD patterns of the prepared samples are given in Figure 3. It is seen that the materials exhibit an amorphous structure. In the XRD pattern of the

BUC0.6 sample, which has a high bentonite ratio, the main peak of the bentonite structure became evident at $2\theta = 6.9^\circ$, expectedly (Atkovska *et al.*, 2016).

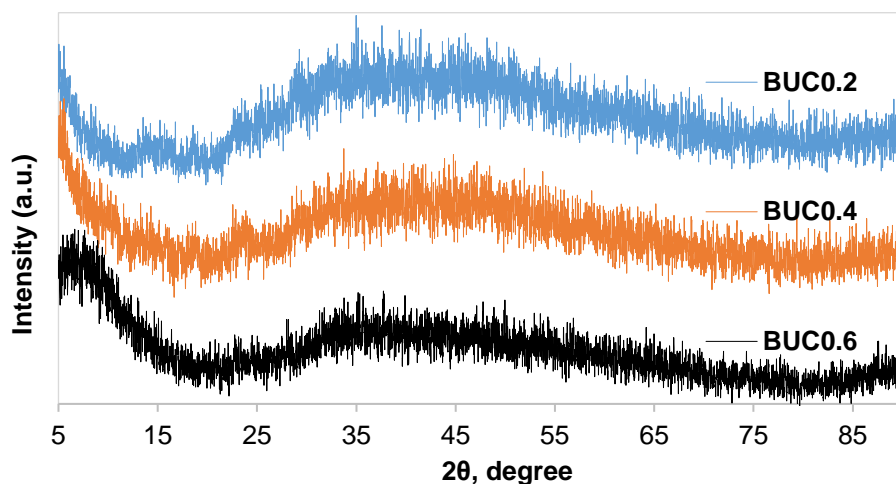


Figure 3: XRD patterns of the prepared fertilizer samples.

The degradation properties of fertilizer materials in soil are fundamental in terms of their environmental effects. For biodegradability analysis of the prepared fertilizers, this study used two different soil types: infertile garden soil (Soil1) and commercial soil (Soil2). Before the degradation tests, soil analyses were carried out for Soil1 and Soil2 samples, and the properties of soil types such

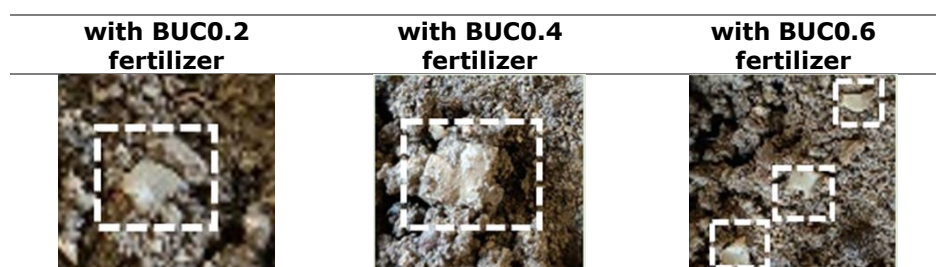
as saturation in water, pH, conductivity, organic matter, phosphorus, potassium, calcium, and magnesium contents were compared (Table 1). It was observed that the water saturation, conductivity, organic matter, potassium, and calcium contents of the Soil1 sample were lower than those of Soil2.

Table 1: Properties of Soil1 and Soil2.

Property	Soil1	Soil2
Saturation with water (%)	78	177
Textural class	Clayey	Clayey
Electrical conductivity (dS/m)	0.92	2.82
Soil pH	7.06	6.66
Lime, CaCO ₃ (%)	5.30	3.60
Organic matter (%)	6.03	25.26
Available P ₂ O ₅ (kg/daa)	55.10	47.20
Available K ₂ O (kg/daa)	357.7	922.6
Available calcium (mg/kg)	5320	9060
Available magnesium (mg/kg)	849.5	969.0

In this study, the degradation properties of nitrogen-containing chitosan/bentonite samples were examined in soil. For this purpose, chitosan/bentonite was prepared as a film. The films were cut into 1 cm*1 cm dimensions and placed in the soil, and photographs were taken on the 15th day (Figure 4). It was observed that the films placed in Soil1 were slightly deformed after 15 days. The samples could not be weighed because they stuck to the soil. BUC0.6 was degraded in the soil. These

observations visually show the deformation of films placed in soil. The films placed in Soil2 could not be observed at the end of the 15th day. This situation was thought to be related to the higher organic matter content of Soil2. Hamid *et al.* (2013) stated that chitosan films containing urea in soil appeared brittle and decreased in size on the 15th day (Hamid *et al.*, 2013). Eddarai *et al.* (2022) stated that 21 days were sufficient for plasticized chitosan films to decompose in soil.

**Figure 4:** Degradation of the samples in soil 1.

The swelling percentages of BUC0.2-0.6 materials containing urea in an aqueous environment are calculated and given in Figure 5. The swelling percentage of the material containing 0.6 bentonite (BUC0.6) was found to be slightly higher than BUC0.2 and BUC0.4. As the bentonite ratio decreased, a decrease in swelling percentages was observed. The swelling percentages of materials containing 0.2 and 0.4 bentonite were found to be very close to each other. It was observed that the swelling rate was 31.6% with BUC0.2, 32.1% with BUC0.4, and 48.6% with BUC 0.6. The swelling test was followed for 120 hours, and it was observed that the swelling percentages fluctuated over time. This fluctuation may be due to nitrogen release during swelling experiments. Santos *et al.* (2015) stated that they observed a similar result in the

release of phosphate from chitosan-montmorillonite microspheres. In their studies, fluctuations were observed in the swelling properties of chitosan-montmorillonite microspheres over time (Santos *et al.*, 2015). In another study, Chitosan-based urea fertilizer was prepared by Hamid *et al.* (2013). The water absorption percentages of these fertilizers were found between 10 and 20%. Piluharto *et al.* (2017), investigated the phosphate-release properties of chitosan-based composite beads. The water absorption by chitosan and chitosan-bentonite composite beads was measured, and it was reported that water absorbance increases with chitosan molecular weight increase. Additionally, it was found that adding chitosan/bentonite composite beads resulted in lower water absorbance when compared to the chitosan addition.

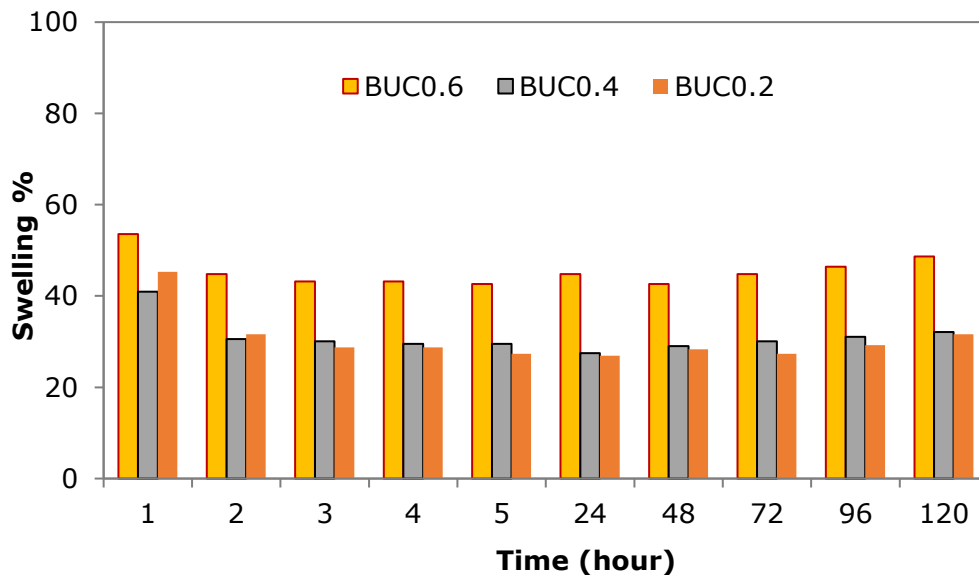


Figure 5: Swelling properties of the prepared fertilizer samples.

Figure 6 shows the nitrogen release profile from beads in water. Release experiments were followed for 32 days. It was observed that a very rapid nitrogen release occurred in the first hours of release in all three release profiles. This was thought to be due to the rapid dissolution of urea in water. It was observed that the cumulative release % showed a slightly decreasing trend in the following days of the release experiment. This meant that the amount of nitrogen in the release medium decreased over time. When nitrogen release profiles from spheres containing different amounts of bentonite were examined, it was observed that the nitrogen release curves were quite close to each

other. The reason for the rapid release of nitrogen from the chitosan/bentonite structure at the beginning of the release experiments can be attributed to the sudden diffusion and dissolution of urea in the solution due to its weak hydrogen bonding to the outer surface of chitosan/bentonite (Arafa *et al.*, 2022). Qudus *et al.* (2021) compared the nitrogen release properties of vinasse-based slow-release of organo-mineral fertilizer (SR-OMF) and vinasse organo-mineral fertilizer (OMF). SR-OMF fertilizer was prepared by mixing OMF with chitosan-bentonite matrix, and it was found that chitosan-bentonite matrix decrease the nitrogen release about 10 %.

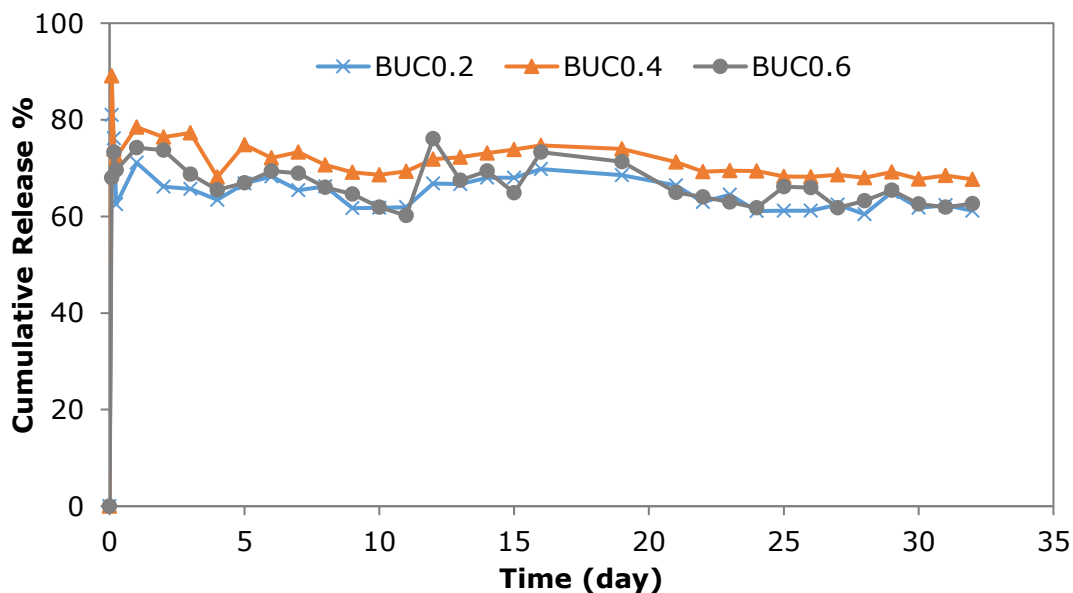


Figure 6: Cumulative nitrogen release % from the prepared fertilizer samples.

4. CONCLUSION

In this study, chitosan/bentonite beads containing urea were prepared, and the urea-nitrogen release properties of these beads in distilled water were examined. The FT-IR and XRD analyses confirmed the presence of bentonite and chitosan in the prepared fertilizer samples. It was seen that the characteristic peaks of the bentonite structure became evident in the BUC0.6 sample, which has a high bentonite ratio, while chitosan peaks were dominant in the BUC0.2 sample, as expected. It was observed that as the amount of bentonite increased, the swelling ratio generally increased. In the nitrogen release experiments, a very rapid nitrogen release occurred in the first hours of release for all three samples. This behavior was thought to be due to the rapid dissolution of urea in water. When nitrogen release profiles of the samples containing different amounts of bentonite were compared, it was observed that the nitrogen release curves were quite close to each other. The observations supported the degradation of fertilizers in soil environment. As a result, it was evaluated that the prepared materials were promising as nitrogen fertilizer.

5. CONFLICT OF INTEREST

No conflict of interest was declared by the authors.

6. ACKNOWLEDGMENTS

"Gazi University Research Fund" (Grant No: FHD-2022-8277) and "Scientific and Technological Research Council of Turkey" (TUBITAK-2209/A, No: 1919B012221923) are gratefully acknowledged.

7. REFERENCES

- Abdelkrim, S., Mokhtar, A., Djelad, A. Bennabi, F., Souna, A., Bengueddach, A., Sassi, M. (2020) Chitosan/Ag-Bentonite Nanocomposites: Preparation, Characterization, Swelling and Biological Properties. *Journal of Inorganic and Organometallic Polymers and Materials*, 30, 831-840. <https://doi.org/10.1007/s10904-019-01219-8>.
- Altunkaynak, F., Okur, M., & Saracoglu, N. (2022). Controlled release of paroxetine from chitosan/montmorillonite composite films. *Journal of Drug Delivery Science and Technology*, 68, 103099. <https://doi.org/10.1016/j.iddst.2022.103099>
- Arafa, E.G., Sabaa, M.W., Mohamed, R.R., Kamel, E.M., Elzanaty, A.M., Mahmoud, A.M., & Abdel-Gawad, O.F. (2022). Eco-friendly and biodegradable sodium alginate/quaternized chitosan hydrogel for controlled release of urea and its antimicrobial activity, *Carbohydrate Polymers*, 291, 119555. <https://doi.org/10.1016/j.carbpol.2022.119555>
- Atkovska, K., Bliznakovska, B., Ruseska, G., Bogoevski, S., Boskovski, B., & Grozdanov, A. (2016). Adsorption of Fe(ii) and Zn(ii) ions from landfill leachate by natural bentonite, *Journal of Chemical Technology and Metallurgy*, 51(2), 215-222.
- Azeem, B., KuShaari, K., Man, Z. B., Basit, A., & Thanh, T. H. (2014). Review on materials & methods to produce controlled release coated urea fertilizer. *Journal of Controlled Release*, 181, 11-21. <https://doi.org/10.1016/j.jconrel.2014.02.020>
- Berber, M. R., & Hafez, I. H. (2018). Synthesis of a new nitrate-fertilizer form with a controlled release behavior via an incorporation technique into a clay material. *Bulletin of Environmental Contamination and Toxicology*, 101, 751-757. <https://doi.org/10.1007/s00128-018-2454-x>
- Bernardo, M. P., Guimarães, G. G. F., Majaron, V. F., & Ribeiro, C. (2018). Controlled phosphate release from layered double hydroxide structures: Dynamics in soil and application as smart fertilizer. *ACS Sustainable Chemistry & Engineering*, 6, 5152-5161. <https://doi.org/10.1021/acssuschemeng.7b04806>
- Bolat, İ., & Kara, Ö. (2017). Bitki besin elementleri: Kaynakları, işlevleri, eksik ve fazlalıkları. *Bartın Orman Fakültesi Dergisi*, 19, 218-228. <https://doi.org/10.24011/barofd.251313>
- Chang, Y. S., Au, P. I., Mubarak, N. M., Khalid, M., Jagadish, P., Walvekar, R., & Abdullah, E. C. (2020). Adsorption of Cu(II) and Ni(II) ions from wastewater onto bentonite and bentonite/GO composite. *Environmental Science and Pollution Research*, 27, 33270-33296. <https://doi.org/10.1007/s11356-020-09423-7>
- Daitx, T. S., Giovanela, M., Carli, L. N., & Mauler, R. S. (2019). Biodegradable polymer/clay systems for highly controlled release of NPK fertilizer. *Polymers Advanced Technologies*, 30, 631-639. <https://doi.org/10.1002/pat.4499>
- Eddarai, E.M., El Mouzahim, M., Boussem, R., Bellaouchou, A., Guenbour, A., & Zarrouk, A. (2022). Chitosan-kaolinite clay composite as durable coating material for slow release NPK fertilizer. *International Journal of Biological Macromolecules*, 195, 424-432, 2022.
- Elgarhy, A. H., Mahran, B. N. A., Liu, G., Salem, T. A., ElSayed, E. E., & Ibrahim, L. A. (2022). Comparative study for removal of phosphorus from aqueous solution by natural and activated bentonite. *Scientific Reports*, 12, 19433. <https://doi.org/10.1038/s41598-022-23178-w>
- França, D., de Barros, J. R. S., & Faez, R. (2021). Spray-dried cellulose nanofibrils microparticles as a vehicle for enhanced efficiency fertilizers. *Cellulose*, 28, 1571-1585. <https://doi.org/10.1007/s10570-020-03609-5>
- França, D., Medina, Â. F., Messa, L. L., Souza, C. F., & Faez, R. (2018). Chitosan spray - dried microcapsule and microsphere as fertilizer host for swellable - controlled release materials. *Carbohydrate Polymers*, 196, 47-55. <https://doi.org/10.1016/j.carbpol.2018.05.014>

- Giroto, A. S., Garcia, R. H. S., Colnago, L. A., Klamczynski, A., Glenn, G. M., & Ribeiro, C. (2020). Role of urea and melamine as synergic co-plasticizers for starch composites for fertilizer application. *International Journal of Biological Macromolecules*, 144, 143–150. <https://doi.org/10.1016/j.ijbiomac.2019.12.094>
- Hamid, N. N. A., Mohamad, N., Hing, L.Y., Dimin, M. F., Azam, M. A., Che-Hasan, M. H., Ahmad, M.K.S.M., & Shaaban, A. (2013). The effect of chitosan content to physical and degradation properties of biodegradable urea fertilizer. *Journal of Scientific and Innovative Research*, 2 (5), 893-902.
- Han, X., Chen, S., & Hu, X. (2009). Controlled-release fertilizer encapsulated by starch/polyvinyl alcohol coating. *Desalination* 240, 21–26. <https://doi.org/10.1016/j.desal.2008.01.047>
- Haseena, P. V., Padmavathy, K. S., Krishnan, P. R., & Madhu, G. (2016). Adsorption of ammonium nitrogen from aqueous systems using chitosan-bentonite film composite. *Procedia Technology*, 24, 733–740. <https://doi.org/10.1016/j.protcy.2016.05.203>
- Jayanudin, Lestari, R. S. D., Kustiningsih, I., Irawanto, D., Bahaudin, R., Wardana, R. L. A., Muhammad, F., Suyuti, M., & Luthfi, M. (2021). Preparation of chitosan microspheres as carrier material to controlled release of urea fertilizer. *South African Journal of Chemical Engineering*, 38, 70–77. <https://doi.org/10.1016/j.sajce.2021.08.005>
- Katip, A. (2020). Kimyasal gübre tüketiminin değerlendirilmesi: Bursa ili örneği. *Uludağ Üniversitesi Mühendislik Fakültesi Dergisi*, 25 (3) 1271–1286. <https://doi.org/10.17482/uumfd.782633>
- Liang, R., Liu, M., & Wu, L. (2007). Controlled release NPK compound fertilizer with the function of water retention. *Reactive & Functional Polymers*, 67, 769–779. <https://doi.org/10.1016/j.reactfunctpolym.2006.12.007>
- Liu, X., Liao, J., Song, H., Yang, Y., Guan, C., Zhang, Z. (2019). A biochar-based route for environmentally friendly controlled release of nitrogen: Urea-loaded biochar and bentonite composite. *Scientific Reports*, 9, 1–12. <https://doi.org/10.1038/s41598-019-46065-3>
- Mann, M., Kruger, J. E., Andari, F., McErlean, J., Gascooke, J. R., Smith, J. A., Worthington, M. J. H., McKinley, C. C. C., Campbell, J. A., Lewis, D. A., Hasell, T., Perkins, M. V., & Chalker, J. M. (2019). Sulfur polymer composites as controlled-release fertilisers. *Organic & Biomolecular Chemistry*, 17, 1929–1936. <https://doi.org/10.1039/c8ob02130a>
- Mushtaq, A., Jamil, N., Rizwan, S., Mandokhel, F., Riaz, M., Hornyak, G. L., Malghani, M. N., & Shahwani, M. N. (2018). Engineered silica nanoparticles and silica nanoparticles containing controlled release fertilizer for drought and saline areas. *IOP Conf. Series: Materials Science and Engineering*, 414, 012029. <https://doi.org/10.1088/1757-899X/414/1/012029>
- Perez, J. J., & Francois, N. J. (2016). Chitosan-starch beads prepared by ionotropic gelation as potential matrices for controlled release of fertilizers. *Carbohydrate Polymers*, 148, 134–142. <https://doi.org/10.1016/j.carbpol.2016.04.054>
- Piluharto, B., Suendo, V., Maulida, I., & Asnawati. (2017). Composite beads of chitosan/bentonite as a matrix for phosphate fertilizer controlled-release. *Journal of Chemical Technology and Metallurgy*, 52, 1027–1031.
- Qudus, N., Kusumaningtyas, R. D., Syamrizal, Z., Hartanto, D., & Zakaria, Z. A. (2021). Vinasse-based slow-release organo-mineral fertilizer with chitosan-bentonite matrix. *Jurnal Bahan Alam Terbarukan*, 10(1), 1–8.
- Queiroz, M. F., Melo, K. R. T., Sabry, D. A., Sasaki, G. L., Rocha, H. A. O. (2015). Does the Use of Chitosan Contribute to Oxalate Kidney Stone Formation?, *Marine Drugs*, 13, 141-158. <https://doi.org/10.3390/md13010141>
- Rahman, M. H., Haque, K. M. S., Khan, M. Z. H. (2021). A review on application of controlled released fertilizers influencing the sustainable agricultural production: A cleaner production process. *Environmental Technology & Innovation*, 23, 101697. <https://doi.org/10.1016/j.eti.2021.101697>
- Santos, B. R., Bacalhau, F. B., Pereira, T. D. S., Souza, C. F., & Faez, R. (2015). Chitosan-montmorillonite microspheres: A sustainable fertilizer delivery system. *Carbohydrate Polymers*, 127, 340–346. <https://doi.org/10.1016/j.carbpol.2015.03.064>
- Sarkar, A., Biswas, D. R., Datta, S. C., Dwivedi, B. S., Bhattacharyya, R., Kumar, R., Bandyopadhyay, K. K., Saha, M., Chawla, G., Saha, J. K., & Patra, A. K. (2021). Preparation of novel biodegradable starch/poly(vinyl alcohol)/bentonite grafted polymeric films for fertilizer encapsulation. *Carbohydrate Polymers*, 259, 117679. <https://doi.org/10.1016/j.carbpol.2021.117679>
- Tian, H., Liu, Z., Zhang, M., Guo, Y., Zheng, L., & Li, Y. C. (2019). Biobased polyurethane, epoxy resin, and polyolefin wax composite coating for controlled-release fertilizer. *ACS Applied Materials & Interfaces*, 11, 5380–5392. <https://doi.org/10.1021/acsami.8b16030>
- Umar, W., Czinkota, I., Gulyás, M., Aziz, T., Hameed, M. K. (2022). Development and characterization of slow-release N and Zn fertilizer by coating urea with Zn fortified nano-bentonite and ZnO NPs using various binders. *Environmental Technology & Innovation*, 26, 102250. <https://doi.org/10.1016/j.eti.2021.102250>
- Ureña-Amate, M. D., Boutarouch, N. D., Socias-Viciano, M. M., & González-Pradas, E. (2011). Controlled release of nitrate from hydrotalcite modified formulations. *Applied Clay Science*, 52, 368–373. <https://doi.org/10.1016/j.clay.2011.03.018>

Zaitan, H., Bianchi, D., Achak, O., & Chafik, T. (2008). A comparative study of the adsorption and desorption of o-xylene onto bentonite clay and alumina, *Journal of Hazardous Materials*, 153, 852-859.
<https://doi.org/10.1016/j.jhazmat.2007.09.070>